DOT/FAA/TC-14/33

Federal Aviation Administration
William J. Hughes Technical Center
Aviation Research Division
Atlantic City International Airport
New Jersey 08405

Penetration Study of Aluminum, Glass Fiber-Reinforced Aluminum Laminate, and Carbon Fiber-Reinforced Plastic

November 2014

Final Report

U.S. Department of Transportation
Federal Aviation Administration

NOTICE

Technical Report Documentation Page

1. Report No.	2. Government Accession No.	3. Recipient's Catalog No.
DOT/FAA/TC-14/33		

4. Title and Subtitle	5. Report Date
PENETRATION STUDY OF ALUMINUM, GLASS FIBER-REINFORCED ALUMINUM LAMINATE, AND CARBON FIBER-REINFORCED PLASTIC	November 2014
	6. Performing Organization Code
7. Author(s) Chris Swin, Prof. Tein-Min Tan, Ph.D., and Prof. Jonathan Awerbuch, Ph.D.	8. Performing Organization Report No.
9. Performing Organization Name and Address Drexel University College of Engineering Department of Mechanical Engineering and Mechanics 3141 Chestnut Street Philadelphia, PA 19104	10. Work Unit No. (TRAIS)
	11. Contract or Grant No. Grant Number: 97-G-032
12. Sponsoring Agency Name and Address Federal Aviation Administration Airport Safety and Operations Division (AAS-300) 800 Independence Avenue SW Washington, DC 20591	13. Type of Report and Period Covered Final Report
	14. Sponsoring Agency Code AAS-300

15. Supplementary Notes

The FAA Airport Technology Research & Development Branch PM was Mr. Keith Bagot.

16. Abstract

The current high-reach extendable turret (HRET) used to fight aircraft fires is equipped with an aircraft skin-penetrating nozzle (ASPN). The ASPN is a long, hollow, aluminum penetrator with a steel conical tip equipped with machined perforations. In an internal aircraft fire, the HRET forces the ASPN through the fuselage aluminum skin to spray water and/or chemical agents to extinguish the fire. This study investigated the effectiveness of the current ASPN design in perforating aluminum, glass fiber-reinforced aluminum laminate (GLARE), and carbon fiber-reinforced plastic (CFRP) laminate panels, which are used in the newer aircraft fuselage structures. A special test fixture was constructed for testing specimens in 90-degree (normal) and 45-degree angle penetration conditions. Strain and deformation data, as well as fracture patterns, were collected to assess the responses and failure modes of the different material systems. The data were used to validate finite element (FE) models developed during the course of this program for simulating the penetration processes of the three material systems tested.

Results showed that under normal penetration conditions, the force required to penetrate the GLARE laminates were 4, 4.5, and 6.4 times the force required to penetrate the nominal 0.04-in.-thick aluminum alloy used in transport aircraft fuselage. For the three CFRP laminate thicknesses, the required penetration force was 3.3, 4.6, and 4.8 times higher. Comparing the penetration/perforation-resisting forces required for same thickness panels showed that aluminum panels require approximately twice the force than the GLARE and CFRP laminates. It should be noted that while the largest penetration force in aluminum alloy occurs at breakthrough, in the GLARE and CFRP laminates, the largest resisting force occurs at the end of the perforation due to the conical shape of the ASPN. Under the 45-degree angle penetration condition, GLARE laminates require 2.9, 3.8, and 5.4, and CFRP panels require 2.2, 2.2, and 3.5 times higher force to penetrate than the 0.04-in.-thick aluminum laminate. Results indicated that loading rate has marginal effect on the load-penetration behavior of all three materials under both angles of perforation.

17. Key Words	18. Distribution Statement
Glass fiber-reinforced aluminum laminate, Carbon fiber-reinforced plastic, Laminate panels, Aircraft rescue and firefighting, Aircraft skin-penetrating nozzle, High-reach extendible turret, Aircraft	This document is available to the U.S. public through the National Technical Information Service (NTIS), Springfield, Virginia 22161. This document is also available from the Federal Aviation Administration William J. Hughes Technical Center at actlibrary.tc.faa.gov.

19. Security Classif. (of this report)	20. Security Classif. (of this page)	21. No. of Pages	22. Price
Unclassified	Unclassified	142	

Form DOT F 1700.7 (8-72) Reproduction of completed page authorized

ACKNOWLEDGEMENTS

Selected portions of the experimental work were performed by undergraduate students as a part of their Honors course. Their contributions were invaluable to the successful completion of this project. These students are: Mr. Patrick Giberson and Ms. Casandra Pisani (class of 2011); Mr. Lihn Bui, Ms. Kelly Collett, and Mr. Christopher Elko (class of 2012); and Mr. Eric Cristofalo (class of 2013).

The aluminum, carbon fiber-reinforced plastic, and glass fiber-reinforced aluminum laminated panels were provided via the Federal Aviation Administration (FAA) William J. Hughes Technical Center under the logistical coordination of Mr. Keith Bagot, of the FAA, who monitored the program throughout its execution. Finally, Dr. John Bakuckas, of the FAA, participated in the many different discussions on the project's results.

TABLE OF CONTENTS

APPENDICES

LIST OF FIGURES

LIST OF TABLES

LIST OF ACRONYMS

Al	Aluminum
ASPN	Aircraft skin-penetrating nozzle
CFRP	Carbon fiber-reinforced plastic
DIC	Digital Image Correlation
FAA	Federal Aviation Administration
FE	Finite element
GLARE	Glass fiber-reinforced aluminum laminate
HRET	High-reach extendable turret
IPPR	Indentation, penetration, perforation, and retraction
PAST	Penetrating Aircraft Skin Trainer

EXECUTIVE SUMMARY

The current high-reach extendable turret (HRET) used to fight aircraft fires is equipped with an aircraft skin-penetrating nozzle (ASPN). The ASPN is a long, hollow, aluminum penetrator nozzle with a machine-perforated, steel conical tip. In an internal aircraft fire, the HRET forces the ASPN through the fuselage skin to spray water and/or chemical agents through the ASPN to extinguish the fire. This study investigated the effectiveness of the current ASPN technology in penetrating and retracting through glass fiber-reinforced aluminum laminate (GLARE) and carbon fiber-reinforced plastic (CFRP) laminate panels, which are used in the newer aircraft fuselage structures. Emphasis was placed on the forces required to penetrate and perforate the test panels and retract the ASPN, and on panel deformation and failure processes during the penetration and perforation of the ASPN.

This report summarizes the experimental results of penetration and retraction testing of panels made of 2024-T3 aluminum alloy and composite laminated materials GLARE and CFRP under both normal and angle-loading conditions. Five thicknesses of aluminum alloy and three thicknesses of GLARE and CFRP laminates were tested. Laminate thickness was key in determining the force necessary for penetration/perforation of the GLARE and the CFRP laminate panels. Tests were conducted at two different angles of penetration/perforation: normal penetration, (i.e., at a 90-degree angle, perpendicular to the panel's surface) and at a 45-degree angle. Tests were conducted for both cases at two different stroke rates, 0.001 and 0.1 in./sec. The Digital Image Correlation (DIC) method was used to capture the full-field deformation as well as to study the damage formation and progression on the back surface of the panels. Additionally, a stereoscope was used to examine the cross-sectional fracture surface morphology of the GLARE at different penetration depths on a polished, cross-sectional surface.

Results showed that under normal penetration condition, the force required to penetrate the three GLARE panels were 4, 4.5, and 6.4 times the force required to penetrate the nominal 0.04-in.-thick aluminum alloy typically used in transport aircraft fuselage. For the three CFRP panel thicknesses, the required penetration force was 3.3, 4.6, and 4.8 times higher. Comparing the penetration/perforation, resisting forces required for same thickness panels showed that the aluminum panels required approximately twice the force required for the GLARE and CFRP panels. It should be noted that while the largest penetration force in aluminum alloy occurred at breakthrough, in the GLARE and CFRP laminates the largest resisting force occurred at the end of the perforation due to the conical shape of the ASPN. Under the 45-degree angle penetration condition, GLARE panels required 2.9, 3.8, and 5.4, and CFRP panels required 2.2, 2.2, and 3.5 times higher force than that used to penetrate than the 0.04-in.-thick aluminum panel. Results indicated that loading rate has marginal effect on the load-penetration behavior of all three materials under both angles of perforation.

The DIC results provided a detailed deformation pattern throughout the penetration process up to penetrator breakthrough as well as a clear indication of failure initiation and progression. Posttest examinations of the failed specimens revealed the following typical failure mechanisms. In the aluminum panel, the initiation and progression of radial cracks yielded the formation of four to eight petals about the penetration point. In the GLARE panels, the formation of matrix crazing in the glass/epoxy layer, debonding between the aluminum sheets and the glass/epoxy layers, localized plastic deformation of the aluminum layers, and radial cracks in the aluminum

layers, yielded four major petals in multiple layers. In the CFRP laminates, there was formation of massive matrix cracks and delamination. These results were used to formulate damage models for the simulation of the penetration process up to panel breakthrough.

1. INTRODUCTION.

The Federal Aviation Administration (FAA) Advisory Circular 150/5220-10D [1] requires that all high-reach extendable turrets (HRETs) used to fight aircraft fires must be equipped with an aircraft skin-penetrating nozzle (ASPN), as shown in figure 1. ASPN technology has been shown to be effective and efficient in penetrating the traditional aluminum fuselage skin of single-decked aircraft. The use of the ASPN with the HRET controls and/or extinguishes interior aircraft fires better than traditional firefighting methods [2].

(a) (b) (c)

Figure 1. Views of an HRET Equipped With an ASPN in Operation [3]

The recent introduction of advanced composites in primary aircraft structures raises the question of whether the current equipment used for penetrating aluminum skins is as effective when applied to advanced materials. Primary interest is in two composite material systems: glass fiber-reinforced aluminum (GLARE) laminate panels and carbon fiber-reinforced plastic (CFRP) laminate panels. Currently, both laminates are widely used in the new wide-body aircraft structures, such as the Boeing 787 (The Dreamliner) and the Airbus A380.

Ideally, the ASPN is positioned at a 90-degree angle, or perpendicular, to the skin of the aircraft fuselage. Typically, the location of penetration is approximately 10 to 12 in. above the passenger window to avoid penetrating into the overhead luggage compartments or other areas that may block the application of extinguishing agent [2]. However, for wide-body aircraft, such as the Airbus A380 shown in figures 1(b) and (c), normal (perpendicular) penetration of the upper level of the fuselage may not be possible and angled penetration/perforation may be necessary. Angled penetrations not only require more force, but they can cause the 6-ft-long ASPN and the 50-ft-long boom to bend. This results in higher stresses in the supporting mechanism of the HRET. Penetration effectiveness may also be compromised, as the tip of the ASPN could skip (or ricochet) over the fuselage surface. Therefore, both normal (perpendicular, 90-degree angle) and angled (45-degree angle) penetration/perforation tests were conducted in this study.

A preliminary perforation demonstration was conducted at the FAA William J. Hughes Technical Center in Atlantic City International Airport, NJ. An aluminum alloy panel was attached to a Penetrating Aircraft Skin Trainer (PAST), figure 2. This training device allows for replaceable panels, representative of aircraft skin, to be pierced by an airport firefighter using the ASPN mounted on the HRET of an ARFF vehicle. The demonstration was conducted using an ASPN installed on a 1992 E-One Titan HPR, an FAA Airport & Technology Research and

Development Branch high-performance research vehicle. The ASPN was able to penetrate the panel, but showed noticeable resistance during retraction.

Figure 2. An ASPN Penetrating an Aluminum Alloy Panel Attached to a PAST [3]

2. PURPOSE.

The increased use of advanced composite materials in the aircraft industry, especially in wide-body aircraft, has raised concerns regarding the capability and effectiveness of the existing ASPN systems to penetrate and fully perforate aircraft skins constructed with these advanced materials under both normal and oblique conditions. This issue is of particular concern since these laminates could be two to four times thicker than the aluminum alloy used in conventional transport aircraft. The forces exerted on composite panels during the retraction process of the ASPN are also of concern. These forces occur during retraction as a result of the radial pressure applied by the composites' petals and fibers on the retracting penetrator. This study examined these issues to determine the effectiveness of the ASPN system for penetration and perforation of thin composite panels and the forces required for retraction.

3. OBJECTIVE.

The objective of this study was to examine the indentation, penetration, perforation, and retraction (IPPR) process of an ASPN used in aircraft rescue and firefighting on aircraft fuselage materials. A special test fixture was constructed to test specimens in 90-degree (normal) and 45-degree angle penetration conditions. Strain and deformation data, as well as fracture patterns, were collected to assess the responses and failure modes of the different material systems. These data were used to develop and validate finite element (FE) models during the course of this program for simulating the penetration processes of the three material systems tested [4]. Highlights of the results reported herein were reported in references 5 through 7.

4. EXPERIMENTAL PROCEDURE.

4.1 Materials and Test Specimens.

The materials tested in this program included three different thicknesses of 2024-T3 clad with high-purity aluminum (Al), table 1, representing the various thicknesses found in typical aircraft fuselage panels. To investigate the thickness effect, two additional aluminum panels with thicknesses of 0.10 in. and 0.19 in., respectively, were conducted under normal penetration condition, recording only load-displacement behavior. GLARE and CFRP panels of three different thicknesses were also selected, including GLARE5x, which is used in the testing of bomb-proof luggage containers. The x in GLARE5x indicates that extra glass/epoxy layers are added in a typical GLARE5 layup.

Table 1. Test Matrix

Material	Material Designation	Layup	Total Thickness (in.)	Aluminum Volume Fraction
Al	2024-T3	NA	0.04	1
Al	2024-T3	NA	0.06	1
Al	2024-T3	NA	0.08	1
Al*	2024-T3	NA	0.10	1
Al*	2024-T3	NA	0.19	1
GLARE	G3-4/3-0.4	[Al/0/90/Al/0/90/Al/90/0/Al]	0.09	0.68
GLARE	G3-5/4-0.3	[Al/0/90/Al/0/90/Al/90/0/Al/90/0/Al]	0.10	0.60
GLARE	G5x-4/3-0.3	[Al/0/90/90/0/90/0/Al/0/90/90/0/90/0 /Al/0/90/90/0/90/0/Al]	0.13	0.35
CFRP	12-ply	$[0/\text{-}45/45/90/0/90]_s$ (BMS 8-276)	0.09	NA
CFRP	16-ply	$[0/\text{-}45/45/90]_{2s}$ (BMS 8-212K)	0.12	NA
CFRP	24-ply	$[0/\text{-}45/45/90/0/90]_{2s}$ (BMS 8-212K)	0.18	NA

*Thickness nearly the same as G3-5/4-0.3 and CFRP [0/-45/45/90/0/90] laminates

4.2 Test Setup and Procedure.

Penetration tests were conducted using a screw-driven, 55-kip capacity Instron® material testing machine (Model 5800R) with a 6.7-kip capacity load cell under stroke (displacement) control. Stroke control tests were conducted at two different stroke rates, 0.001 and 0.1 in./s, to investigate the effect of loading rate on the material responses. The test rig assembly and test setup are shown in figure 3, and the engineering drawings are included in appendix A. The 16-in.-square panels were sandwiched between two 1-in.-thick, low-carbon steel rings with a 16-in. outer diameter and 12-in. inner diameter, and secured with 20 equally spaced 0.625-in. steel bolts, forming a 14-in.-diameter circular disk. Each bolt was tightened to a 100 lbf-ft torque resulting in a fixed boundary condition. This setup also secured the system during the retraction process. For angled penetration, the panel and ring assembly were tilted 45 degrees, as shown in figure 4. Strain and deformation measurement were obtained by using strain gages and the Digital Image Correlation (DIC) method. The DIC method is an optical method that employs tracking and image registration techniques for accurate two- and three-dimensional measurements of changes in images.

Each panel was instrumented with uniaxial or rosette strain gages at 2-in. radial distance from the center of the panel, as shown in figure 5. Strain gage layouts for all panels tested are reported in appendix E. Depending on specimen type and testing condition, panels were instrumented with two to eight uniaxial or rosette strain gages on the front and back surfaces. The strain gages used were purchased from Vishay Precision Group Micro-Measurements part numbers C2A-13-125LW-350 (uniaxial) and C2A-13-125LR-350 (rosette), and installation was done according to the Vishay installation specification. The strain gage had a resistance of 350 ohms, a measured length of 0.125 in., and was capable of measuring strain up to 3% in tension or compression. The strain data acquisition system used was HBM's MGCplus system capable of acquiring up to 64 channels of strain gage data. The primary purpose of using strain gages was to ensure that the fixture was aligned properly, that the panel was seated securely, and to ensure the repeatability of the test results.

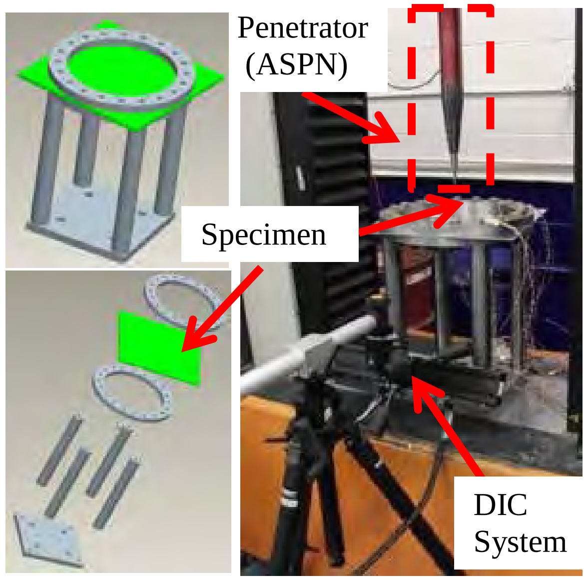

Figure 3. Experimental Setup of Normal Penetration Showing the Specimen, the Penetrator, Test Fixture, and DIC System

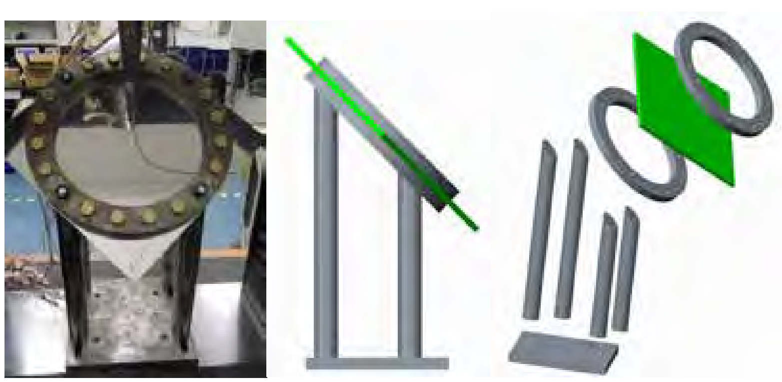

Figure 4. Experimental Setup for 45-Degree Angled Penetration Test

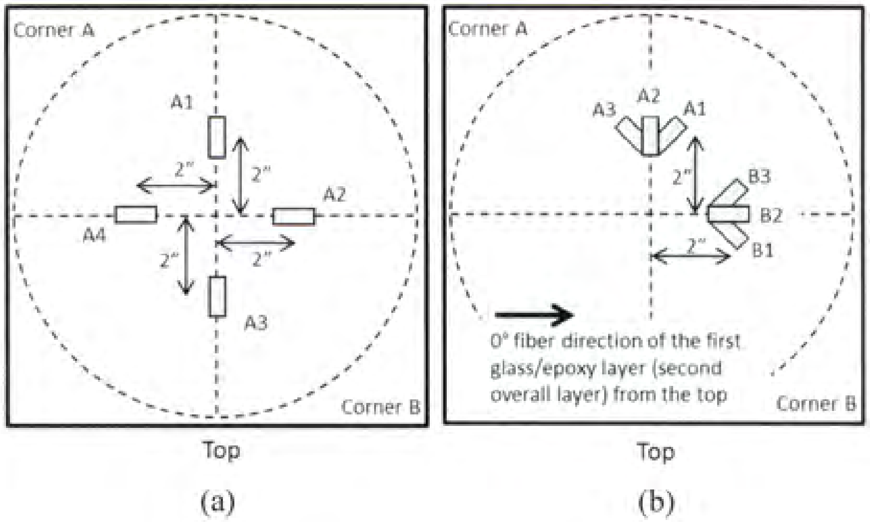

Figure 5. Strain Gage Location Maps on the top Panel Surfaces for (a) Uniaxial and (b) Rosette Strain Gages

The DIC method is a noncontact, optical measurement technique, which allows for the full-field capturing of strain and displacement data that would otherwise not be able to be captured with single-point, data-measuring methods such as strain gages and dial gages. The DIC system used was an ARAMIS 4M system from GOM, which used two charge-coupled device (CCD) cameras of 4 megapixels resolution. A high-contrast, stochastic (random), speckled pattern was coated onto the test panel by spattering black paint over evenly distributed, flat, white paint. Images were captured at a predetermined time increment. The ARAMIS software tracks the gray-scale intensity of a given predetermined area and calculates the relative movement of the pattern. Using the principle of continuum mechanics, displacement and in-plane strain components then can be calculated.

Although the DIC method allows full-field strain measurement, it has lower resolution and a higher noise level than strain gage techniques. In this series of tests, a typical strain gage noise was a few microstrain, while the DIC noise level, depending on the size of the interested area can be as high as 200-300 microstrain. The vicinity of the site of penetration was the only area in which the intensity of strain field was high enough to obtain with reasonable accuracy using DIC. At far-field locations where strain intensity was much lower, more sensitive measuring devices, such as strain gages, were used. Several pretests were conducted, and the optimal location to install strain gage was determined to be at a 2-in. radial distance from the center of the panel. The out-of-plane deformation was relatively large, yielding reliable accuracy in DIC measurements.

In this test, the minimal acceptable noise levels for principal strain and out-of-plane deformation used for the DIC results were set to be 250 microstrain and 0.001 in., respectively. Two baseline images were analyzed before the start of each test to ensure the magnitude of the experimental noise level was acceptable. Approximately 150 images were taken for each panel during loading, at 20-second intervals. The first 2030 images were analyzed in detail and are included in this report. Figure 3 shows the complete test setup, including the DIC system.

4.3 Penetrator Configuration.

The penetrator used was an existing FAA ASPN (shown in figure 6), which consists of three segments. Segment 1 is a 3.6-in.-long, steel cone with a 1-in. base diameter, heat-treated to a Rockwell Hardness of 45R. The machining of the cone's tip results in a partially spherical shape with a nominal tip diameter of approximately 0.015 in. Segment 2 consists of a 5.6-in.-long nozzle made of 8620 steel alloy and is a truncated cone perforated to perform as a nozzle for spraying, with a 1.4-in.-long cylindrical section with a 2.25-in. base diameter. Segment 3 is an 11-in.-long aluminum alloy cylindrical extension, which is attached at the other end to the load cell. The engineering drawings of the penetrator are included in appendix B. The three segments were not aligned smoothly at the joints, which resulted in discontinuities in the applied loads during perforation and retraction of the penetrator through the test panels.

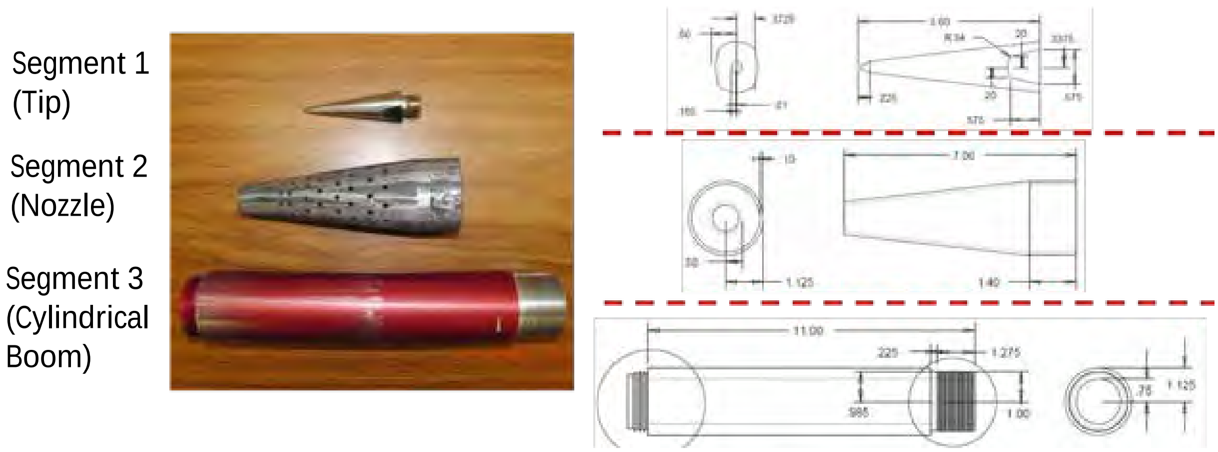

(a)

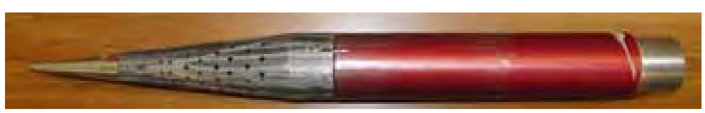

(b)

Figure 6. The ASPN Penetrator Used in This Program: (a) the Individual ASPN Segments and (b) the Assembled ASPN

5. EXPERIMENTAL RESULTS.

5.1 Strain Gage Results.

Strain gages were used to ensure that the fixture was aligned and the panel was properly seated in its fixture. A representative strain gage layout for a 0.04-in. aluminium alloy panel is shown in figure 7(a). Figure 7(b) shows strain-crosshead displacement behavior of stain gages located at the top surface of a 0.04-in.-thick aluminum panel. Initial strain is linear with increasing strain up to the breakthrough, shown as point A in figure 7(b). All four strain gages yielded very similar results up to the breakthrough, point A, indicating that the fixture was aligned properly, and the panel was seated securely. Thereafter, the strain dropped due to the formation of through-the-thickness radial cracks, emanating from the tip of the penetrator. This formed a set of four to eight petals that increased in size with increasing perforation depth. The sudden disturbance in the radial strain, at approximately 4 in. of crosshead displacement, corresponded to the machined fittings of the 3.6-in.-long steel cone and the steel nozzle, shown as point B in figure 7(b). As mentioned in the previous paragraph, the edges of these segments were not perfectly aligned with each other, which caused an abrupt disturbance in the strain field. Therefore, a stick-and-slide pattern occurred as the two segments of the penetrator passed through the panel thickness and were partially locked by the aluminum petals. Upon further perforation, the radial strain increased because of the conical shape of the ASPN, which continued to deflect the panel and increase the radial strains. The axisymmetric plate deformation was maintained through almost the entire perforation of the ASPN. The radial strain was constant through the retraction process of the cylindrical segment of the ASPN. The retraction force, and thus the radial strain, dropped once the retraction reached the conical segment. The permanent strain of approximately 2000 microstrain indicates the magnitude of the permanent deformation of the panel.

Representative results for a GLARE laminate are shown in figure 8. Similar to the behavior of the aluminum panels, GLARE panel initial strain increased linearly up until breakthrough, shown as point A in figure 8(b). The GLARE panel strain drop, point A, corresponds with back surface cracking. The sudden disturbance at approximately 4 in. of crosshead displacement (shown as point B in figure 8(b)) corresponds to the machined fittings of the 3.6-in.-long steel cone and the steel nozzle. Upon further perforation, the radial strain increased because of the conical shape of the ASPN, which continued to deflect the panel, thus increasing the radial strains. At approximately 10 in. of displacement (shown as point C in figure 8(b)), another sudden disturbance occurred that corresponds to the transition of the nozzle shape from the conical to the cylindrical. The radial strain was constant through the retraction process of the cylindrical segment of the ASPN. The retraction force and the radial strain dropped once the retraction reached the conical segment. Small, permanent strain was recorded in the GLARE panels indicating that most of the panel was still under elastic deformation. Strain gages, SG-A3 and SG-B3, showed strain values that were nearly identical throughout the test.

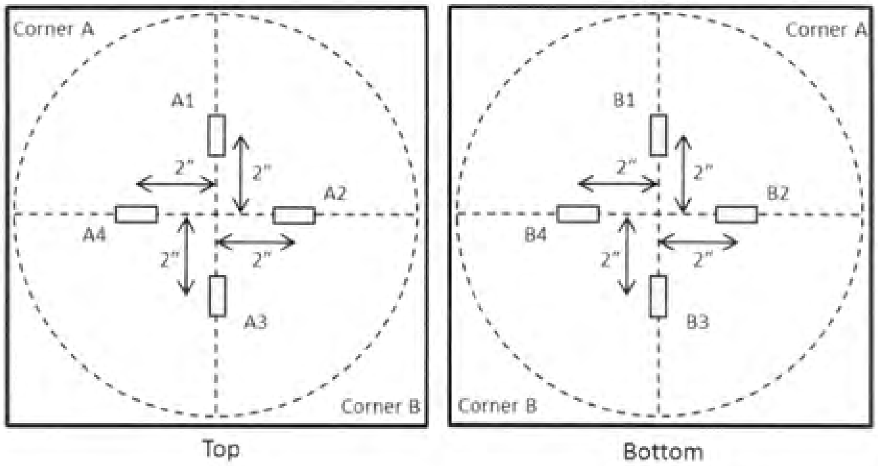

(a)

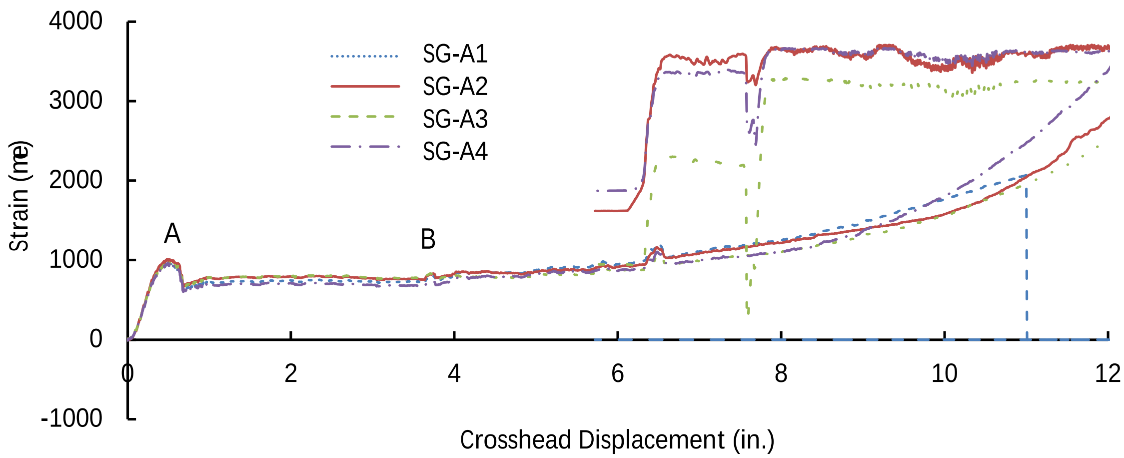

(b)

Figure 7. Results of a 0.04-in.-Thick Aluminum Panel Under Normal Penetration Condition Showing (a) the Strain Gage Location of top and Bottom Surfaces and (b) the Results of Four Strain Gages Located at the top Surface

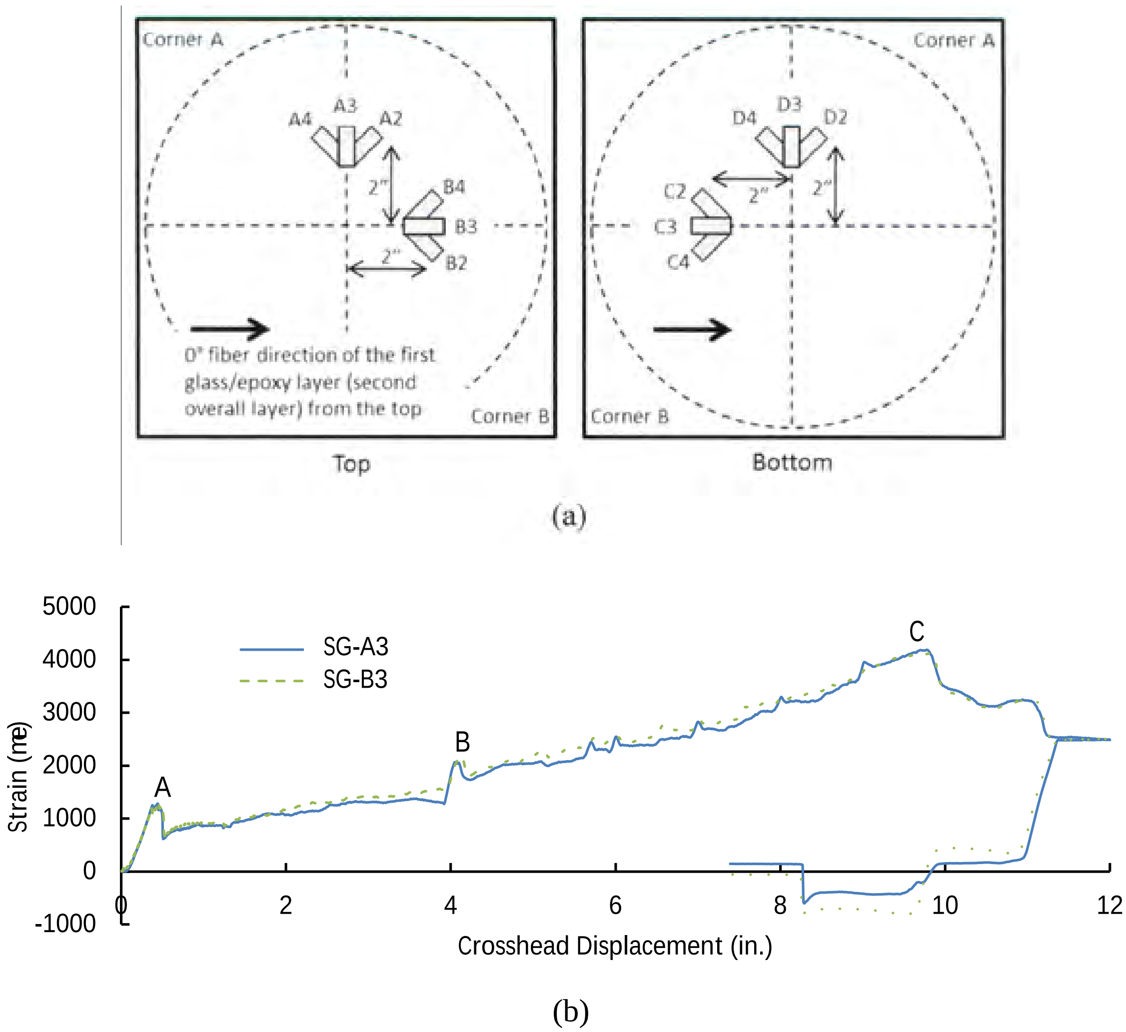

Figure 8. Results of a GLARE3-4/3-0.3 Panel Under Normal Penetration Condition Showing (a) the Strain Gage Location of top and Bottom Surfaces and (b) the Results of Strain Gages SG-A3 and SG-B3

A 16-ply CFRP panel is shown in figure 9. The CFRP strain profile is similar to GLARE, initially linear with distinct strain-drop at points A, B, and C in figure 9(b). The strain drop in the CFRP laminate at points A and B correspond with the sudden formation and growth of matrix cracking. Strain drops at point C correspond to the transition of the nozzle shape from conical to cylindrical. Strain gages SG-A2 and SG-B2 followed the same trend, but the values were different after the breakthrough, point A. After the breakthrough, strain at gage SG-B2 (along the fiber direction) was less than SG-A2 (orthogonal to the fiber direction), because the latter was more compliant. During retraction, the strain was almost constant until the conical segment was reached. Small permanent strain was recorded at the end of the test.

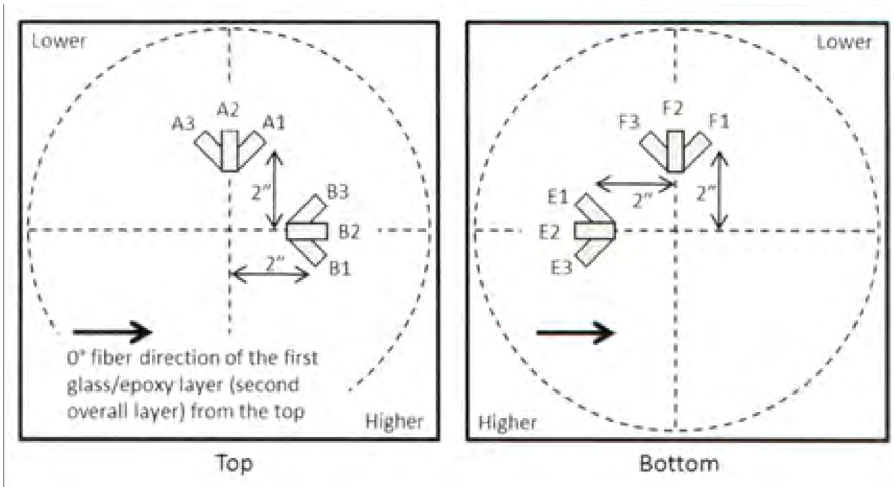

(a)

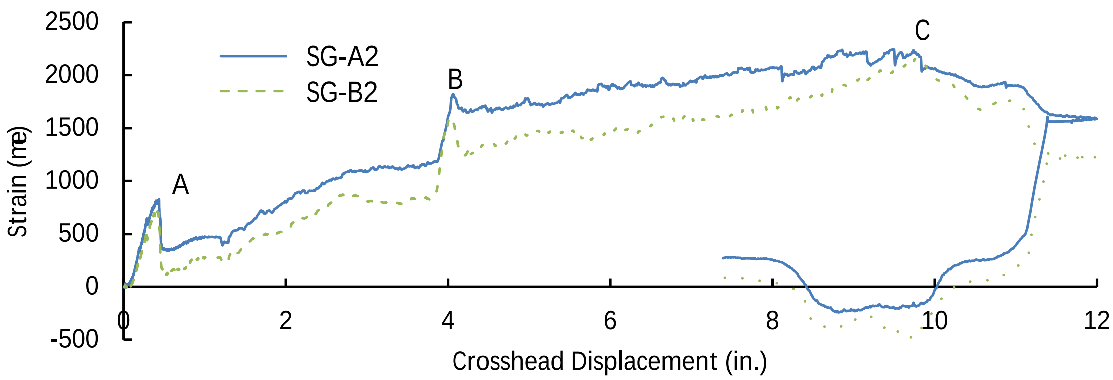

(b)

Figure 9. Results of a 16-ply CFRP Panel Under Normal Penetration Condition Showing (a) Strain Gage Location of top and Bottom Surfaces and (b) the Results of Strain Gages SG-A2 and SG-B2

<u>5.2 Force and Displacement Data</u>.

<u>5.2.1 The ASPN Penetration Load-Displacement Curves</u>.

Typical ASPN IPPR process load-displacement curves of aluminum, GLARE, and CFRP panels are shown in figure 10. The penetration and retraction processes of the long conical ASPN penetrator is divided into four distinct regions, namely, (1) indentation and tip penetration, (2) cone and nozzle perforation, (3) cylindrical perforation, and (4) retraction.

(1) <u>Indentation and Tip Penetration</u>—The penetration process of the aluminum panel was associated with an increasing load up to panel breakthrough, which was accompanied with back surface radial cracks, observed via the DIC. The formation of these cracks caused an immediate load drop, by approximately half of the maximum. Similar load drops occurred regardless of aluminum panel thickness, as shown in figure 11; this was

also true for the GLARE and the CFRP laminates, as shown in figures 12 and 13, respectively. In the GLARE panels (figure 12), the load drop was associated with back surface matrix cracking in the 0- or 90-degree direction of the fiber; however, in the CFRP panels (figure 13), the load drop was associated with matrix splitting along the 0-degree direction. In all three material systems, the load-displacement curves were nearly linear up to the point of panel breakthrough. In the aluminum panel, the breakthrough is preceded with local plastic deformation and bulging. In the GLARE and CFRP panel back surface cracking occurs while the tip of the penetrator is still embedded within the panel. As a consequence, the load drop was more pronounced in the composite laminates.

(2) <u>Cone and Nozzle Perforation</u>—The load-displacement curves were smooth during the initial perforation of the 3.6-in.-long steel cone. However, it should be noted that once the penetrator broke through, petals formed on the back surfaces of the aluminum panels and GLARE panels. The small load spikes observed in this region were caused by the petals gripping the penetrator, yielding a repeated stick-slip action. For the CFRP panels, the gripping was caused by the friction between the fiber bundles and the penetrator.

A relatively large spike in the load occurred at approximately 4 in. of crosshead displacement. It coincided with the transition from the steel cone to the 5.6-in.-long nozzle of the ASPN, due to the edge formed at the joint between the two segments. The load fluctuations shown in figure 10 were caused by the perforations machined into the conical nozzle, as it passed through the thickness of the plate, causing frictional and stick-slip forces between the rims of the nozzle's holes and the gripping panel. These load fluctuations were more pronounced in the GLARE panels, as a result of the repeated interaction between the nozzle and the individual aluminum layers and glass/epoxy plies.

The perforation of the conical segment of the ASPN in the aluminum panels and the CFRP panels was quite different from that recorded for GLARE. The load required for the continued perforation of the aluminum panels and CFRP remained constant throughout the perforation process of the conical segment. The radial cracks in the aluminum and the matrix splitting in the CFRP had little resistance to hole expansion (caused by the continued perforation of the conical segment of the penetrator), resulting in negligible axial frictional forces. For GLARE panel, however, crack progression in the well-bonded aluminum layers and glass/epoxy plies required added radial forces, thus, increasing the axial frictional forces necessary during the continuous penetration process.

(3) <u>Cylindrical Perforation</u>—In all cases, a load drop was observed once the cylindrical portion of the penetrator engaged with the panel. The abrupt load spike, observed at 10-in. crosshead displacement, occurred at the point where the attachment between the conical steel segment with the aluminum cylinder of the ASPN traveled through the panel. As mentioned, the joint between these two segments of the ASPN did not provide a smooth transition. The petals of the GLARE gripped more tightly to the cylindrical penetrator than the CFRP and aluminum panels, requiring a continuously higher perforation load. Beyond that point, the frictional forces were quite constant in all three materials; thus, the test was terminated, and the ASPN was retracted.

(4) The ASPN Retraction—The aluminum, GLARE, and CFRP panels all exerted frictional forces on the penetrator throughout the retraction process of the cylindrical portion, thereby requiring a certain amount of retraction force. Initially, the frictional force exerted by the panels on the penetrator was nearly identical for all three materials. Further retraction increased the frictional forces caused by the petals (in the aluminum and GLARE panels) and the fiber bundles (in the CFRP panels), gripping the retracting cylinder. The load spike observed thereafter was again caused by the misalignment of the cylindrical and the nozzle segment of the penetrator. The load dropped to zero once the cylindrical portion of the ASPN was fully retracted, as expected.

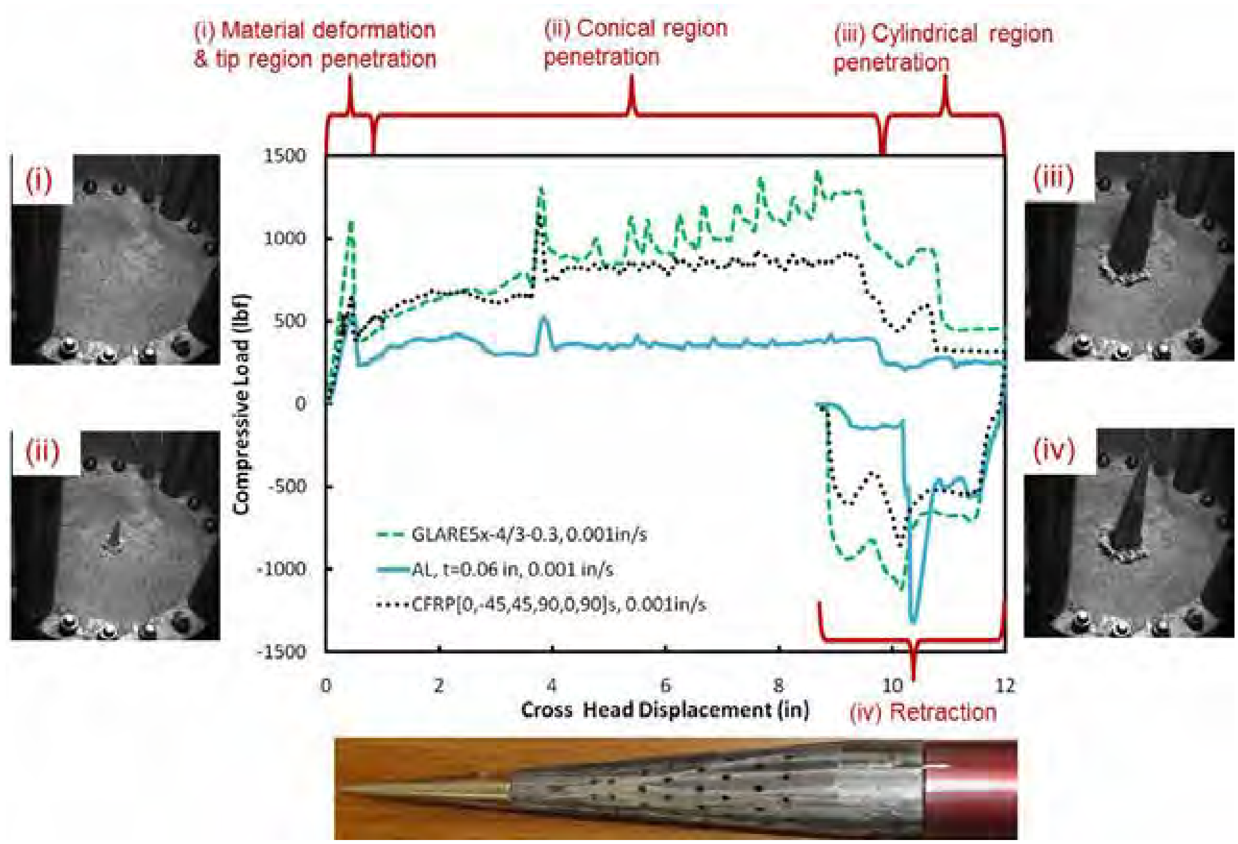

Figure 10. Typical Load Versus Crosshead Displacement Curves of the IPPR Process

5.2.2 Normal Penetration.

The load-crosshead displacement curves for normal penetration condition of 0.04-, 0.06-, and 0.08-in.-thick aluminum panels at a loading rate of 0.001 in./s are shown in figure 11. The initial portion of the penetration is shown in figure 11(a) and (b). Each curve represents the average of three repeated tests. Similar results for GLARE and CFRP panels are shown in figures 12 and 13, respectively. Load-versus-crosshead displacement of normal penetration at 0.001 in./s loading rate results of all tests are presented in appendix C, figures C-1 through C-9. These results showed that for all three materials, the load-crosshead displacement curves were highly reproducible, despite the complex failure process, indicating the reliability of the test procedure.

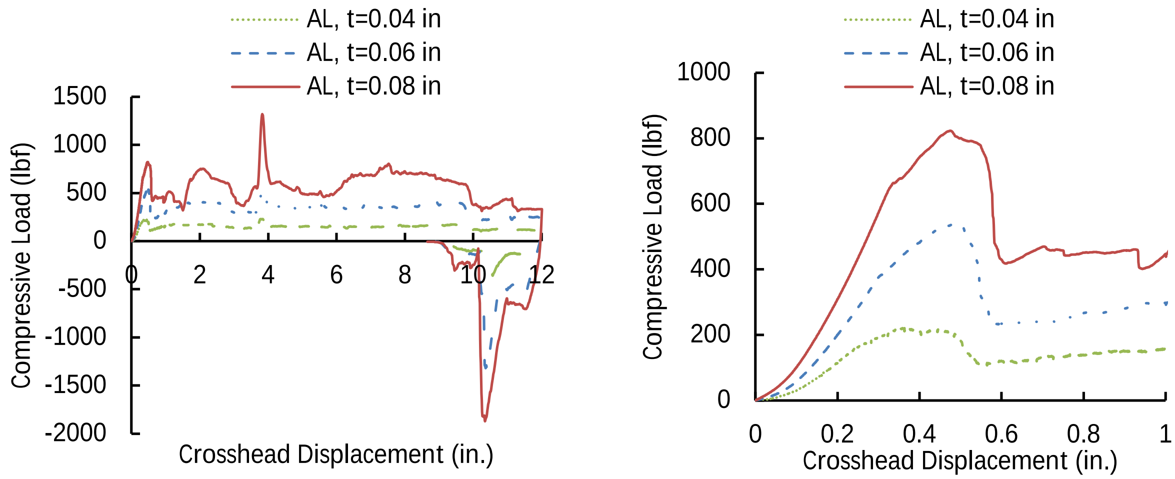

(a) (b)

Figure 11. Comparison of Normal Penetration of 0.04-, 0.06-, and 0.08-in.-Thick Aluminum Panels at 0.001 in./s Loading Rate Showing (a) the Entire ASPN IPPR Process and (b) the Initial Penetration and Perforation, up to 1-in. Crosshead Displacement

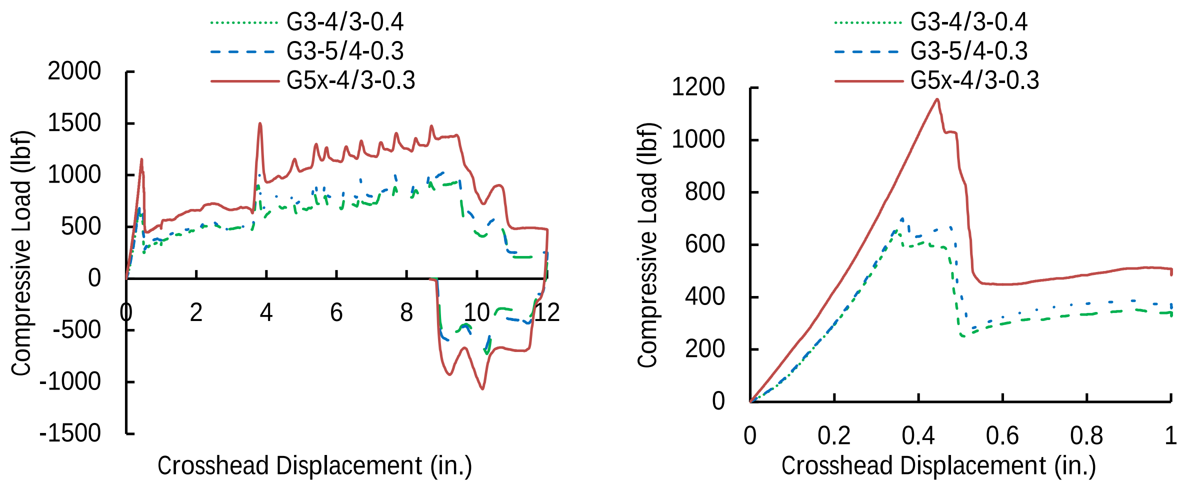

(a) (b)

Figure 12. Comparison of Normal Penetration of GLARE Panels G3-4/3-0.4, G3-5/4-0.3, and G5x-4/3-0.3 at 0.001 in./s Loading Rate Showing (a) the Entire ASPN IPPR Process and (b) the Initial Penetration and Perforation, up to 1-in. Crosshead Displacement

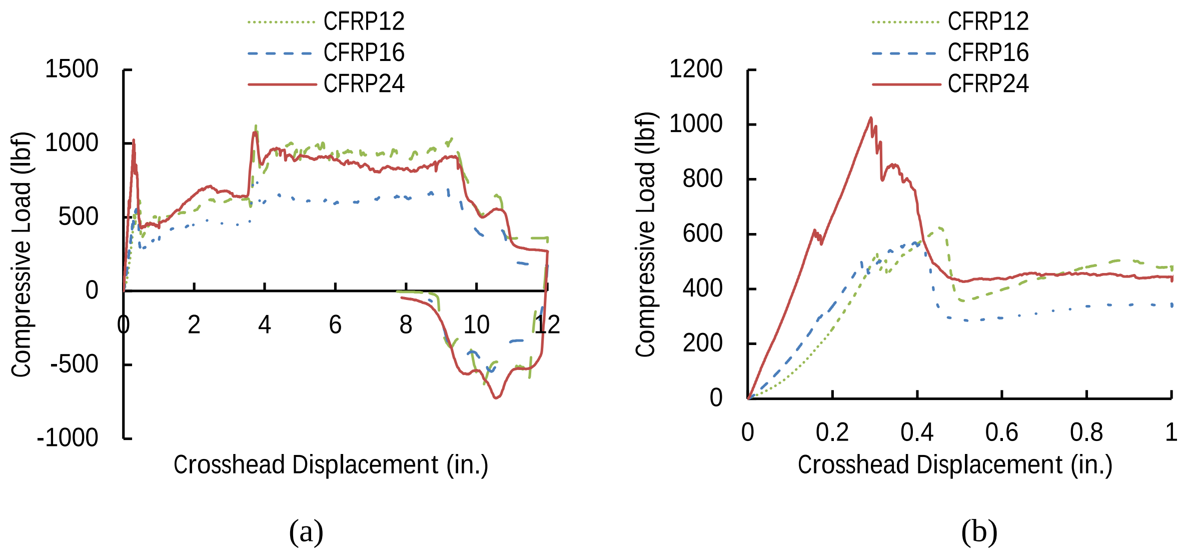

Figure 13. Comparison of Normal Penetration of 12-, 16-, and 18-ply CFRP Panels at 0.001 in./s Loading Rate Showing (a) the Entire ASPN IPPR Process and (b) the Initial Penetration and Perforation, up to 1-in. Crosshead Displacement

5.2.3 The 45-Degree Angle Penetration.

The 45-degree angle penetration characteristic of aluminum, GLARE, and CFRP panels at a loading rate of 0.001 in./s are shown in figures 14 through 16, respectively. Each case was repeated three times, and the average values are used in the figures. Each figure shows the results for three different thicknesses or layups of the same material system. A complete load-crosshead displacement of 45-degree penetration at 0.001 in./s loading rate result are presented in appendix C, figures C-10 through C-18.

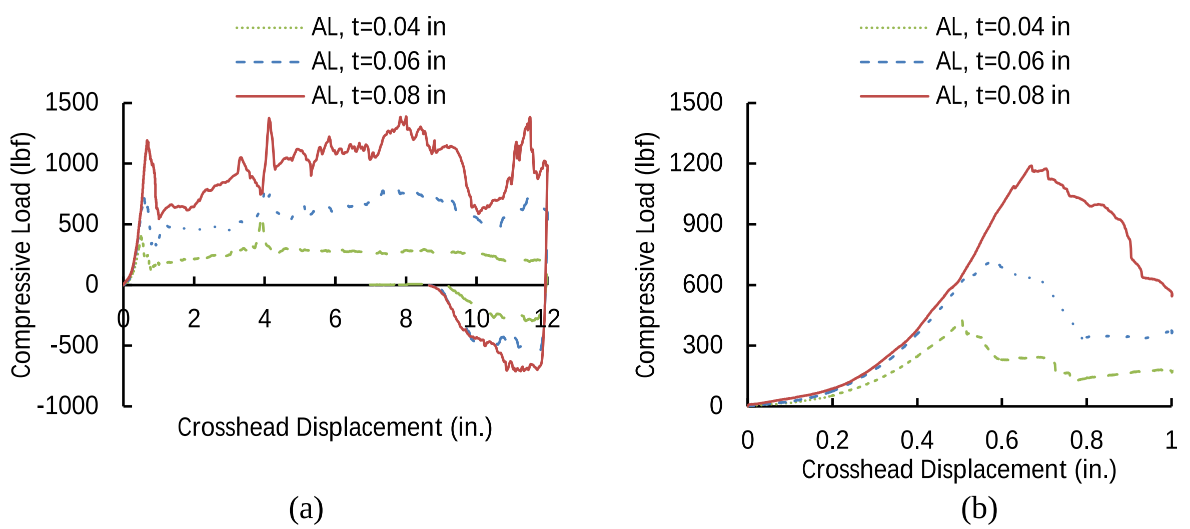

Figure 14. Comparison of 45-Degree Angle Penetration of 0.04-, 0.06-, and 0.08-in.-Thick Aluminum Panels at 0.001 in./s Loading Rate Showing (a) the Entire ASPN Process and (b) Initial Penetration up to 1-in. Crosshead Displacement

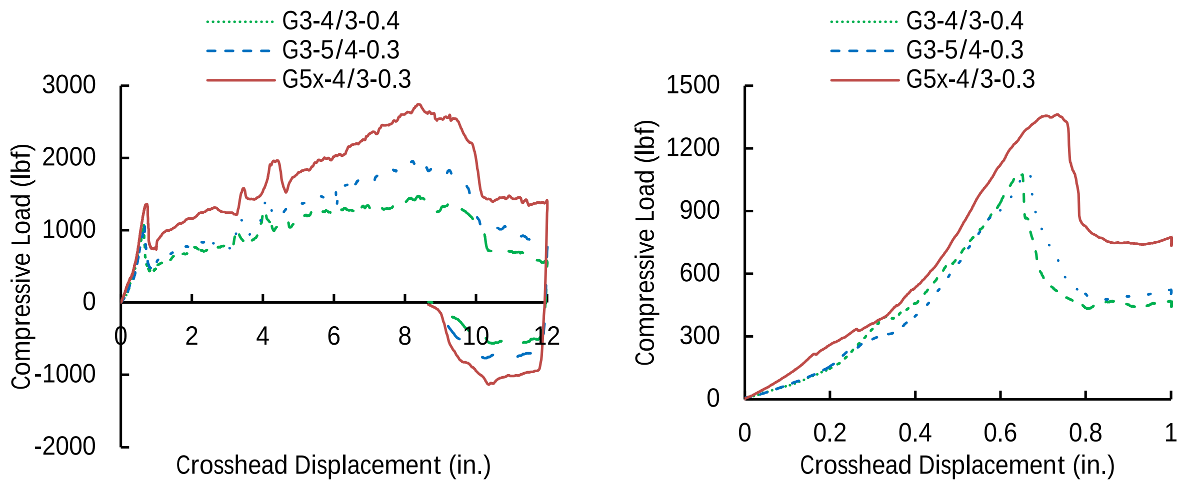

(a) (b)

Figure 15. Comparison of 45-Degree Angle Penetration of GLARE Panels G3-4/3-0.4, G3-5/4-0.3, and G5x-4/3-0.3 at 0.001 in./s Loading Rate Showing (a) the Entire ASPN Process and (b) Initial Penetration up to 1-in. Crosshead Displacement

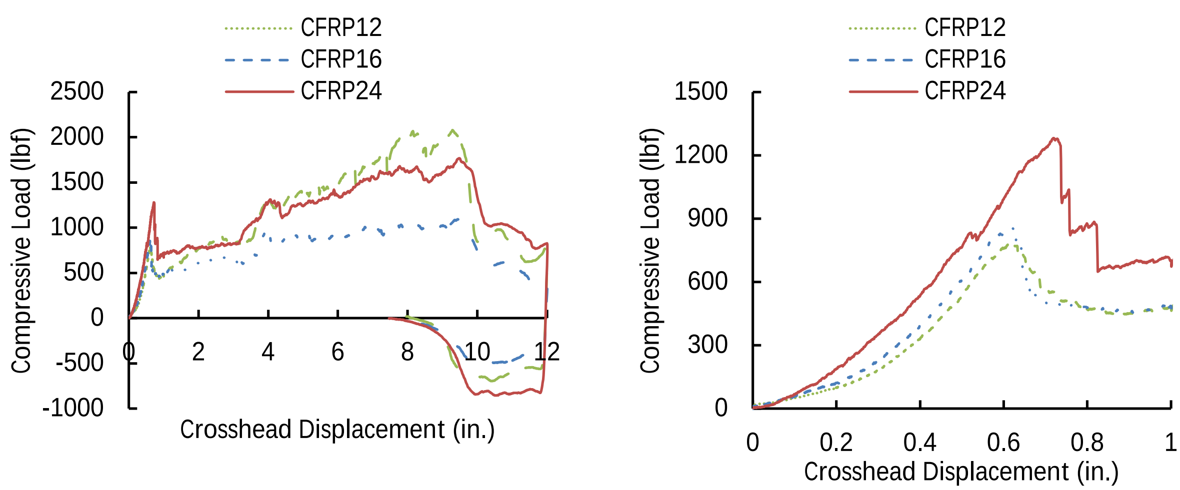

(a) (b)

Figure 16. Comparison of 45-Degree Angle Penetration of 12-, 16-, and 18-ply CFRP Panels at 0.001 in./s Loading Rate Showing (a) the Entire ASPN Process and (b) Initial Penetration up to 1-in. Crosshead Displacement

The 45-degree angle penetration case required higher penetration force than the normal penetration force needed to break through the back surface of the panel. The aluminum panels required an average of 88%, 44%, and 54% higher force to break through the 0.04-, 0.06-, and 0.08-in. thicknesses, respectively, table 2. For the GLARE panels, the 45-degree penetration force required was higher by 61%, 53%, and 19% for G3-4/3-0.4, G3-5/4-0.3, and G5x-4/3-0.3, respectively. The load-crosshead displacement characteristics for all three GLARE panels were essentially similar. For the CFRP panels, the normal and inclined penetration force was nearly the same for the12-ply panels; however, the required force was higher by 52% for 16-ply panels and 20% for 24-ply panels, as compared with the normal penetration cases. For both the GLARE and CFRP panels, the rate of increase of the load-crosshead displacement was higher for the thicker panels.

Table 2. Summary of Breakthrough Load, Maximum Penetration Load, and Maximum Retraction Load for Normal and 45-Degree Angle Loading Conditions

Panel Identification	Breakthrough Load (lbf)			Maximum Penetration Load (lbf)			Maximum Retraction Load (lbf)		
	Normal	45°	% Difference	Normal	45°	% Difference	Normal	45°	% Difference
AL4	226	426	88	241	512	113	327	328	1
AL6	546	786	44	555	888	60	1445	599	-59
AL8	811	1247	54	1261	1496	19	1684	837	-50
G3-4/3	666	1069	61	958	1488	55	742	654	-12
G3-5/4	715	1092	53	1073	1967	83	732	820	12
G5x-4/3	1157	1372	19	1553	2757	78	1073	1151	7
12-ply CFRP	627	631	1	1153	1149	0	685	726	6
16-ply CFRP	582	887	52	788	1106	40	597	497	17
24-ply CFRP	1078	1295	20	1109	1780	61	730	806	10

The comparison of the breakthrough loads that caused back surface panel cracking for both the normal and the 45-degree angle penetration is shown in figures 17 and 18, respectively, and is tabulated in table 3. The breakthrough loads required to penetrate the GLARE panels were 2.9 to 5.1 times higher than the loads required to penetrate the 0.04-in.-thick aluminum under normal penetration condition. For the CFRP panels, it was 2.6 to 4.8 times higher. Under the 45-degree angle penetration condition, the GLARE panels required 2.5 to 3.2 and CFRP panels required 1.5 to 3 times higher loads than that required to penetrate the 0.04-in.-thick aluminum.

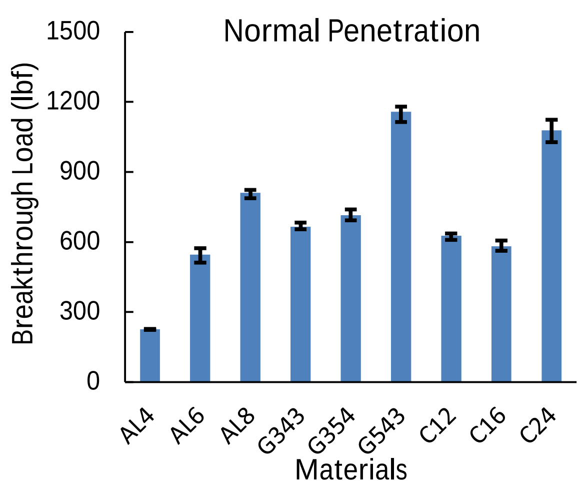

Figure 17. Comparison of Breakthrough Load of Normal Penetration at 0.001 in./s

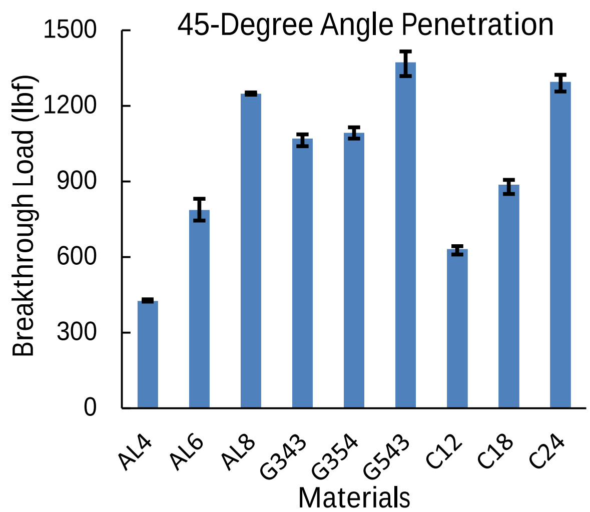

Figure 18. Comparison of Breakthrough Load of 45-Degree Angle Penetration at 0.001 in./s

Table 3. Summary of Breakthrough Load and Maximum Penetration Load Ratios of Composite Panels With Respect to 0.04-in.-Thick Aluminum Panel Under Normal and 45-Degree Angle Loading Conditions

Panel Identification	Breakthrough Load Ratio		Maximum Penetration Load Ratio	
	Normal	45°	Normal	45°
G3-4/3/AL4	2.9	2.5	4.0	2.9
G3-5/4/AL4	3.2	2.6	4.4	3.8
G5x-4/3/AL4	5.1	3.2	6.4	5.4
C12/AL4	2.8	1.5	4.8	2.2
C16/AL4	2.6	2.1	3.3	2.2
C24/AL4	4.8	3.0	4.6	3.5

The comparison of the maximum penetration loads for normal and 45-degree penetration angles are shown in figures 19 and 20, respectively, and tabulated in table 3. Under normal penetration, the maximum loads required to penetrate the GLARE panels were 4 to 6.4 times higher than the loads required to penetrate the 0.04-in.-thick aluminum. For the CFRP panels, the required penetration loads were 3.3 to 4.8 times higher. Under the 45-degree angle penetration condition, the GLARE panels required 2.9 to 5.4 and CFRP panels required 2.2 to 3.5 times higher penetration loads than that required for the 0.04-in.-thick aluminum panels.

The average maximum loads required to perforate the of 0.04-, 0.06-, and 0.08-in.-thick aluminum panels at 45 degrees were higher by 113%, 60%, and 19%, respectively, compared to the normal penetration, table 2. The loads required to perforate the GLARE panels G3-4/3-0.4, G3-5/4-0.3, and G5x-4/3-0.3 at 45 degrees are higher by 55%, 83%, and 78%, respectively. The loads required to perforate the CFRP laminates were nearly the same for the 12-ply panel, but at 45 degrees, the penetration loads required were higher by 40% for the 16-ply panel and 61% for 24-ply panel, respectively.

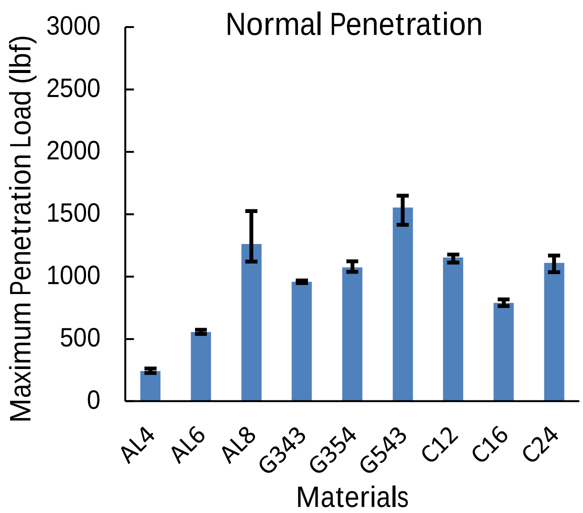

Figure 19. Comparison of Maximum Penetration Load for Normal Penetration at 0.001 in./s

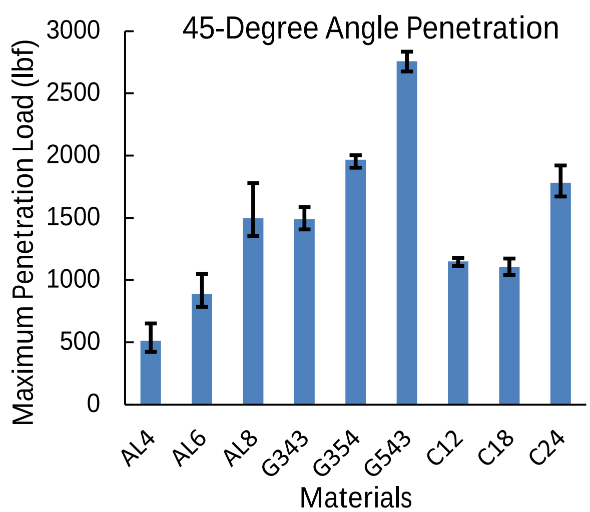

Figure 20. Comparison of Maximum Penetration Load of 45-Degree Penetration at 0.001 in./s

The comparison of the maximum retraction loads for normal and 45-degree penetration angles are shown in figure 21 and 22, respectively. In general, it was determined that the maximum retraction loads for normal and 45-degree conditions were similar. Exceptions occurred in the cases of 0.06-in.- and 0.08-in.-thick aluminum panels, the normal retraction force was double that of the 45-degree retraction force.

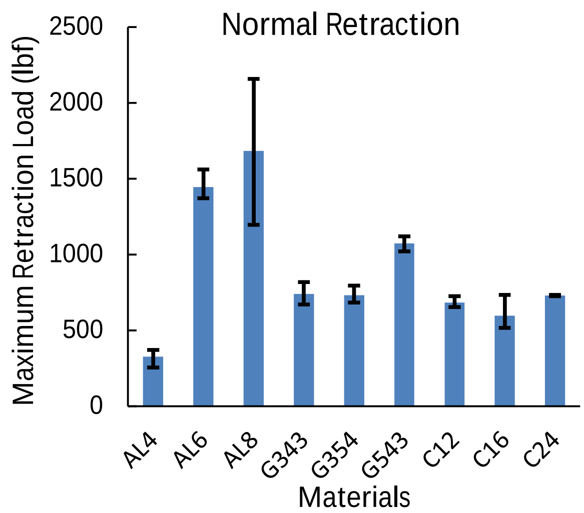

Figure 21. Comparison of Maximum Retraction Loads for Normal Retraction at 0.001 in./s

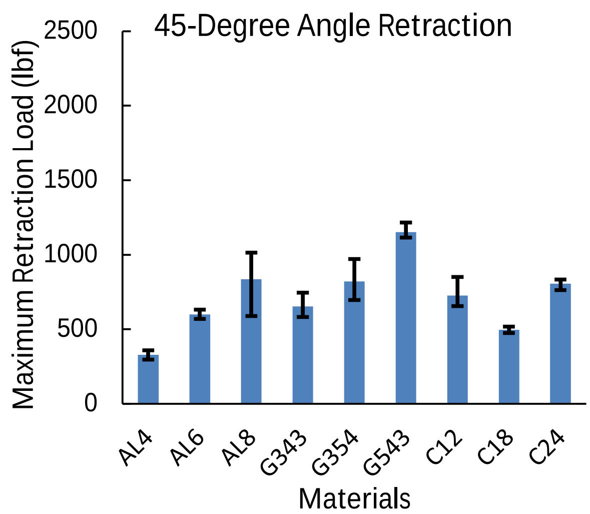

Figure 22. Maximum Retraction Load Comparison of 45-Degree Retraction at 0.001 in./s

The final perforated panels are shown in figure 23 for all three material systems. In the aluminum panels, radial cracks developed during penetration forming four to eight petals upon perforation. In the GLARE panels, only four major petals formed upon perforation, which propagated along the 0-degree and 90-degree fiberglass/epoxy layers. However, numerous secondary petals also formed associated with each individual aluminum layer, resulting from the extensive aluminum-glass/epoxy debonding in the vicinity of the perforation. In the CFRP panels, numerous fiber breakages accompanying the significant matrix splitting were observed along the outer layer fiber directions. The overall failure process was independent of panel thickness or laminate configuration.

(a) AL 0.04, normal

(b) GLARE3-5/4-0.3, normal

(c) CFRP12, normal

(d) AL 0.04, 45°

(e) GLARE3-5/4-0.3, 45°

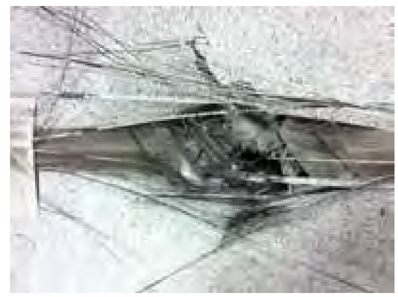

(f) CFRP12, 45°

Figure 23. The Perforated Panels
(The aluminum panels have four to eight petals. The GLARE panels have four major petals with multiple minor petals. The CFRP panels show numerous fiber breaks along with significant matrix splitting.)

5.3 Thickness Effect.

To compare the thickness effect, tests were conducted on two additional panels of 0.10- and 0.19-in.-thick aluminum under normal penetration. The two thicknesses were chosen to closely match the laminate panels tested based on the availability of aluminum sheet thicknesses manufactured by ALCOA. Only load-displacement data were recorded and compared. Results of aluminum panels of all five thicknesses under normal penetration are shown in figure 24. The load-crosshead displacement curves were similar for all five aluminum panels, with load drop occurring due to panel breakthrough around the crosshead displacement of 0.5 in. In the thinner aluminum panels, failure was dominated by bending, which caused the membrane of the panels' back surfaces to stretch until breakage Alternatively, the thicker aluminum panels experienced a higher localized penetration damage, which caused shear dominant failure.

The load-crosshead displacement curves under normal penetration condition for the 0.1-in.-thick aluminum panel and the three GLARE panels are shown in figure 25. The total thicknesses for the three GLARE panels were 0.09 in., 0.1 in., and 0.12 in., respectively. As observed in the figure, the force needed to penetrate the 0.1-in.-thick aluminum panel was higher than for all three GLARE panels. The penetrating forces for the two thinnest GLARE panels, G3-4/3-0.4 and G3-5/4-0.3, were almost half of the force needed to penetrate the 0.1-in.-thick aluminum panel.

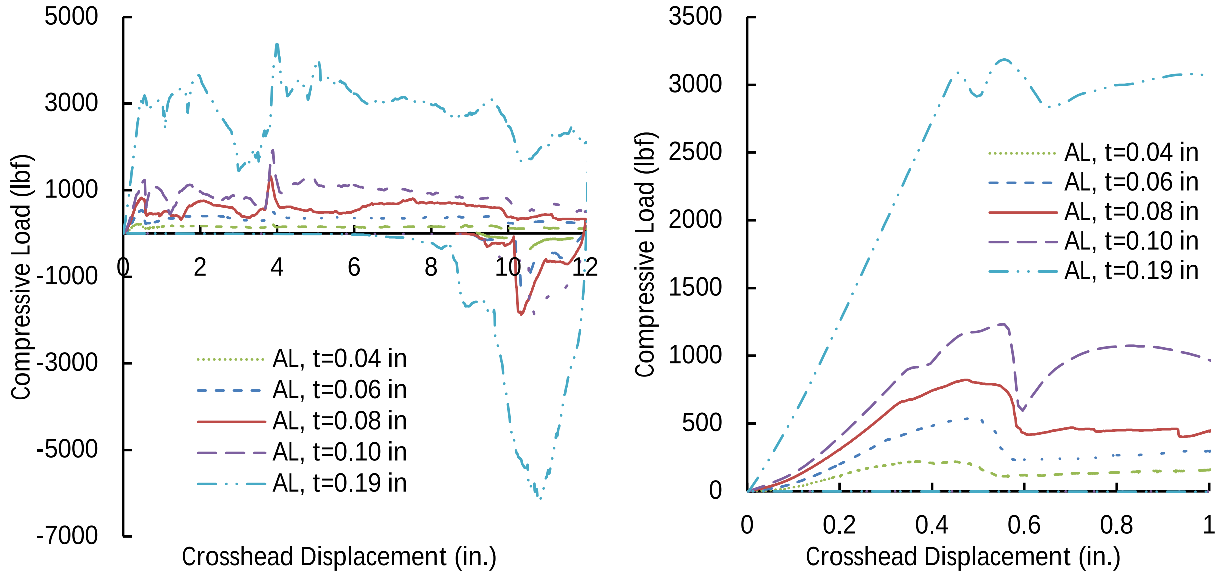

(a) (b)

Figure 24. Comparison of Normal Penetration of Aluminum Panels of 0.04-, 0.06-, 0.08-, 0.10-, and 0.19-in.Thickness at 0.001 in./s Loading Rate Showing (a) the Entire ASPN IPPR Process and (b) the Initial Penetration and Perforation, up to 1-in. Crosshead Displacement

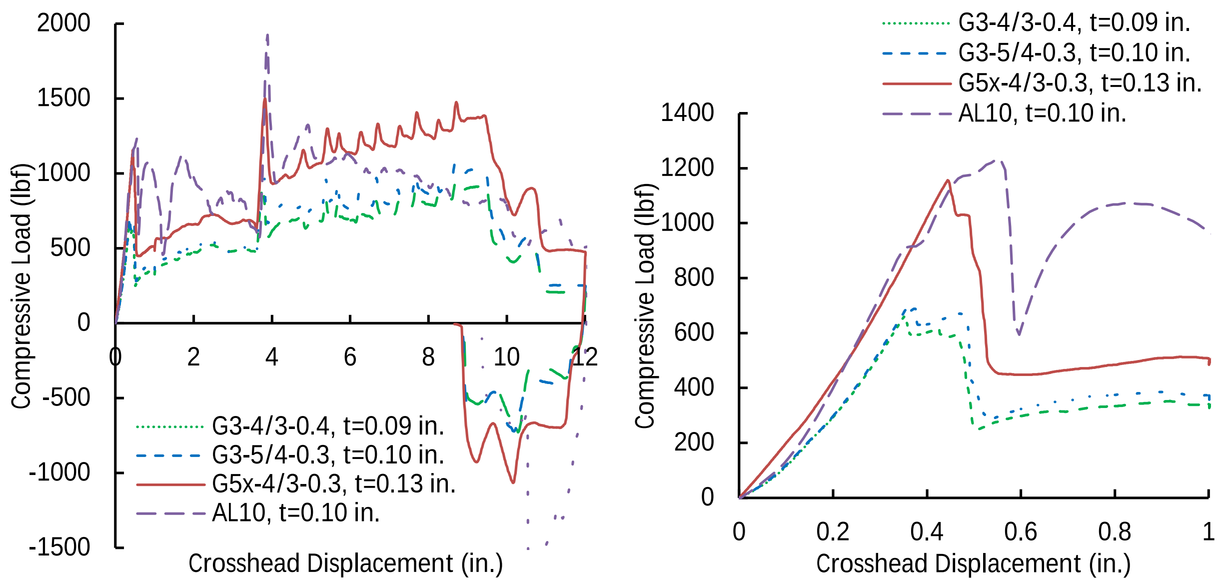

(a) (b)

Figure 25. Comparison of Normal Penetration of G3-4/3-0.4, G3-5/4-0.3, and G5x-4/3-0.3 GLARE Panels and 0.10-in.-Thick Aluminum Panel at 0.001 in./s Loading Rate Showing (a) the Entire ASPN IPPR Process and (b) the Initial Penetration and Perforation, up to 1-in. Crosshead Displacement

Figure 26 shows a comparison of the results from the three CFRP panels and the 0.1- and 0.19-in.-thick aluminum panels. The total thicknesses for the 12-, 16-, and 24-ply CFRP panels were 0.09, 0.12, and 0.18 in., respectively. As shown in the figure, the force needed to penetrate the 0.1-in.-thick aluminum panel was more than twice of that needed to penetrate the 12- and 16-ply CFRP panels. For the 0.19-in.-thick aluminum, the penetrating force was approximately four times of that needed to penetrate the 0.18-in.-thick, 24-ply CFRP panel.

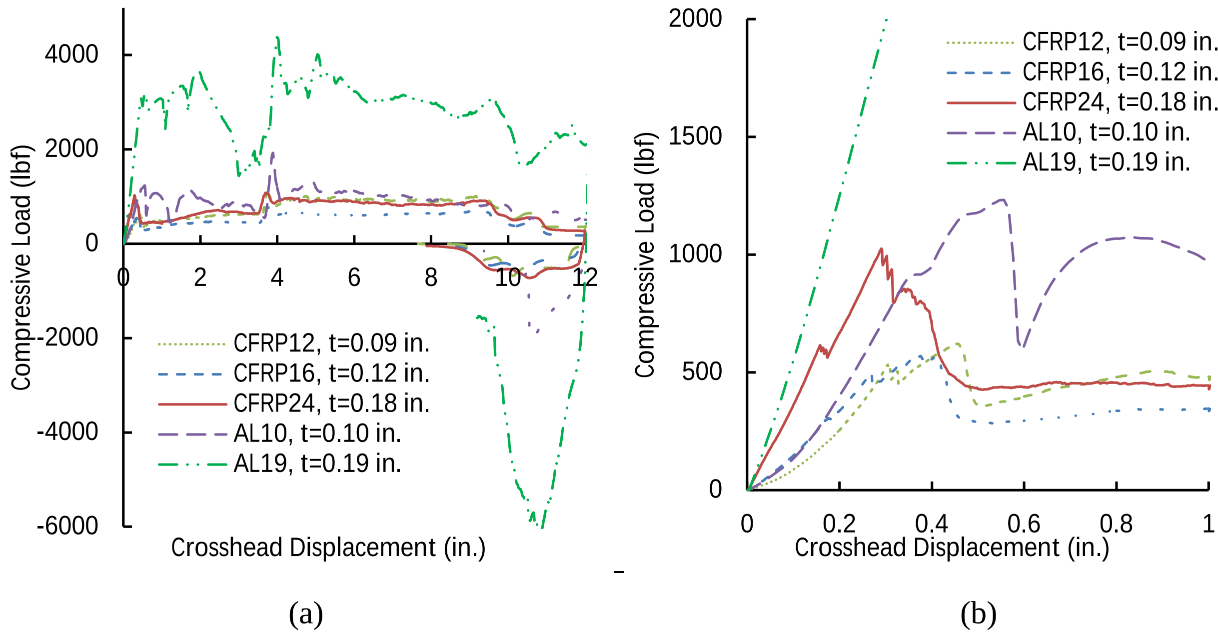

Figure 26. Comparison of Normal Penetration of 12-, 16-, and 18-ply CFRP Panels and 0.10-in.-Thick Aluminum Panel at 0.001 in./s Loading Rate Showing (a) the Entire ASPN IPPR Process and (b) the Initial Penetration and Perforation, up to 1-in. Crosshead Displacement

5.4 Loading Rate Effect.

The rate of penetration depends on the speed at which the HRET operates. To account for an extreme case of 100 times increase in the nominal penetration rate, the effect of loading rate on the perforation force and panel response was tested at a loading rate of 0.1 in./s, with one panel for each case in the test matrix, shown in table 1. The force-crosshead displacement plots of normal penetration under two loading conditions of 0.001 in./s and 0.1 in./s for 0.06-in. aluminum, G3-4/3-0.4, and 16-ply CFRP panels are shown in figure 27. The rate effect is shown to be negligible. Similar results were obtained for all other cases. The complete data for 0.1 in./s loading rate are shown in appendix D.

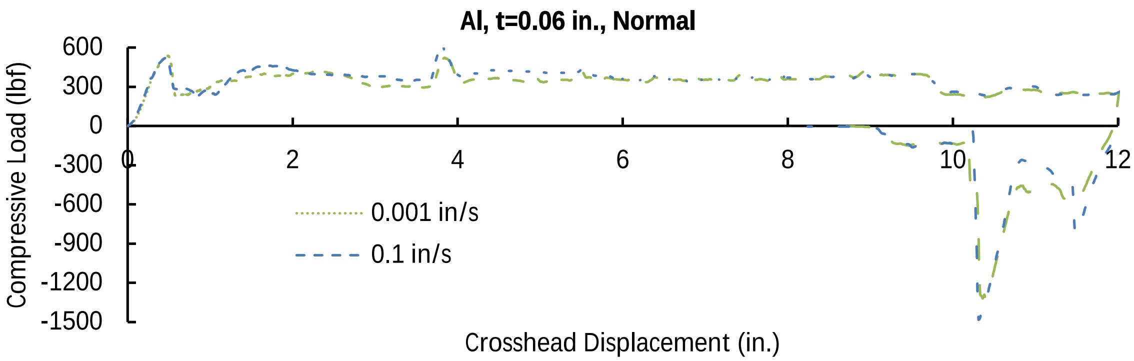

(a)

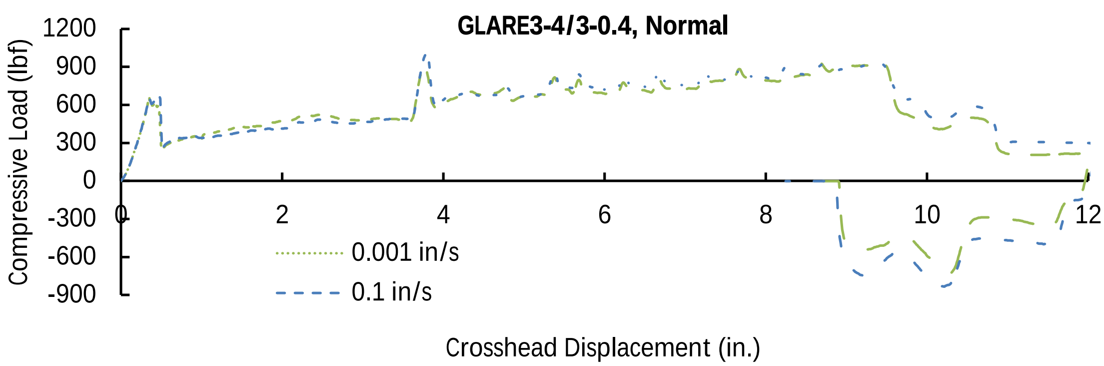

(b)

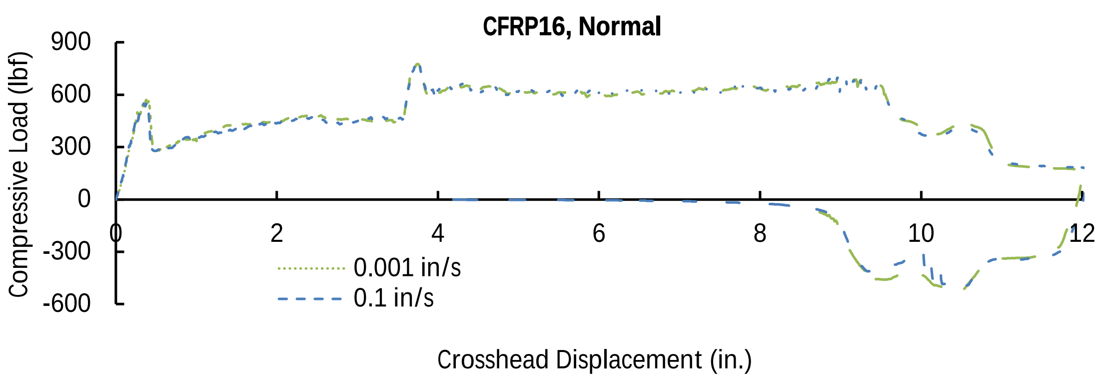

(c)

Figure 27. Comparison of Normal ASPN Penetration of (a) 0.06-in.-Thick Aluminum, (b) G3-4/3-0.4 GLARE Panel, and (c) 16-ply CFRP Panel at 0.001 in./s and 0.1 in./s Loading Rates (The rate effect is negligible.)

5.5 Penetrator Boom Bending.

During the 45-degree angle penetration tests, the boom of the ASPN experienced significant bending moment, in addition to the axial compression. To quantify this bending effect, 16 strain gages were installed around the boom, as shown in figure 28, to capture the strain distribution in it during the IPPR process. The strain gages were spaced every 2 in. along the cylindrical shaped boom at 0, 90, 180, and 270 degrees. Basic bending stress revealed that the axial force and bending moment developed during the IPPR process was constant and linear, as shown in figure 29.

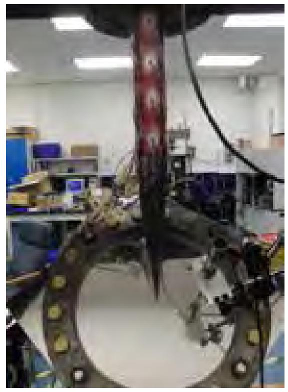

Figure 28. Setup of 45-Degree Angle Penetration Test With Strain Gage Installed Around the Boom

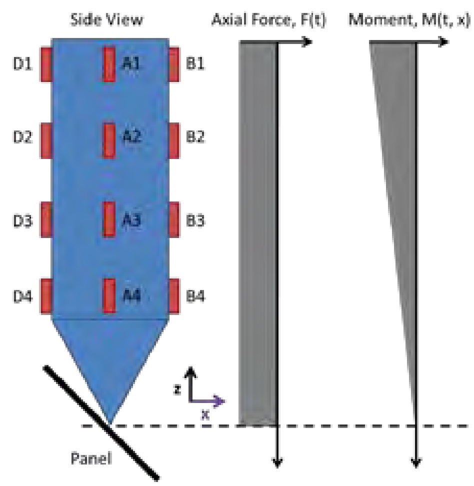

Figure 29. Axial Force and Bending Moment Diagram in the Strain-Gaged Boom (Axial force remains constant while bending moment varies linearly along the length of the boom.)

The strain recorded throughout the IPPR in strain gages A2, A3, B2, B3, C2, C3, D2, and D3 for 45-degree penetration test in the G5x-4/3-0.3 GLARE panel are shown in figure 30. The strain data recorded by the four top gages (A1, B1, C1, and D1) and the four bottom gages (A4, B4, C4, and D4) exhibited significant edge effects and therefore are not presented herein. The precise nature of the edge effect in the actual ASPN requires further research to determine the bending effect in case of angled perforation. The results for the GLARE laminate G5x-4/3-0.3, shown in figure 30, represent the worst-case scenario, because this laminate required the highest penetration force, thus yielding the highest total combined strains in the boom.

The largest total strain value in the G5x-4/3-0.3 GLARE panel was approximately 1200 microstrain, resulting from the axial force and the bending moment. The maximum penetration load was 2757 lbf (see figure 15), from which the axial strain (for the aluminum portion of the ASPN) was calculated to be 125 microstrain. It could be concluded that the bending strain was dominant (i.e., 90% of the total strain). The total maximum normal stress the boom experienced during the penetration of the thickest GLARE panel, G5x-4/3-0.3, due to the combined loading, was approximately 26 ksi, which is less than yield stress of ~40 ksi. In the two thinner GLARE panels and the three CFRP panels, the stress developed was less than 10 ksi, where the largest load was approximately 2000 lbf. However, in field applications, the ASPN boom is 65 in. long compared to the 20-in.-long penetrator used in this study. Thus, the bending stresses in the actual ASPN could be significantly higher.

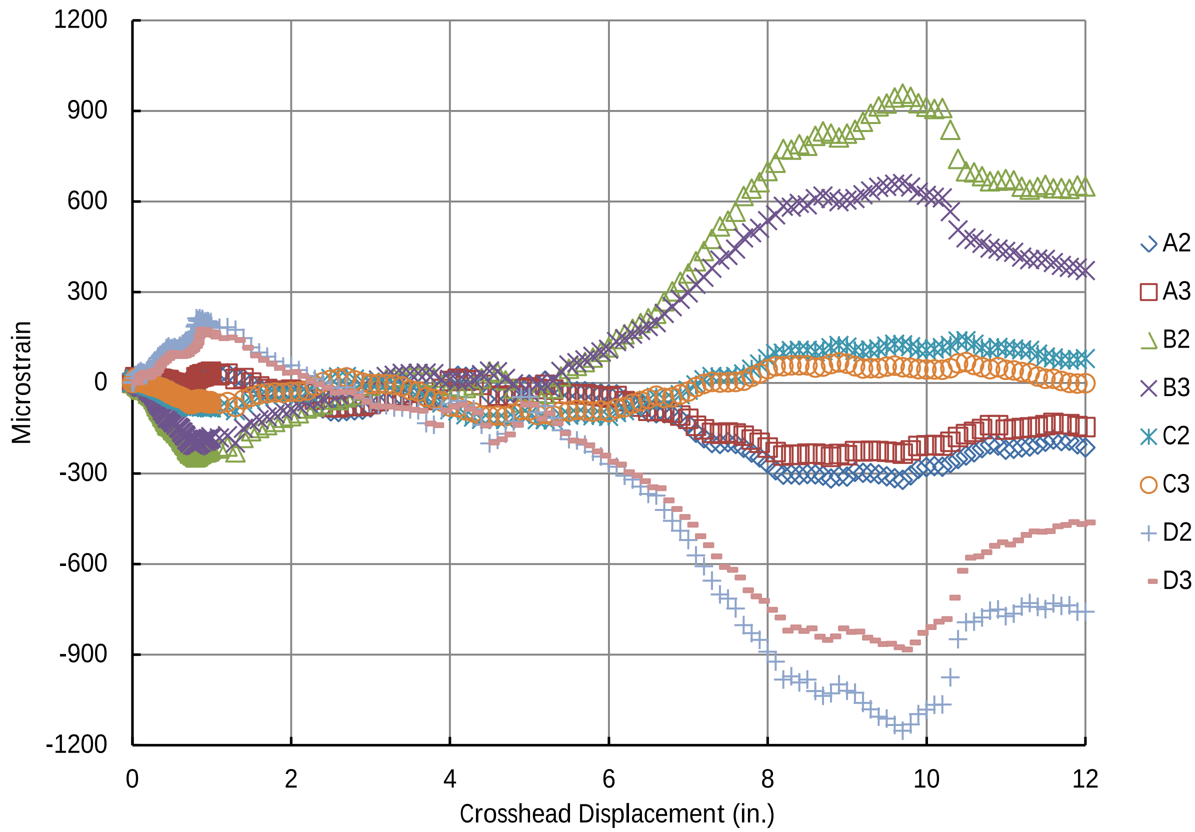

Figure 30. Strain Histories of a 45-Degree Penetration Condition of Strain Gages A2, A3, B2, B3, C2, C3, D2, and D3 From a GLARE Panel G5x-4/3-0.3 Test

5.6 Digital Image Correlation Results.

5.6.1 Out-of-Plane Deformation.

Figure 31 shows the full-field, out-of-plane deformation results of a 0.08-in.-thick aluminum panel under normal penetration. Figure 31(a) shows the full-field deformation fringe pattern overlay on the speckle-coated back surface of the panel at the stage right before panel breakthrough occurs. The contour of the fringe pattern indicates that the deformation was axisymmetric at that stage. The vicinity of the penetration site is enlarged and shown in figure 31(b). The deformation at increasing load along a section line (red line on figure 31(a)) is shown in figure 31(c). The central deflection of the panel, at increasing load, is plotted in figure 31(d), showing a nearly linear central deflection up to breakthrough. Similarly, plots are shown for representative GLARE and CFRP panels in figures 32 and 33, respectively. Initially, the deformation was axisymmetic; however, as the penetration process progressed, the deformation became nearly elliptical as a result of the formation of the first crack. The out-of-plane deformation results were used to validate the FE simulation model developed [3]. Similar DIC measurements and data reduction were performed for nearly all panels tested. Appendix F includes the DIC-generated strain and displacement fields for each test condition for all materials tested (18 out of 54 tests performed and analyzed) during the course of this program.

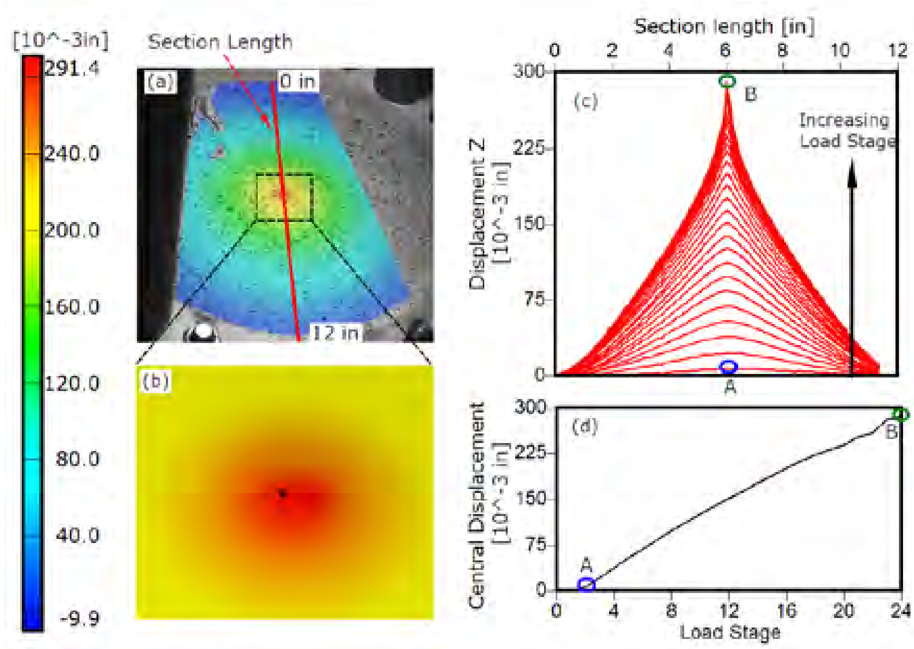

Figure 31. Strain Field and Deformation Plot Recorded for a 0.08-in.-Thick Aluminum Panel Under Normal Penetration Condition Under a Loading Rate of 0.001 in./s Showing (a) Strain Field at Breakthrough, (b) Closeup of the Strain Field at Breakthrough, (c) Panel Deflection at Increasing Loads up to Initial Back Surface Crack Initiation (i.e., panel breakthrough) Along the Section Marked in Strain Field Image (a), and (d) Central Deflection up to Breakthrough

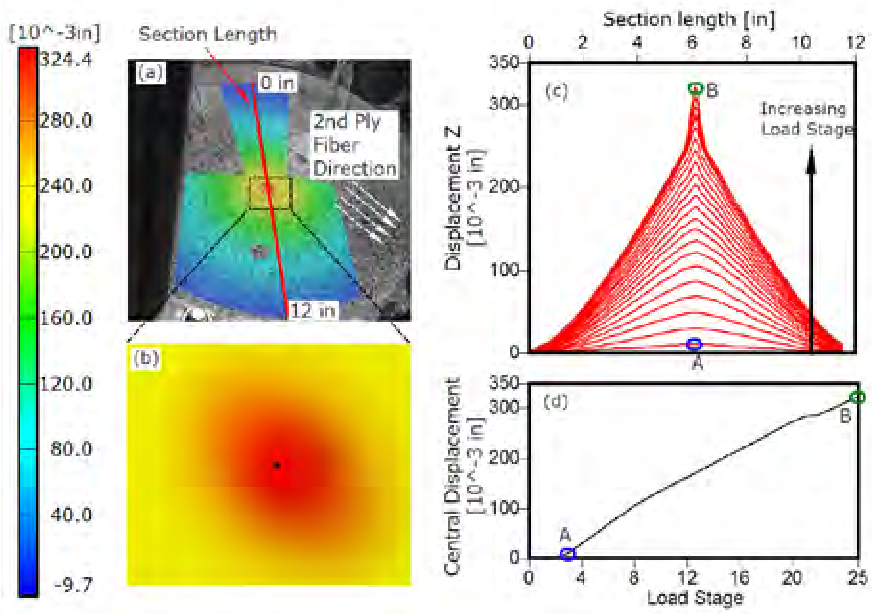

Figure 32. Strain Field and Deformation Plot Recorded for a GLARE Panel G3-5/4-0.3 Under Normal Penetration Condition Under a Loading Rate of 0.001 in./s Showing (a) Strain Field at Breakthrough, (b) Closeup of the Strain Field at Breakthrough, (c) Panel Deflection at Increasing Loads up to Initial Back Surface Crack Initiation (i.e., panel breakthrough) Along the Section Marked in Strain Field Image (a), and (d) Central Deflection up to Breakthrough

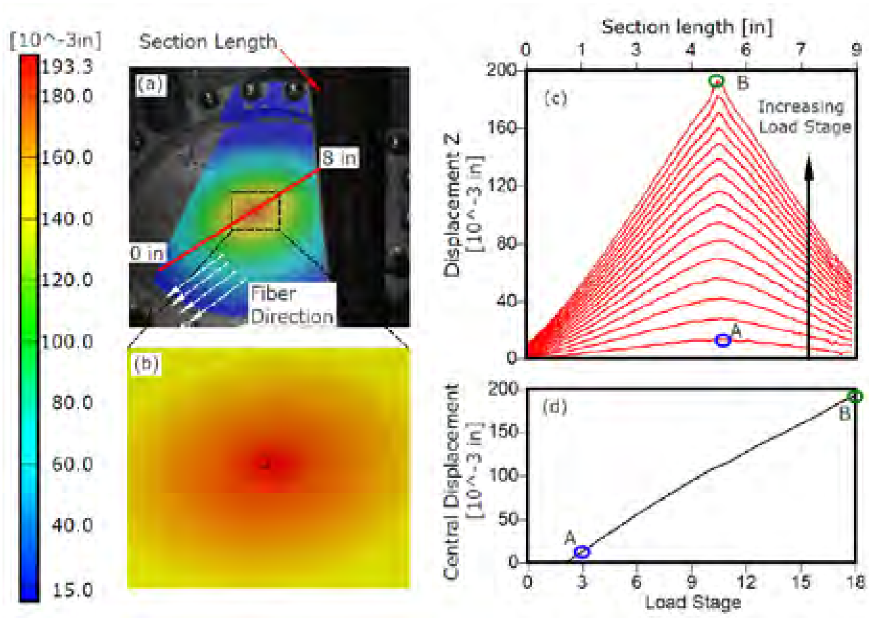

Figure 33. Strain Field and Deformation Plot Recorded for a 12-ply CFRP Panel Under Normal Penetration Condition Under a Loading Rate of 0.001 in./s Showing (a) Strain Field at Breakthrough, (b) Closeup of the Strain Field at Breakthrough, (c) Panel Deflection at Increasing Loads up to Initial Back Surface Crack Initiation (i.e., panel breakthrough) Along the Section Marked in Strain Field Image (a), and (d) Central Deflection up to Breakthrough

5.6.2 Back Surface Damage Progression.

The DIC method was also used to monitor damage initiation, growth, and progression during the penetration process up to breakthrough. By tracking the strain loci, the direction of crack and damage growth can be determined. This approach is particularly advantageous in studying damage evolution in composite laminates because the effect of the dominant strain components on damage initiation and growth could be determined.

DIC images of von Mises strain contour profiles at different crosshead displacements, before and after breakthrough, are shown in figure 34 for a representative G3-5/4-0.3 GLARE panel. Prior to breakthrough, the von Mises strain contours were circular, indicating that there was little, if any, effect of the directionality of the neighboring unidirectional (0- and 90- degree) glass/epoxy layers. It should be noted that other GLARE panels behaved differently, depending upon lay-up and laminate configuration. For example, in the G3-4/3-0.4 GLARE panel, directionality effect was noticed at earlier loading stages [6], as shown in figure 35.

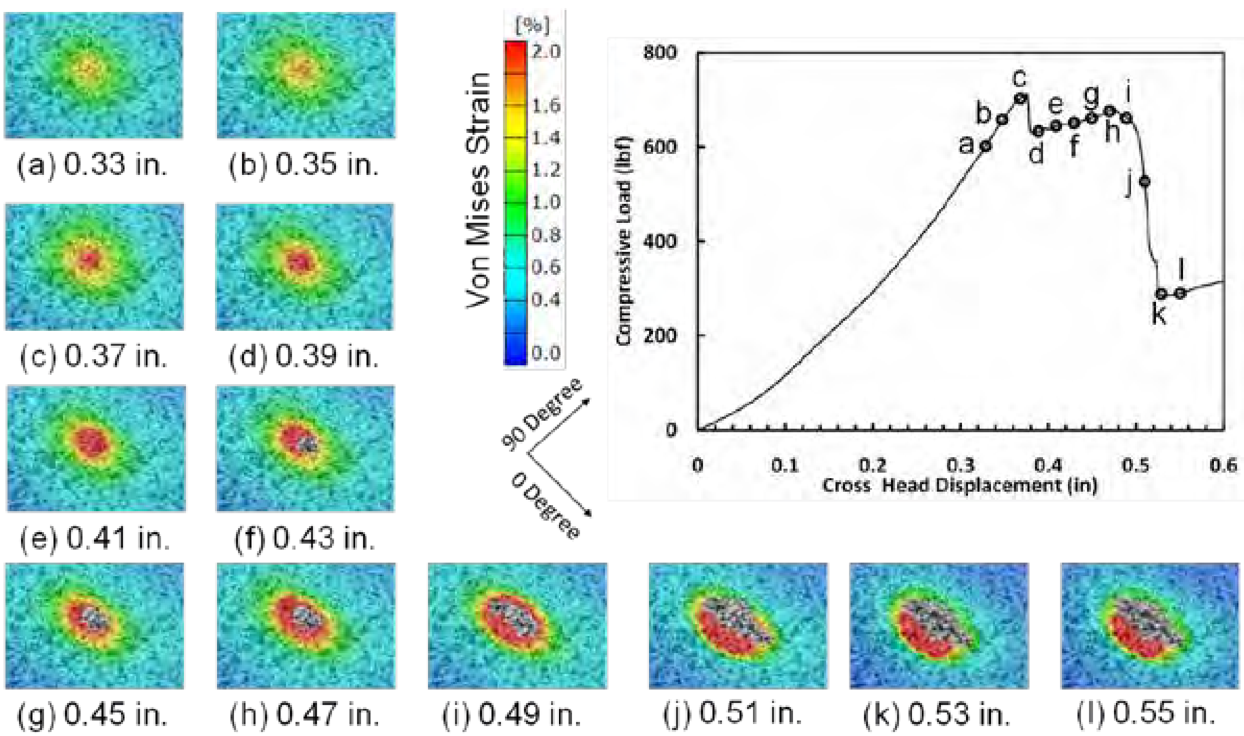

Figure 34. Von Mises Strain Fields of a Section Near the Perforation Zone of a G3-5/4-0.3 GLARE Panel at Various Load Steps Before and After the Breakthrough
(The crosshead displacement is indicated at each load step. Breakthrough occurred at 0.43-in. crosshead displacement.)

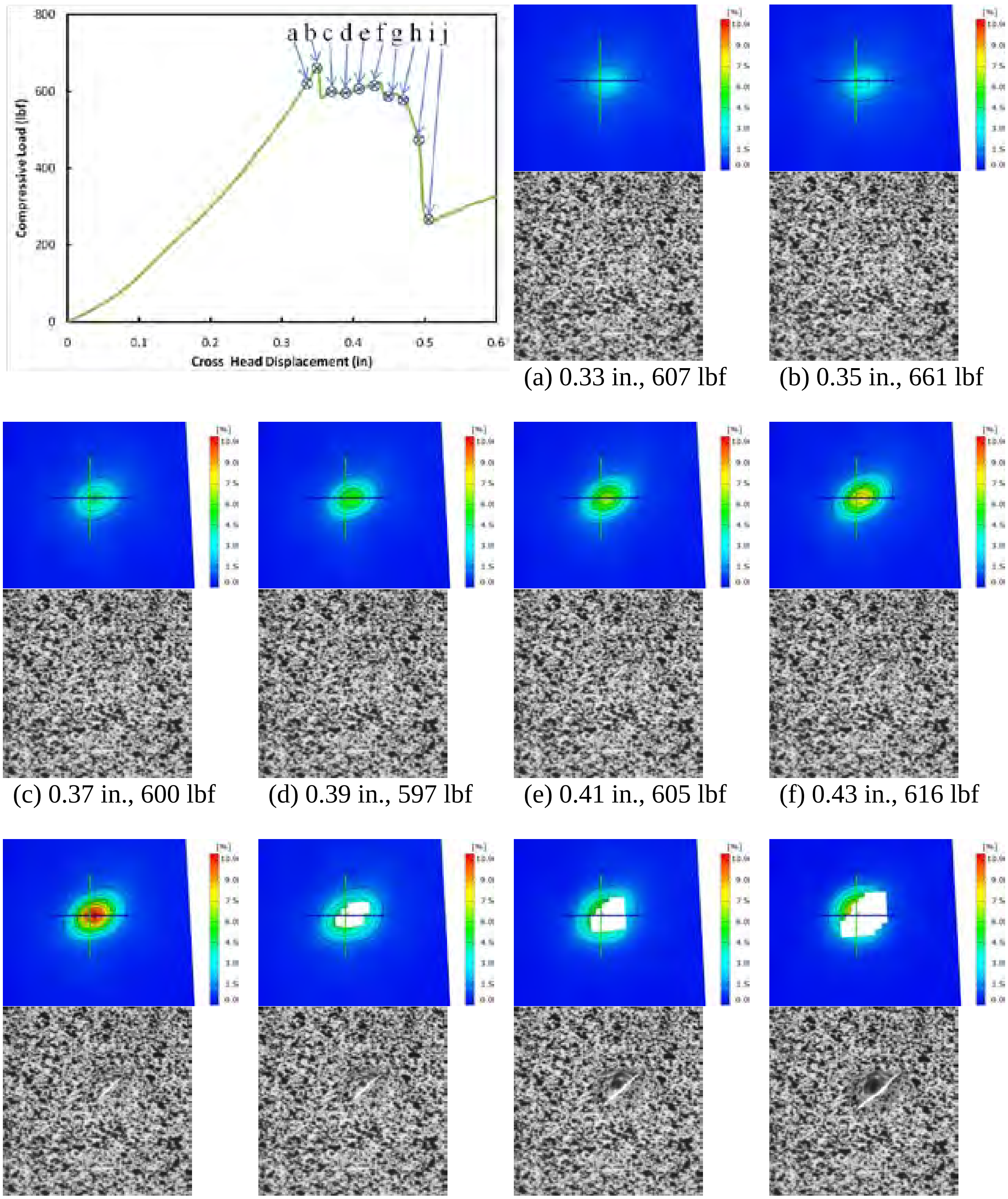

(a) 0.33 in., 607 lbf (b) 0.35 in., 661 lbf

(c) 0.37 in., 600 lbf (d) 0.39 in., 597 lbf (e) 0.41 in., 605 lbf (f) 0.43 in., 616 lbf

(g) 0.45 in., 589 lbf (h) 0.47 in., 579 lbf (i) 0.49 in., 486 lbf (j) 0.51 in., 262 lbf

Figure 35. Von Mises Strain Fields and Speckle-Coated Photographs of a Section Near the Perforation Zone Before and After Complete tip Penetration of a G3-4/3-0.4 GLARE Panel at Loading Rate of 0.001 in./s

The effect of ply sequence and fiber orientation became more noticeable with increased penetration, where the higher strains on the back surface extend along the direction of the fibers of the adjacent glass/epoxy layer. This elongated, nearly ellipse-shaped, strain field indicated the occurrence of internal damage, primarily in the form matrix cracking, extending along the 0-degree fiber direction. At 0.37-in. crosshead displacement, figure 35(c), the photograph of the speckle coating shows a hairline crack at the outer aluminum layer, along the 0-degree fiber direction of the adjacent glass/epoxy ply. This corresponded to the sudden load drop and was accompanied by an audible noise level. With increased penetration of the conical-shaped penetrator, the crack extended further, figures 35(d) to 35(i). Prior to complete perforation, i.e., at breakthrough, when the penetrator exited the back surface, figure 35(j), a short second crack in the aluminum layer was formed.

The directionality of the cracks formed in the back surface aluminum layer during the perforation process of a conical penetrator depends on the particular GLARE panel considered. The G3-5/4-0.3 and G3-4/3-0.4 GLARE panels exhibited a similar failure pattern, where the first hairline crack observed on the outer aluminum layer was along the direction of fibers (i.e., 0-degree fiber direction) of the adjacent glass/epoxy ply. Conversely, different G5x-4/3-0.3 GLARE panels exhibited different failure sequences on the outer aluminum layer surface: In two panels, the first hairline crack occurred orthogonal to the direction of fibers of the adjacent glass/epoxy ply (i.e., 90-degree fiber direction), whereas in the other two panels tested, the first hairline crack occurred along the direction of fibers (i.e., 0-degree fiber direction). It should be noted, however, that the stacking sequence of the G5x-4/3-0.3 panel is different than the other two laminates (see table 1). There are six glass/epoxy plies sandwiched between adjacent aluminum layers; whereas, the G3-4/3-0.4 and G3-5/4-0.3 GLARE panels have only two glass/epoxy plies sandwiched between the aluminum layers. Having a large number of 0/90 glass/epoxy layers may have contributed to the random pattern of crack direction.

The von Mises strain contour profiles, recorded at different crosshead displacements for a representative CFRP panel are shown in figure 36. The images shown were recorded at selected crosshead displacements, just prior to back surface damage becoming visible and during the formation and extension of the matrix splitting. The von Mises strain contours are elongated along the outer 0-degree plies, with the intense strain fields at the tip of the matrix split. The matrix split extended with increasing penetration depth of the conical-shaped penetrator. At crosshead displacements of 0.32-in. and 0.34-in., two other matrix splits formed sequentially, as shown in figure 36(c) and figure 36(d), and extended with further penetration depth.

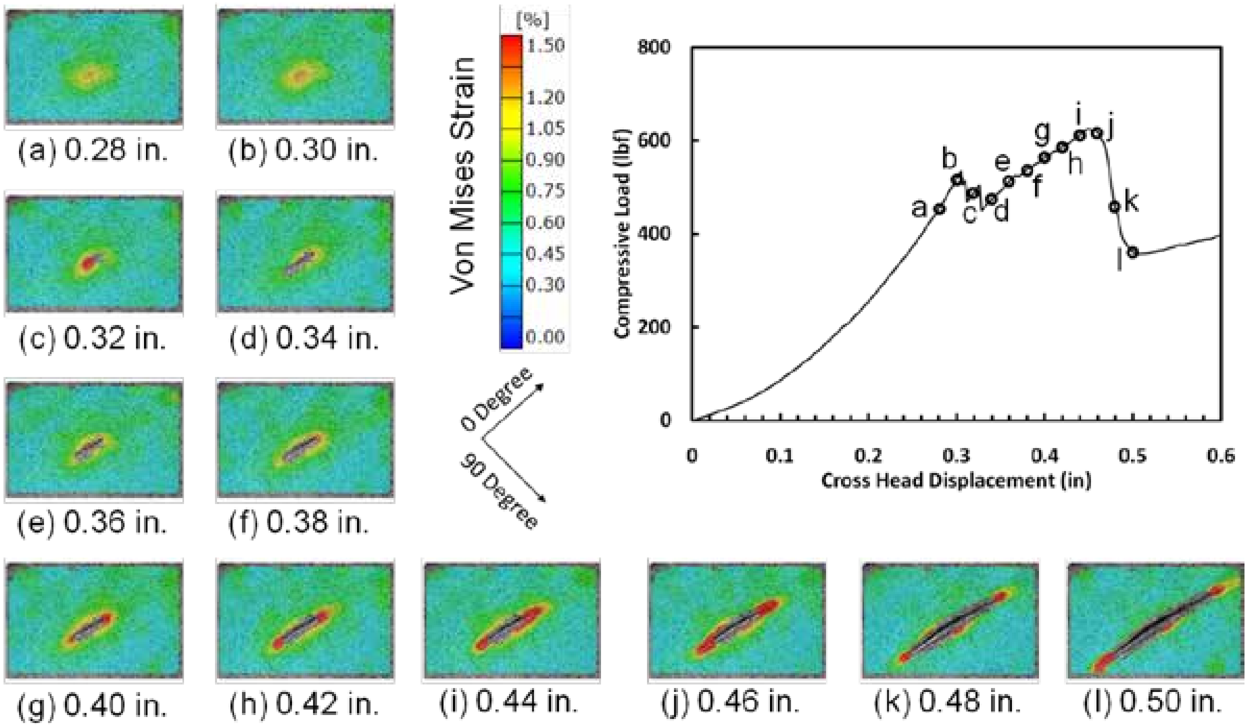

Figure 36. Von Mises Strain Fields of a Section Near the Perforation Zone of a 12-ply CFRP Panel at Various Load Steps Before and After the Breakthrough
(The crosshead displacement is indicated at each load step. Breakthrough occurred at 0.32-in. crosshead displacement.)

5.7 Cross-Sectional Fracture Morphology of GLARE.

To gain insight into the internal failure process and damage evolution in the GLARE laminate panel during the penetration process, cross-sectional surfaces of GLARE panels were examined under a low-magnification stereoscope. For this purpose, the GLARE panels were subjected to different levels of indentation depths and partial penetration at different locations along a panel under stroke-controlled mode, until panel breakthrough. Subsequently, the specimens were cut approximately 0.25 in. away from center of penetration to avoid introduction of additional damage from cutting at the penetration site. The cut specimens were then cold-mounted and carefully polished until the center of penetration was reached. The cold-mounted and polished fractographs of the G3-5/4-0.3 cross sections are shown in figure 37, showing the sequence of damage formation. Matrix crazing, followed by matrix cracking, occurred in the front glass/epoxy ply soon after initial indentation. With increasing penetration depth, significant plastic deformation and ultimately complete perforation of the first aluminum layer occurred. Once the first aluminum layer has been perforated, matrix crazing and cracking were observed in the second glass/epoxy layer. The remaining glass/epoxy layers experienced significant matrix crazing accompanied by debonding between the aluminum and glass/epoxy layers. This process repeated until the entire laminate deformed and the bottom aluminum layer fractured, which occurred while the penetrator was still embedded inside the laminate. Similar failure sequence occurred in the G3-4/3-0.4 and G5x-4/3/0.3 panels, as shown in appendix G.

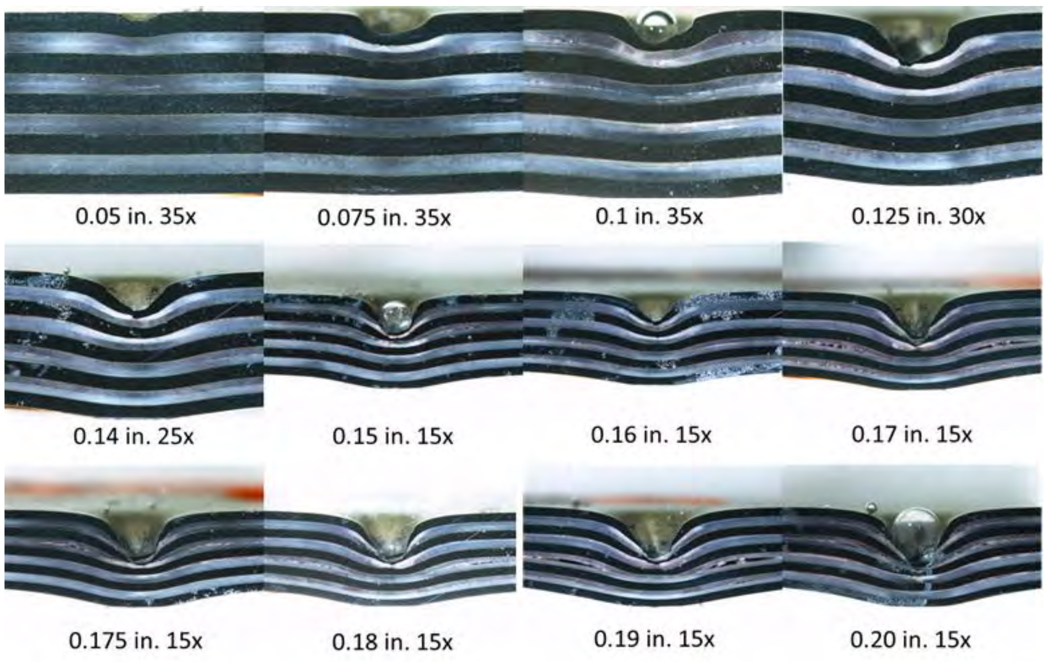

Figure 37. Stereoscope Images Showing the Damage Evolution of G3-5/4-0.3 GLARE Panel at Different Penetration Depths
(For clarity, images were taken at different magnifications.)

6. SUMMARY.

A test program was conducted to study the IPPR process of an ASPN used in aircraft rescue and firefighting. Fixed, supported, circular plates were perforated by an actual ASPN, which consisted of a spherical tip attached to a long conical penetrator having an extended cylindrical tail. Loading was applied under normal and 45-degree penetration conditions. Materials studied included five different thicknesses of aluminium alloy panels, three different thicknesses of GLARE laminate panels, and three different thicknesses of CFRP laminate panels. Primary emphasis was given to the penetration process of the conical penetrator and to the forces associated with the IPPR. The deformation of the panels was analyzed in detail via the DIC method. Strain gages were used to ensure proper load was applied to the panels.

The DIC method was used to capture the full-field deformation and to study the damage progression as viewed from the back surface of the panels. The formation and directionality of the cracks formed in the back surface layer during the perforation were identified. Cross-sectional fracture surface morphology was examined by using stereoscope on polished cross-sectional surface. The evolution of cross-sectional damage formation, such as matrix crazing, cracking, debonding, and delamination, was observed at increasing penetration depths.

The forces required to penetrate the GLARE and CFRP panels were 3.3 to 6.4 (median 4.5) times higher than the force required to penetrate a 0.04-in.-thick aluminum panel under normal penetration. Under the 45-degree penetration, GLARE and CFRP panels required 2.2 to 5.4 (median 3.2) times higher force to penetrate compare to a 0.04-in.-thick aluminum panel. When comparing the G3-4/3-0.4 (total thickness of 0.09-in.) and G3-5/4-0.3 (total thickness of 0.1-in.)

GLARE panels with the 0.1-in.-thick aluminum panel, the aluminum panel required two times higher force to perforate. The results also show that the penetration load, required during quasi-static penetration, dropped abruptly with the occurrence of first back surface cracking (i.e., breakthrough). In the aluminum panel the breakthrough is preceded with local plastic deformation and bulging. In the GLARE and CFRP panels, back surface cracking occurred while the tip of the penetrator was still embedded within the panel. As a consequence, the load drop was more pronounced in the composite laminate panels. Similarly, the panel deflection gradient at the penetration site was significantly larger in the composite laminates. The effect of loading rate was investigated and shown to be negligible.

The bending moment developed during the 45-degree penetration angle was also investigated. It was determined that at angled penetration, the bending strain is dominant (90% of the total strain). The stress developed in the boom was less than 10 ksi for tests of the two thinner GLARE panels, the three thicknesses of aluminum panels, and the three CFRP panels. Strain results of G5x-4/3-0.3 GLARE panel revealed that the stress developed in the boom was as high as 26 ksi. In field applications, the ASPN boom is 65 in. long compared to the 20-in. long penetrator used in this study. Thus, the bending stresses in the actual ASPN could be significantly higher.

7. REFERENCES.

1. Federal Aviation Administration, Advisory Circular (AC) 150/5220-10C, "Guide Specification for Water/Foam Aircraft Rescue and Firefighting Vehicles," Cancelled February 18, 2002.

2. Bagot, K. and Subbotin, N., "High-Reach Extendable Turrets With Skin-Penetrating Nozzle," FAA report DOT/FAA/AR-05/53, November 2005.

3. Private communication with Mr. Keith Bagot, FAA Airport & Technology Research and Development (R&D) Branch and Mr. John Hode, SRA International, Inc.

4. Swin, C., "An Experimental and Numerical Study of Quasi-Static Penetration in Aluminum, GLARE and CFRP Composite Panels," PhD Thesis, In Preparation.

5. Swin, C., Bagot, K., Bakuckas, J., Hode, J., Awerbuch, J., and Tan, T. "Penetration Study of Aluminum and Glass Fiber-Reinforced Metal Composites," *Proceedings of 2010 Aircraft Airworthiness and Sustainment Conference*, Austin, Texas, May 10-13, 2010.

6. Swin, C., Bagot, K., Bakuckas, J., Hode, J., Awerbuch, J., and Tan, T. "Penetration Study of Glass Fiber Reinforced Metal Composite Plates," *Proceedings of 14th US-Japan Conference on Composite Materials*, Dayton, Ohio, September 20-22, 2010.

7. Swin, C., Bagot, K., Bakuckas, J., Awerbuch, J., and Tan, T. "Finite Element Simulation of the Quasi-Static Penetration and Perforation in GLARE and CFRP Panels," *Proceedings of the 2nd U.S.-Canada Conference on Composite Materials*, Montreal, Quebec, Canada, September 26-28, 2011.

APPENDIX A—TEST FIXTURES AND PANELS ENGINEERING DRAWINGS

Figures A-1 through A-10 present detailed engineering drawings of the normal (90-degree angle) penetration and the 45-degree angle penetration test fixtures.

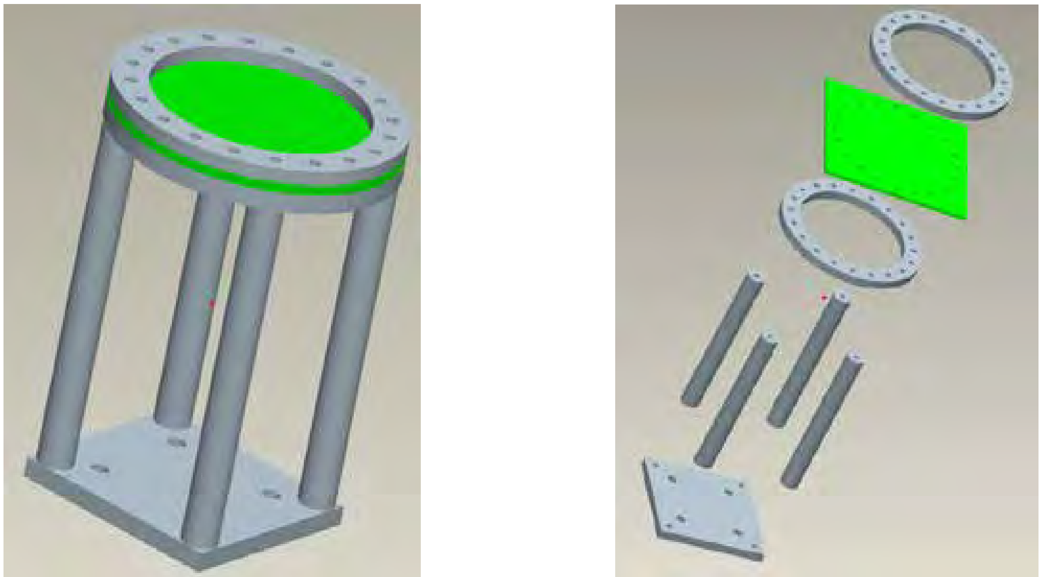

(a) (b)

Figure A-1. The Normal Penetration Test Fixture Showing the Sandwiched Specimen (green object), Including (a) the Test Fixture Assembly and (b) the Exploded View

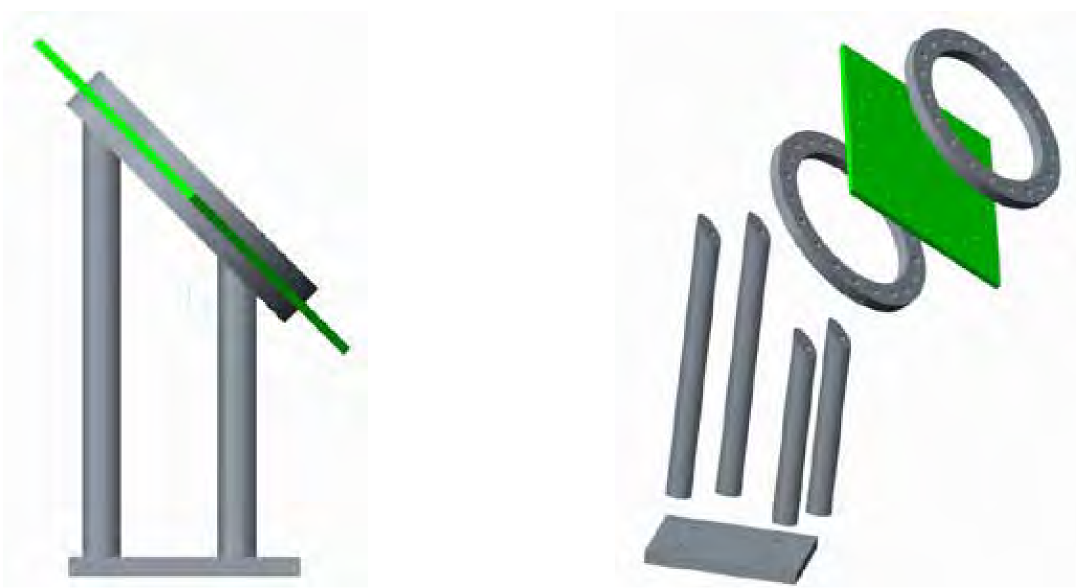

Figure A-2. The 45-Degree Angle Penetration Test Fixture Without Base Plate and Specimen

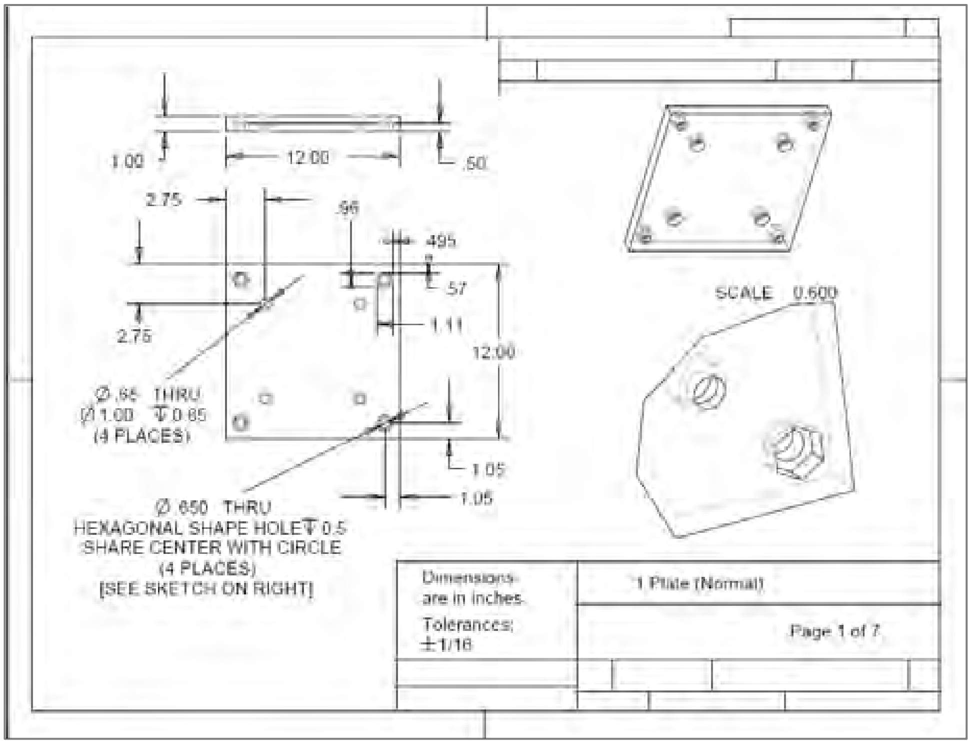

Figure A-3. Base Plate for Normal Penetration Test Setup

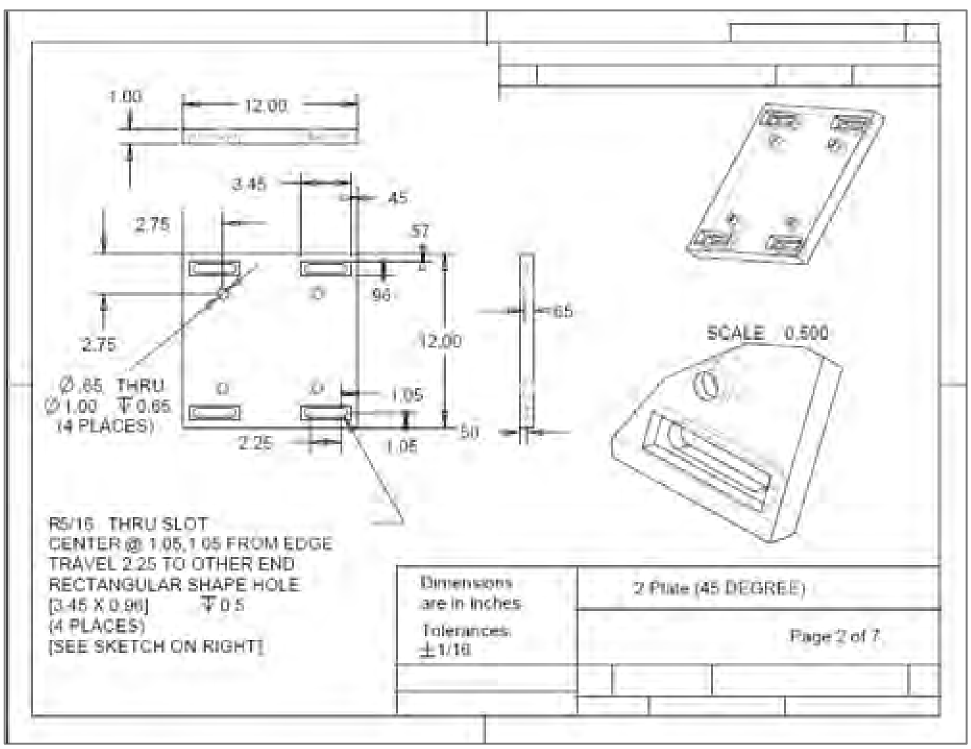

Figure A-4. Base Plate for 45-Degree Angle Penetration Test Setup

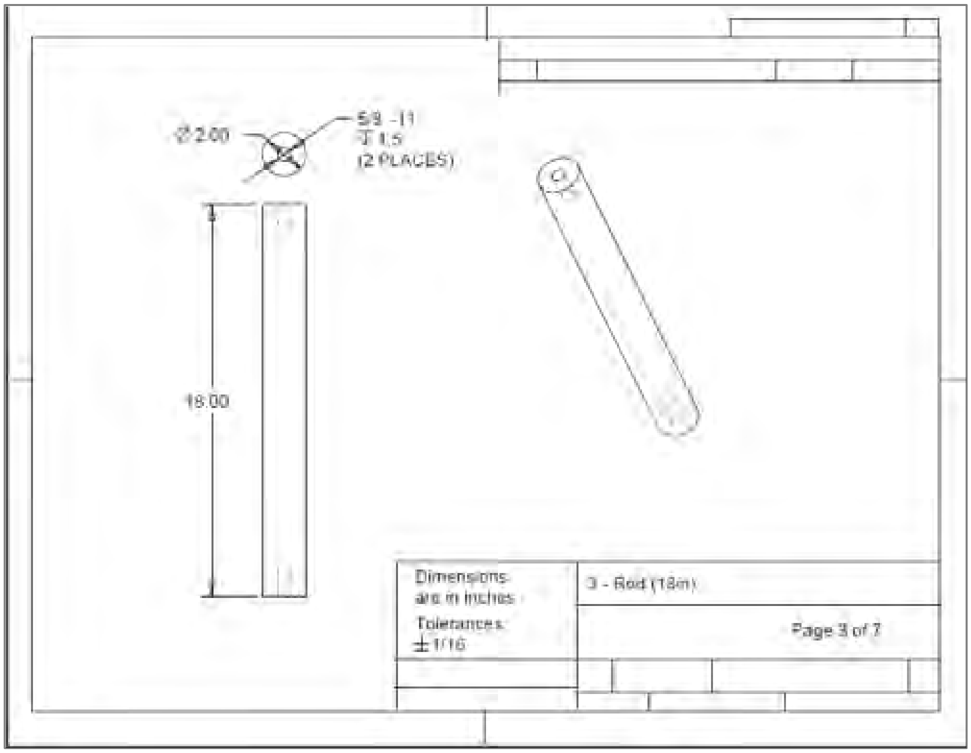

Figure A-5. Fixture Support Rod for Normal Penetration Test Setup

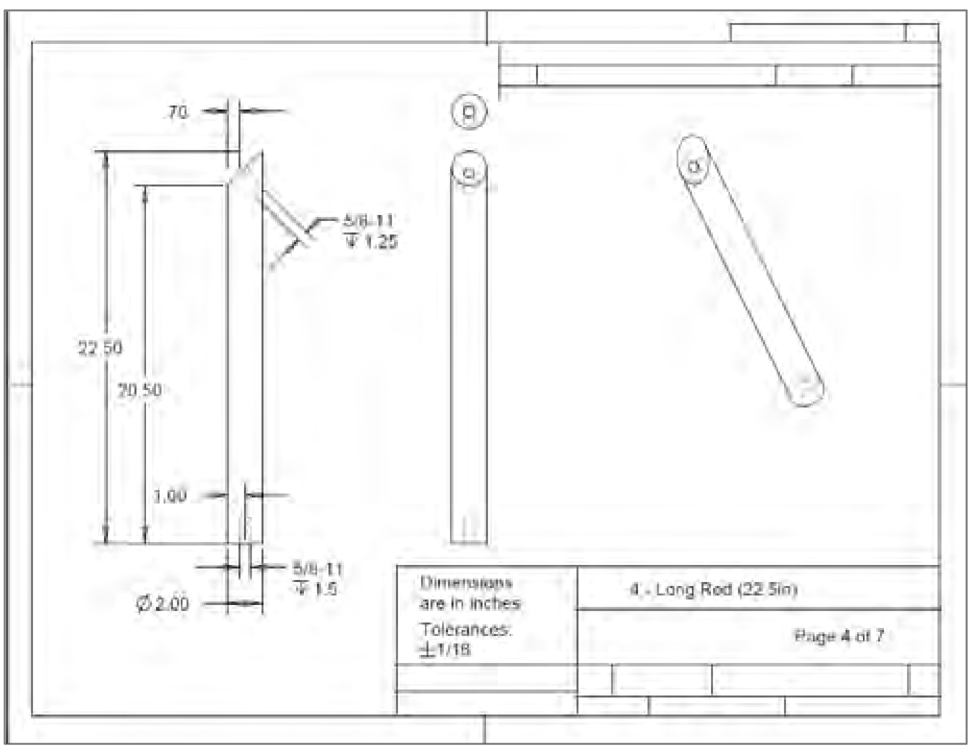

Figure A-6. Fixture Support Long Rod for 45-Degree Angle Penetration Test Setup

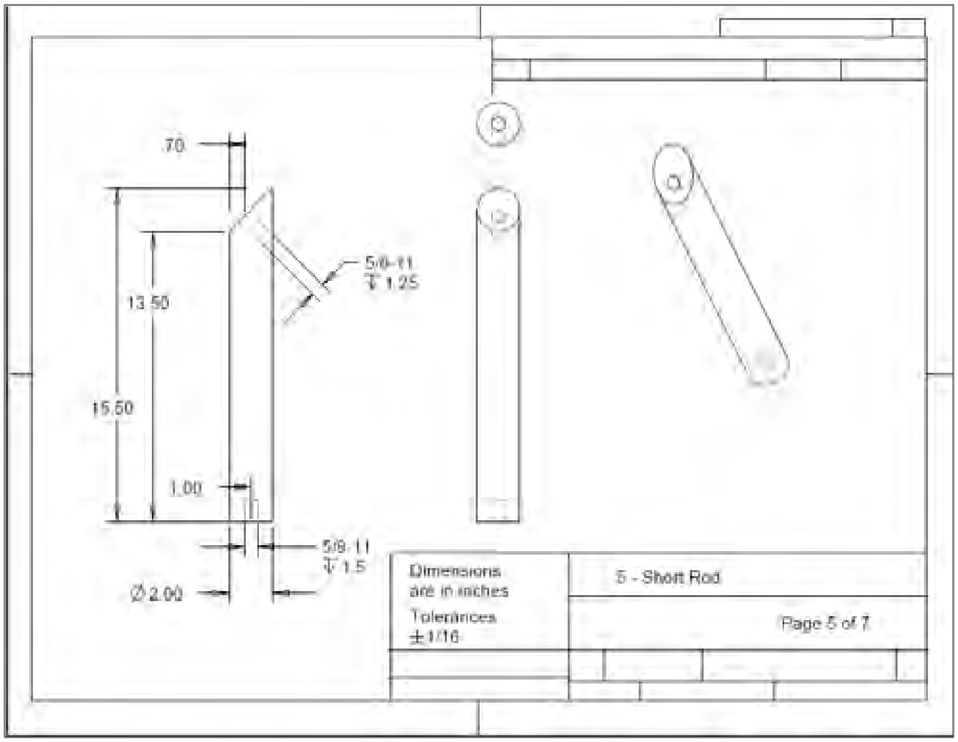

Figure A-7. Fixture Support Short Rod for 45-Degree Angle Penetration Test Setup

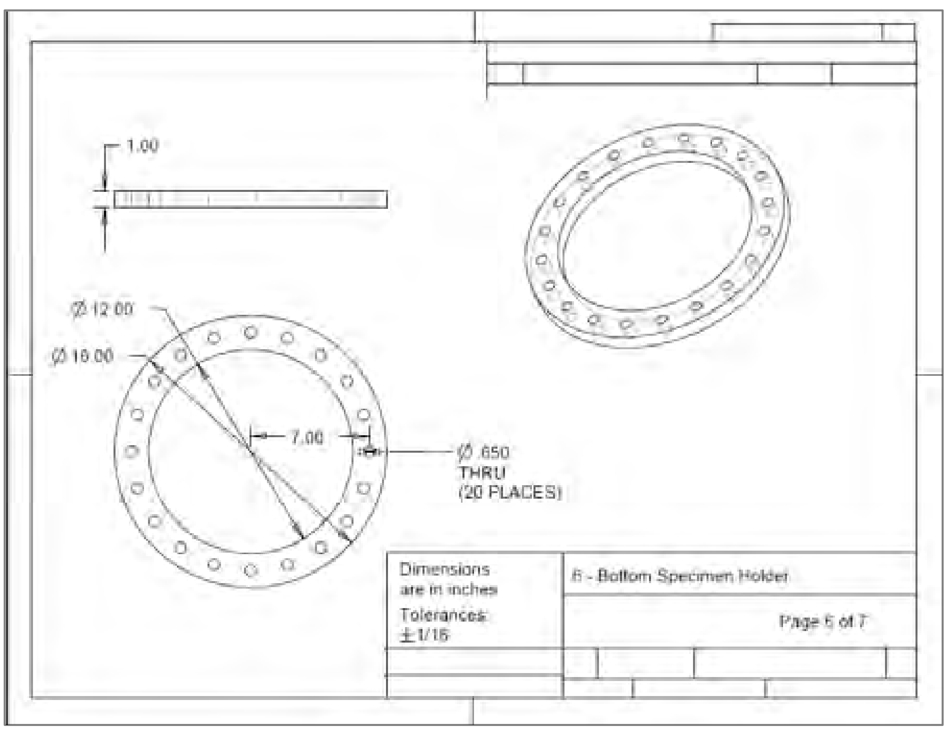

Figure A-8. Bottom Specimen Holder for Both Normal and 45-Degree Angle Penetration Test Setups

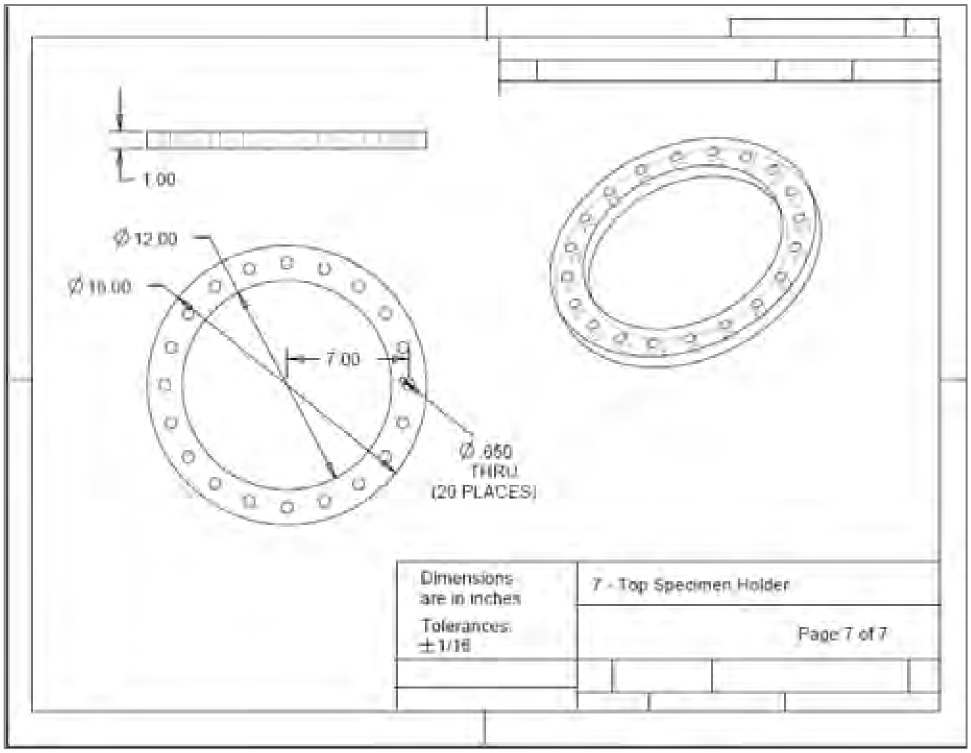

Figure A-9. Top Specimen Holder for Both Normal and 45-Degree Angle Penetration Test Setups

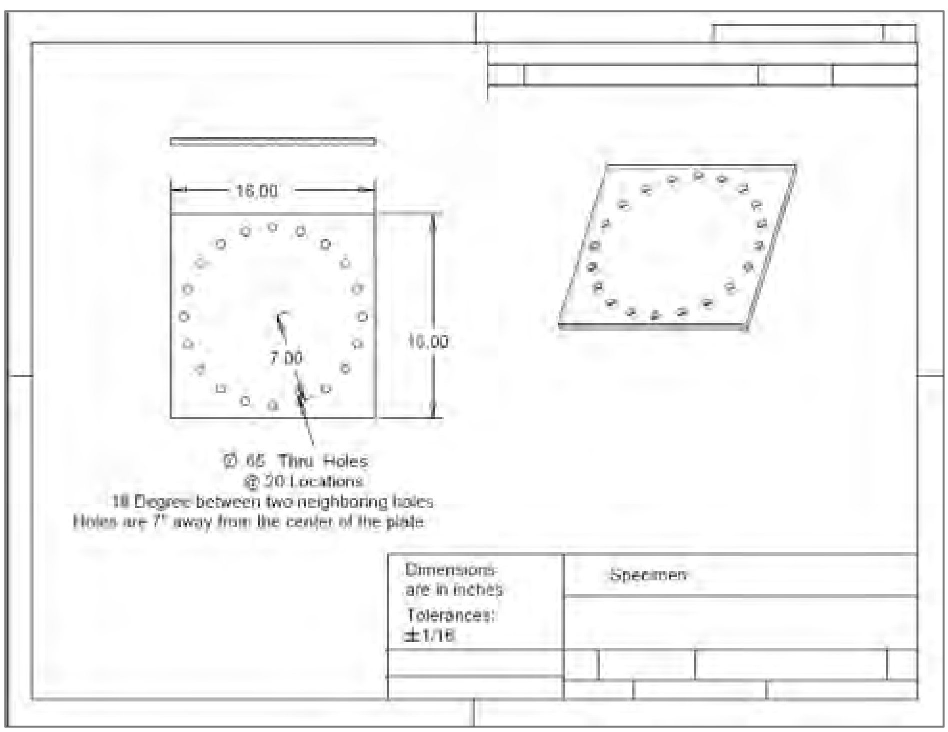

Figure A-10. The 16-in.-Square Specimen Showing Location of Bolt Holes

APPENDIX B—PENETRATOR ENGINEERING DRAWINGS

Detailed engineering drawings of the aircraft skin-penetrating nozzle (ASPN) components are presented in figures B-1 through B-4.

Figure B-1. The ASPN

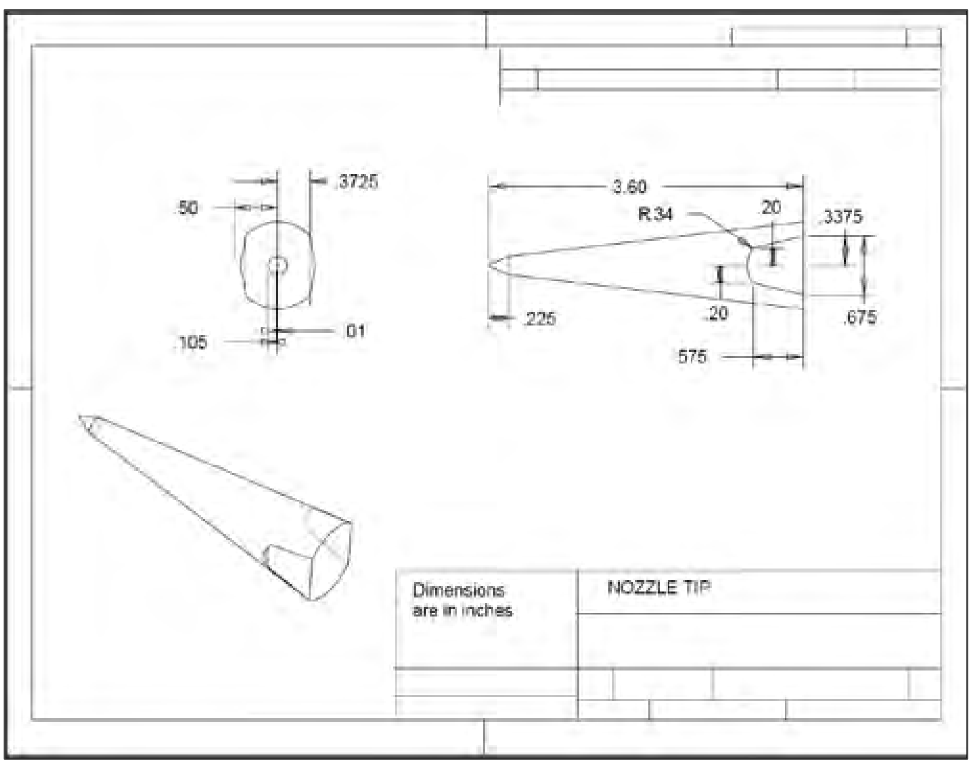

Figure B-2. The ASPN Penetrator

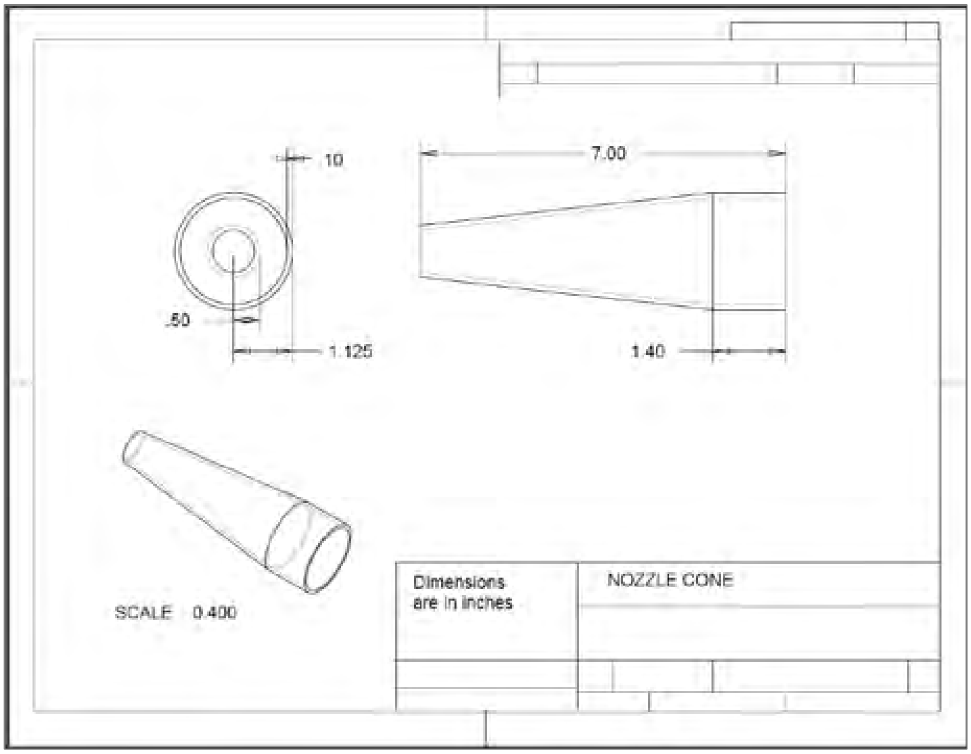

Figure B-3. Fixture Support Rod for Normal Penetration Test Setup

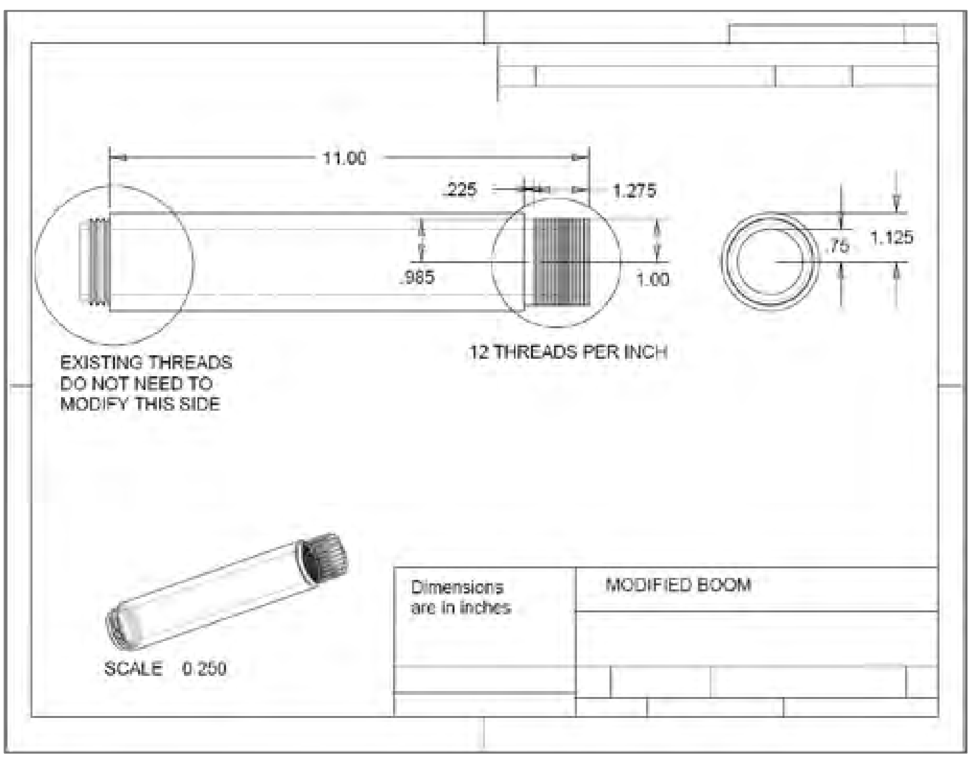

Figure B-4. The ASPN Boom

APPENDIX C—COMPLETE LOAD-VERSUS-CROSSHEAD DISPLACEMENT CURVES AT 0.001 IN./S LOADING RATE

C.1 NORMAL PENETRATION.

Figures C-1 through C-9 show the load-versus-crosshead displacement curves resulting from the normal penetration tests of aluminum, glass fiber-reinforced (GLARE) aluminum laminate panels, and carbon fiber-reinforced plastic (CFRP) laminate panels of varying thickness. Section C.1 focuses on the normal (90-degree angle) penetration condition.

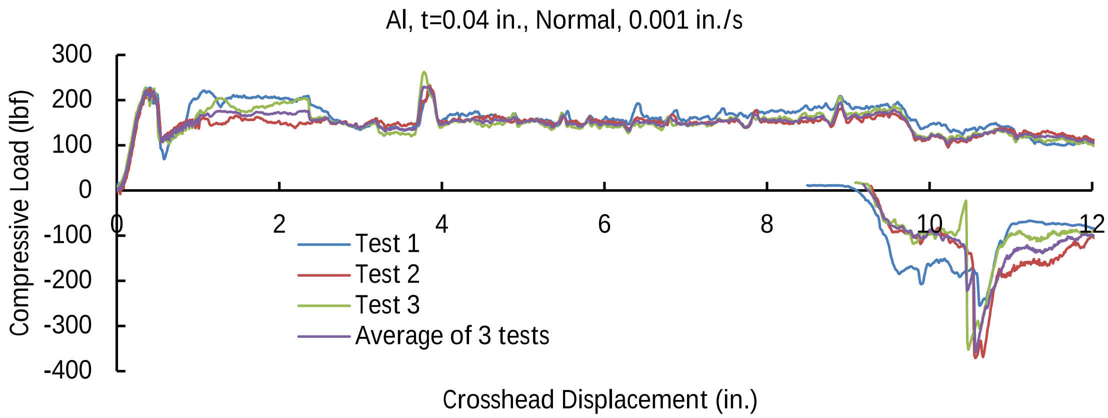

Figure C-1. Results of Three Repeated Tests and Average Value of 0.04-in.-Thick Aluminum Panels Under Normal Penetration at 0.001 in./s Loading Rate

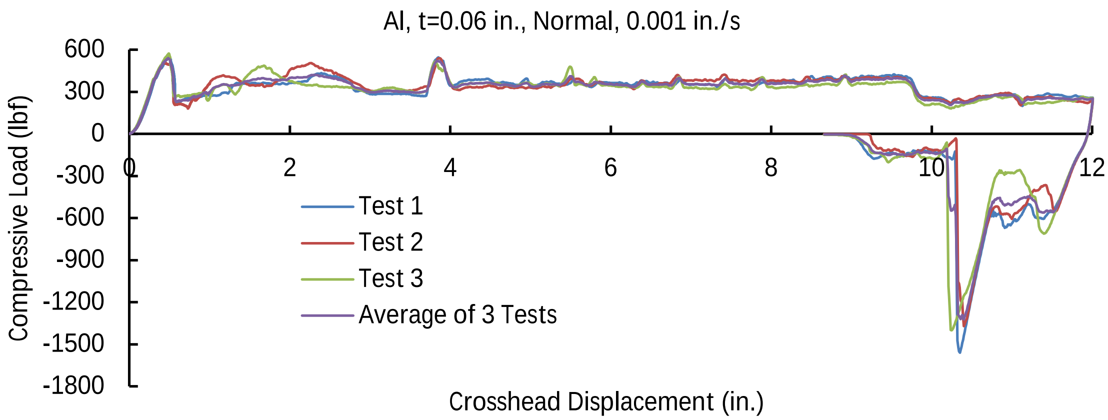

Figure C-2. Results of Three Repeated Tests and Average Value of 0.06-in.-Thick Aluminum Panels Under Normal Penetration at 0.001 in./s Loading Rate

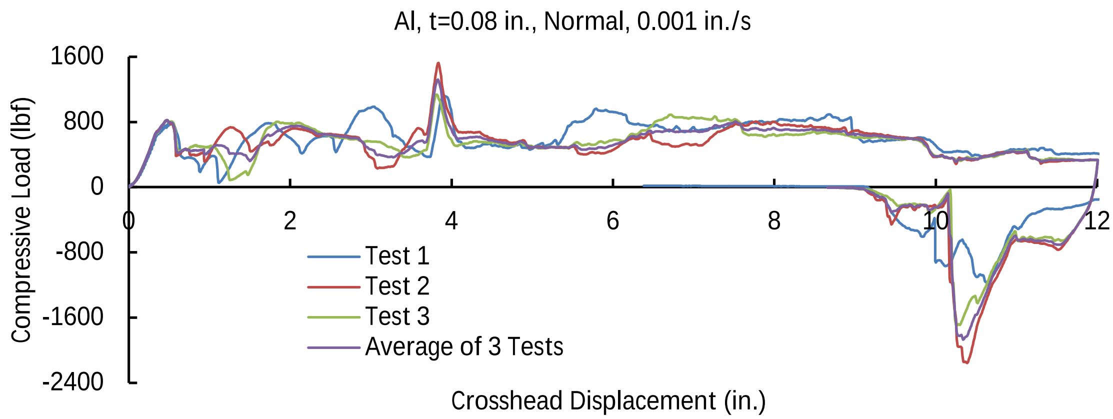

Figure C-3. Results of Three Repeated Tests and Average Value of 0.08-in.-Thick Aluminum Panels Under Normal Penetration at 0.001 in./s Loading Rate

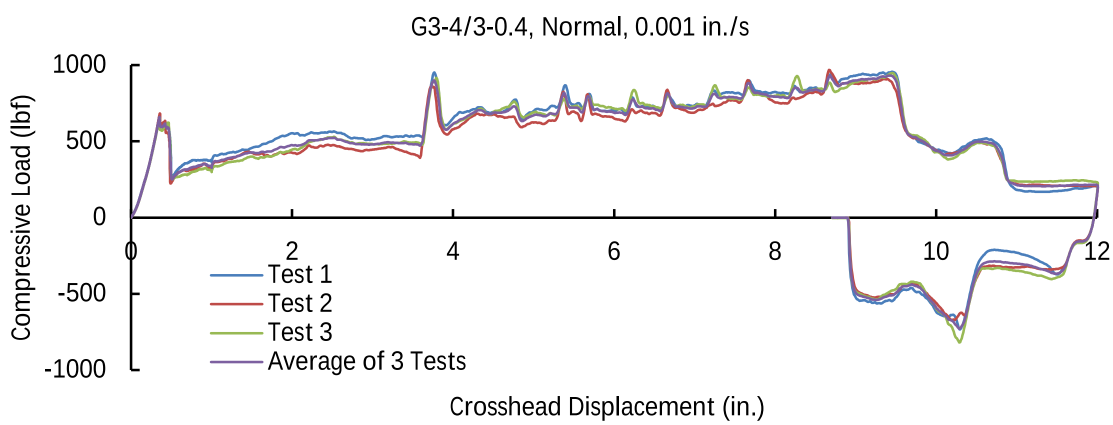

Figure C-4. Results of Three Repeated Tests and Average Value of G3-4/3-0.4 GLARE Panels Under Normal Penetration at 0.001 in./s Loading Rate

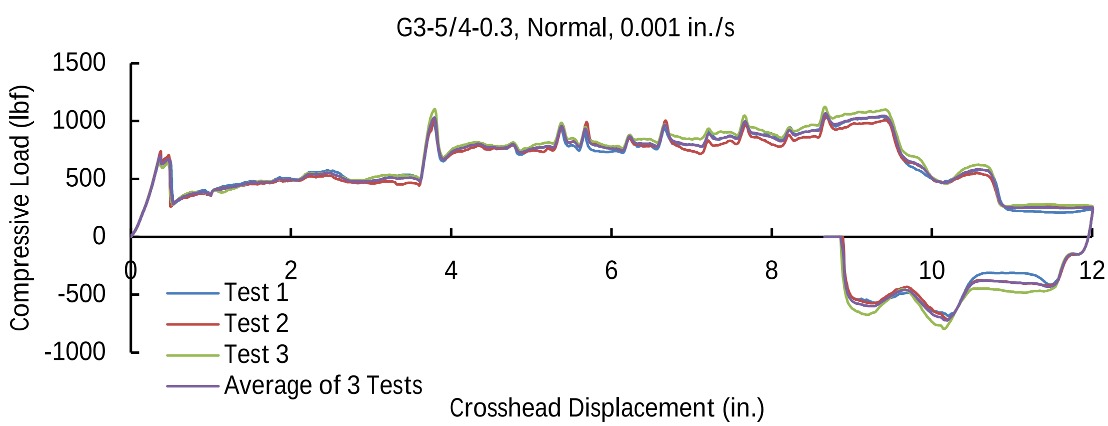

Figure C-5. Results of Three Repeated Tests and Average Value of G3-5/4-0.3 GLARE Panels Under Normal Penetration at 0.001 in./s Loading Rate

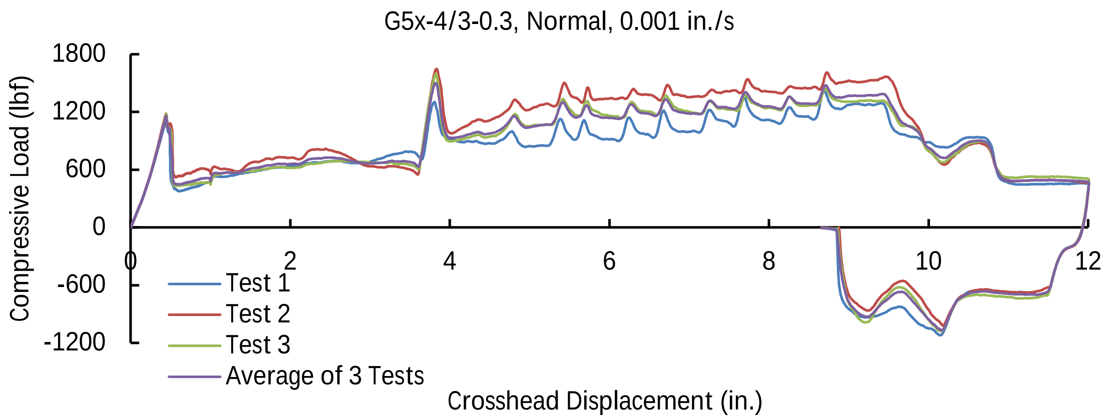

Figure C-6. Results of Three Repeated Tests and Average Value of G5x-4/3-0.3 GLARE Panels Under Normal Penetration at 0.001 in./s Loading Rate

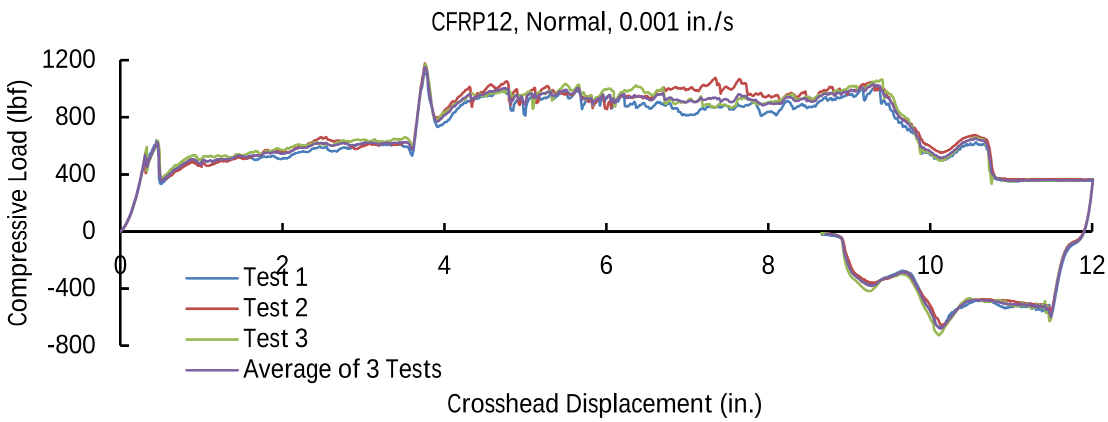

Figure C-7. Results of Three Repeated Tests and Average Value of 12-ply CFRP Panels Under Normal Penetration at 0.001 in./s Loading Rate

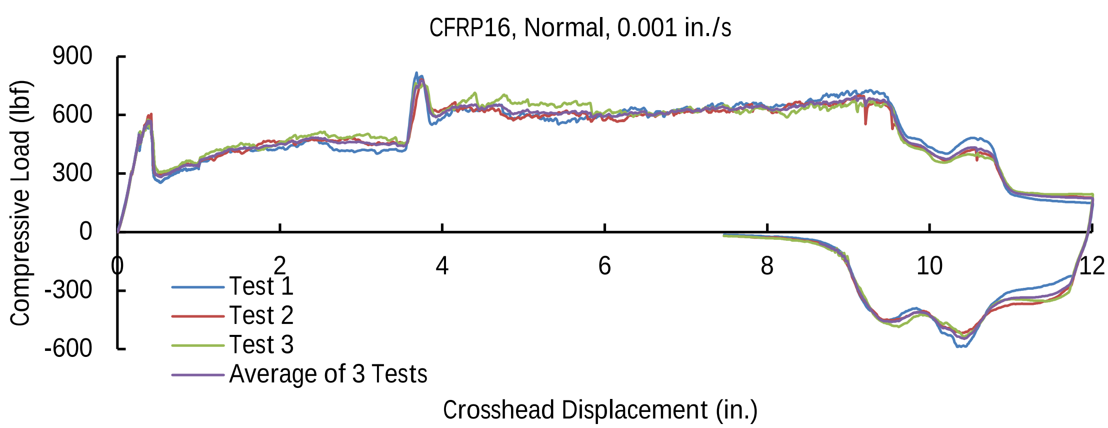

Figure C-8. Results of Three Repeated Tests and Average Value of 16-ply CFRP Panels Under Normal Penetration at 0.001 in./s Loading Rate

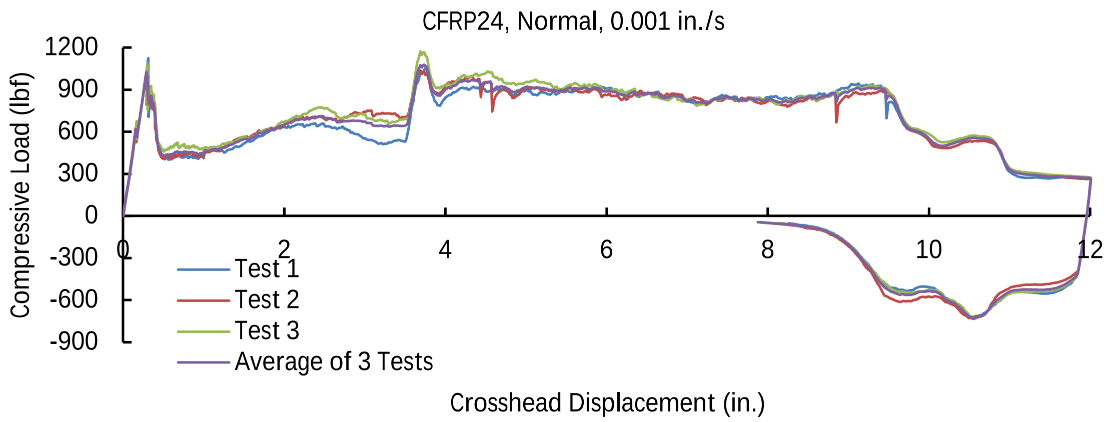

Figure C-9. Results of Three Repeated Tests and Average Value of 24-ply CFRP Panels Under Normal Penetration at 0.001 in./s Loading Rate

C.2 THE 45-DEGREE ANGLE PENETRATION.

Figures C-10 through C-18 show the load-versus-crosshead displacement curves resulting from the 45-degree angle penetration tests of aluminum, GLARE, and CFRP panels of varying thickness.

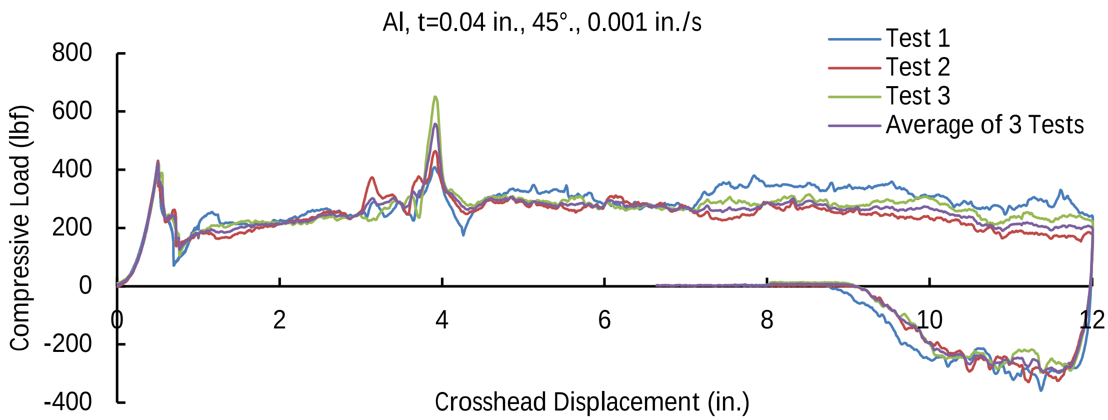

Figure C-10. Results of Three Repeated Tests and Average Value of 0.04-in.-Thick Aluminum Panels Under 45-Degree Angle Penetration at 0.001 in./s Loading Rate

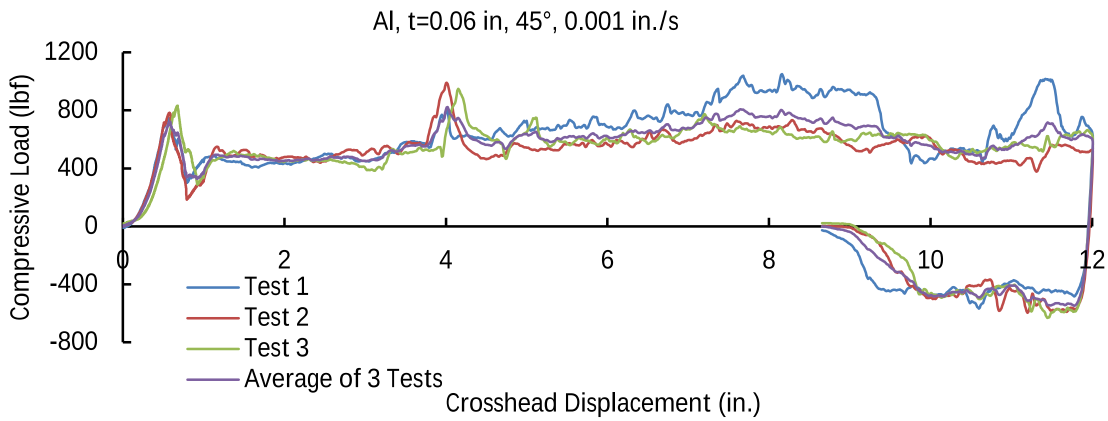

Figure C-11. Results of Three Repeated Tests and Average Value of 0.06-in.-Thick Aluminum Panels Under 45-Degree Angle Penetration at 0.001 in./s Loading Rate

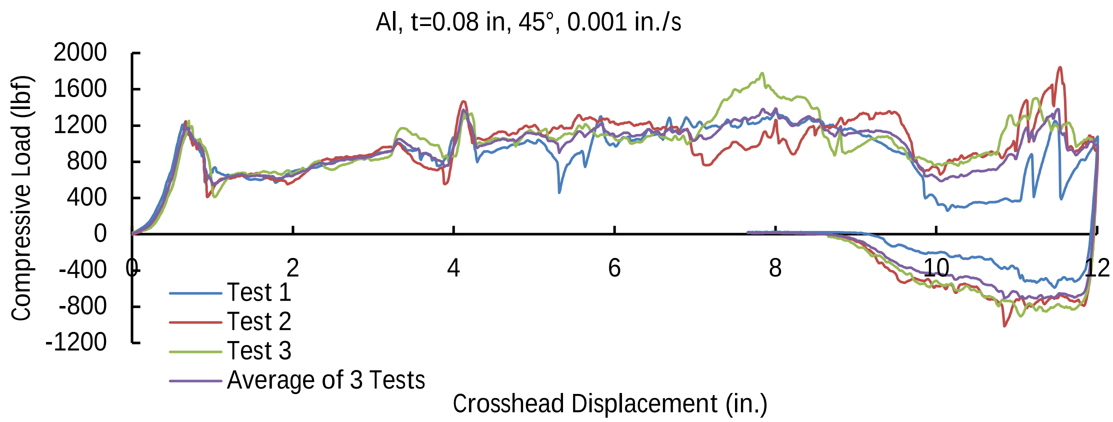

Figure C-12. Results of Three Repeated Tests and Average Value of 0.08-in.-Thick Aluminum Panels Under 45-Degree Angle Penetration at 0.001 in./s Loading Rate

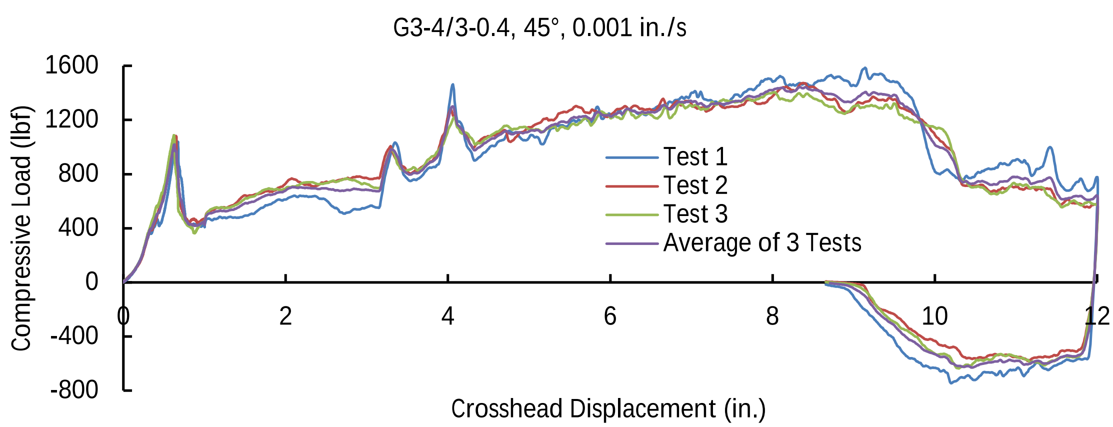

Figure C-13. Results of Three Repeated Tests and Average Value of G3-4/3-0.4 GLARE Panels Under 45-Degree Angle Penetration at 0.001 in./s Loading Rate

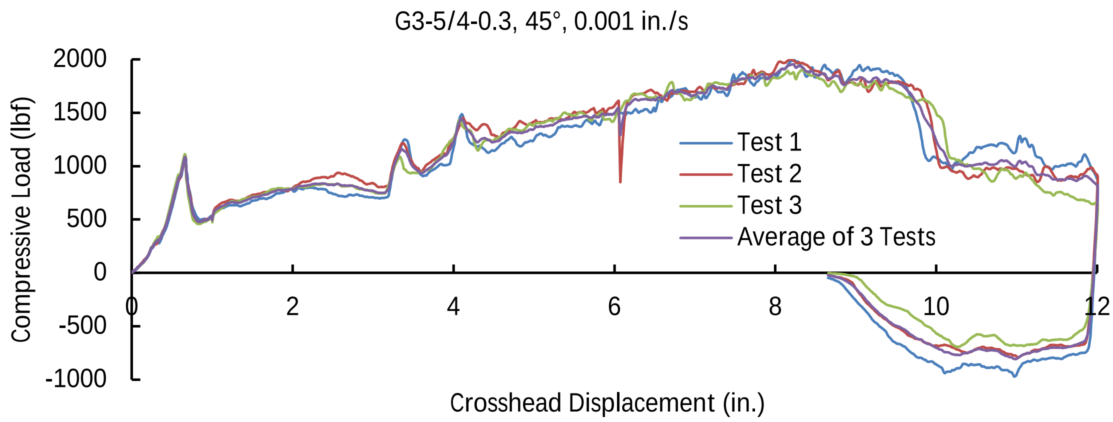

Figure C-14. Results of Three Repeated Tests and Average Value of G3-5/4-0.3 GLARE Panels Under 45-Degree Angle Penetration at 0.001 in./s Loading Rate

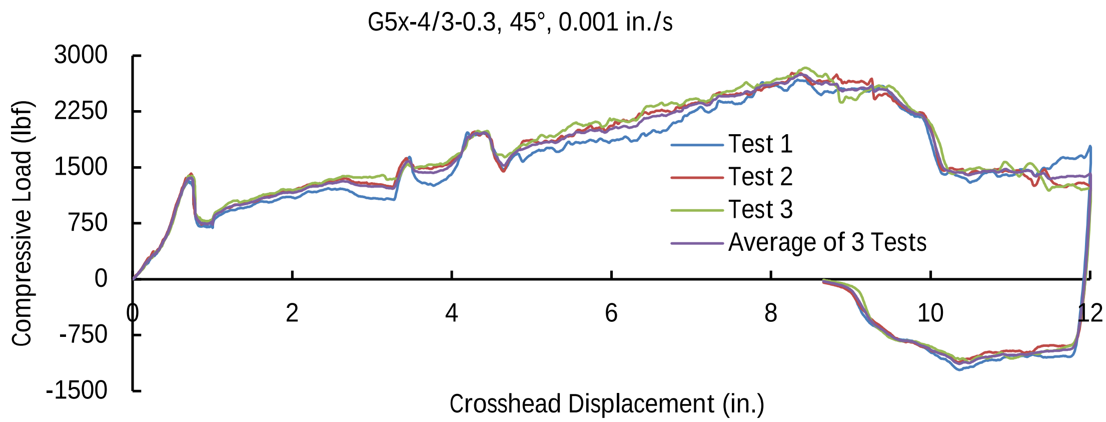

Figure C-15. Results of Three Repeated Tests and Average Value of G5x-4/3-0.3 GLARE Panels Under 45-Degree Angle Penetration at 0.001 in./s Loading Rate

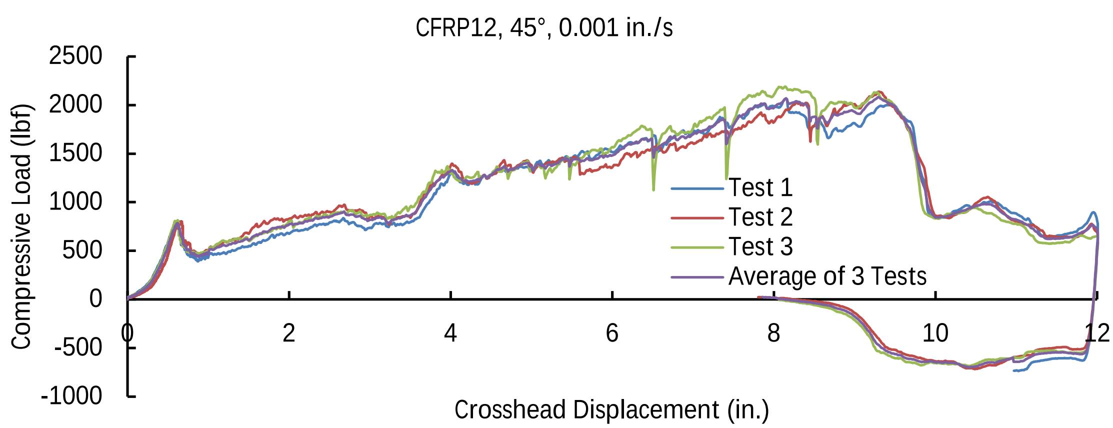

Figure C-16. Results of Three Repeated Tests and Average Value of 12-ply CFRP Panels Under 45-Degree Angle Penetration at 0.001 in./s Loading Rate

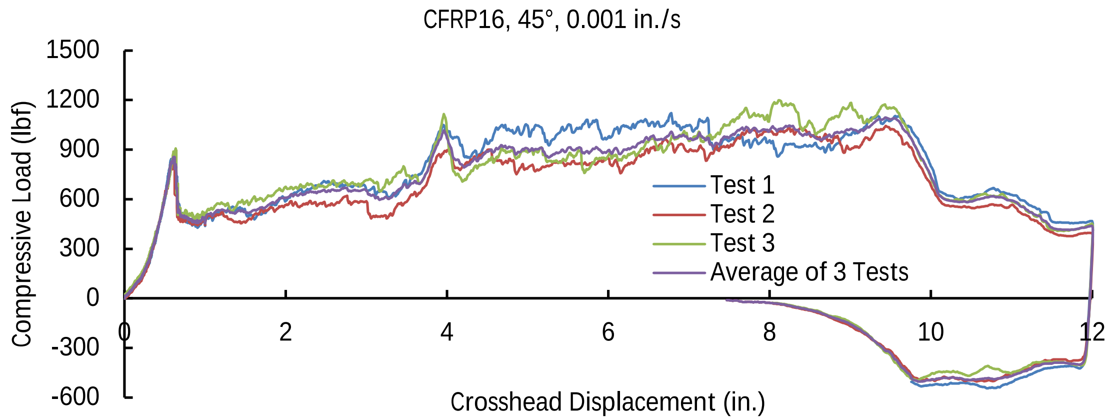

Figure C-17. Results of Three Repeated Tests and Average Value of 16-ply CFRP Panels Under 45-Degree Angle Penetration at 0.001 in./s Loading Rate

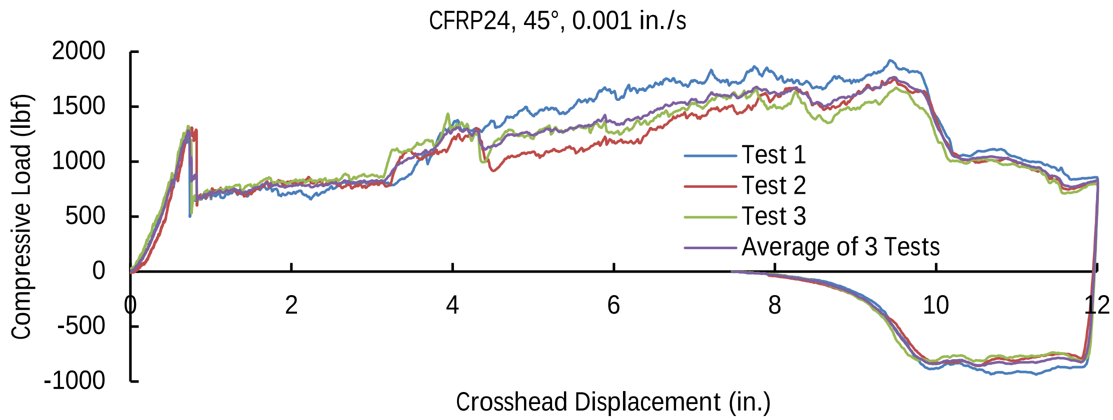

Figure C-1. Results of Three Repeated Tests and Average Value of 24-ply CFRP Panels Under 45-Degree Angle Penetration at 0.001 in./s Loading Rate

APPENDIX D—LOADING RATE EFFECT

D.1 NORMAL PENETRATION.

Figures D-1 through D-9 depict the comparison of the different loading rates under normal 90-degree angle penetration conditions on the three different thicknesses of test panels: aluminum, glass fiber-reinforced (GLARE) aluminum laminate, and carbon fiber-reinforced plastic (CFRP) laminate.

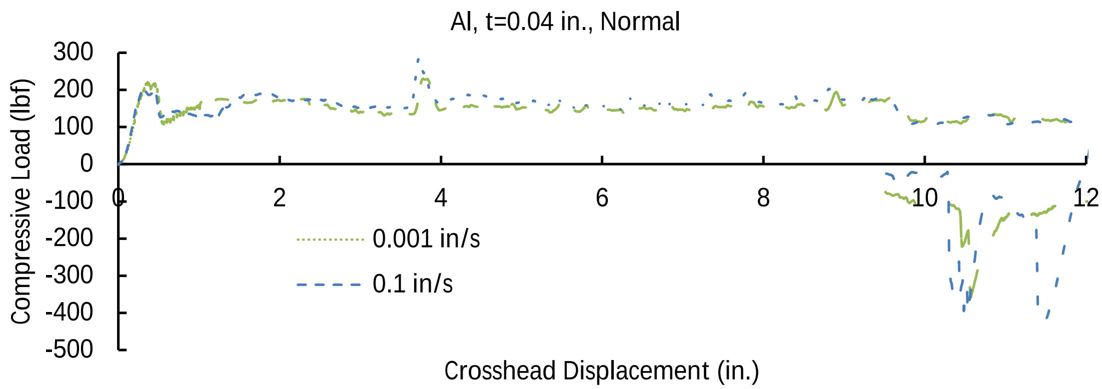

Figure D-1. Comparison of Normal Penetration of a 0.04-in.-Thick Aluminum Panel at 0.001 in./s and 0.1 in./s Loading Rates

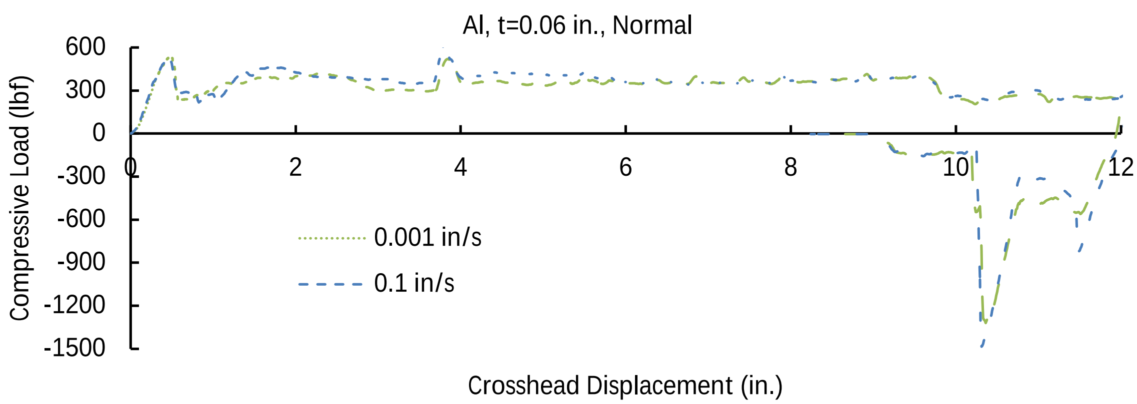

Figure D-2. Comparison of Normal Penetration of a 0.06-in.-Thick Aluminum Panel at 0.001 in./s and 0.1 in./s Loading Rates

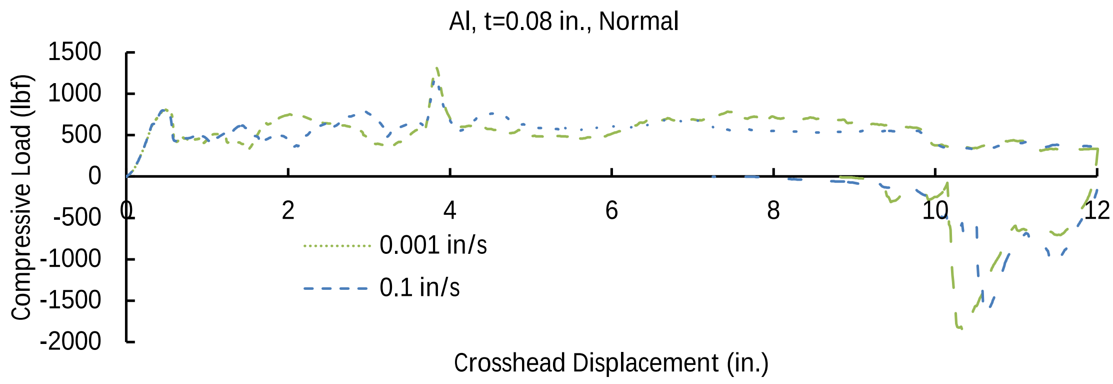

Figure D-3. Comparison of Normal Penetration of a 0.08-in.-Thick Aluminum Panel at 0.001 in./s and 0.1 in./s Loading Rates

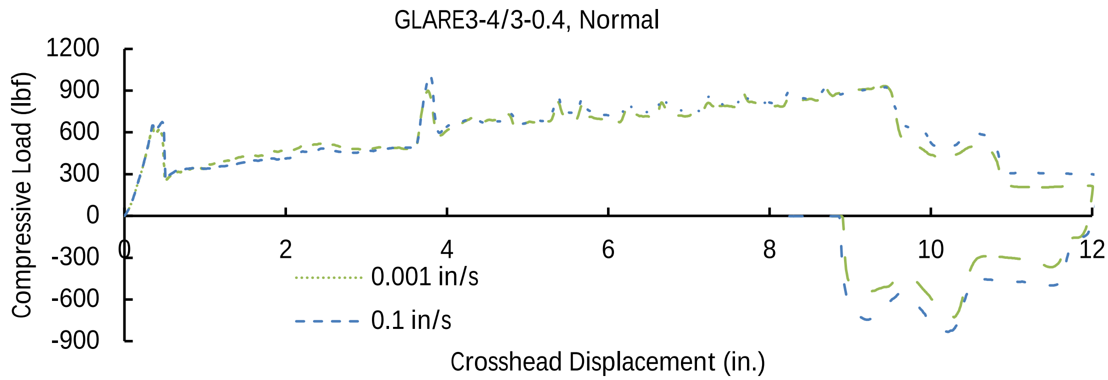

Figure D-4. Comparison of Normal Penetration of a G3-4/3-0.4 GLARE Panel at 0.001 in./s and 0.1 in./s Loading Rates

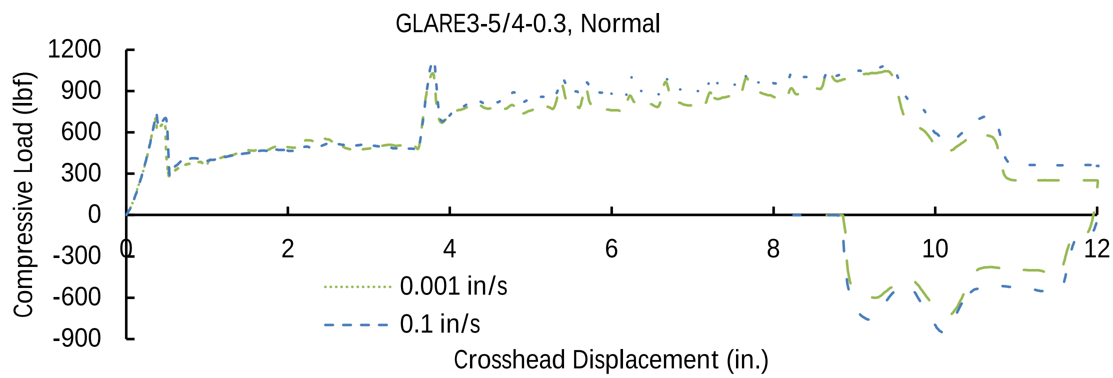

Figure D-5. Comparison of Normal Penetration of a G3-5/4-0.3 GLARE Panel at 0.001 in./s and 0.1 in./s Loading Rates

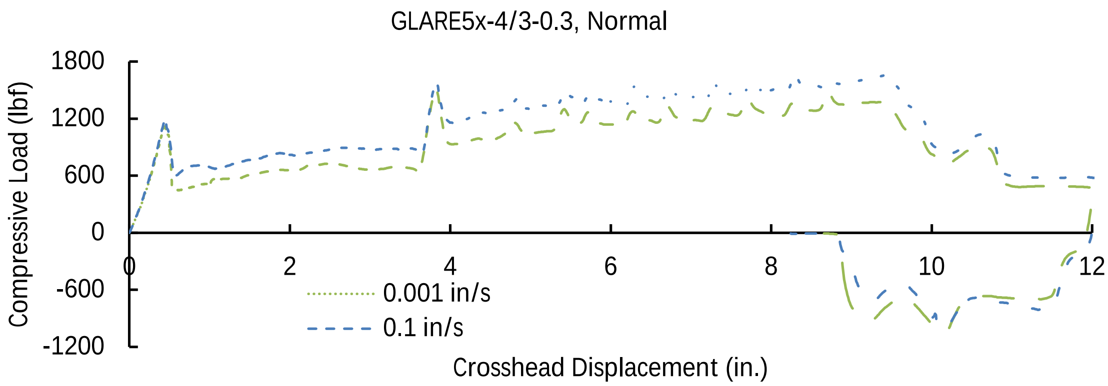

Figure D-6. Comparison of Normal Penetration of a G5x-4/3-0.3 GLARE Panel at 0.001 in./s and 0.1 in./s Loading Rates

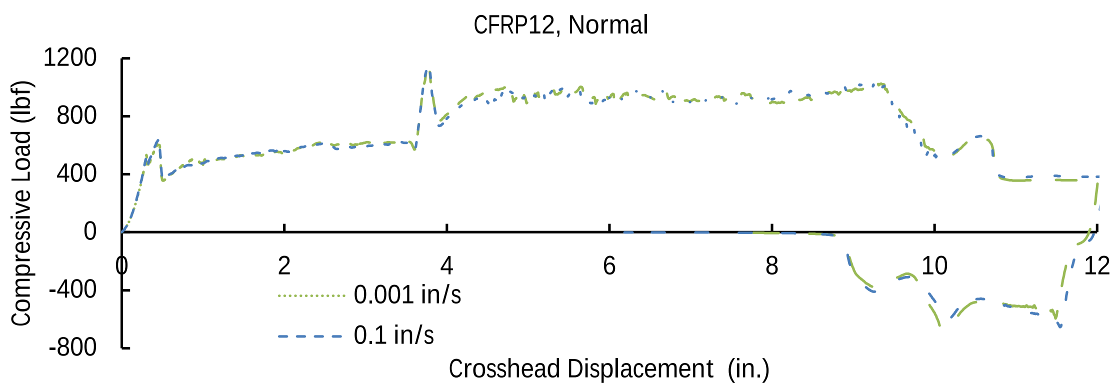

Figure D-7. Comparison of Normal Penetration of a 12-ply CFRP Panel at 0.001 in./s and 0.1 in./s Loading Rates

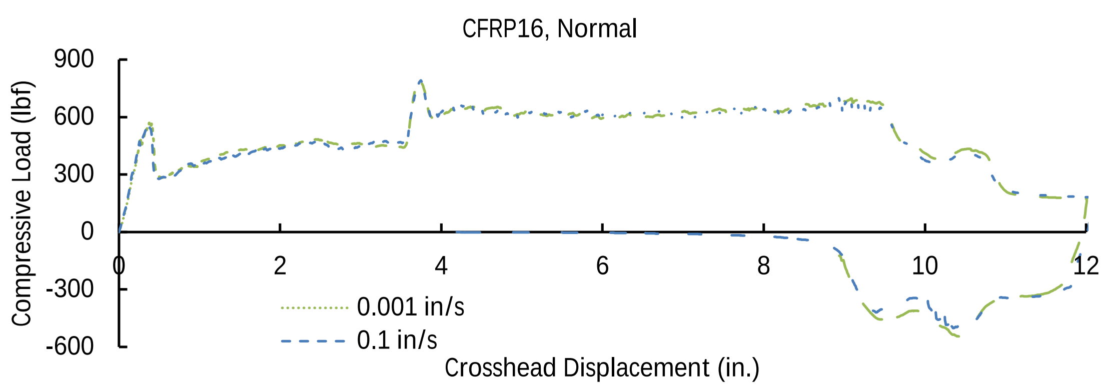

Figure D-8. Comparison of Normal Penetration of a 16-ply CFRP Panel at 0.001 in./s and 0.1 in./s Loading Rates

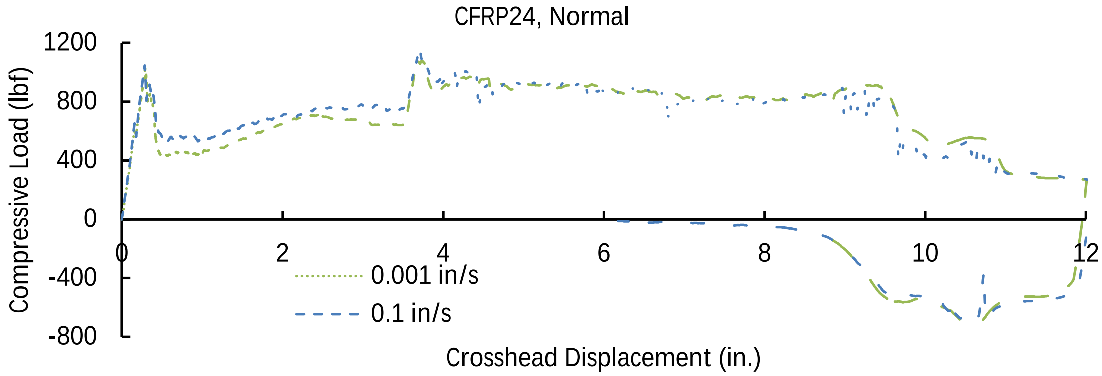

Figure D-9. Comparison of Normal Penetration of a 24-ply CFRP Panel at 0.001 in./s and 0.1 in./s Loading Rates

D.2 THE 45-DEGREE ANGLE PENETRATION.

Figures D-10 through D-18 depict the comparison of the different loading rates under 45-degree angle penetration conditions on the three different thicknesses of test panels: aluminum, GLARE, and CFRP panels.

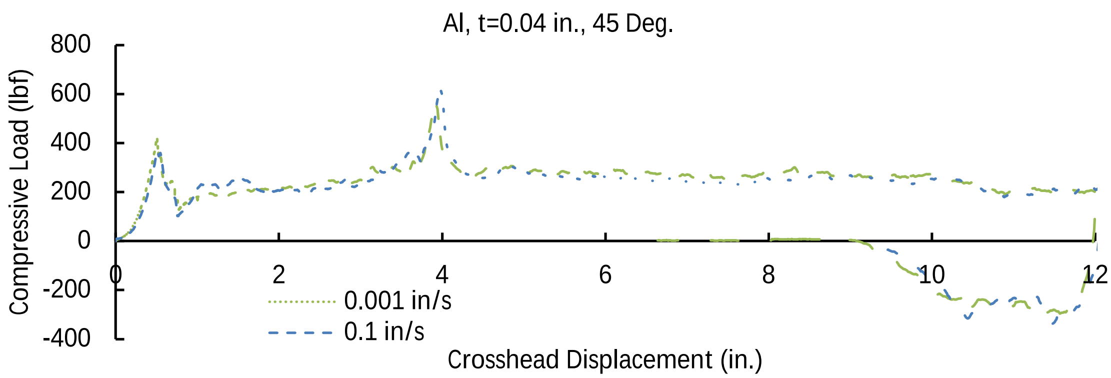

Figure D-10. Comparison of 45-Degree Angle Penetration of a 0.04-in.-Thick Aluminum Panel at 0.001 in./s and 0.1 in./s Loading Rates

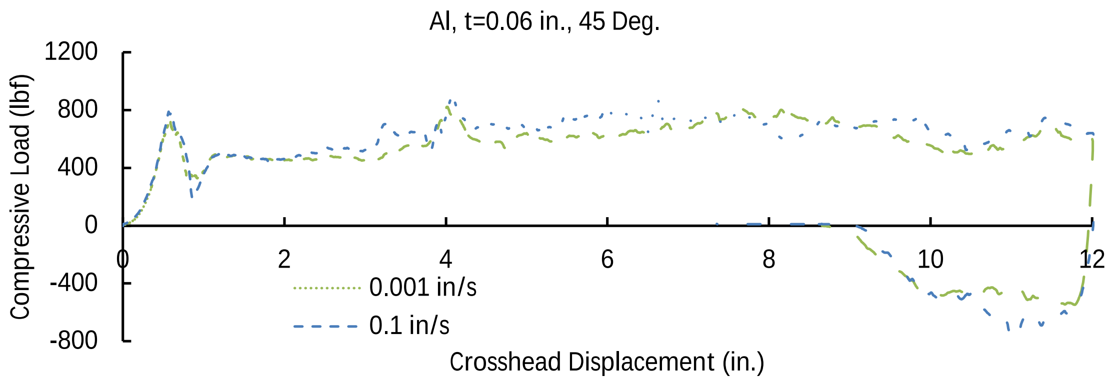

Figure D-11. Comparison of 45-Degree Angle Penetration of a 0.06-in.-Thick Aluminum Panel at 0.001 in./s and 0.1 in./s Loading Rates

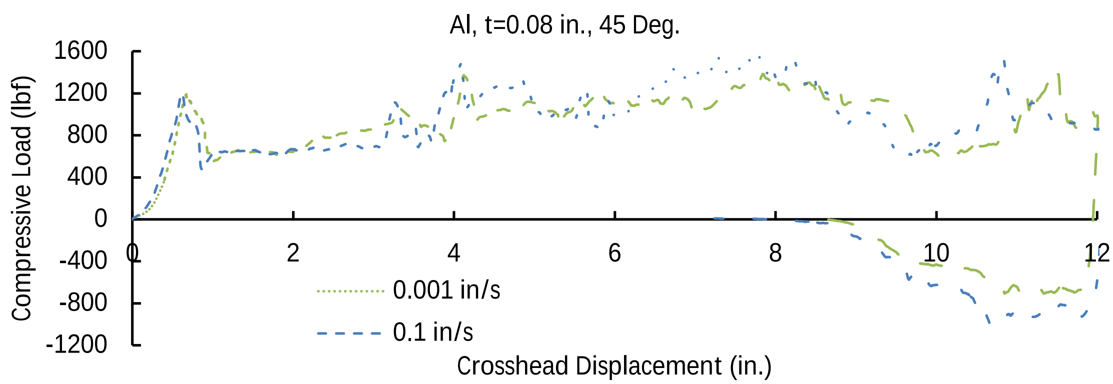

Figure D-12. Comparison of 45-Degree Angle Penetration of a 0.08-in.-Thick Aluminum Panel at 0.001 in./s and 0.1 in./s Loading Rates

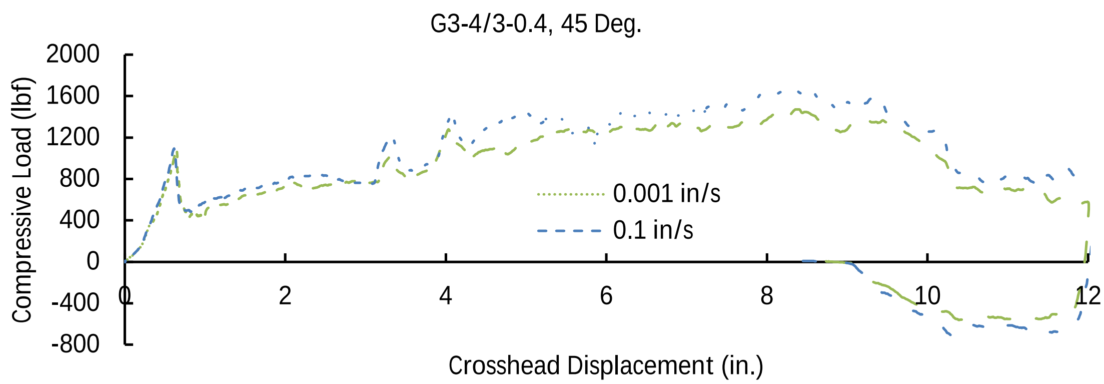

Figure D-13. Comparison of 45-Degree Angle Penetration of a G3-4/3-0.4 GLARE Panel at 0.001 in./s and 0.1 in./s Loading Rates

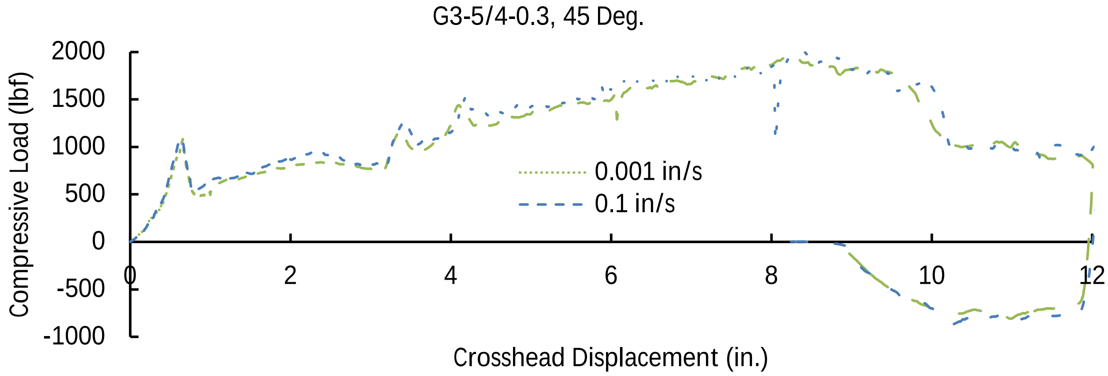

Figure D-14. Comparison of 45-Degree Angle Penetration of a G3-5/4-0.3 GLARE Panel at 0.001 in./s and 0.1 in./s Loading Rates

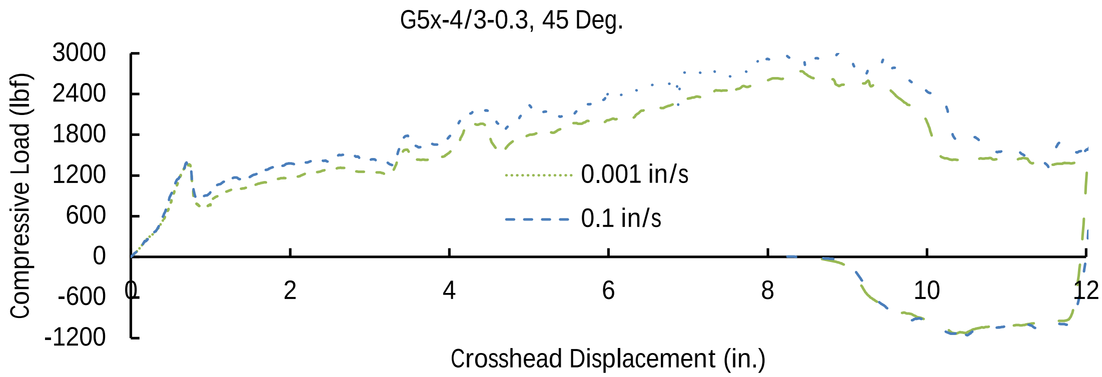

Figure D-15. Comparison of 45-Degree Angle Penetration of a G5x-4/3-0.3 GLARE Panel at 0.001 in./s and 0.1 in./s Loading Rates

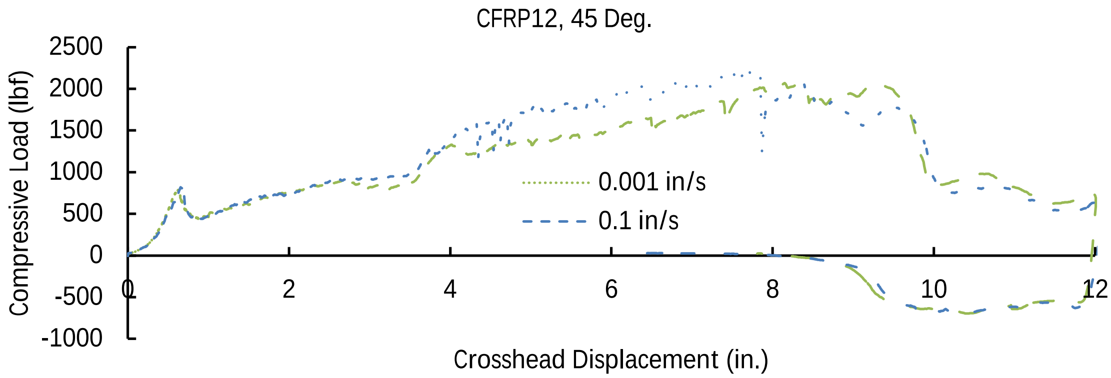

Figure D-16. Comparison of 45-Degree Angle Penetration of a 12-ply CFRP Panel at 0.001 in./s and 0.1 in./s Loading Rates

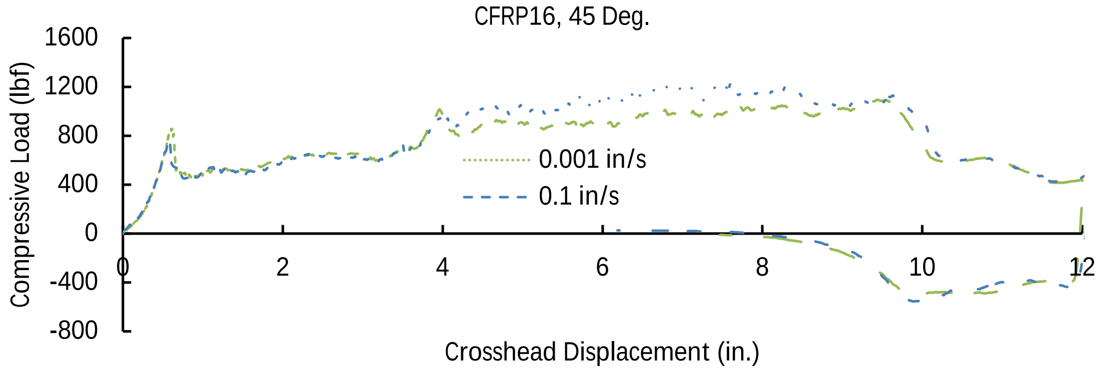

Figure D-17. Comparison of 45-Degree Angle Penetration of a 16-ply CFRP Panel at 0.001 in./s and 0.1 in./s Loading Rates

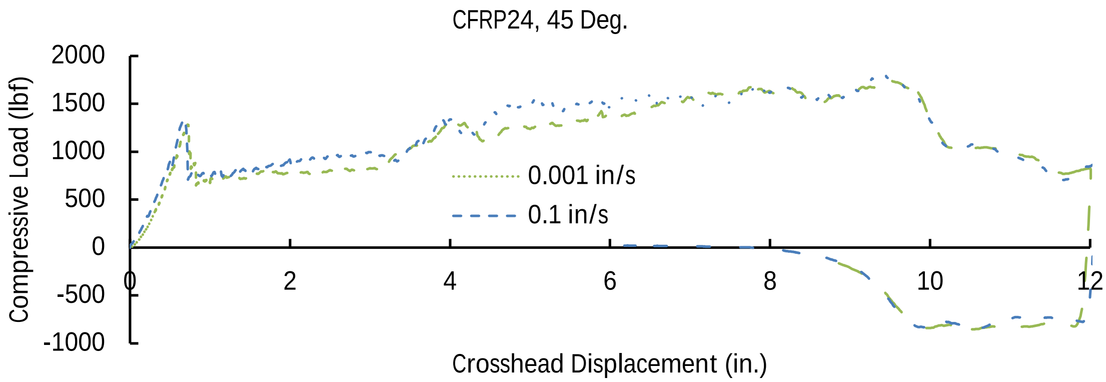

Figure D-18. Comparison of 45-Degree Angle Penetration of a 24-ply CFRP Panel at 0.001 in./s and 0.1 in./s Loading Rates

APPENDIX E—STRAIN GAGE RESULTS

E.1 NORMAL PENETRATION.

Strains were measured on top and bottom surfaces of the aluminum, glass fiber-reinforced (GLARE) aluminum laminate, and carbon fiber-reinforced plastic (CFRP) laminate panels using strain gages. In normal 90-degree penetration condition, each panel was instrumented with strain gages. Strain results are used to ensure the proper load introduction to the panel and the repeatability of the tests.

E.1.1 The 0.04-in.-Thick Aluminum Panel Under Normal Penetration.

The strain gage locations of the first of three repeated tests (Test1) for the 0.04-in.-thick aluminum under normal penetration are shown in figure E-1. A total of eight uniaxial strain gages were instrumented: four on the top surface, A1 to A4, and four on the bottom surface, B1 to B4. All eight were mounted 2-in. radial distance from center to measure radial strain. In the subsequent two tests (Test2 and Test3), only strain gages A1 and B1 were instrumented. The radial strain results of strain gages A1 through A4 of Test1 are shown in figure E-2. The results show the axisymmetric strain distribution up to breakthrough and confirm the repeatability of the tests. The comparison of strain gage location A1 for three repeated tests is shown in figure E-3. Similar to the top surface, the bottom surface radial strain results are plotted and compared in figures E-4 and E-5.

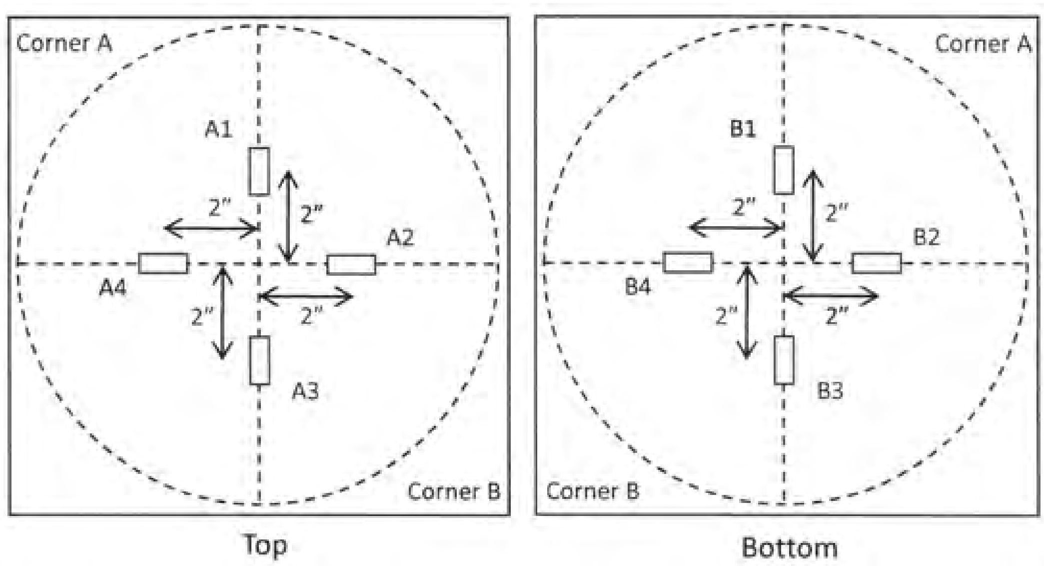

Figure E-1. Strain Gage Locations of 0.04-in.-Thick Aluminum Panel Under Normal Penetration

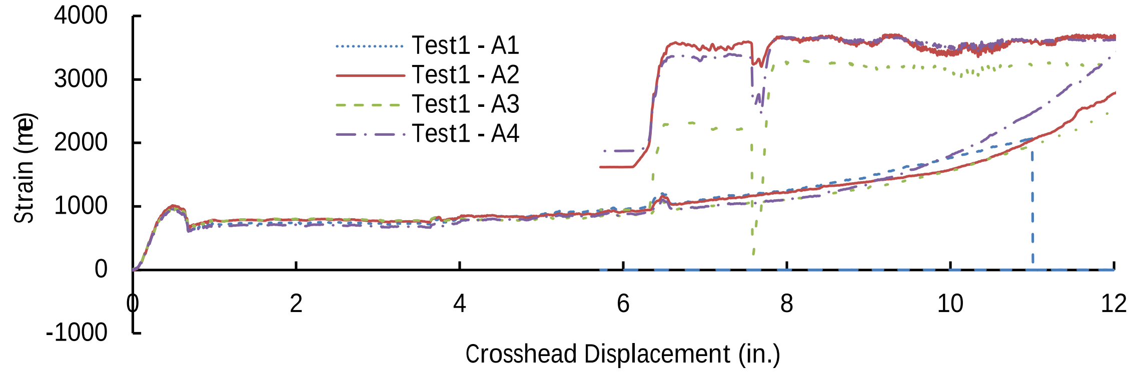

Figure E-2. Results of Four Strain Gages Located at the top Surface of the First 0.04-in. Aluminum Panel Under Normal Penetration

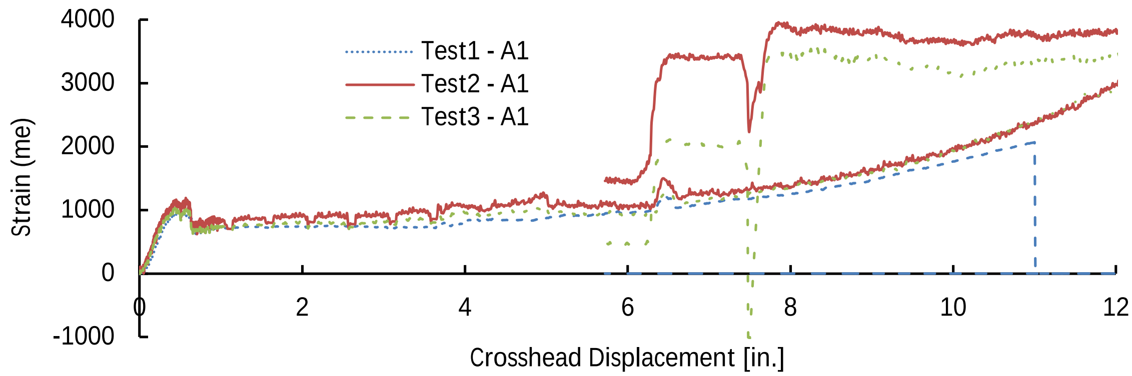

Figure E-3. Comparison of Strain Gages Located on the top Surface at A1 Position for Three Repeated Tests of a 0.04-in. Aluminum Panel Under Normal Penetration

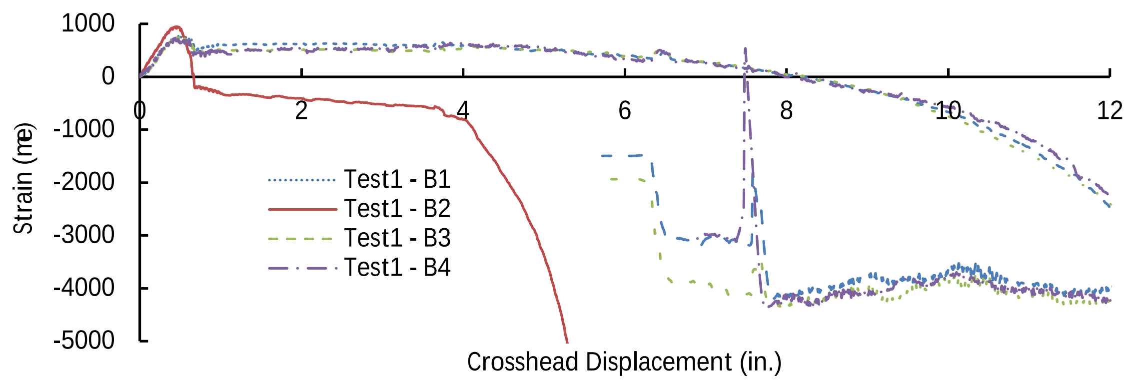

Figure E-4. Results of Four Strain Gages Located at the Bottom Surface of the First 0.04-in. Aluminum Panel Under Normal Penetration

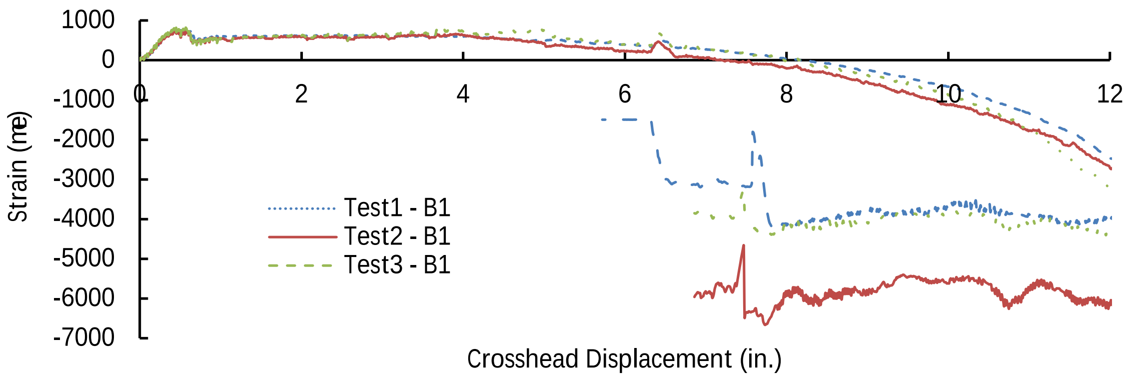

Figure E-5. Comparison of Strain Gages Located on the Bottom Surface at B1 Position for Three Repeated Tests of 0.04-in. Aluminum Panel Under Normal Penetration

E.1.2 The 0.06-in.-Thick Aluminum Panel Under Normal Penetration.

The strain gage locations of the first of three repeated tests (Test1) for the 0.06-in.-thick aluminum panel under normal penetration are shown in figure E-6. A total of three uniaxial strain gages were instrumented: two on the top surface, A1 and A2, and one on the bottom surface, B1. All three were mounted 2-in. radial distance from center to measure radial strain. In the subsequent two tests (Test2 and Test3), only A1 and B1 were instrumented. The radial strain results of strain gages A1 and A2 from Test1, strain gage A1 of Test2, and strain gage A1 of Test3 are plotted and compared in figure E-7. The results show the axisymmetric strain distribution up to breakthrough and confirm the repeatability of the tests. Similar to the top surface, the bottom surface radial strain results are plotted and compared in figure E-8.

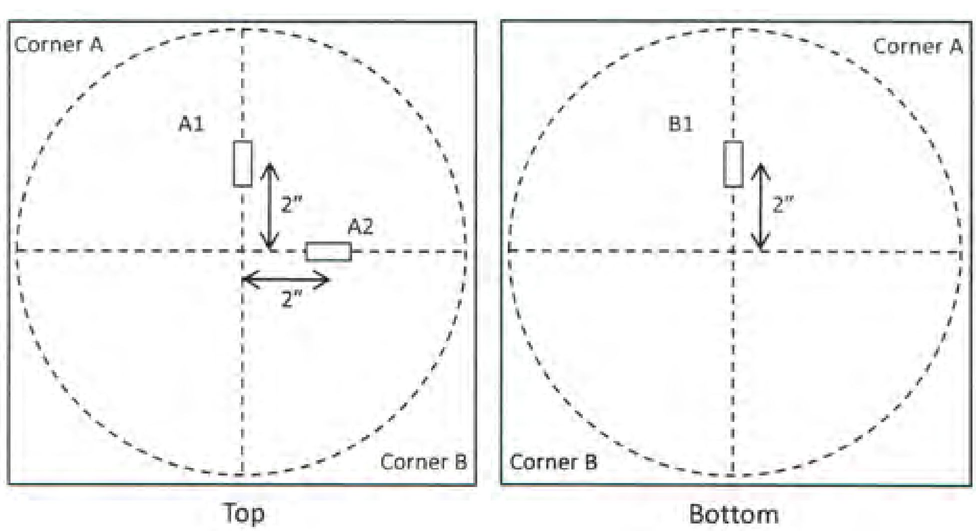

Figure E-6. Strain Gage Location of the 0.06-in.-Thick Aluminum Panel Under Normal Penetration

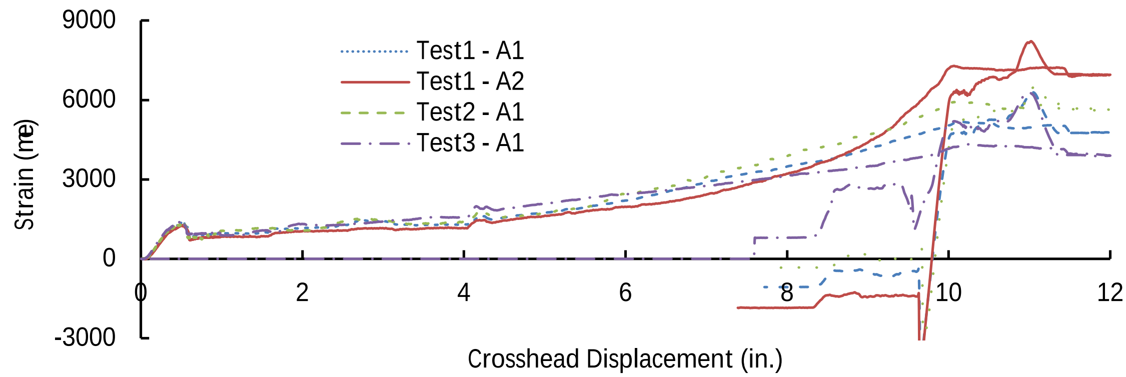

Figure E-7. Results of top Surface Strain Gages of Three Repeated Tests of the 0.06-in. Aluminum Panel Under Normal Penetration

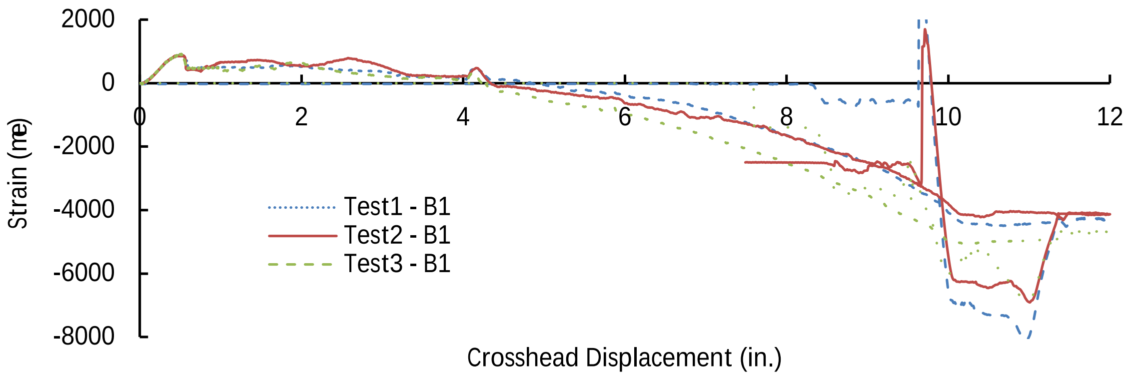

Figure E-8. Results of Bottom Surface Strain Gages of Three Repeated Tests of the 0.06-in. Aluminum Panel Under Normal Penetration

E.1.3 The 0.08-in.-Thick Aluminum Panel Under Normal Penetration.

The strain gage locations of the first of three repeated tests (Test1) for the 0.08-in.-thick aluminum panel under normal penetration are shown in figure E-9. A total of four uniaxial strain gages were instrumented: two on the top surface, A1 and A2, and two on the bottom surface, B1 and B2. All four were mounted 2-in. radial distance from center to measure radial strain. In the subsequent two tests (Test2 and Test3), only A1 and B1 were instrumented. The radial strain results of strain gages A1 and A2 from Test1, strain gage A1 of Test2, and strain gage A1 of Test3 are plotted and compared in figure E-10. The results show the axisymmetric strain distribution up to breakthrough and confirm the repeatability of the tests. Similar to the top surface, bottom surface radial strain results are plotted and compared in figure E-11.

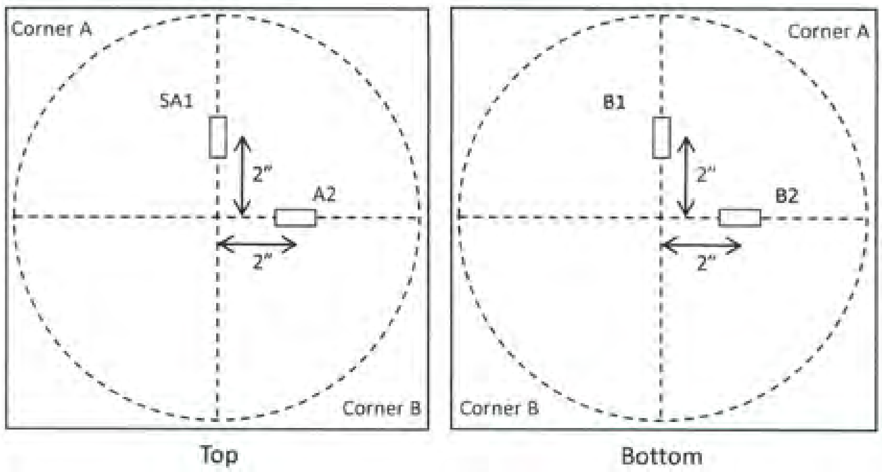

Figure E-9. Strain Gage Location of the 0.08-in.-Thick Aluminum Panel Under Normal Penetration

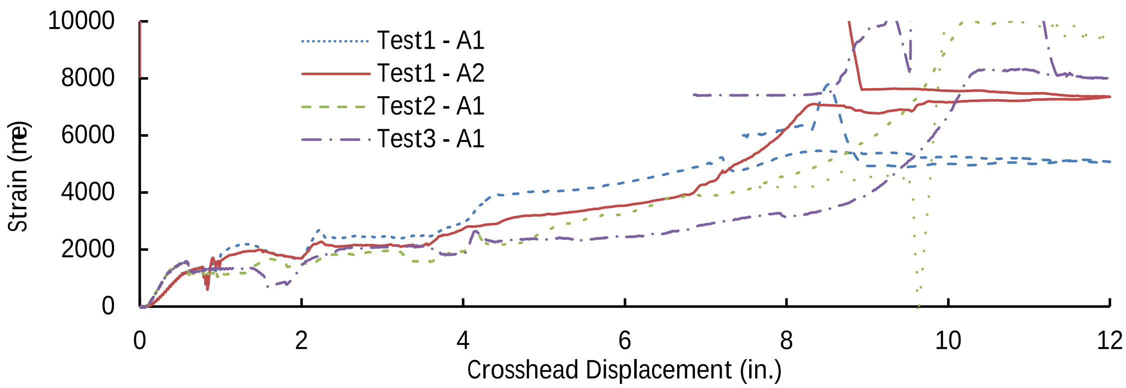

Figure E-10. Results of top Surface Strain Gages of Three Repeated Tests of the 0.08-in. Aluminum Panel Under Normal Penetration

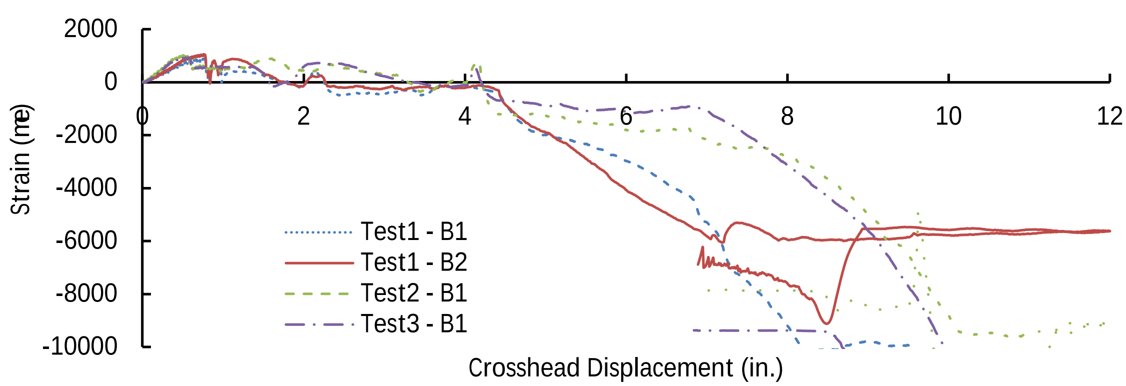

Figure E-11. Results of Bottom Surface Strain Gages of Three Repeated Tests of 0.08-in. Aluminum Panel Under Normal Penetration

E.1.4 The G3-4/3-0.3 GLARE Panel Under Normal Penetration.

The strain gage location of the first of three repeated tests (Test1) for the G3-4/3-0.3 GLARE panel under normal penetration are shown in figure E-12. A total of four rosette strain gages were instrumented: two on the top surface, A series (A2, A3, A4) and B series (B2, B3, B4), and two on the bottom surface, C series (C2, C3, C4) and D series (D2, D3, D4). All four rosette strain gages were mounted 2-in. radial distance from center. Strain gages A3, B3, C3, and D3 were mounted to measure radial strain and the rest of the strain gages were mounted to measure ±45-degree angle strain with respect to the radial direction. The same strain gage configuration was used in subsequent two tests (Test2 and Test3). The arrow in the figure indicates the fiber direction of the first glass/epoxy layer (second overall layer) from the top or penetrating side of the panel. The strain comparison of the three repeated tests of strain gages A2, A3, A4, B2, B3, B4, C2, C3, C4, D2, D3, and D4 are shown in figures E-13 through E-24. The results confirm the repeatability of the tests.

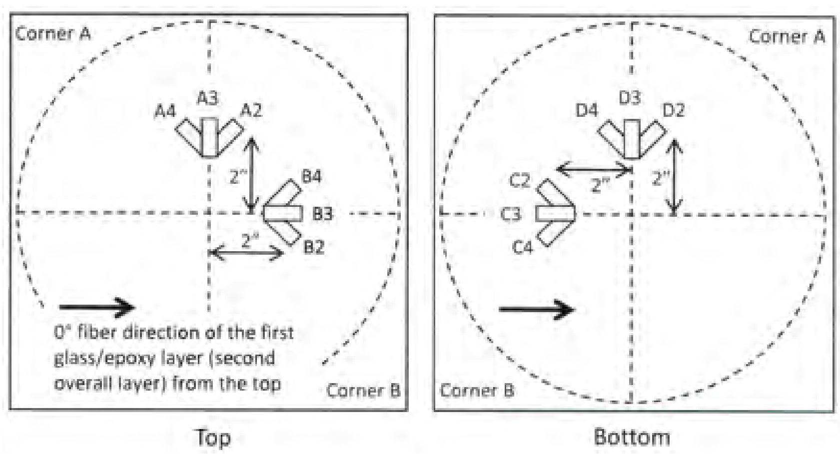

Figure E-12. Strain Gage Location of the G3-4/3-0.3 GLARE Panel Under Normal Penetration

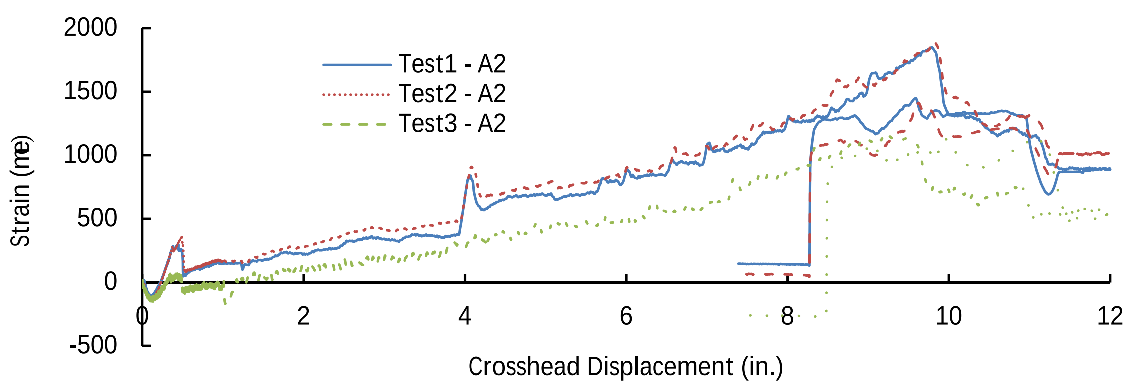

Figure E-13. Strain Gage A2 Response of Three Repeated Tests of the G3-4/3-0.3 GLARE Panel Under Normal Penetration

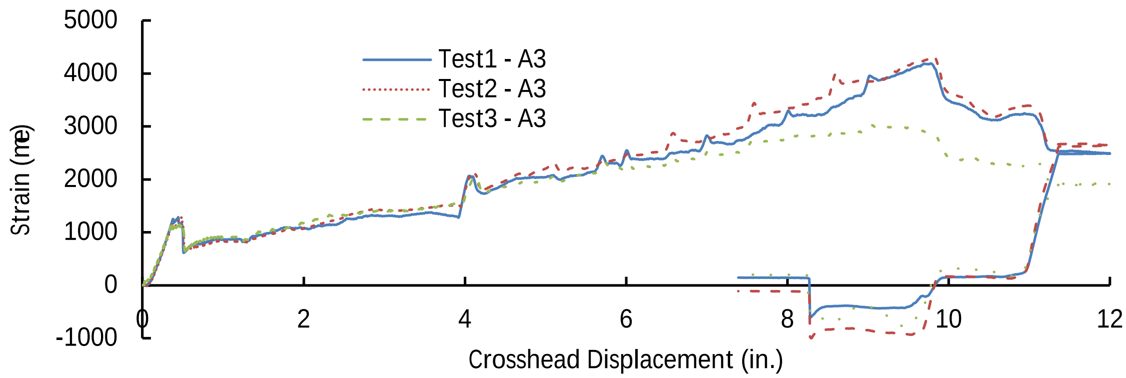

Figure E-14. Strain Gage A3 Response of Three Repeated Tests of the G3-4/3-0.3 GLARE Panel Under Normal Penetration

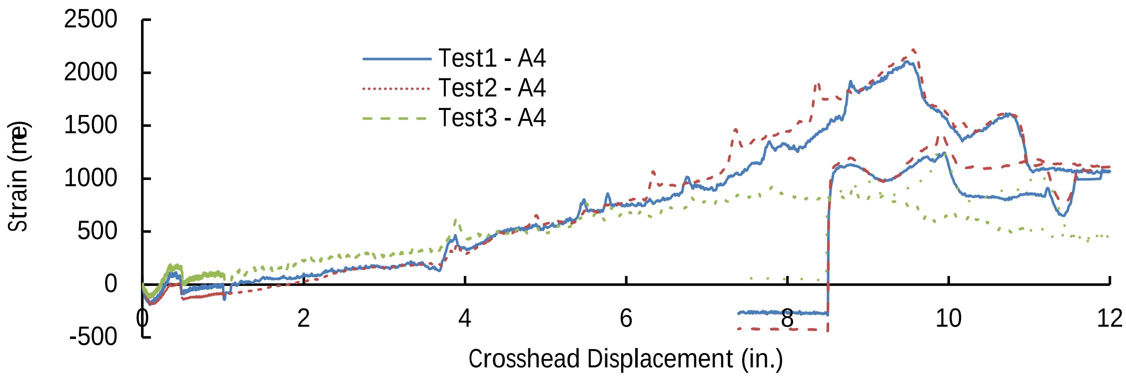

Figure E-15. Strain Gage A4 Response of Three Repeated Tests of the G3-4/3-0.3 GLARE Panel Under Normal Penetration

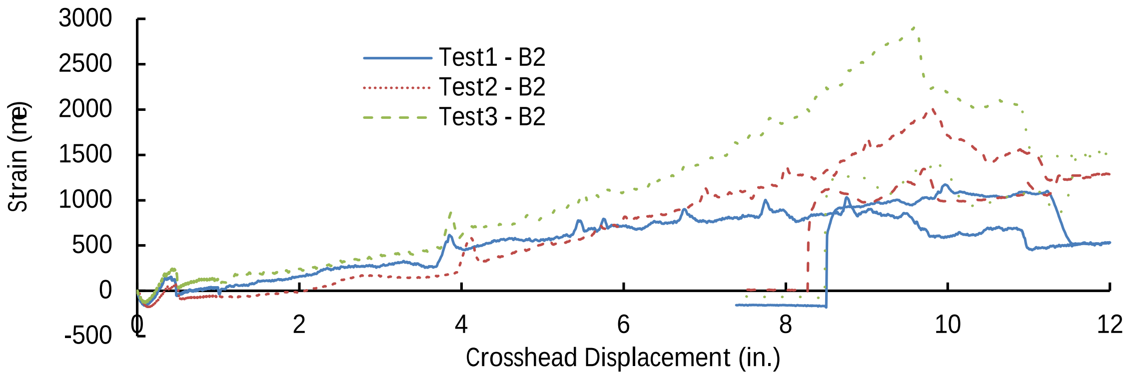

Figure E-16. Strain Gage B2 Response of Three Repeated Tests of the G3-4/3-0.3 GLARE Panel Under Normal Penetration

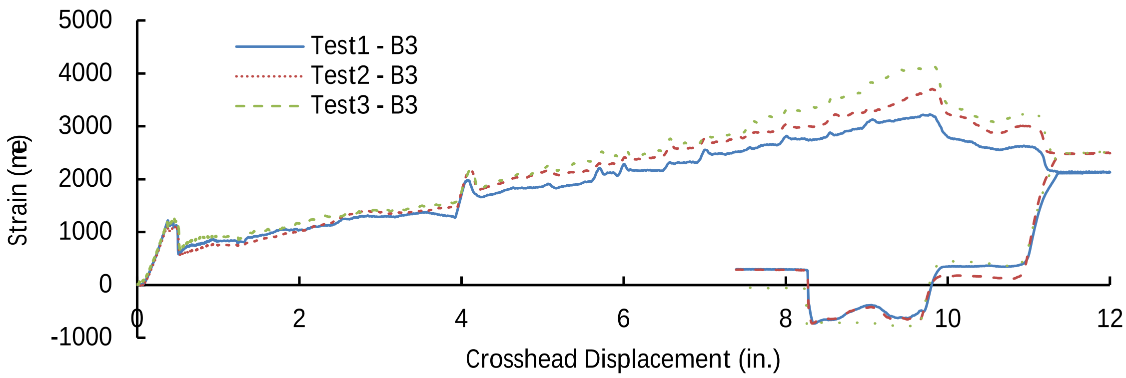

Figure E-17. Strain Gage B3 Response of Three Repeated Tests of the G3-4/3-0.3 GLARE Panel Under Normal Penetration

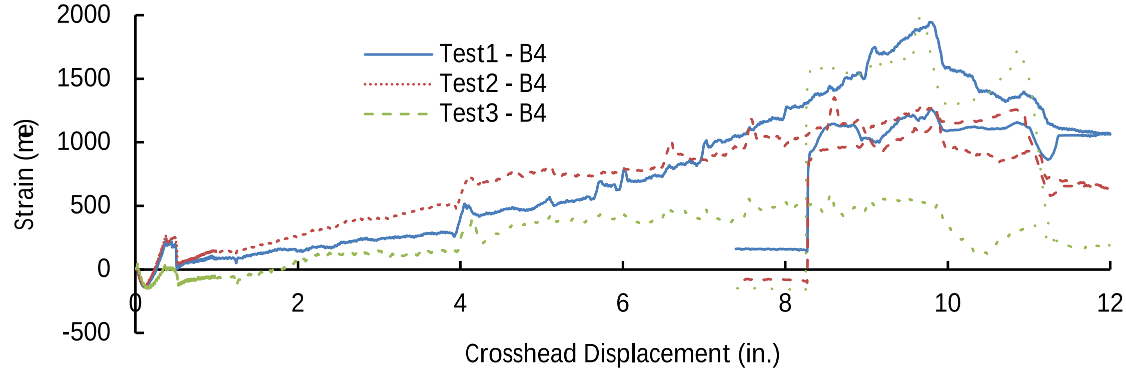

Figure E-18. Strain Gage B4 Response of Three Repeated Tests of the G3-4/3-0.3 GLARE Panel Under Normal Penetration

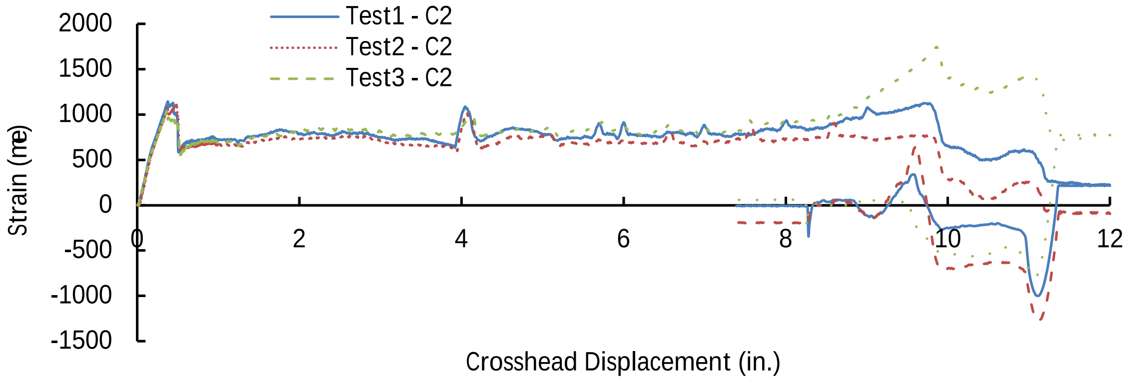

Figure E-19. Strain Gage C2 Response of Three Repeated Tests of the G3-4/3-0.3 GLARE Panel Under Normal Penetration

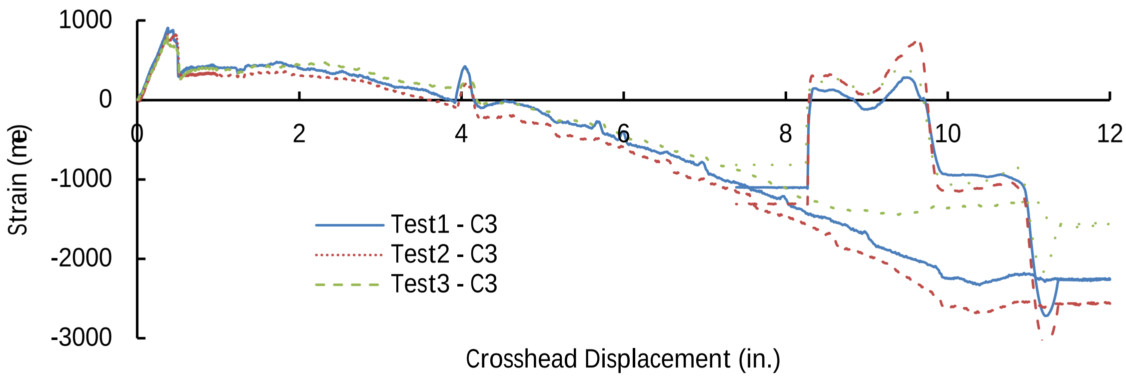

Figure E-20. Strain Gage C3 Response of Three Repeated Tests of the G3-4/3-0.3 GLARE Panel Under Normal Penetration

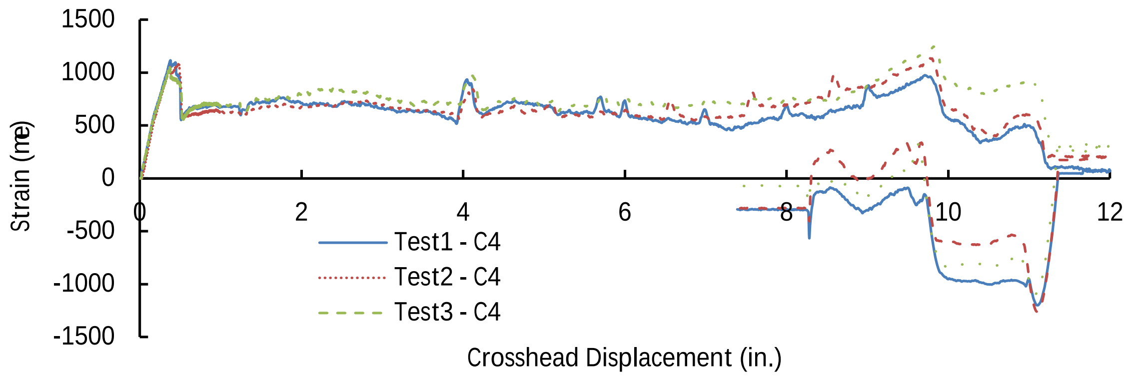

Figure E-21. Strain Gage C4 Response of Three Repeated Tests of the G3-4/3-0.3 GLARE Panel Under Normal Penetration

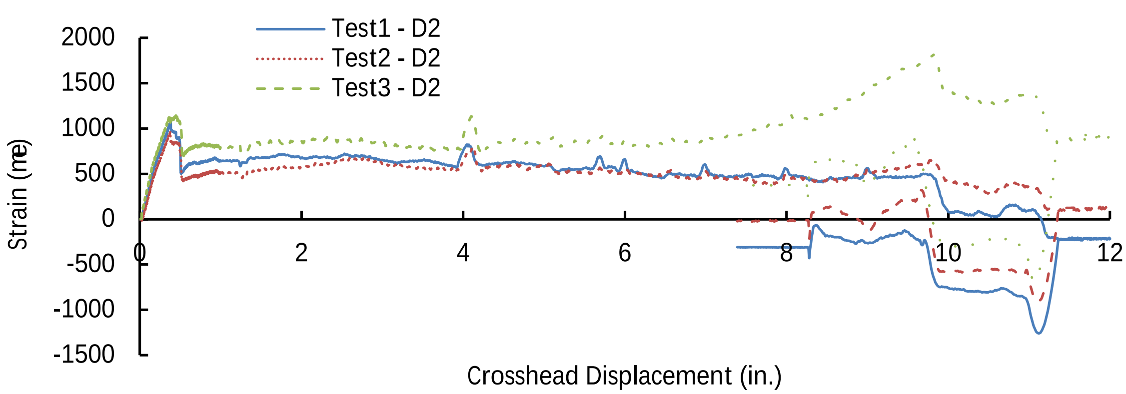

Figure E-22. Strain Gage D2 Response of Three Repeated Tests of the G3-4/3-0.3 GLARE Panel Under Normal Penetration

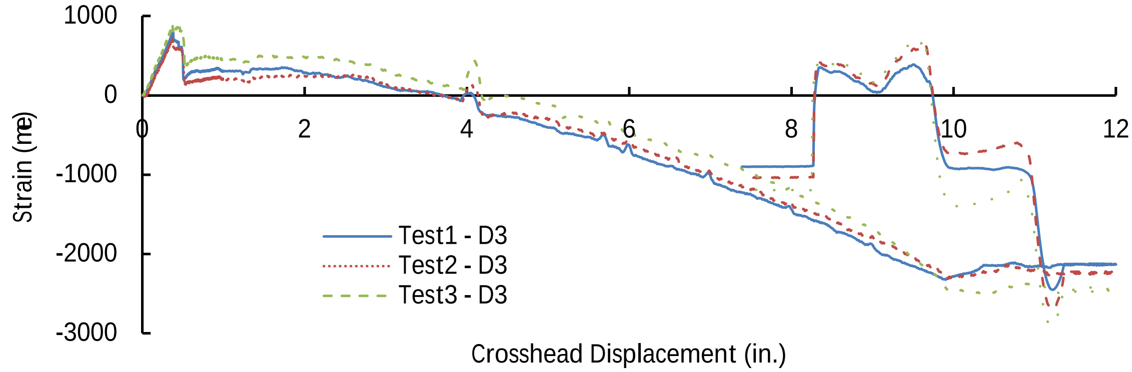

Figure E-23. Strain Gage D3 Response of Three Repeated Tests of the G3-4/3-0.3 GLARE Panel Under Normal Penetration

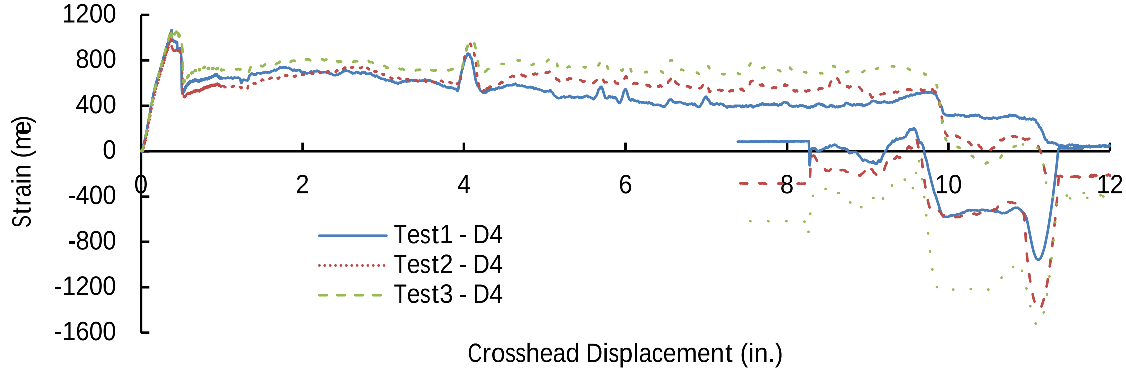

Figure E-24. Strain Gage D4 Response of Three Repeated Tests of the G3-4/3-0.3 GLARE Panel Under Normal Penetration

E.1.5 The G3-5/4-0.4 GLARE Panel Under Normal Penetration.

The strain gage locations of the first of three repeated tests (Test1) for the G3-5/4-0.4 GLARE panel under normal penetration are shown in figure E-25. A total of four rosette strain gages were instrumented: two on the top surface, A series (A2, A3, A4) and B series (B2, B3, B4), and two on the bottom surface, C series (C2, C3, C4) and D series (D2, D3, D4). All four rosette strain gages were mounted 2-in. radial distance from center. Strain gages A3, B3, C3, and D3 were mounted to measure radial strain, and the remaining strain gages were mounted to measure ±45-degree angle strain with respect to the radial direction. The same strain gage configuration was used in subsequent two tests (Test2 and Test3). The arrow in the figure indicates the fiber direction of the first glass/epoxy layer (second overall layer) from the top or penetrating side of the panel. The strain comparison of the three repeated tests of strain gages A2, A3, A4, B2, B3, B4, C2, C3, C4, D2, D3, and D4 are shown in figures E-26 through E-37. The results confirm the repeatability of the tests.

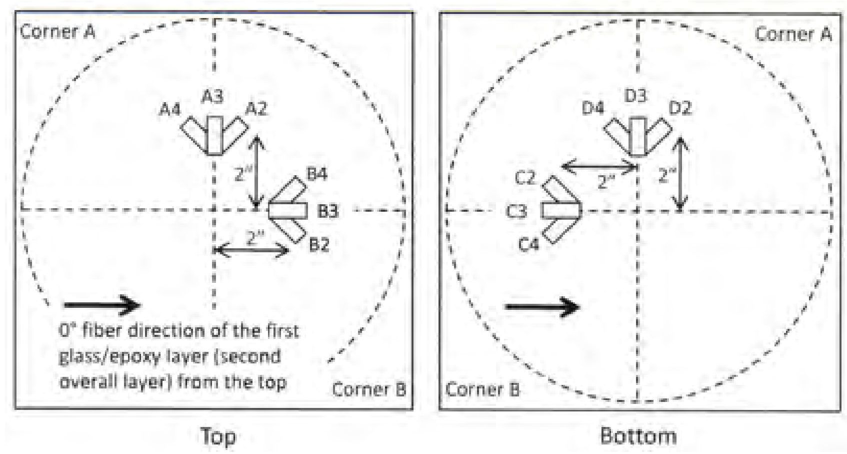

Figure E-25. Strain Gage Locations of the G3-5/4-0.4 GLARE Panel Under Normal Penetration

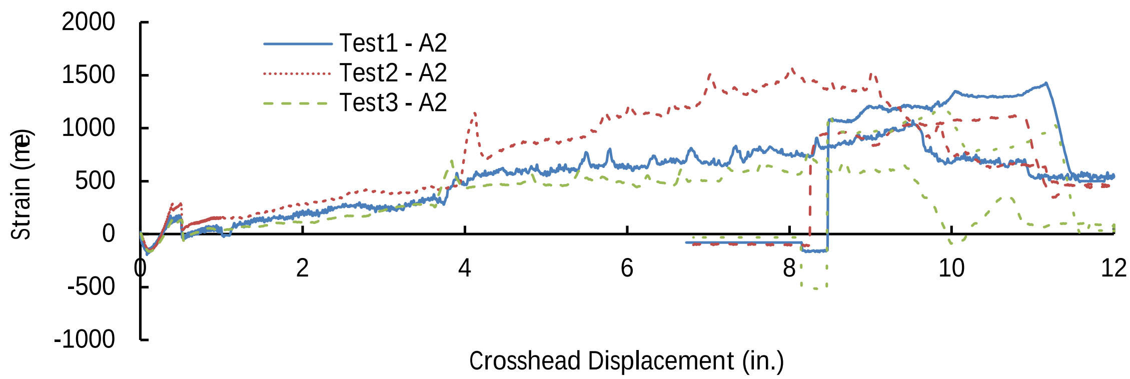

Figure E-26. Strain Gage A2 Response of Three Repeated Tests of the G3-5/4-0.4 GLARE Panel Under Normal Penetration

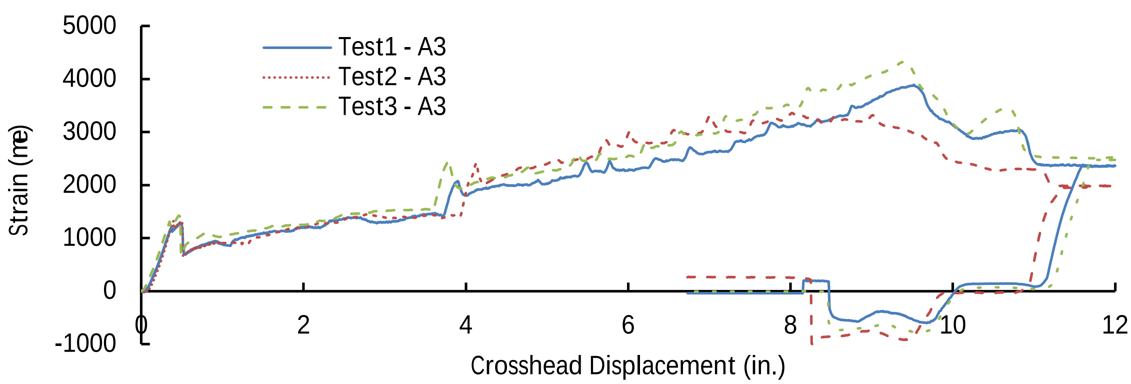

Figure E-27. Strain Gage A3 Response of Three Repeated Tests of the G3-5/4-0.4 GLARE Panel Under Normal Penetration

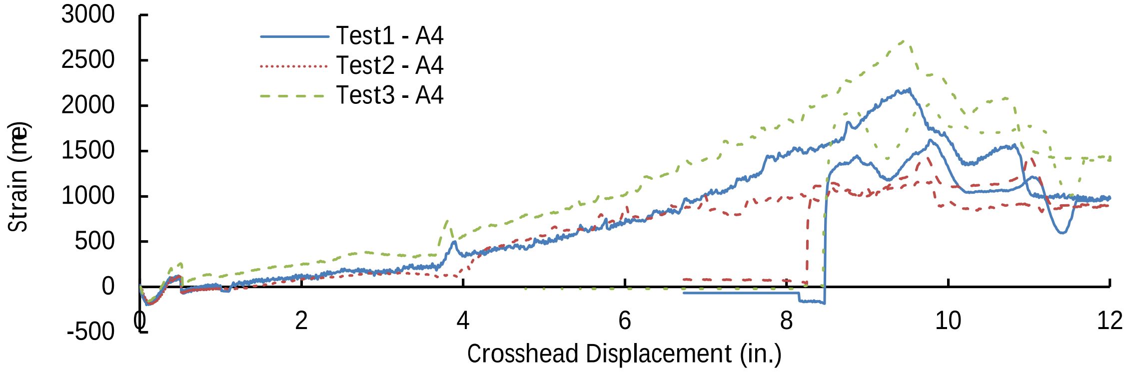

Figure E-28. Strain Gage A4 Response of Three Repeated Tests of the G3-5/4-0.4 GLARE Panel Under Normal Penetration

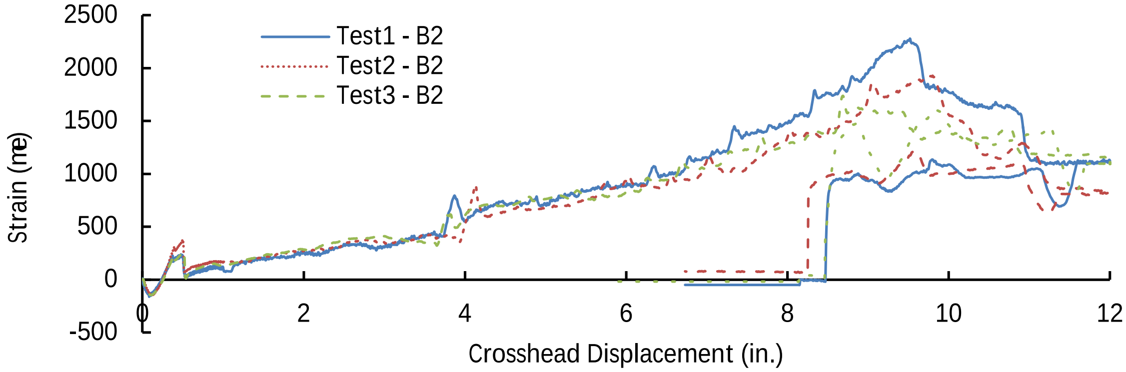

Figure E-29. Strain Gage B2 Response of Three Repeated Tests of the G3-5/4-0.4 GLARE Panel Under Normal Penetration

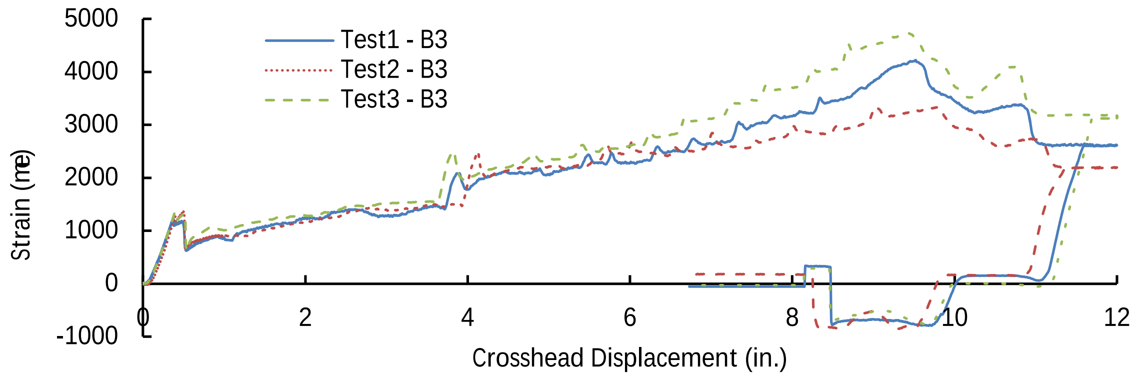

Figure E-30. Strain Gage B3 Response of Three Repeated Tests of the G3-5/4-0.4 GLARE Panel Under Normal Penetration

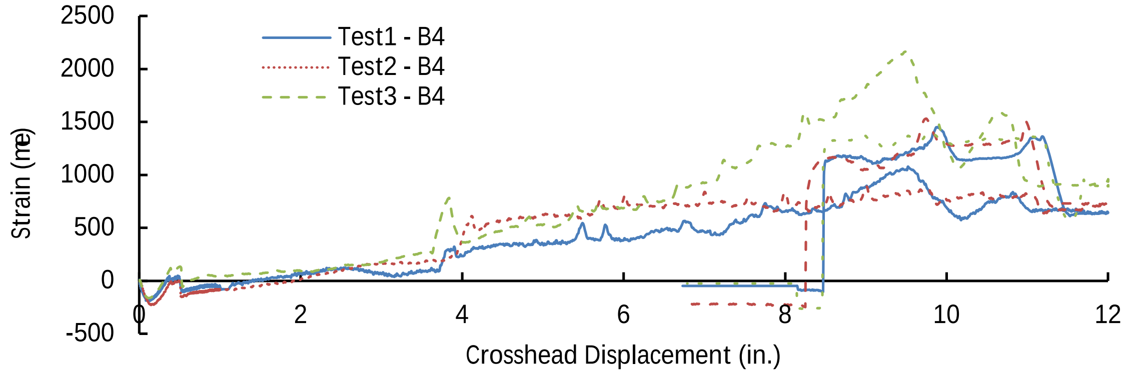

Figure E-31. Strain Gage B4 Response of Three Repeated Tests of the G3-5/4-0.4 GLARE Panel Under Normal Penetration

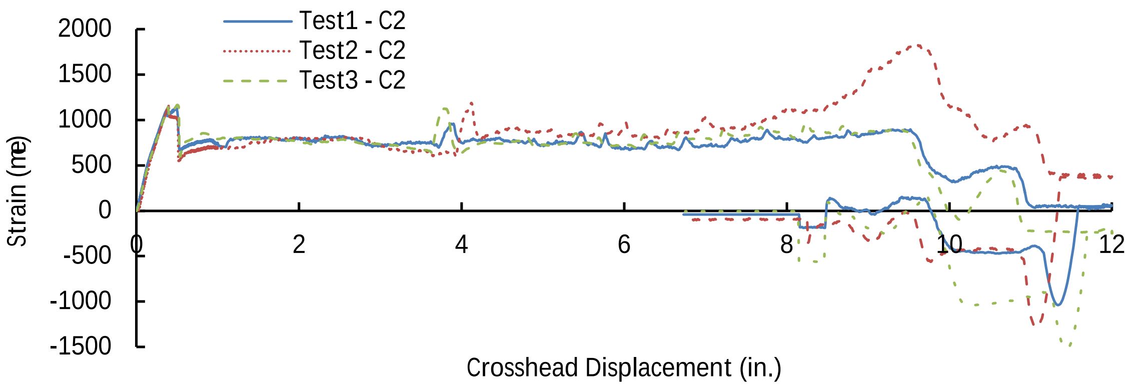

Figure E-32. Strain Gage C2 Response of Three Repeated Tests of the G3-5/4-0.4 GLARE Panel Under Normal Penetration

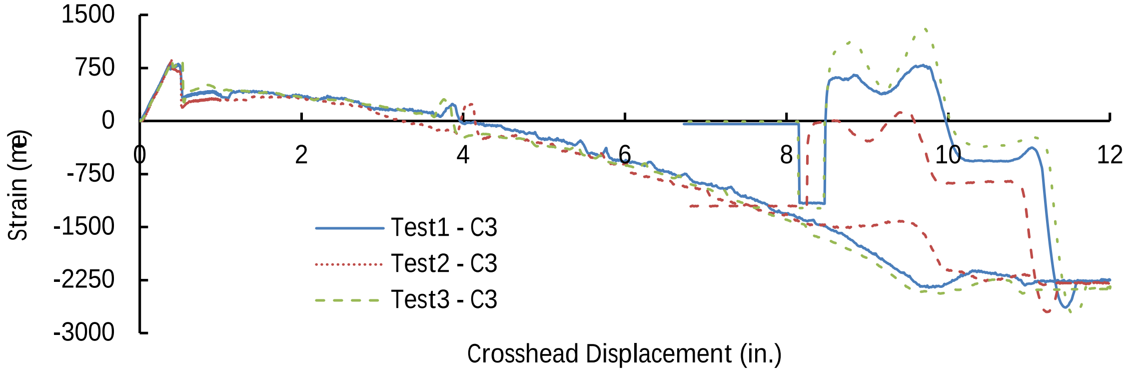

Figure E-33. Strain Gage C3 Response of Three Repeated Tests of the G3-5/4-0.4 GLARE Panel Under Normal Penetration

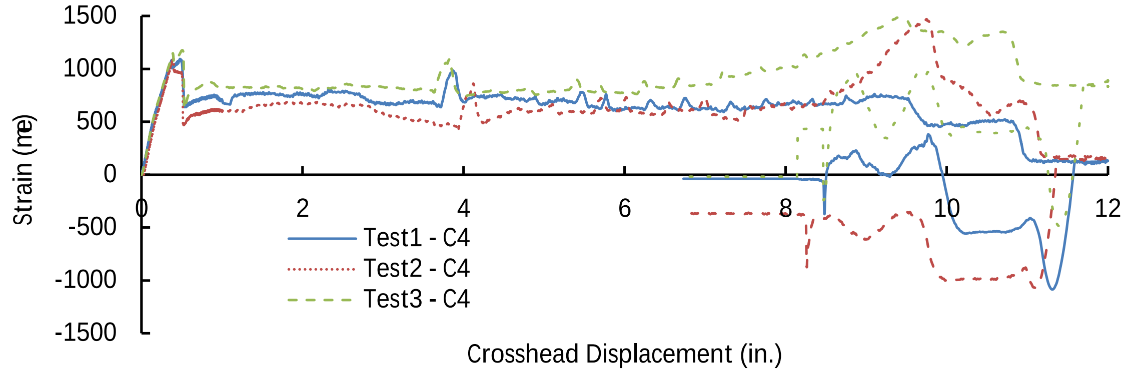

Figure E-34. Strain Gage C4 Response of Three Repeated Tests of the G3-5/4-0.4 GLARE Panel Under Normal Penetration

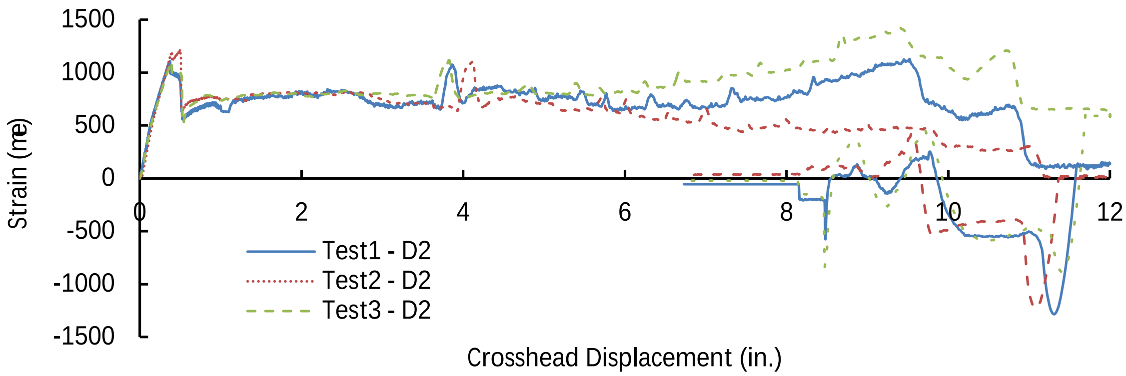

Figure E-35. Strain Gage D2 Response of Three Repeated Tests of the G3-5/4-0.4 GLARE Panel Under Normal Penetration

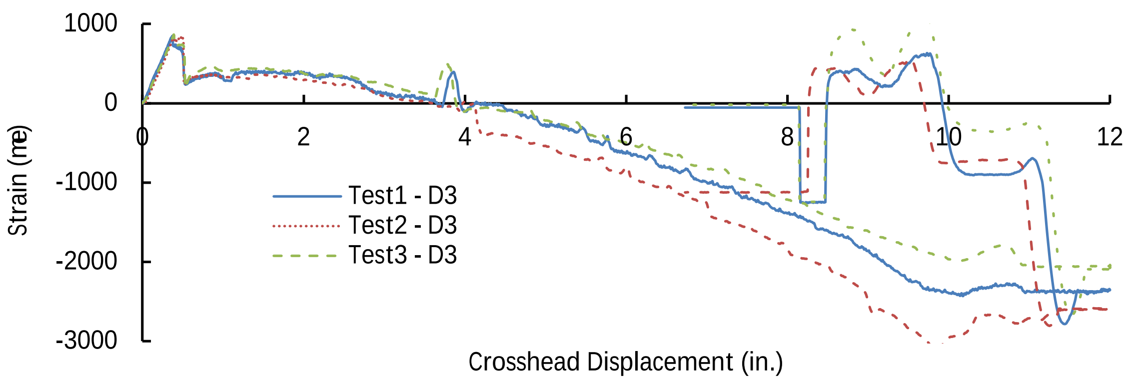

Figure E-36. Strain Gage D3 Response of Three Repeated Tests of the G3-5/4-0.4 GLARE Panel Under Normal Penetration

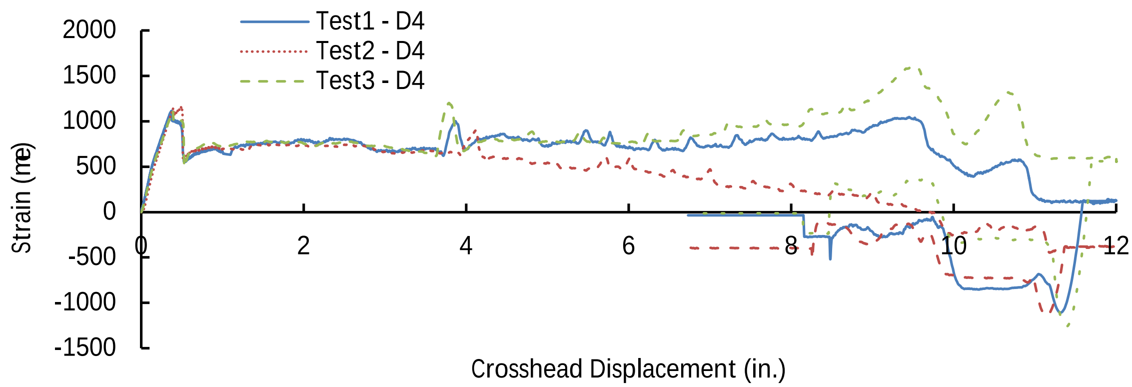

Figure E-37. Strain Gage D4 Response of Three Repeated Tests of the G3-5/4-0.4 GLARE Panel Under Normal Penetration

E.1.6 The G5x-4/3-0.3 GLARE Panel Under Normal Penetration.

The strain gage locations of the first of three repeated tests (Test1) for the G5x-4/3-0.3 GLARE panel under normal penetration are shown in figure E-38. A total of four rosette strain gages were instrumented: two on the top surface, A series (A2, A3, A4) and B series (B2, B3, B4), and two on the bottom surface, C series (C2, C3, C4) and D series (D2, D3, D4). All four rosette strain gages were mounted 2-in. radial distance from center. Strain gages A3, B3, C3, and D3 were mounted to measure radial strain and the remaining strain gages were mounted to measure ±45-degree angle strain with respect to the radial direction. The same strain gage configuration was used in subsequent test (Test2) and the last test (Test3) was not instrumented with strain gages. The arrow in the figure indicates the fiber direction of the first glass/epoxy layer (second overall layer) from the top or penetrating side of the panel. The strain comparison of the two repeated tests of strain gages A2, A3, A4, B2, B3, B4, C2, C3, C4, D2, D3, and D4 are shown in figures E-39 through E-50. The results confirm the repeatability of the tests.

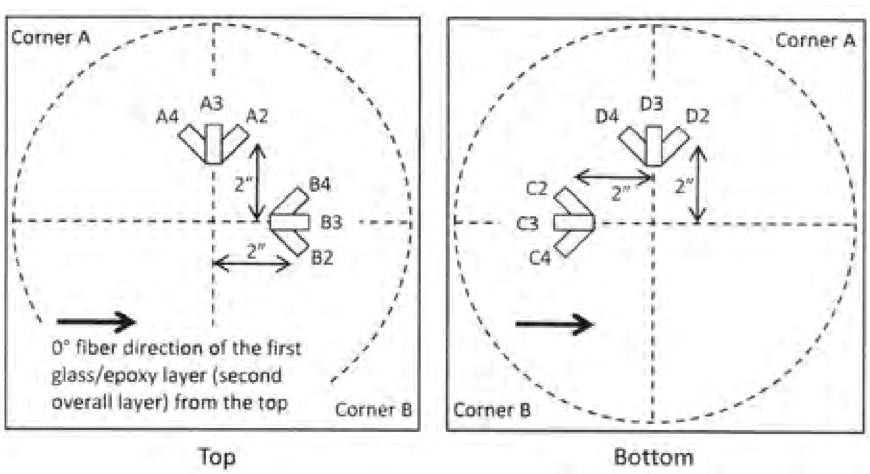

Figure E-38. Strain Gage Locations of the G5x-4/3-0.3 GLARE Panel Under Normal Penetration

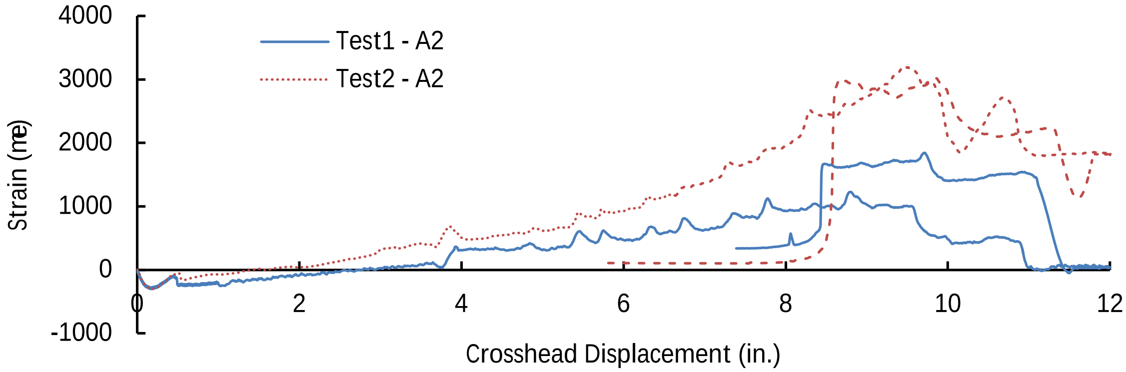

Figure E-39. Strain Gage A2 Response of Two Repeated Tests of the G5x-4/3-0.3 GLARE Panel Under Normal Penetration

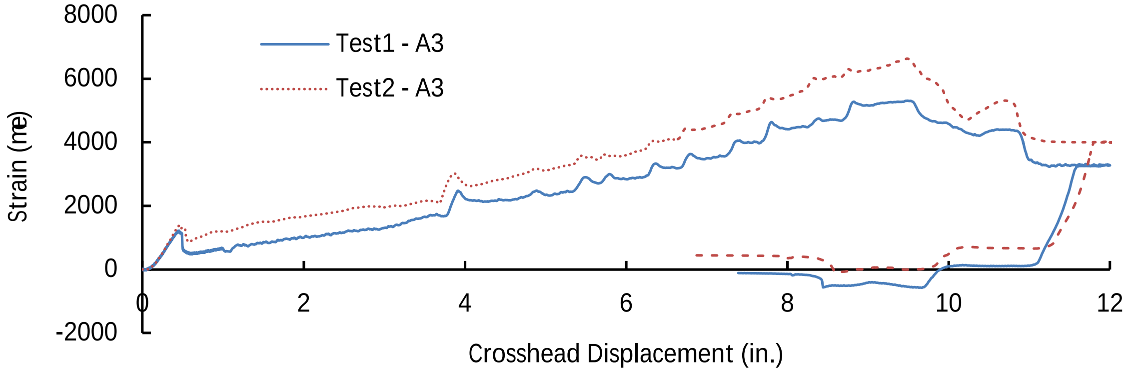

Figure E-40. Strain Gage A3 Response of Two Repeated Tests of the G5x-4/3-0.3 GLARE Panel Under Normal Penetration

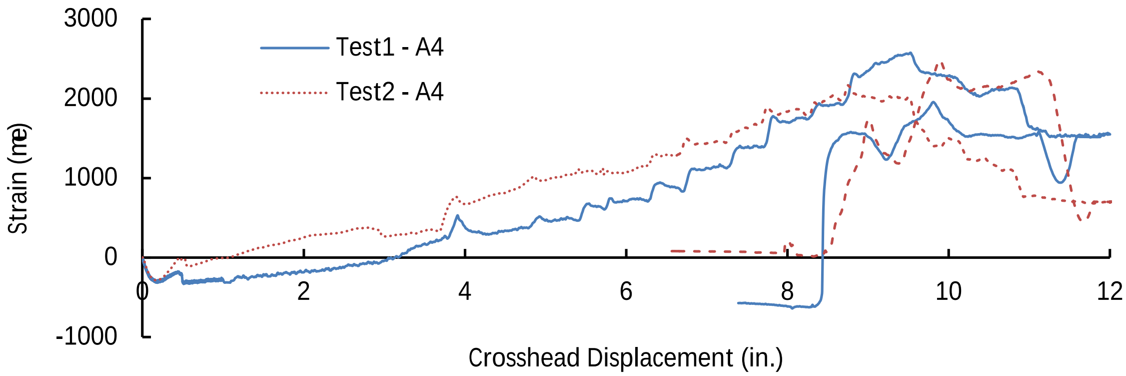

Figure E-41. Strain Gage A4 Response of Two Repeated Tests of the G5x-4/3-0.3 GLARE Panel Under Normal Penetration

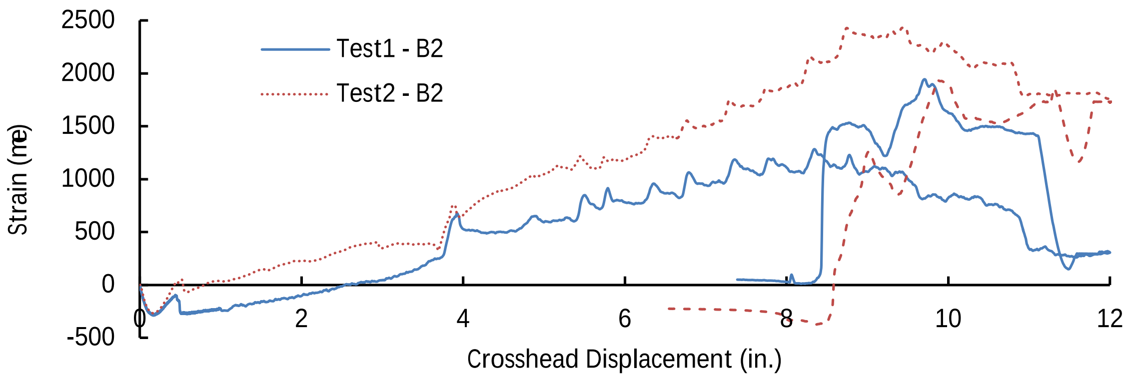

Figure E-42. Strain Gage B2 Response of Two Repeated Tests of the G5x-4/3-0.3 GLARE Panel Under Normal Penetration

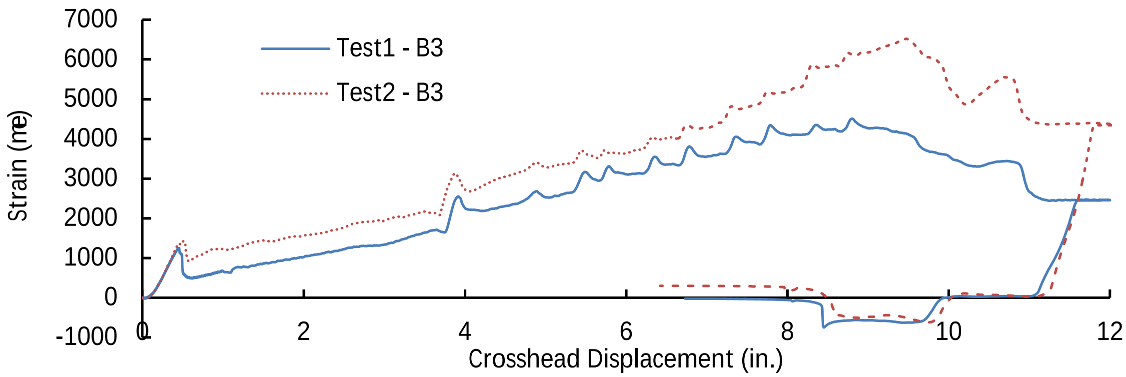

Figure E-43. Strain Gage B3 Response of Two Repeated Tests of the G5x-4/3-0.3 GLARE Panel Under Normal Penetration

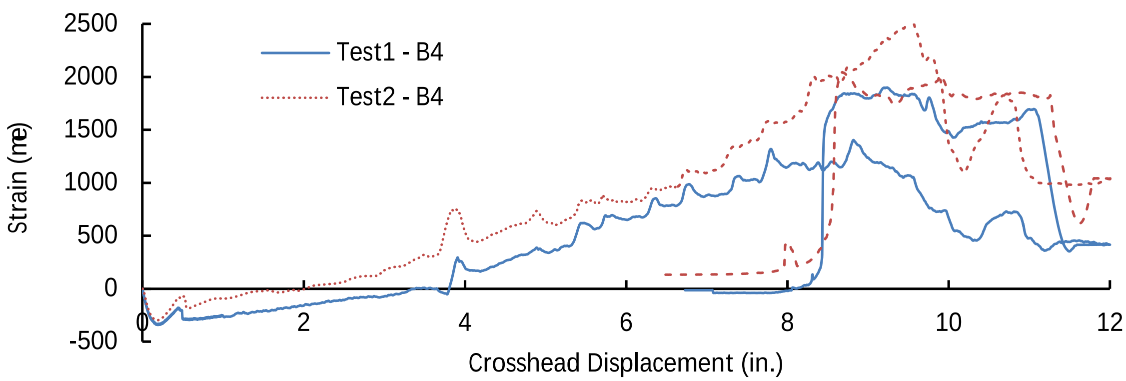

Figure E-44. Strain Gage B4 Response of Two Repeated Tests of the G5x-4/3-0.3 GLARE Panel Under Normal Penetration

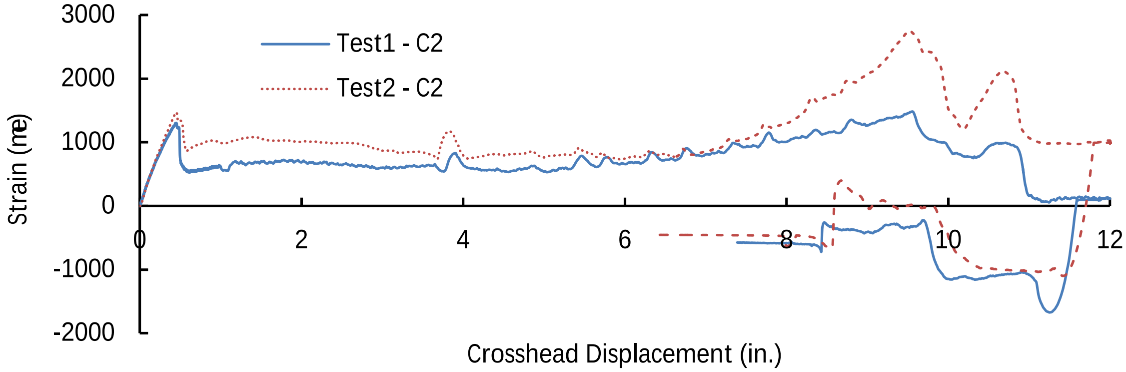

Figure E-45. Strain Gage C2 Response of Two Repeated Tests of the G5x-4/3-0.3 GLARE Panel Under Normal Penetration

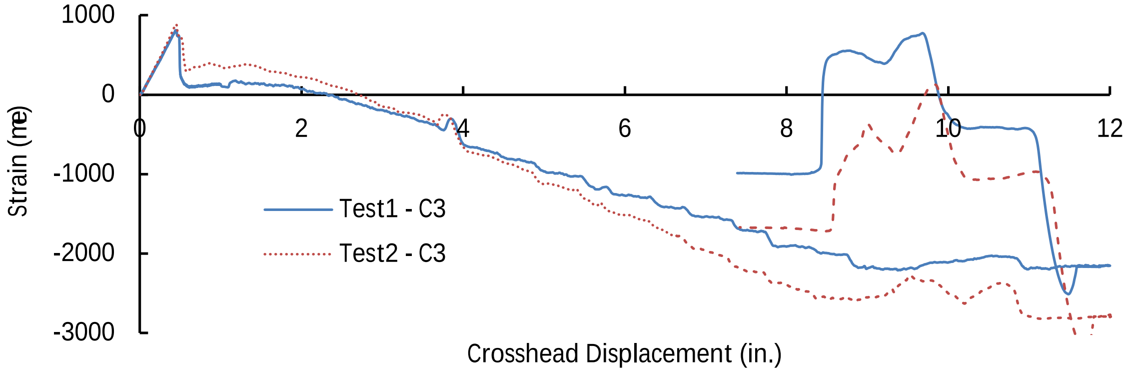

Figure E-46. Strain Gage C3 Response of Two Repeated Tests of the G5x-4/3-0.3 GLARE Panel Under Normal Penetration

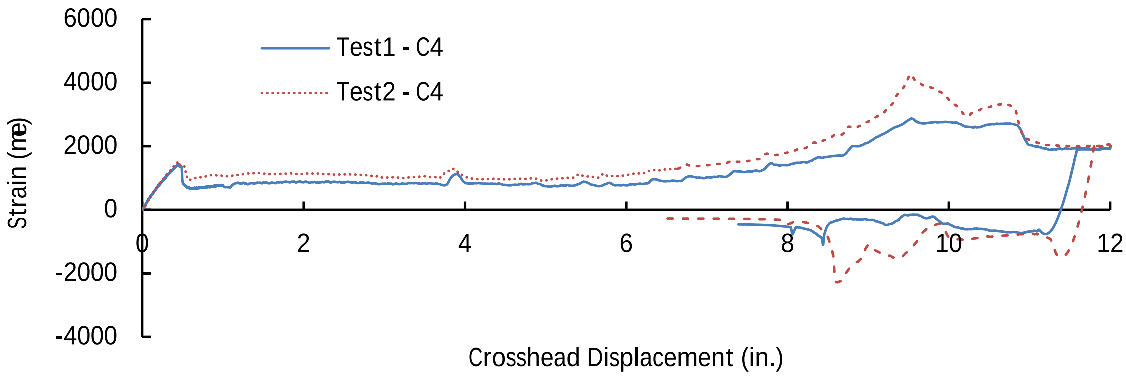

Figure E-47. Strain Gage C4 Response of Two Repeated Tests of the G5x-4/3-0.3 GLARE Panel Under Normal Penetration

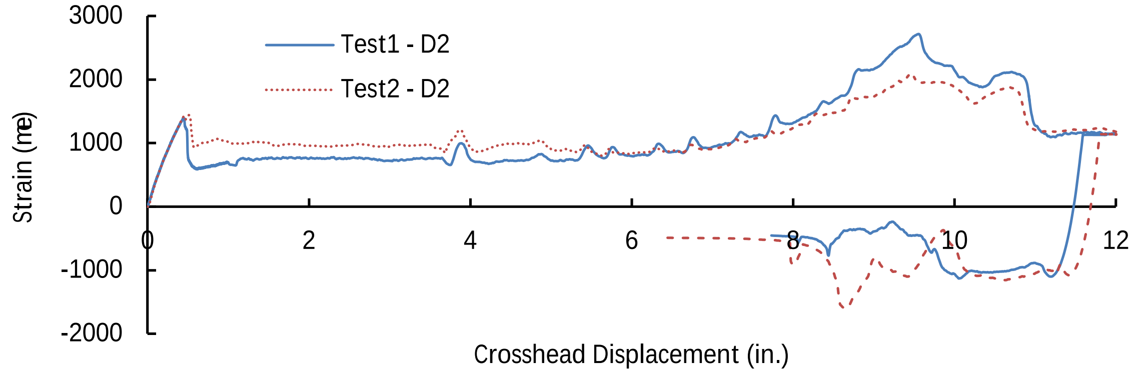

Figure E-48. Strain Gage D2 Response of Two Repeated Tests of the G5x-4/3-0.3 GLARE Panel Under Normal Penetration

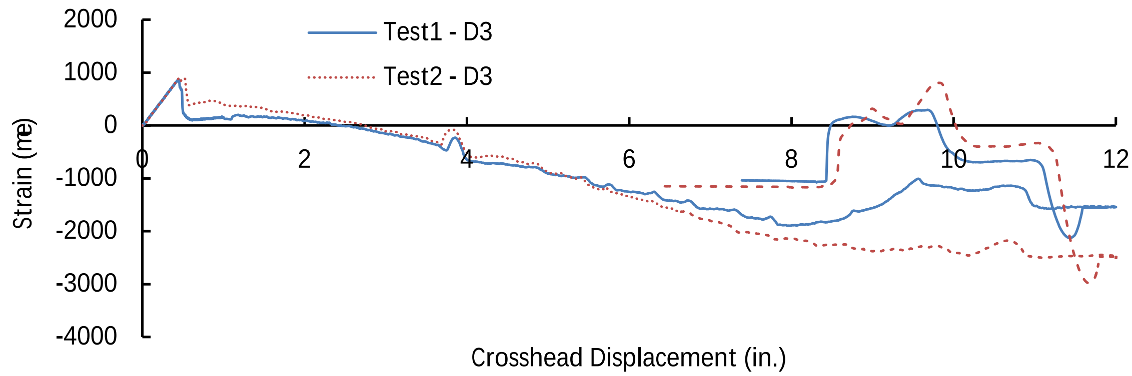

Figure E-49. Strain Gage D3 Response of Two Repeated Tests of the G5x-4/3-0.3 GLARE Panel Under Normal Penetration

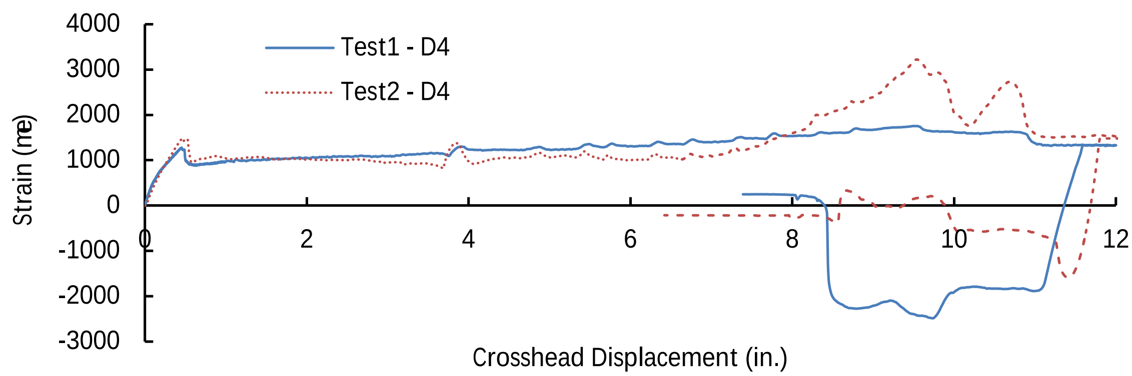

Figure E-50. Strain Gage D4 Response of Two Repeated Tests of the G5x-4/3-0.3 GLARE Panel Under Normal Penetration

E.1.7 The 12-Ply CFRP Panel Under Normal Penetration.

The strain gage locations of the first of three repeated test (Test1) for the 12-ply CFRP panel under normal penetration are shown in figure E-51. A total of four rosette strain gages were instrumented: two on the top surface, A series (A2, A3, A4) and B series (B2, B3, B4), and two on the bottom surface, C series (C2, C3, C4) and D series (D2, D3, D4). All four rosette strain gages were mounted 2-in. radial distance from center. Strain gages A3, B3, C3, and D3 were mounted to measure radial strain and the remaining strain gages were mounted to measure ±45-degree angle strain with respect to the radial direction. The same strain gage configuration was used in subsequent tests (Test2 and Test3). The arrow in the figure indicates the fiber direction of the first graphite/epoxy layer from the top or penetrating side of the panel. The entire data set was lost due to hardware malfunction.

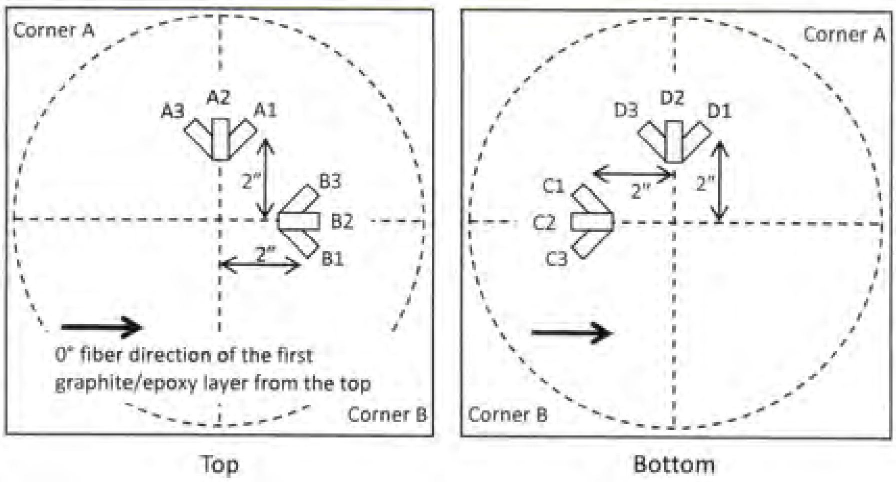

Figure E-51. Strain Gage Locations for the 12-ply CFRP Panel Under Normal Penetration

E.1.8 The 16-Ply CFRP Panel Under Normal Penetration.

The strain gage locations of the first of three repeated tests (Test1) for the 16-ply CFRP panel under normal penetration are shown in figure E-38. A total of four rosette strain gages were instrumented: two on the top surface, A series (A1, A2, A3) and B series (B1, B2, B3), and two on the bottom surface, C series (C1, C2, C3) and D series (D1, D2, D3). All four rosette strain gages were mounted 2-in. radial distance from center. Strain gages A2, B2, C2, and D2 were mounted to measure radial strain and the rest of the strain gages were mounted to measure ±45-degree angle strain with respect to the radial direction. The same strain gage configuration was used in subsequent tests (Test2 and Test3). The arrow in the figure indicates the fiber direction of the first graphite/epoxy layer from the top or penetrating side of the panel. The strain comparison of the two repeated tests of strain gages A1, A2, A3, B1, B2, B3, C1, C2, C3, D1, D2, and D3 are shown in figures E-53 through E-64. The results confirm the repeatability of the tests.

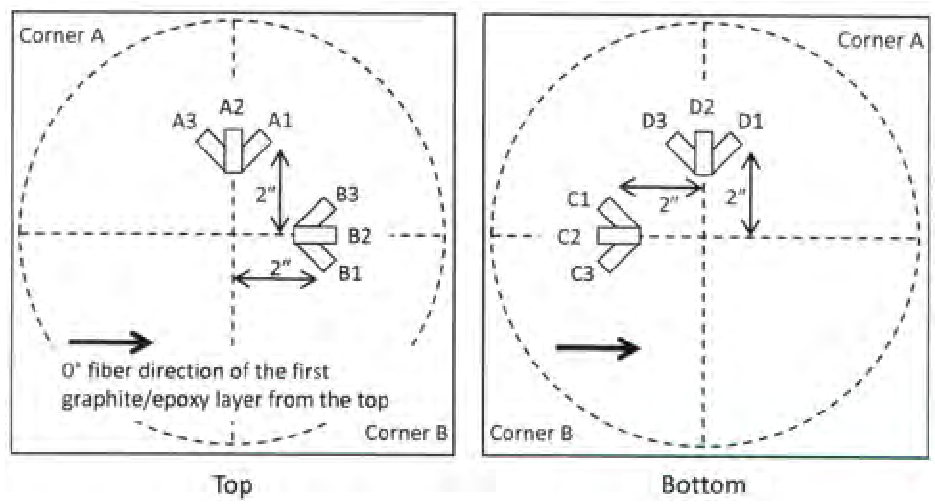

Figure E-52. Strain Gage Locations of the 16-ply CFRP Panel Under Normal Penetration

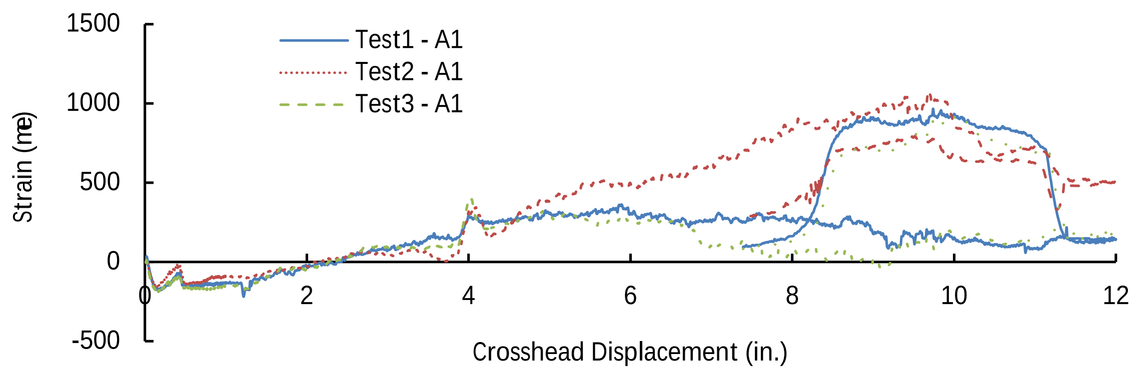

Figure E-53. Strain Gage A1 Response of Three Repeated Tests of the 16-ply CFRP Panel Under Normal Penetration

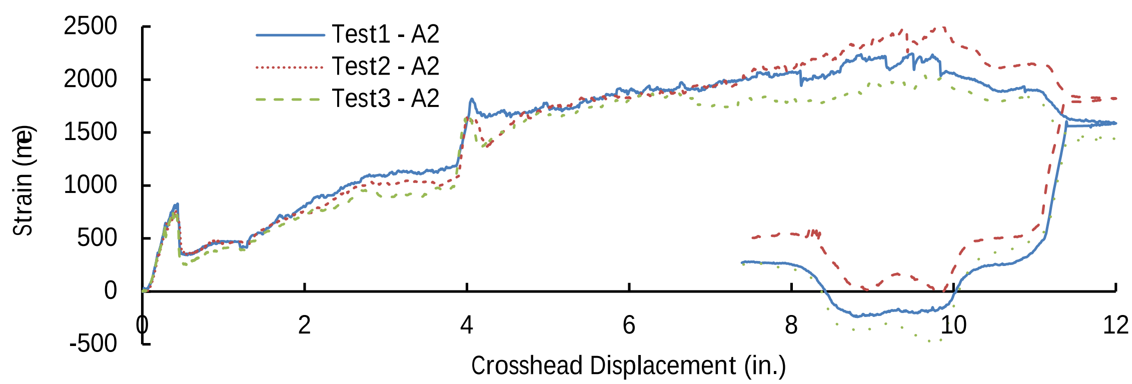

Figure E-54. Strain Gage A2 Response of Three Repeated Tests of the 16-ply CFRP Panel Under Normal Penetration

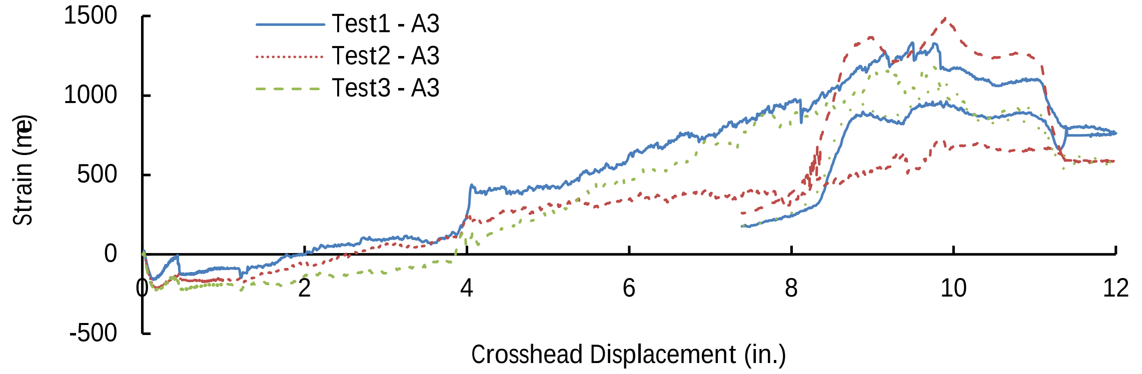

Figure E-55. Strain Gage A3 Response of Three Repeated Tests of the 16-ply CFRP Panel Under Normal Penetration

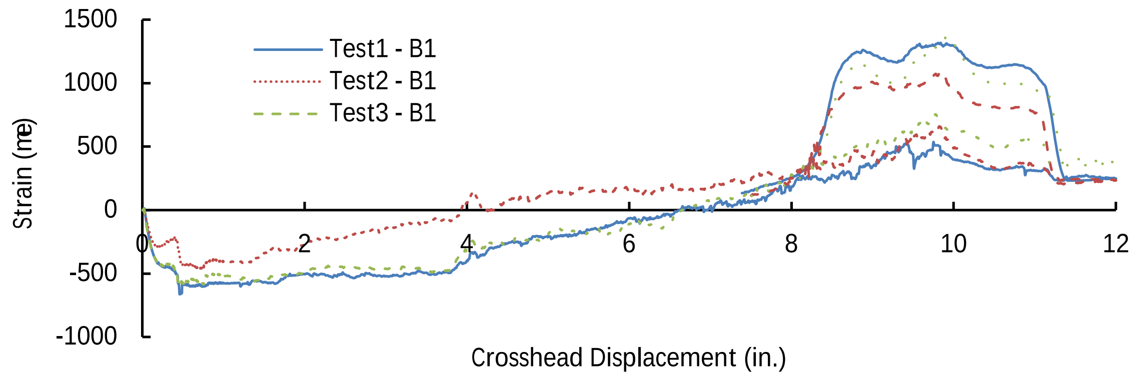

Figure E-56. Strain Gage B1 Response of Three Repeated Tests of the 16-ply CFRP Panel Under Normal Penetration

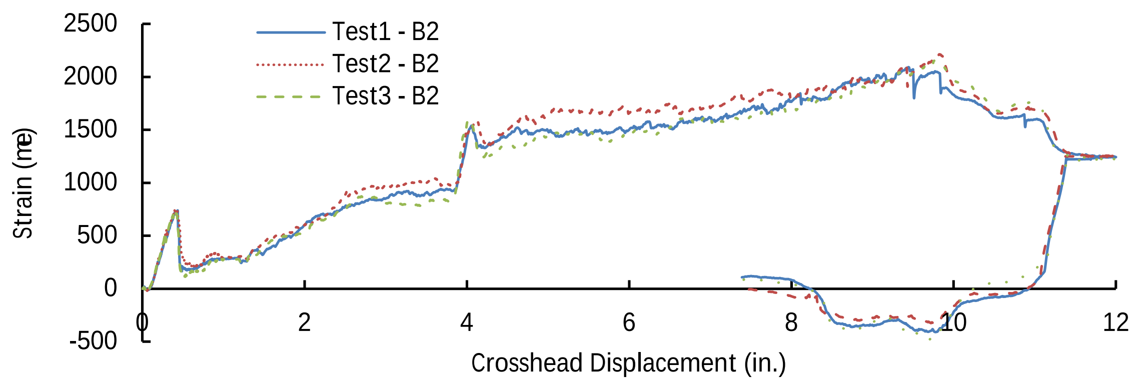

Figure E-57. Strain Gage B2 Response of Three Repeated Tests of the 16-ply CFRP Panel Under Normal Penetration

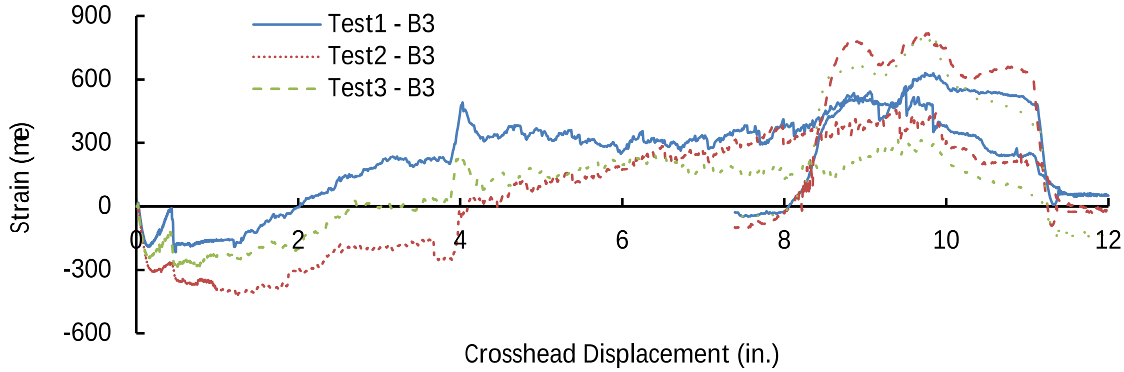

Figure E-58. Strain Gage B3 Response of Three Repeated Tests of the 16-ply CFRP Panel Under Normal Penetration

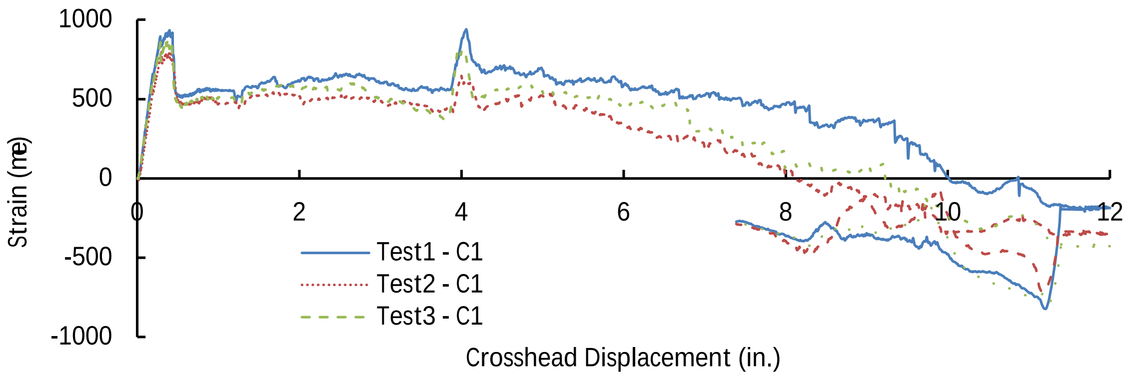

Figure E-59. Strain Gage C1 Response of Three Repeated Tests of the 16-ply CFRP Panel Under Normal Penetration

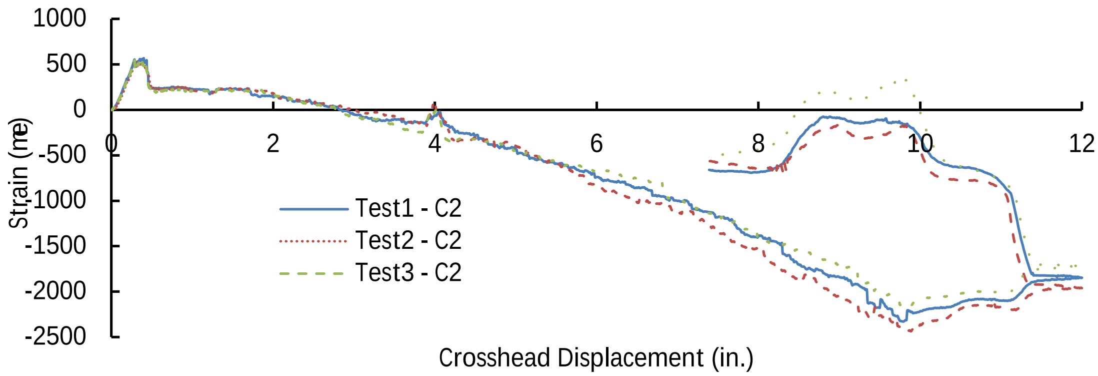

Figure E-60. Strain Gage C2 Response of Three Repeated Tests of the 16-ply CFRP Panel Under Normal Penetration

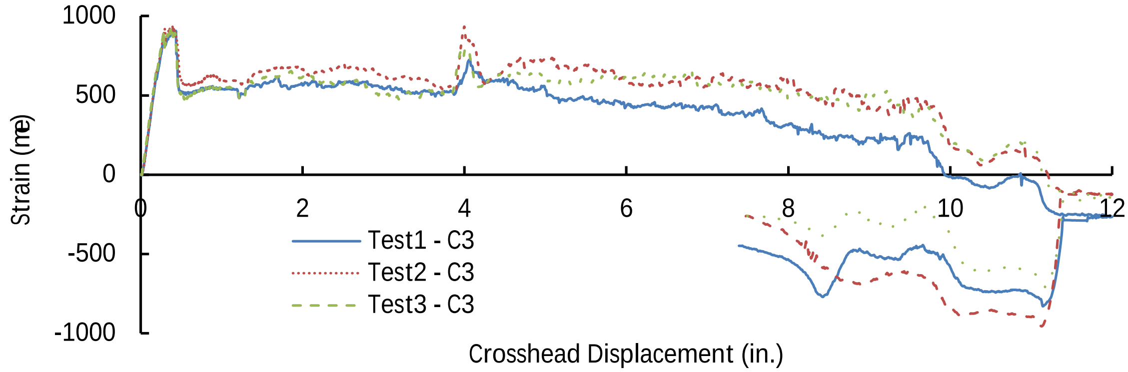

Figure E-61. Strain Gage C3 Response of Three Repeated Tests of the 16-ply CFRP Panel Under Normal Penetration

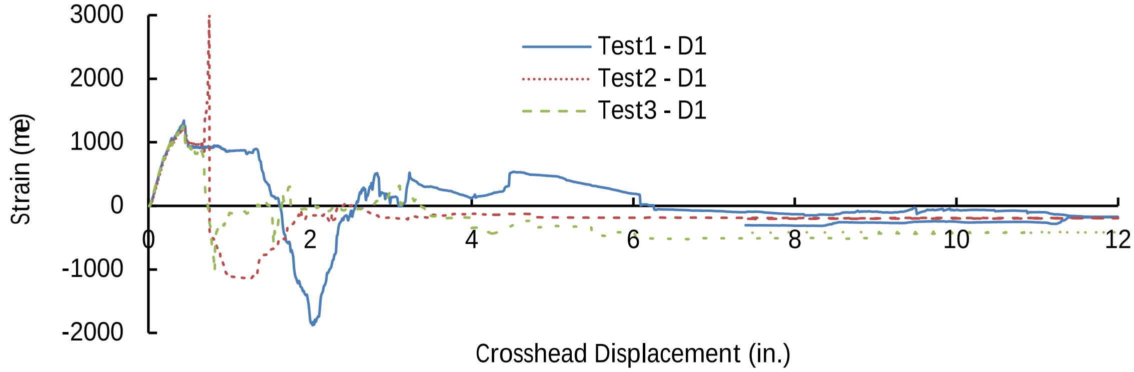

Figure E-62. Strain Gage D1 Response of Three Repeated Tests of the 16-ply CFRP Panel Under Normal Penetration

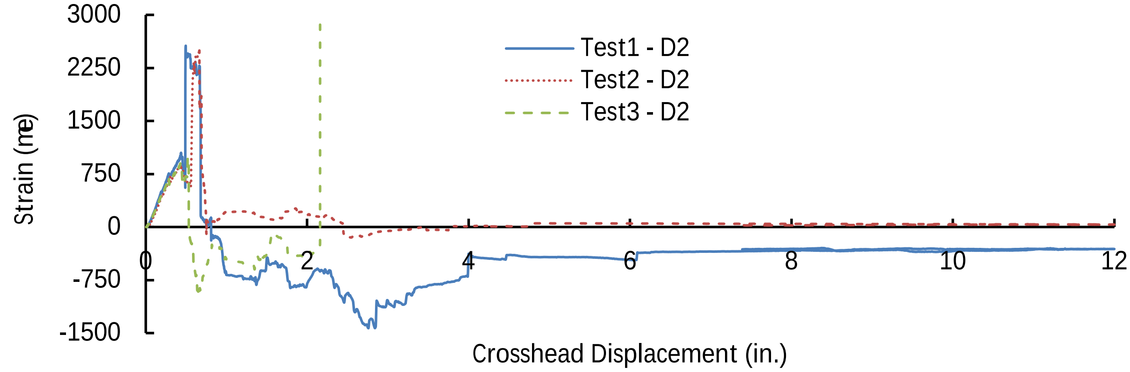

Figure E-63. Strain Gage D2 Response of Three Repeated Tests of the 16-ply CFRP Panel Under Normal Penetration

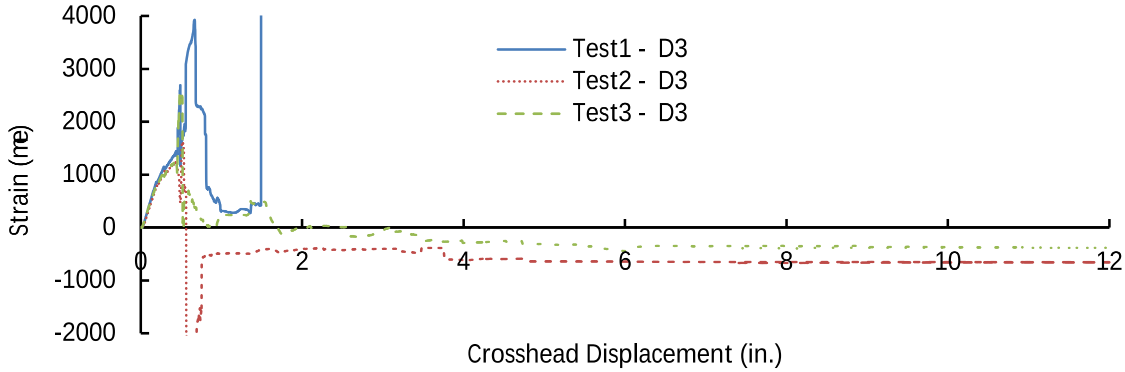

Figure E-64. Strain Gage D3 Response of Three Repeated Tests of the 16-ply CFRP Panel Under Normal Penetration

E.1.9 The 24-Ply CFRP Panel Under Normal Penetration.

The strain gage locations of the first of three repeated test (Test1) for the 24-ply CFRP panel under normal penetration are shown in figure E-65. A total of four rosette strain gages were instrumented: two on the top surface, A series (A1, A2, A3) and B series (B1, B2, B3), and two on the bottom surface, C series (C1, C2, C3) and D series (D1, D2, D3). All four rosette strain gages were mounted 2-in. radial distance from center. Strain gages A2, B2, C2, and D2 were mounted to measure radial strain and the rest of the strain gages were mounted to measure ±45-degree angle strain with respect to the radial direction. The same strain gage configuration was used in subsequent tests (Test2 and Test3). The arrow in the figure indicates the fiber direction of the first graphite/epoxy layer from the top or penetrating side of the panel. The strain comparison of the two repeated tests of strain gages A1, A2, A3, B1, B2, B3, C1, C2, C3, D1, D2, and D3 are shown in figures E-66 through E-77. The results confirm the repeatability of the tests.

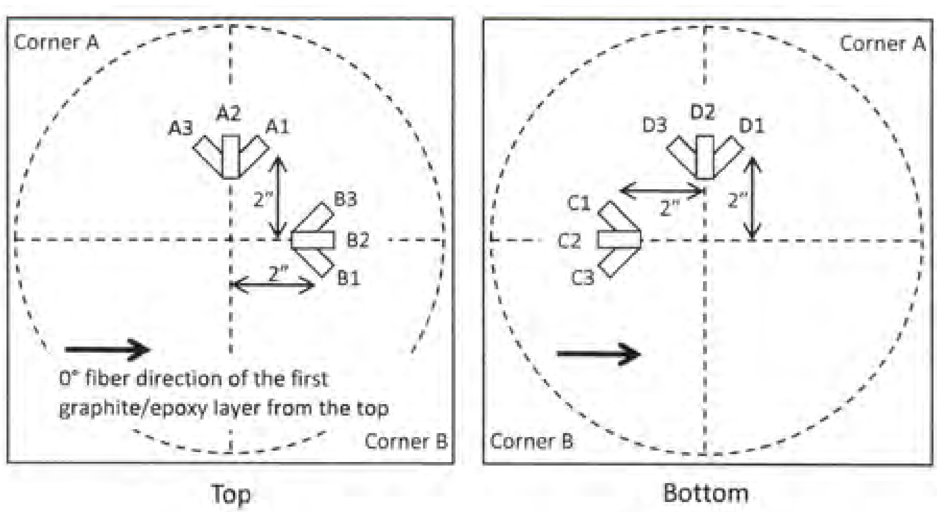

Figure E-65. Strain Gage Locations of the 24-ply CFRP Panel Under Normal Penetration

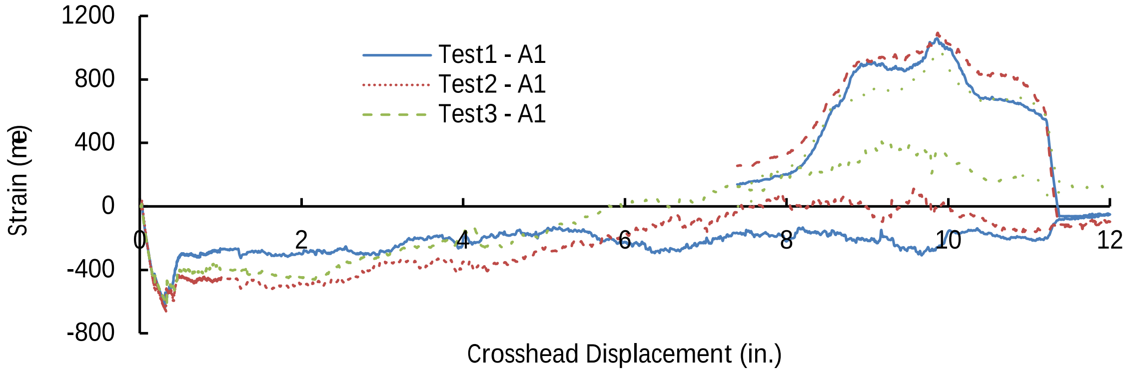

Figure E-66. Strain Gage A1 Response of Three Repeated Tests of the 24-ply CFRP Panel Under Normal Penetration

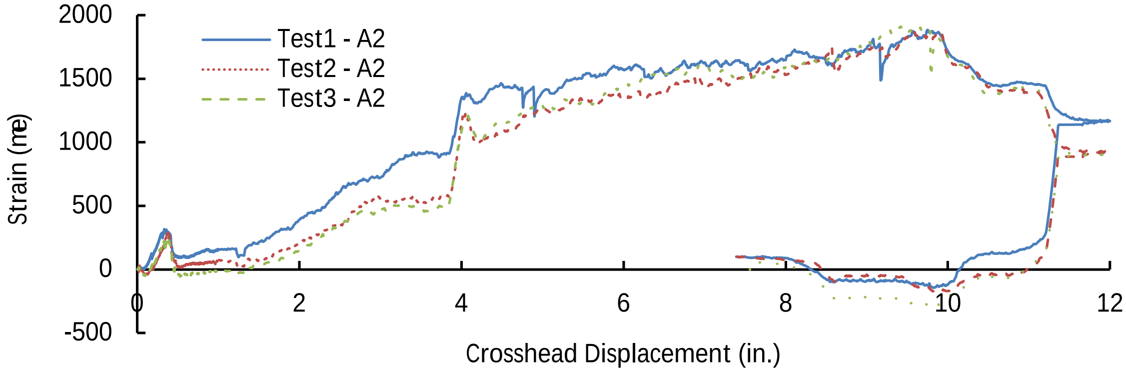

Figure E-67. Strain Gage A2 Response of Three Repeated Tests of the 24-ply CFRP Panel Under Normal Penetration

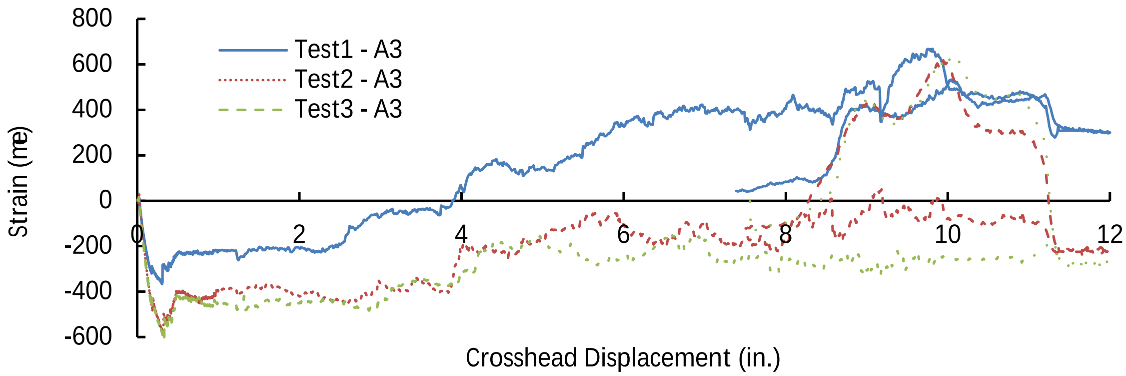

Figure E-68. Strain Gage A3 Response of Three Repeated Tests of the 24-ply CFRP Panel Under Normal Penetration

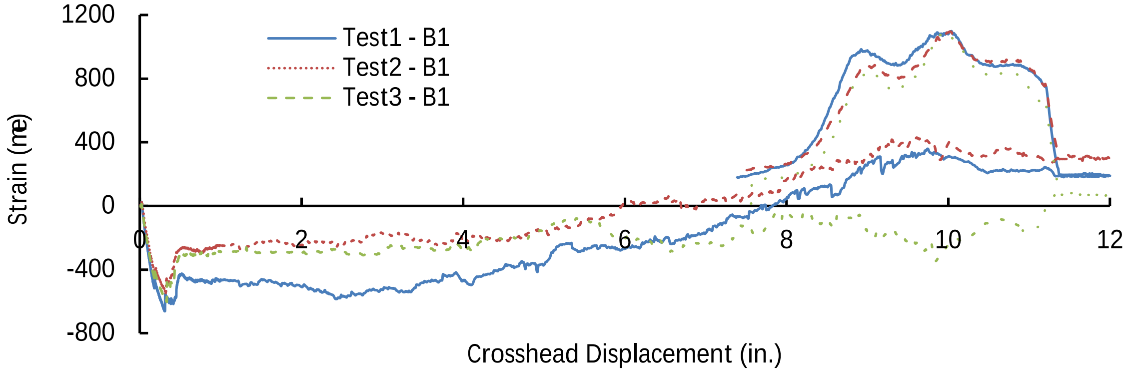

Figure E-69. Strain Gage B1 Response of Three Repeated Tests of the 24-ply CFRP Panel Under Normal Penetration

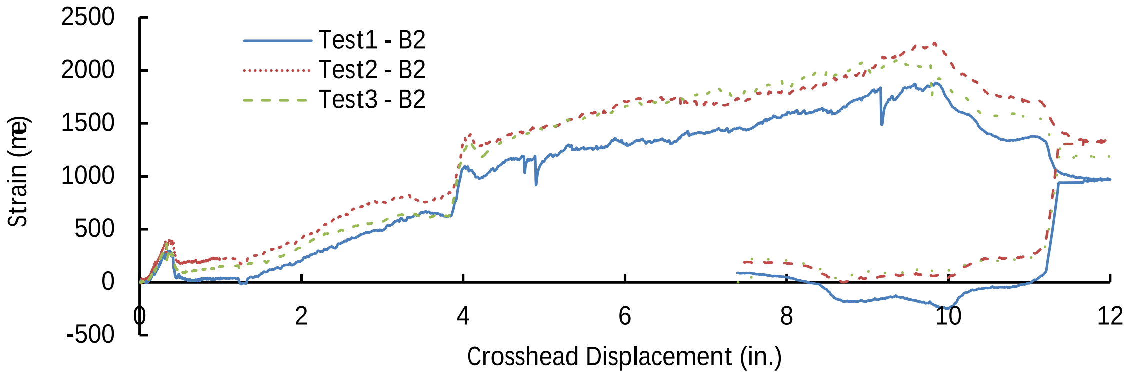

Figure E-70. Strain Gage B2 Response of Three Repeated Tests of the 24-ply CFRP Panel Under Normal Penetration

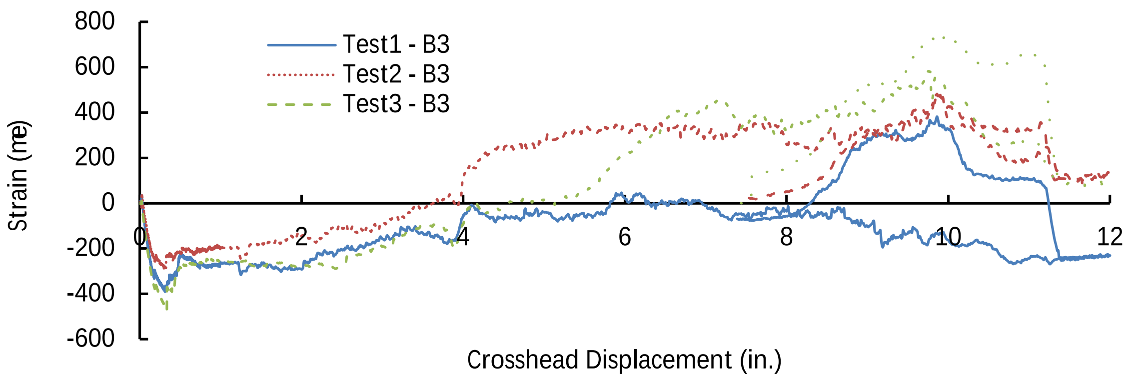

Figure E-71. Strain Gage B3 Response of Three Repeated Tests of the 24-ply CFRP Panel Under Normal Penetration

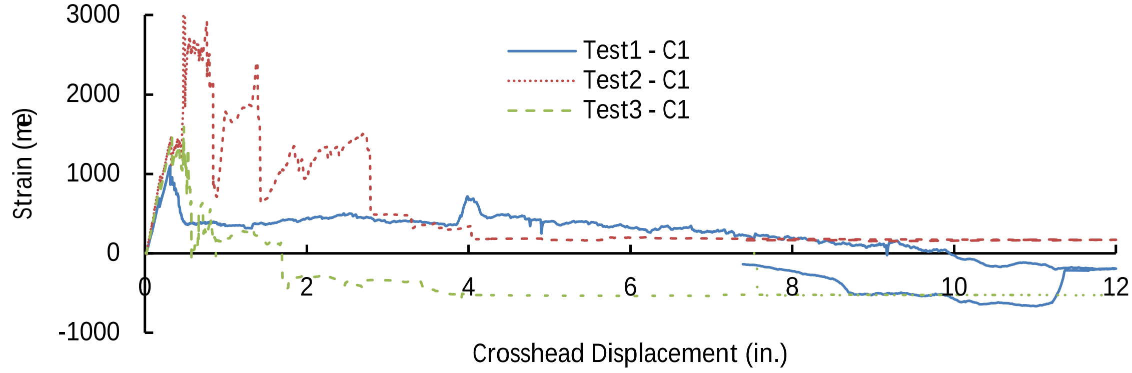

Figure E-72. Strain Gage C1 Response of Three Repeated Tests of the 24-ply CFRP Panel Under Normal Penetration

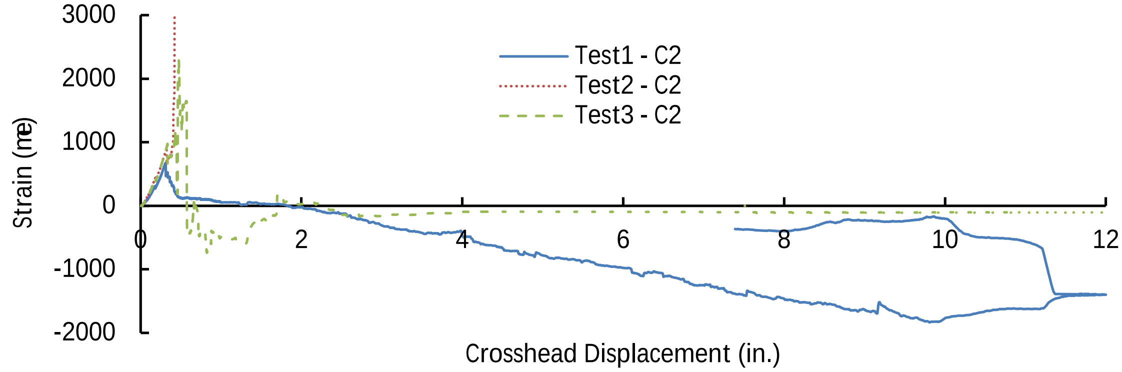

Figure E-73. Strain Gage C2 Response of Three Repeated Tests of the 24-ply CFRP Panel Under Normal Penetration

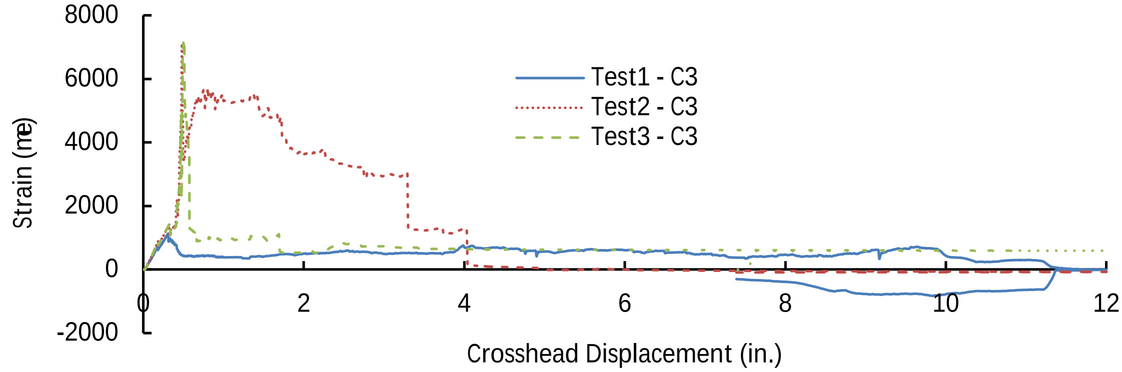

Figure E-74. Strain Gage C3 Response of Three Repeated Tests of the 24-ply CFRP Panel Under Normal Penetration

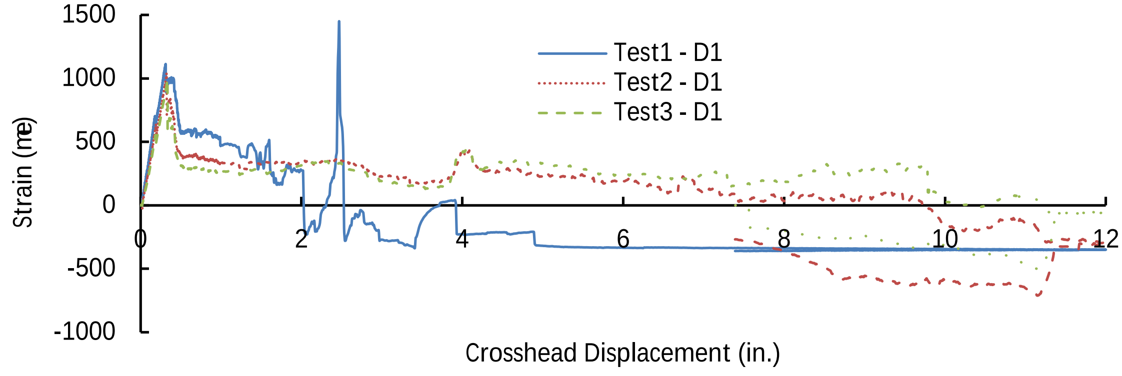

Figure E-75. Strain Gage D1 Response of Three Repeated Tests of the 24-ply CFRP Panel Under Normal Penetration

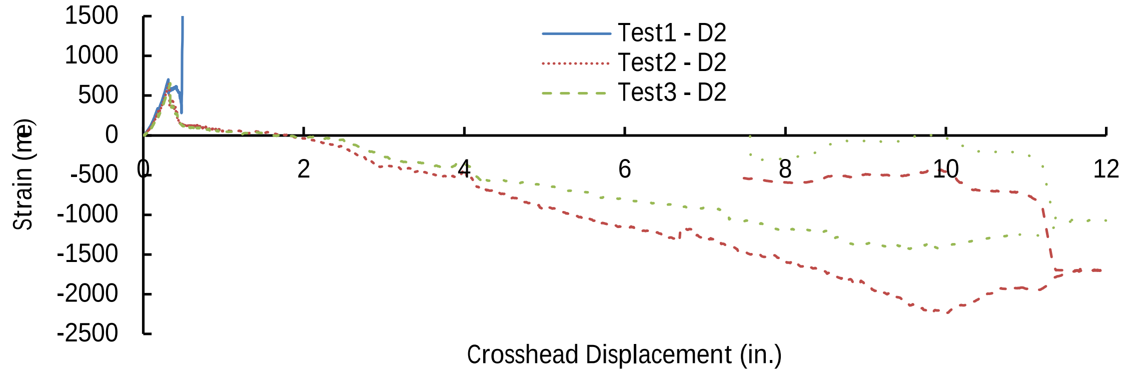

Figure E-76. Strain Gage D2 Response of Three Repeated Tests of the 24-ply CFRP Panel Under Normal Penetration

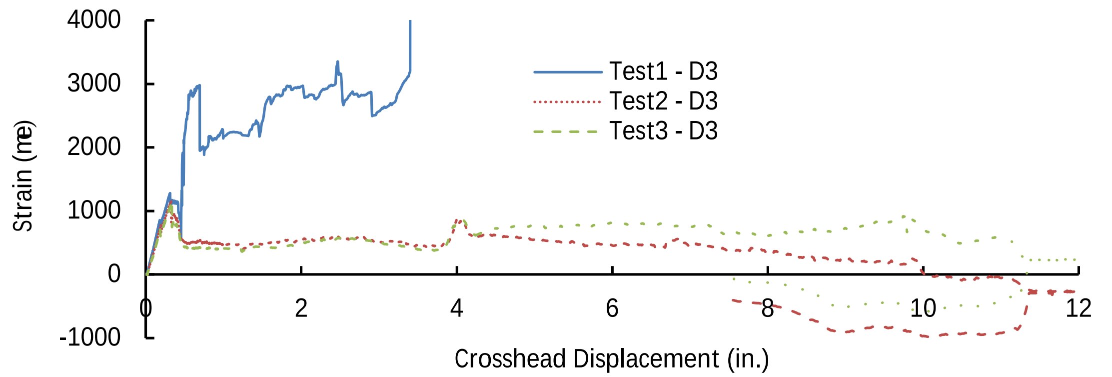

Figure E-77. Strain Gage D3 Response of Three Repeated Tests of the 24-ply CFRP Panel Under Normal Penetration

E.2 THE 45-DEGREE ANGLE PENETRATION.

In the 45-degree angle penetration condition, each aluminum, GLARE, and CFRP panel was instrumented with strain gages. Strain results were used to ensure the proper load introduction to the panel and the repeatability of the tests. Figure E-78 shows the direction of penetration with respect to the higher and lower ends of the panel from top and side views.

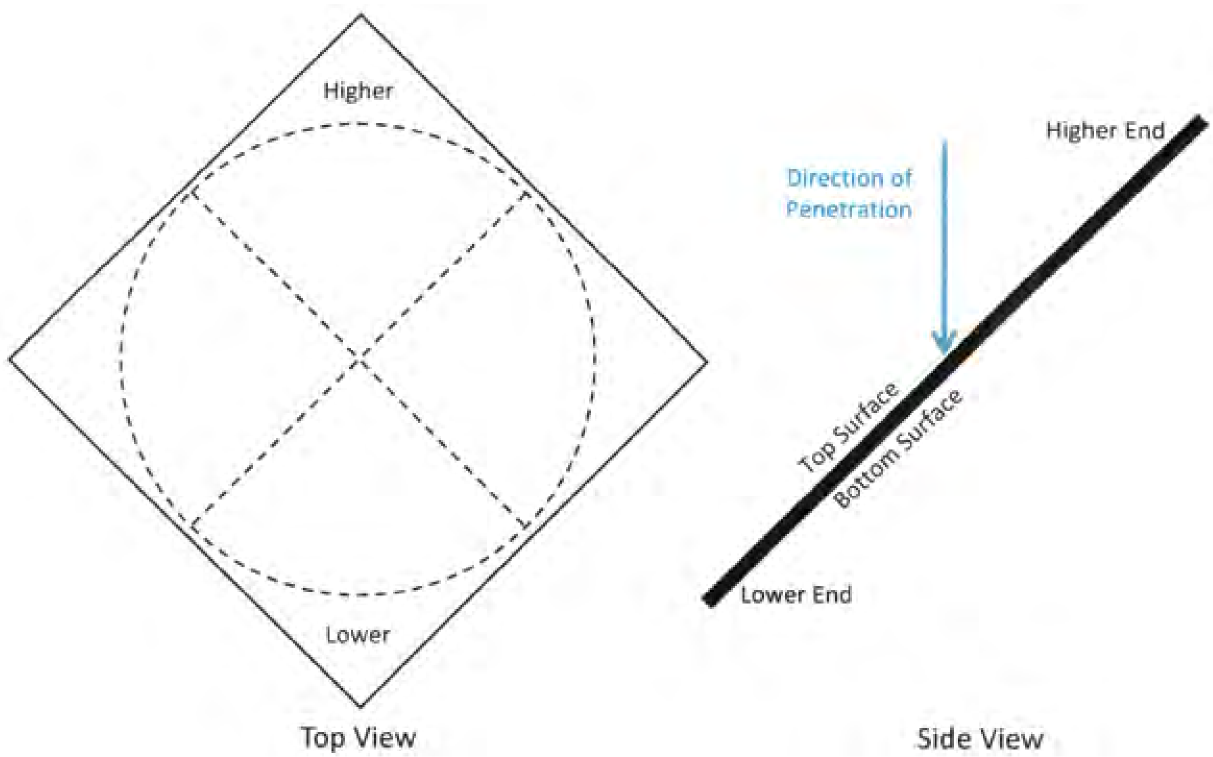

Figure E-78. The Direction of Penetration With Respect to the Higher and Lower Ends of the Panel From Top and Side Views

E.2.1 The 0.04-in.-Thick Aluminum Panel Under 45-Degree Angle Penetration.

The strain gage locations of the first of three repeated tests (Test1) for the 0.04-in.-thick aluminum panel under angle penetration are shown in figure E-79. A total of four rosette strain gages were instrumented: two on the top surface, A series (A1, A2, A3) and B series (B1, B2, B3), and two on the bottom surface, C series (C1, C2, C3) and D series (D1, D2, D3). All four rosette strain gages were mounted 2-in. radial distance from center. Strain gages A2, B2, C2, and D2 were mounted to measure radial strain and the rest of the strain gages were mounted to measure ±45-degree angle strain with respect to the radial direction. The same strain gage configuration was used in subsequent tests (Test2 and Test3). The entire data set was lost due to hardware malfunction.

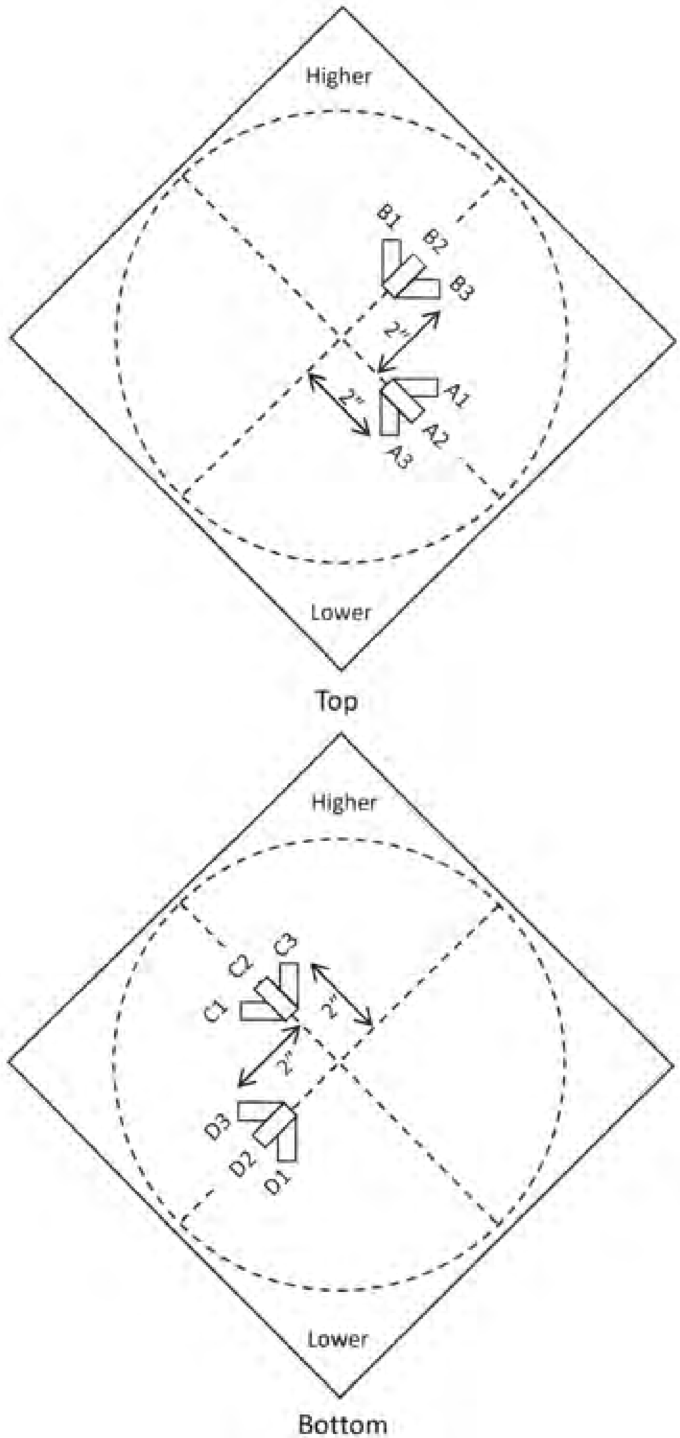

Figure E-79. Strain Gage Locations of the 0.04-in.-Thick Aluminum Panel Under 45-Degree Angle Penetration

E.2.2 The 0.06-in.-Thick Aluminum Panel Under 45-Degree Angle Penetration.

The strain gage locations of the first of three repeated tests (Test1) for the 0.06-in.-thick aluminum panel under 45-degree angle penetration are shown in figure E-80. A total of four rosette strain gages were instrumented: two on the top surface, A series (A1, A2, A3) and B series (B1, B2, B3), and two on the bottom surface, C series (C1, C2, C3) and D series (D1, D2, D3). All four rosette strain gages were mounted 2-in. radial distance from center. Strain gages A2, B2, C2, and D2 were mounted to measure radial strain and the rest of the strain gages were mounted to measure ±45-degree angle strain with respect to the radial direction. The same strain gage configuration was used in subsequent tests (Test2 and Test3). The entire data set was lost due to hardware malfunction.

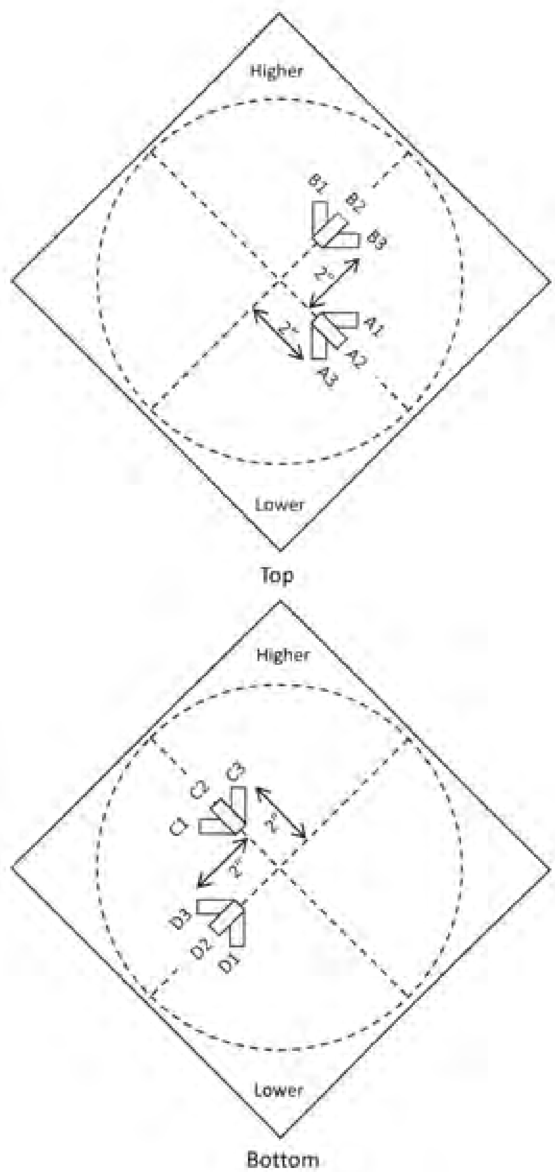

Figure E-80. Strain Gage Locations of the 0.06-in.-Thick Aluminum Panel Under 45-Degree Angle Penetration

E.2.3 The 0.08-in.-Thick Aluminum Panel Under 45-Degree Angle Penetration.

The strain gage locations of the first of three repeated test (Test1) for the 0.08-in.-thick aluminum panel under angle penetration are shown in figure E-81. A total of four rosette strain gages were instrumented: two on the top surface, A series (A1, A2, A3) and B series (B1, B2, B3), and two on the bottom surface, C series (C1, C2, C3) and D series (D1, D2, D3). All four rosette strain gages were mounted at location 2-in. radial distance away from center. Strain gages A2, B2, C2, and D2 were mounted to measure radial strain and the rest of the strain gages were mounted to measure ±45-degree angle strain with respect to the radial direction. The same strain gage configuration was used in subsequent tests (Test2 and Test3). The entire data set was lost due to hardware malfunction.

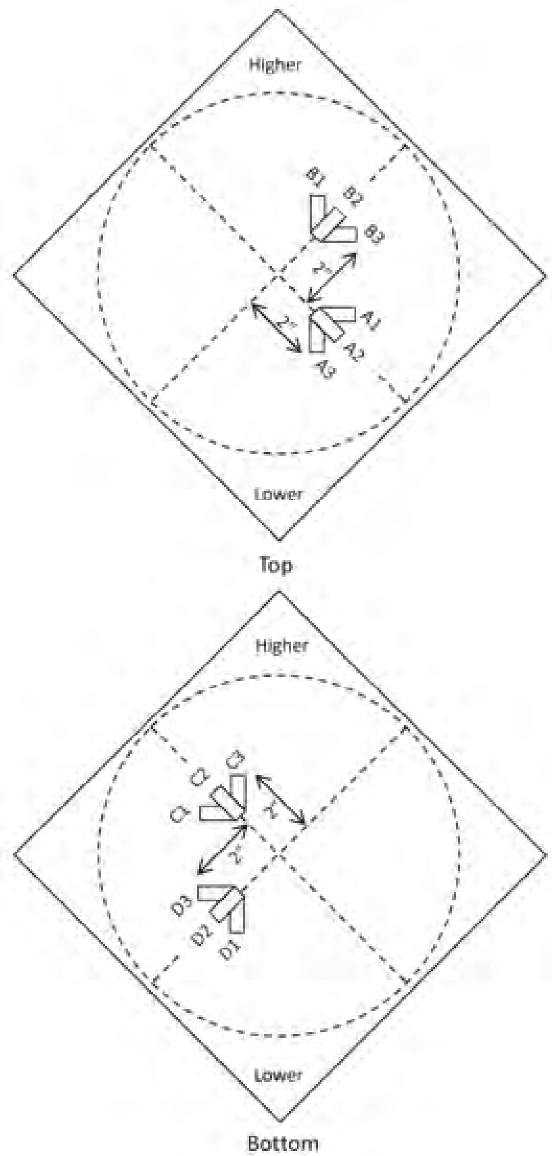

Figure E-81. Strain Gage Locations of the 0.08-in.-Thick Aluminum Panel Under 45-Degree Angle Penetration

E.2.4 The G3-4/3-0.3 GLARE Panel Under 45-Degree Angle Penetration.

The strain gage locations of the first of three repeated test (Test1) for G3-4/3-0.4 GLARE panel under 45-degree angle penetration is shown in figure E-82. A total of four rosette strain gages were instrumented: two on the top surface, A series (A1, A2, A3) and B series (B1, B2, B3), and two on the bottom surface, E series (E1, E2, E3) and F series (F1, F2, F3). All four rosette strain gages were mounted at location 2-in. radial distance away from center. Strain gages A2, B2, E2, and F2 were mounted to measure radial strain and the rest of the strain gages were mounted to measure ±45-degree angle strain with respect to the radial direction. The same strain gage configuration was used in subsequent tests (Test2 and Test3). The arrow in the figure indicates the fiber direction of the first glass/epoxy layer (second overall layer) from the top or penetrating side of the panel. The strain comparison of the three repeated test of strain gages A1, A2, A3, B1, B2, B3, E1, E2, E3, F1, F2, and F3 are shown in figures E-83 through E-94. The results confirm the repeatability of the tests.

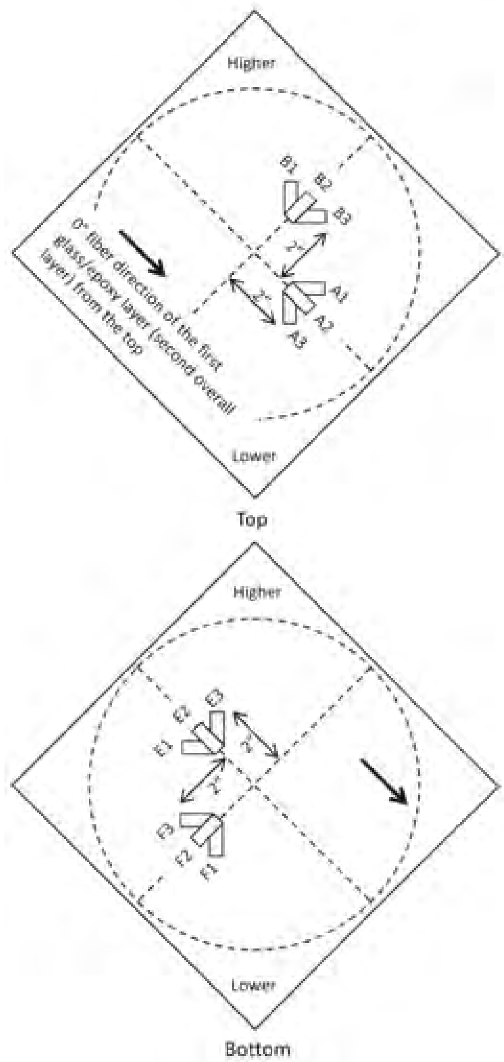

Figure E-82. Strain Gage Locations of the G3-4/3-0.4 GLARE Panel Under 45-Degree Angle Penetration

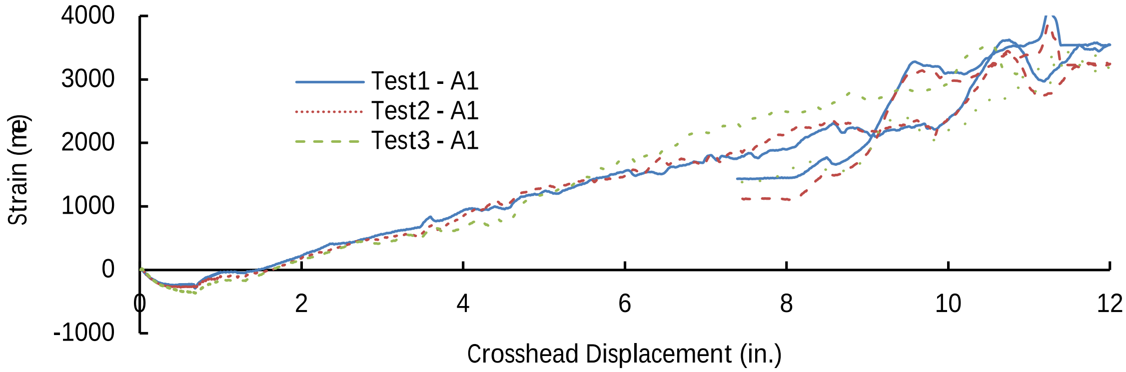

Figure E-83. Strain Gage A1 Response of Three Repeated Tests of the G3-4/3-0.4 GLARE Panel Under 45-Degree Angle Penetration

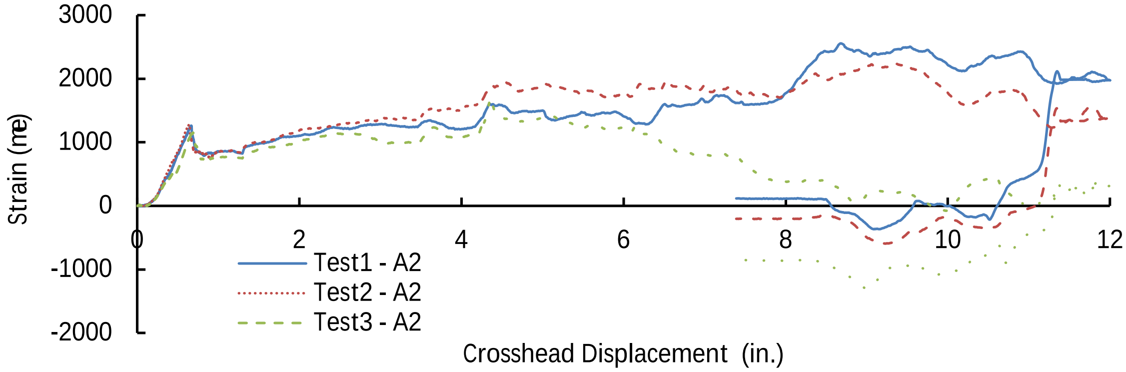

Figure E-84. Strain Gage A2 Response of Three Repeated Tests of the G3-4/3-0.4 GLARE Panel Under 45-Degree Angle Penetration

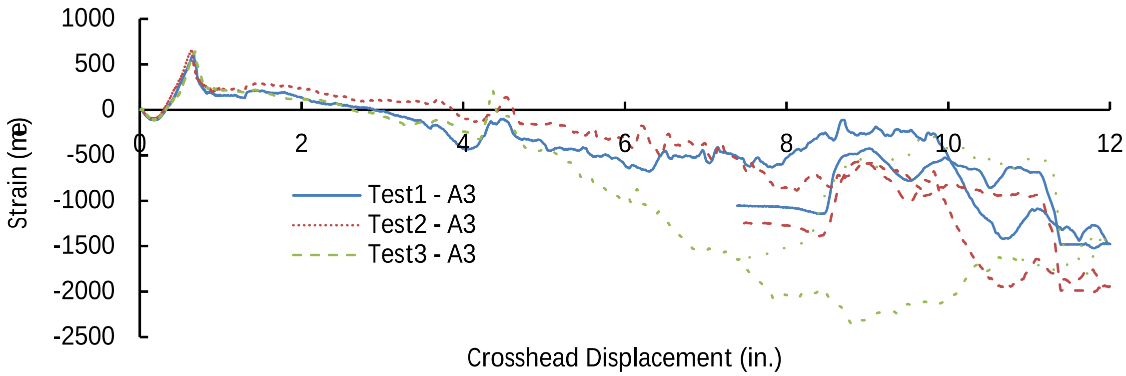

Figure E-85. Strain Gage A3 Response of Three Repeated Tests of the G3-4/3-0.4 GLARE Panel Under 45-Degree Angle Penetration

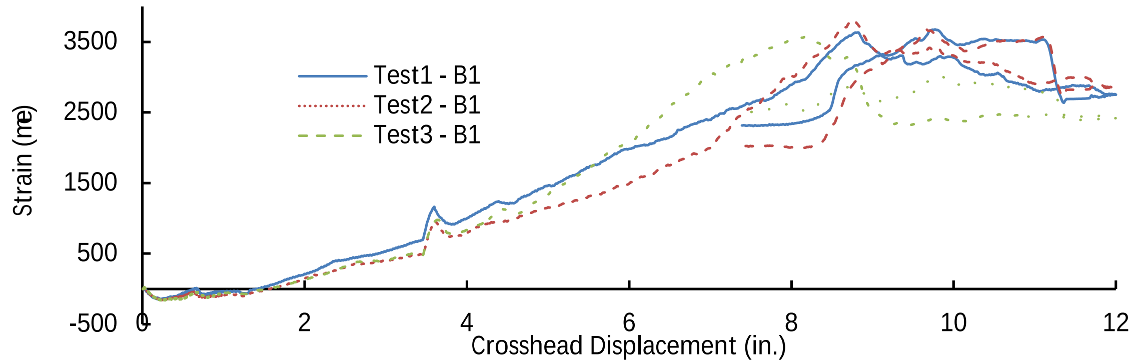

Figure E-86. Strain Gage B1 Response of Three Repeated Tests of the G3-4/3-0.4 GLARE Panel Under 45-Degree Angle Penetration

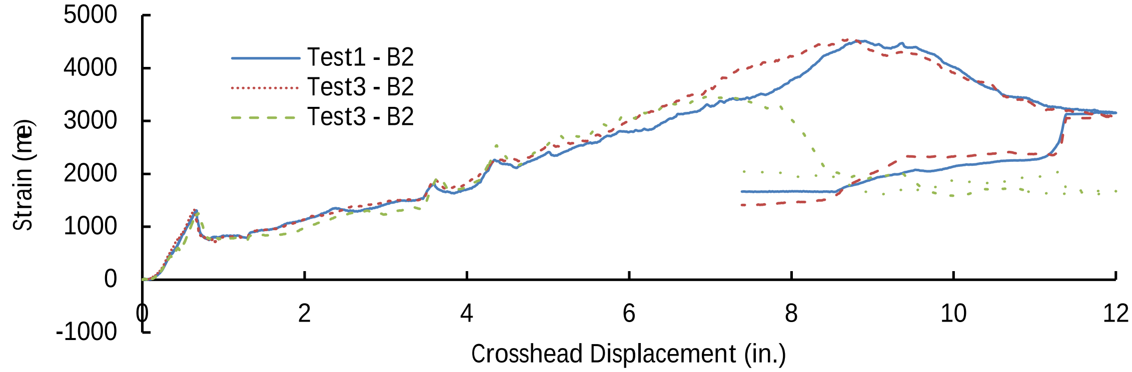

Figure E-87. Strain Gage B2 Response of Three Repeated Tests of the G3-4/3-0.4 GLARE Panel Under 45-Degree Angle Penetration

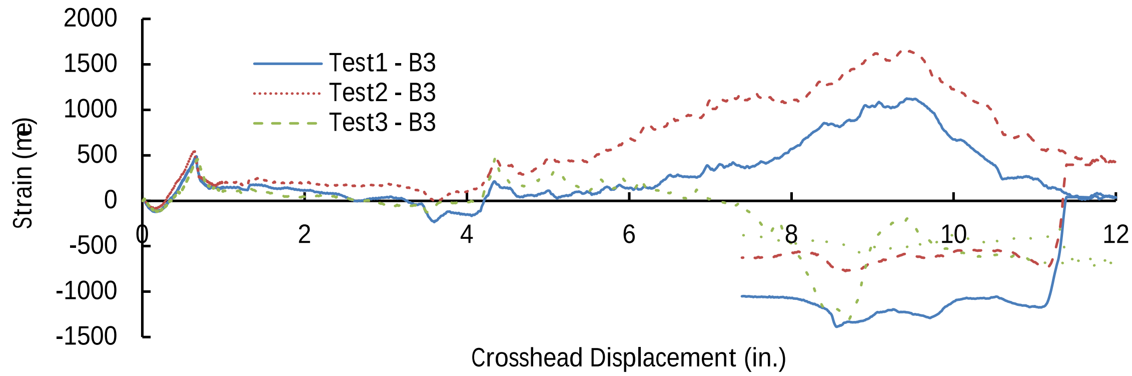

Figure E-88. Strain Gage B3 Response of Three Repeated Tests of the G3-4/3-0.4 GLARE Panel Under 45-Degree Angle Penetration

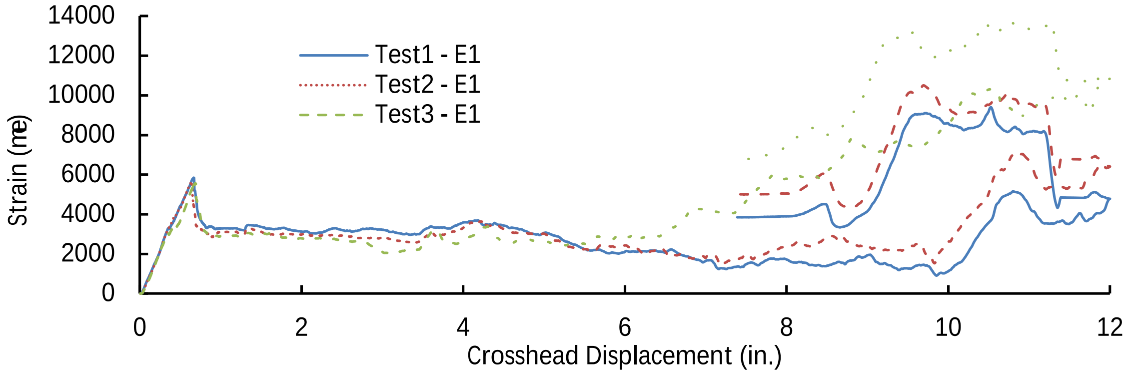

Figure E-89. Strain Gage E1 Response of Three Repeated Tests of the G3-4/3-0.4 GLARE Panel Under 45-Degree Angle Penetration

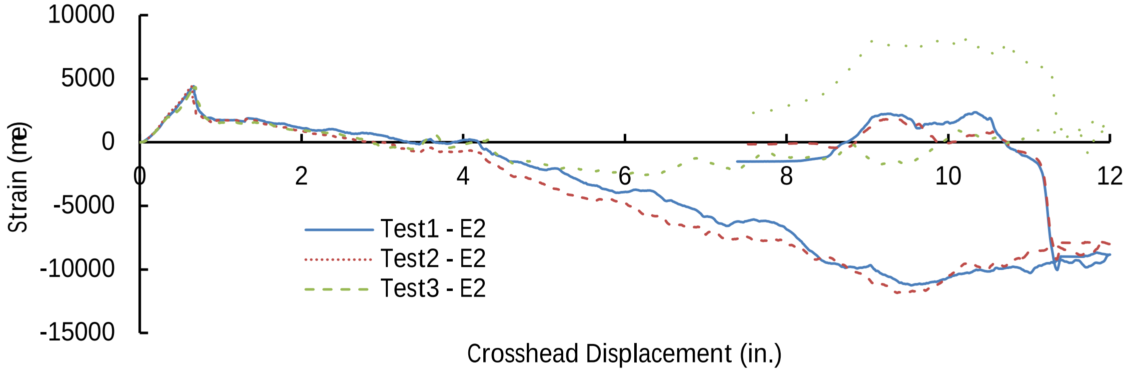

Figure E-90. Strain Gage E2 Response of Three Repeated Tests of the G3-4/3-0.4 GLARE Panel Under 45-Degree Angle Penetration

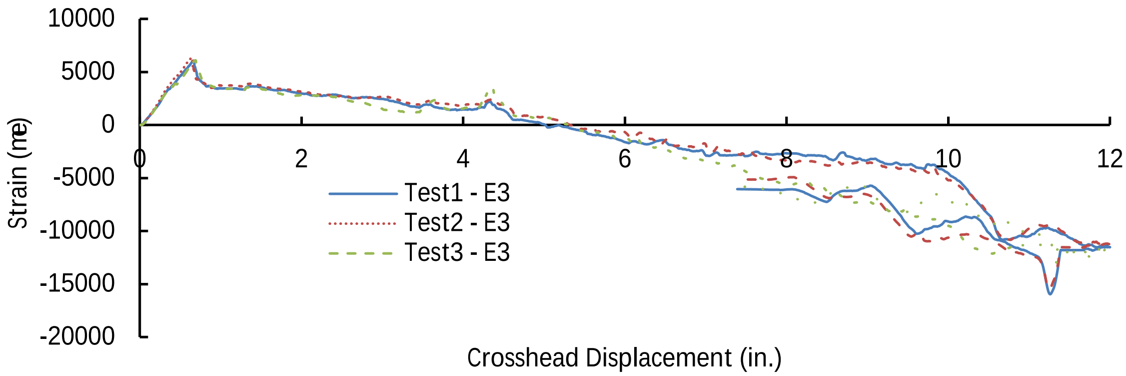

Figure E-91. Strain Gage E3 Response of Three Repeated Tests of the G3-4/3-0.4 GLARE Panel Under 45-Degree Angle Penetration

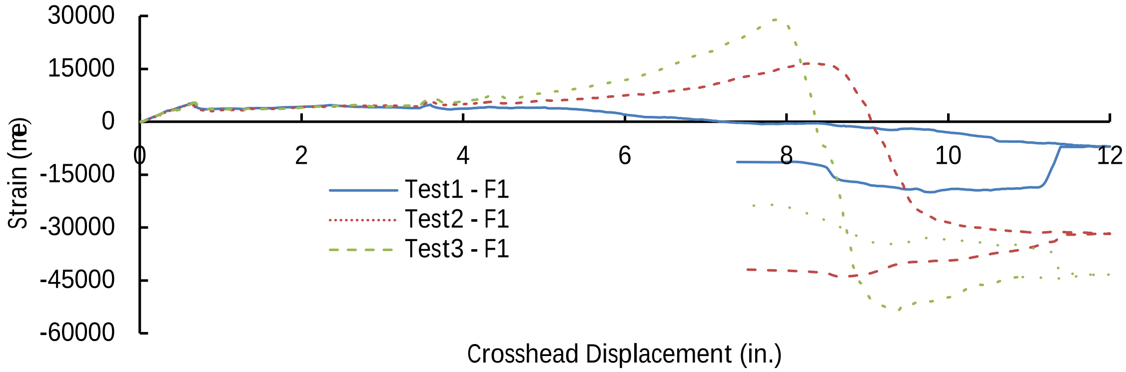

Figure E-92. Strain Gage F1 Response of Three Repeated Tests of G3-4/3-0.4 GLARE Panel Under 45-Degree Angle Penetration

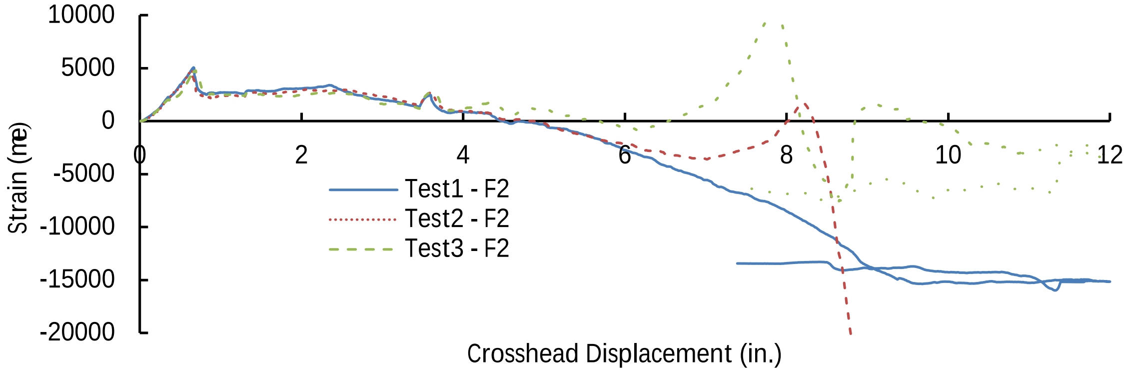

Figure E-93. Strain Gage F2 Response of Three Repeated Tests of the G3-4/3-0.4 GLARE Panel Under 45-Degree Angle Penetration

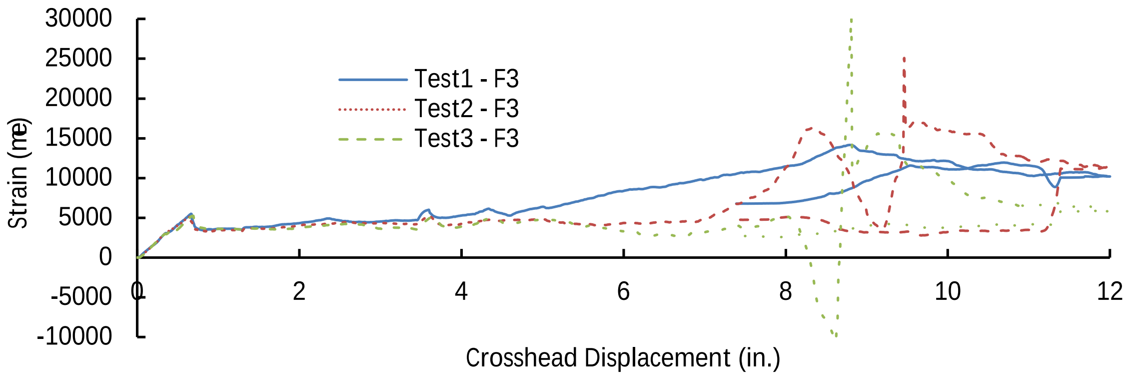

Figure E-94. Strain Gage F3 Response of Three Repeated Tests of the G3-4/3-0.4 GLARE Panel Under 45-Degree Angle Penetration

E.2.5 The G3-5/4-0.4 GLARE Panel Under 45-Degree Angle Penetration.

The strain gage locations of the first of three repeated tests (Test1) for the G3-5/4-0.3 GLARE panel under angle penetration are shown in figure E-95. A total of four rosette strain gages were instrumented: two on the top surface, A series (A1, A2, A3) and B series (B1, B2, B3), and two on the bottom surface, E series (E1, E2, E3) and F series (F1, F2, F3). All four rosette strain gages were mounted 2-in. radial distance from center. Strain gages A2, B2, E2, and F2 were mounted to measure radial strain and the rest of the strain gages were mounted to measure ±45-degree angle strain with respect to the radial direction. The same strain gage configuration was used in subsequent tests (Test2 and Test3). The arrow in the figure indicates the fiber direction of the first glass/epoxy layer (second overall layer) from the top or penetrating side of the panel. The strain comparison of the three repeated test of strain gages A1, A2, A3, B1, B2, B3, E1, E2, E3, F1, F2, and F3 are shown in figures E-96 through E-120. The results confirm the repeatability of the tests.

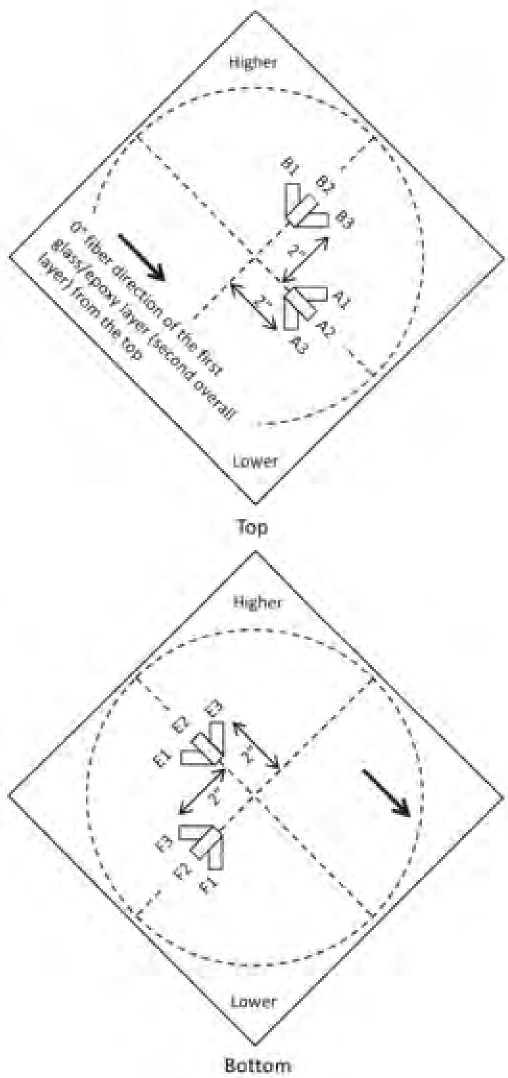

Figure E-95. Strain Gage Location of the G3-5/4-0.3 GLARE Panel Under 45-Degree Angle Penetration

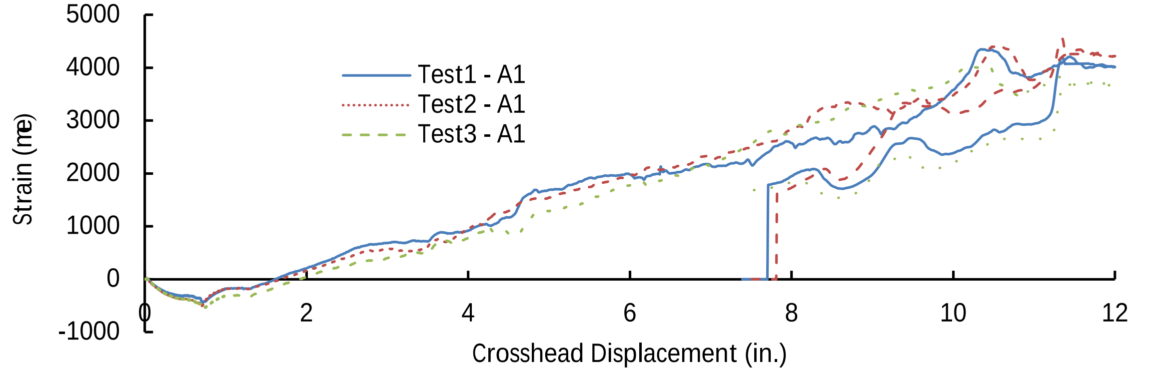

Figure E-96. Strain Gage A1 Response of Three Repeated Tests of the G3-5/4-0.3 GLARE Panel Under 45-Degree Angle Penetration

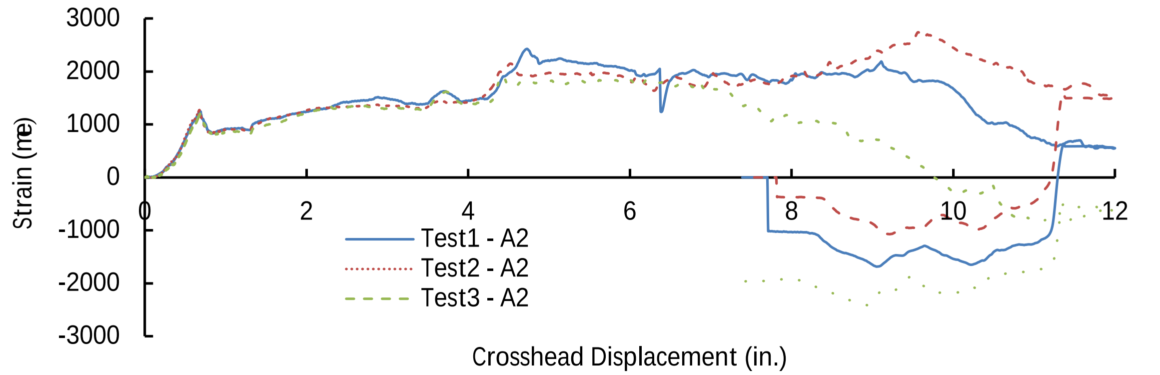

Figure E-97. Strain Gage A2 Response of Three Repeated Tests of the G3-5/4-0.3 GLARE Panel Under 45-Degree Angle Penetration

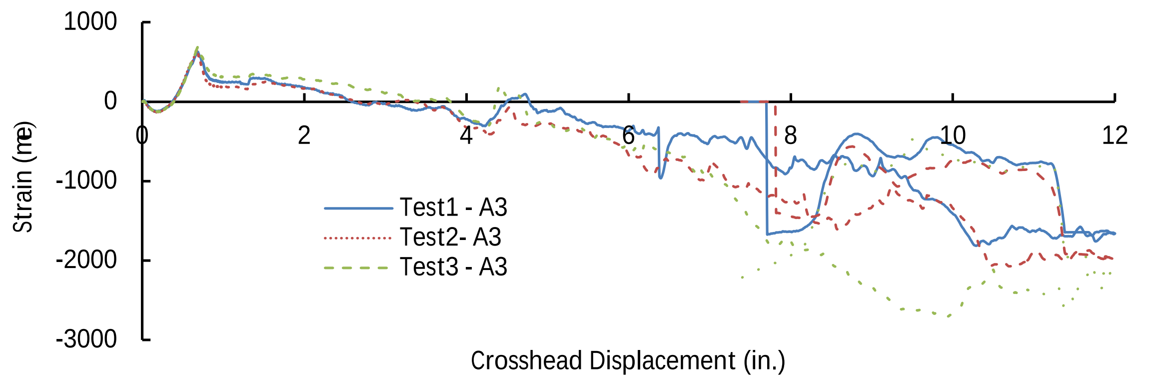

Figure E-98. Strain Gage A3 Response of Three Repeated Tests of the G3-5/4-0.3 GLARE Panel Under 45-Degree Angle Penetration

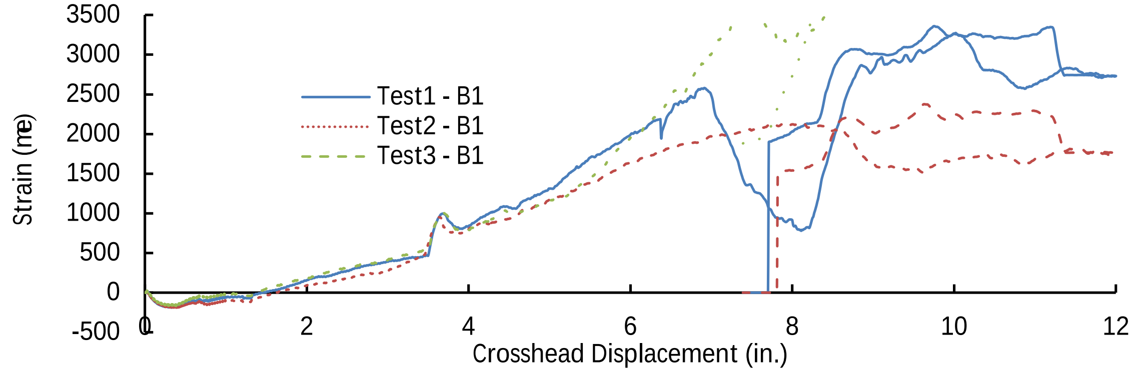

Figure E-99. Strain Gage B1 Response of Three Repeated Tests of the G3-5/4-0.3 GLARE Panel Under 45-Degree Angle Penetration

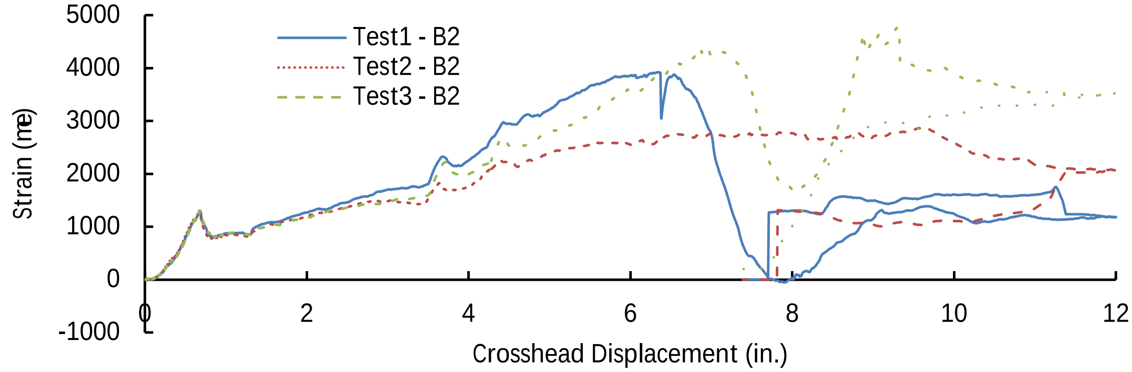

Figure E-100. Strain Gage B2 Response of Three Repeated Tests of the G3-5/4-0.3 GLARE Panel Under 45-Degree Angle Penetration

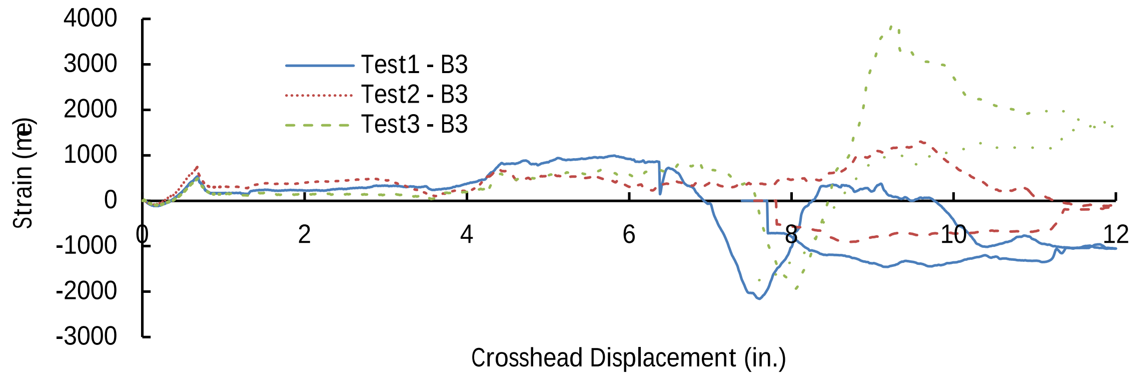

Figure E-101. Strain Gage B3 Response of Three Repeated Tests of the G3-5/4-0.3 GLARE Panel Under 45-Degree Angle Penetration

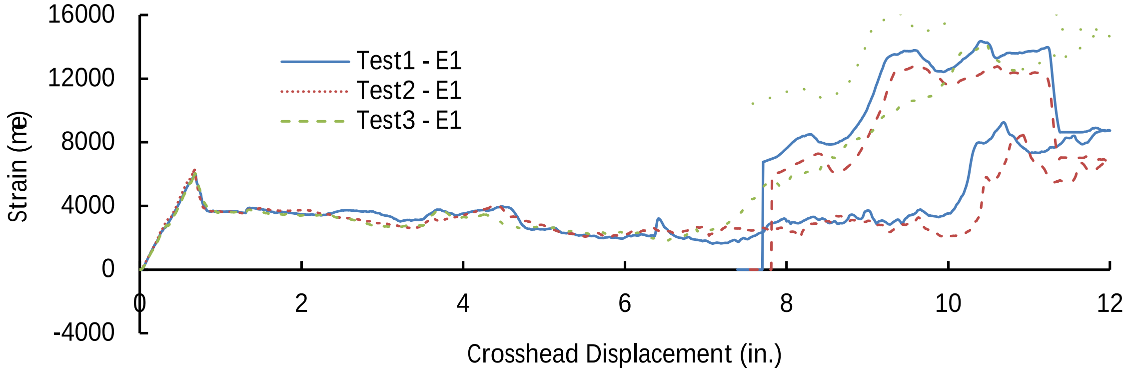

Figure E-102. Strain Gage E1 Response of Three Repeated Tests of the G3-5/4-0.3 GLARE Panel Under 45-Degree Angle Penetration

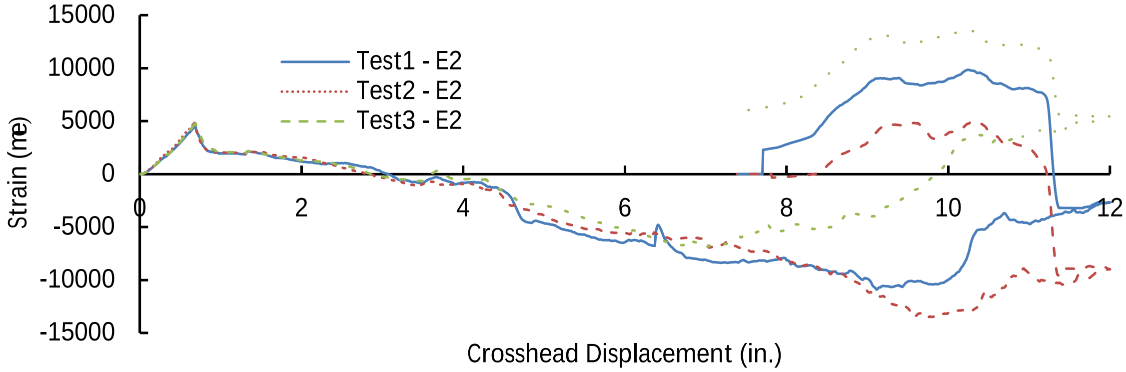

Figure E-103. Strain Gage E2 Response of Three Repeated Tests of the G3-5/4-0.3 GLARE Panel Under 45-Degree Angle Penetration

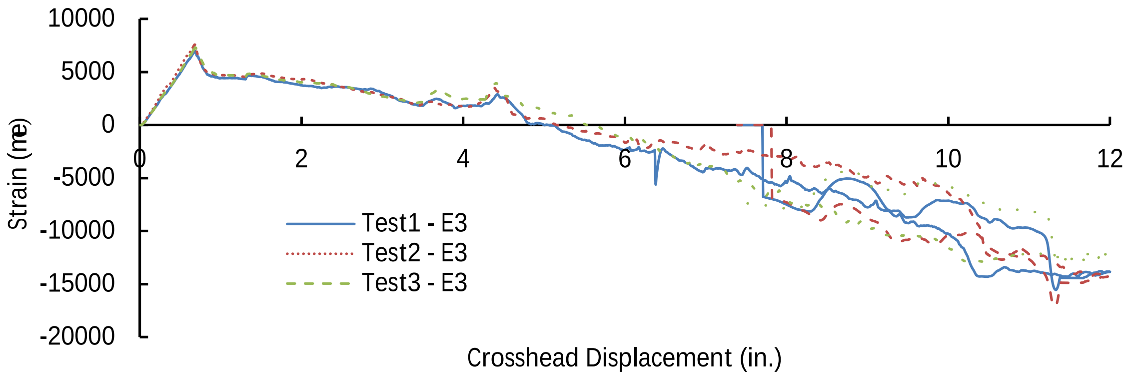

Figure E-104. Strain Gage E3 Response of Three Repeated Tests of the G3-5/4-0.3 GLARE Panel Under 45-Degree Angle Penetration

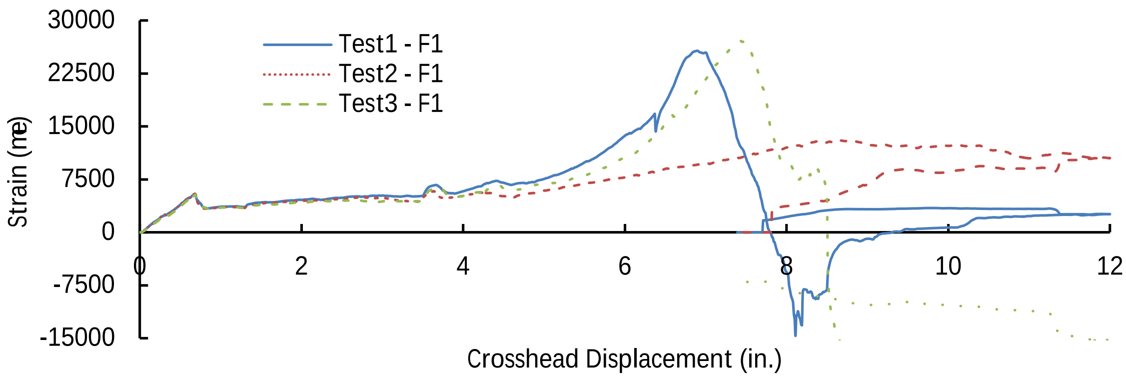

Figure E-105. Strain Gage F1 Response of Three Repeated Tests of the G3-5/4-0.3 GLARE Panel Under 45-Degree Angle Penetration

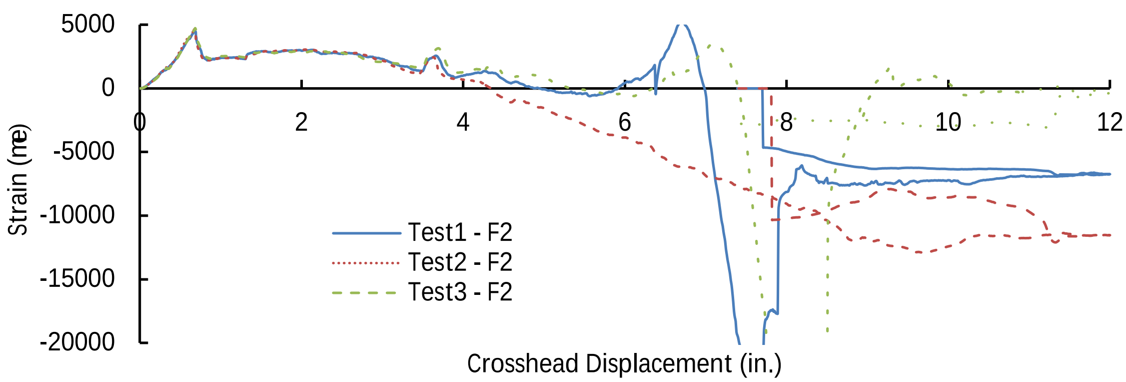

Figure E-106. Strain Gage F2 Response of Three Repeated Tests of the G3-5/4-0.3 GLARE Panel Under 45-Degree Angle Penetration

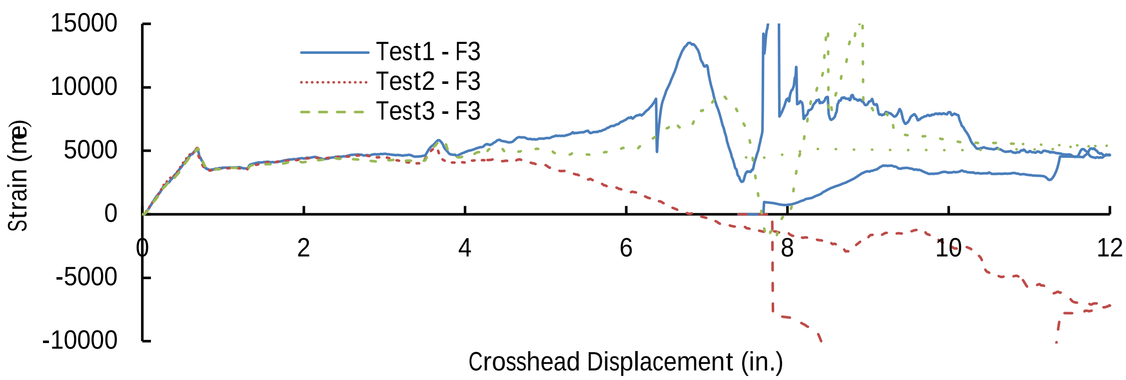

Figure E-107. Strain Gage F3 Response of Three Repeated Tests of the G3-5/4-0.3 GLARE Panel Under 45-Degree Angle Penetration

E.2.6 The G5x-4/3-0.3 GLARE Panel Under 45-Degree Angle Penetration.

The strain gage locations of the first of three repeated tests (Test1) for the G5x-4/3-0.3 GLARE panel under angle penetration are shown in figure E-108. A total of four rosette strain gages were instrumented: two on the top surface, A series (A1, A2, A3) and B series (B1, B2, B3), and two on the bottom surface, E series (E1, E2, E3) and F series (F1, F2, F3). All four rosette strain gages were mounted 2-in. radial distance from center. Strain gages A2, B2, E2, and F2 were mounted to measure radial strain and the remaining strain gages were mounted to measure ±45-degree angle strain with respect to the radial direction. The same strain gage configuration was used in subsequent tests (Test2 and Test3). The arrow in the figure indicates the fiber direction of the first glass/epoxy layer (second overall layer) from the top or penetrating side of the panel. The strain comparison of the three repeated tests of strain gages A1, A2, A3, B1, B2, B3, E1, E2, E3, F1, F2, and F3 are shown in figures E-109 through E-120. The results confirm the repeatability of the tests.

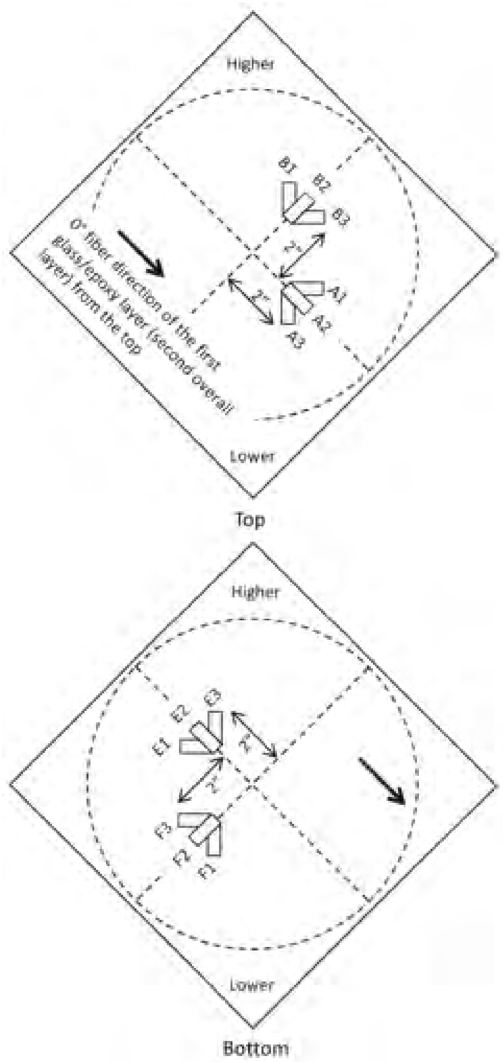

Figure E-108. Strain Gage Locations of the G5x-4/3-0.3 GLARE Panel Under 45-Degree Angle Penetration

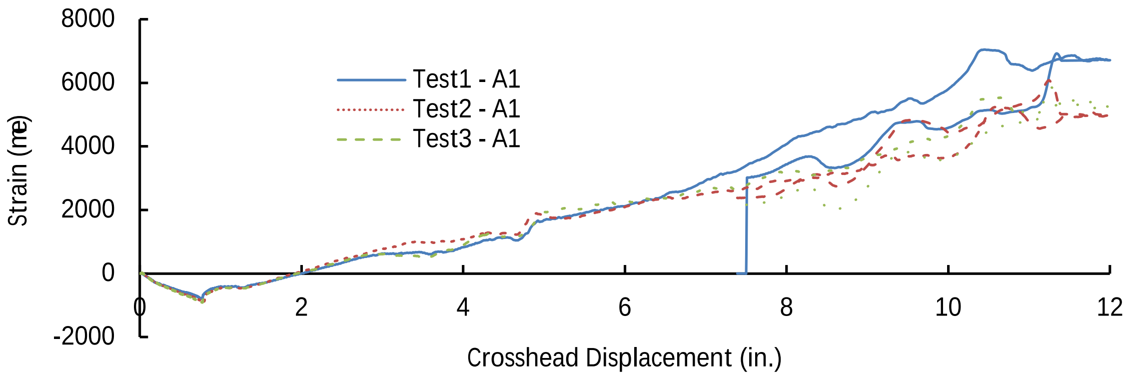

Figure E-109. Strain Gage A1 Response of Three Repeated Tests of the G5x-4/3-0.3 GLARE Panel Under 45-Degree Angle Penetration

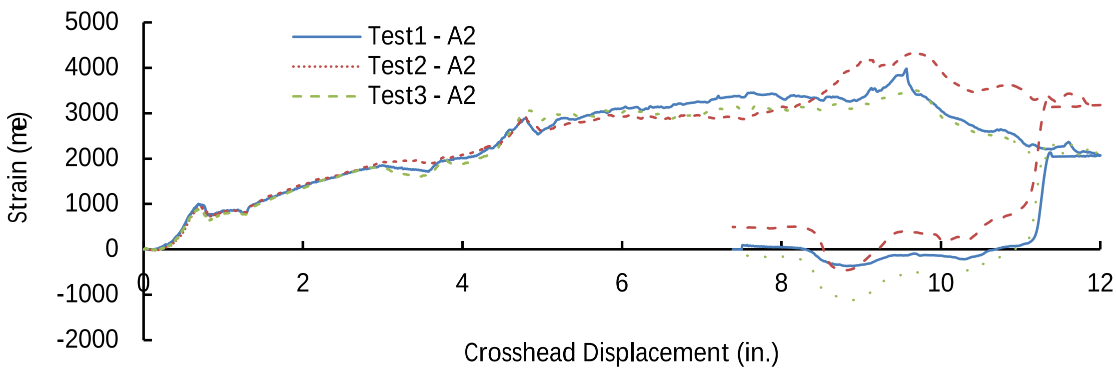

Figure E-110. Strain Gage A2 Response of Three Repeated Tests of the G5x-4/3-0.3 GLARE Panel Under 45-Degree Angle Penetration

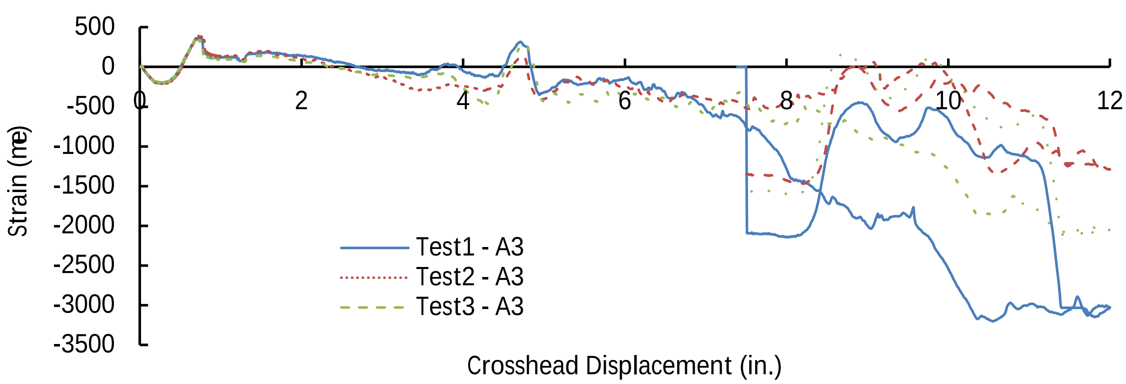

Figure E-111. Strain Gage A3 Response of Three Repeated Tests of the G5x-4/3-0.3 GLARE Panel Under 45-Degree Angle Penetration

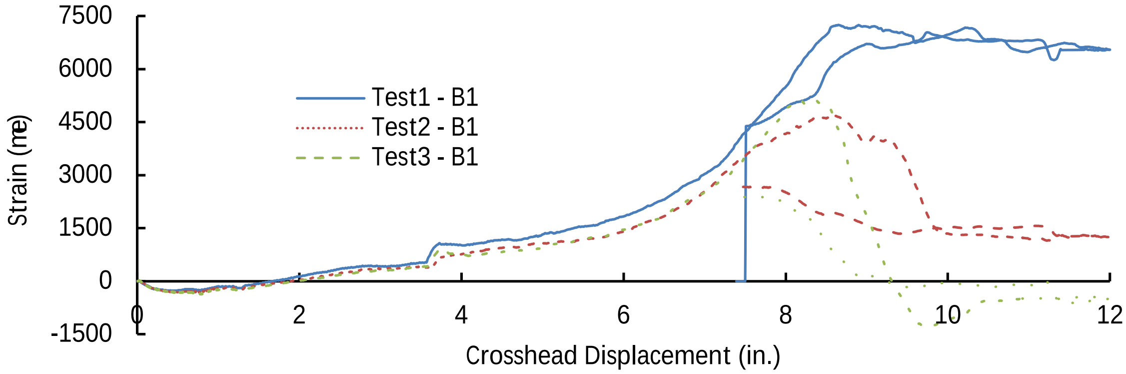

Figure E-112. Strain Gage B1 Response of Three Repeated Tests of the G5x-4/3-0.3 GLARE Panel Under 45-Degree Angle Penetration

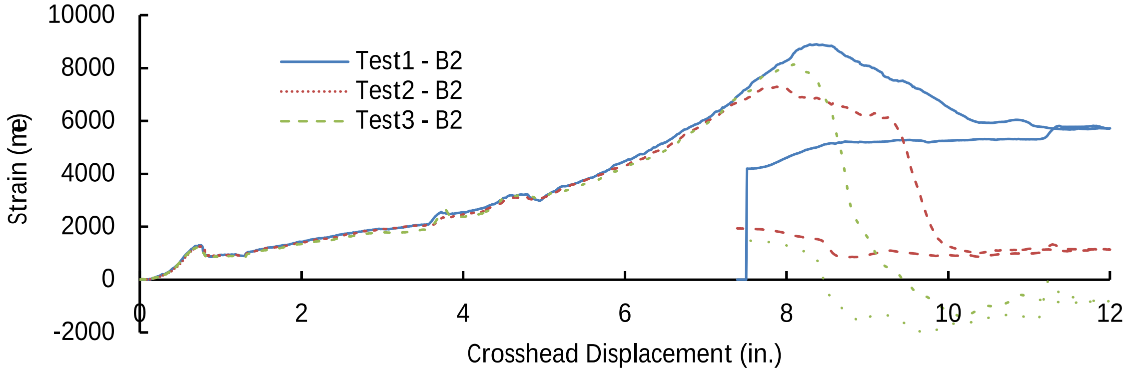

Figure E-113. Strain Gage B2 Response of Three Repeated Tests of the G5x-4/3-0.3 GLARE Panel Under 45-Degree Angle Penetration

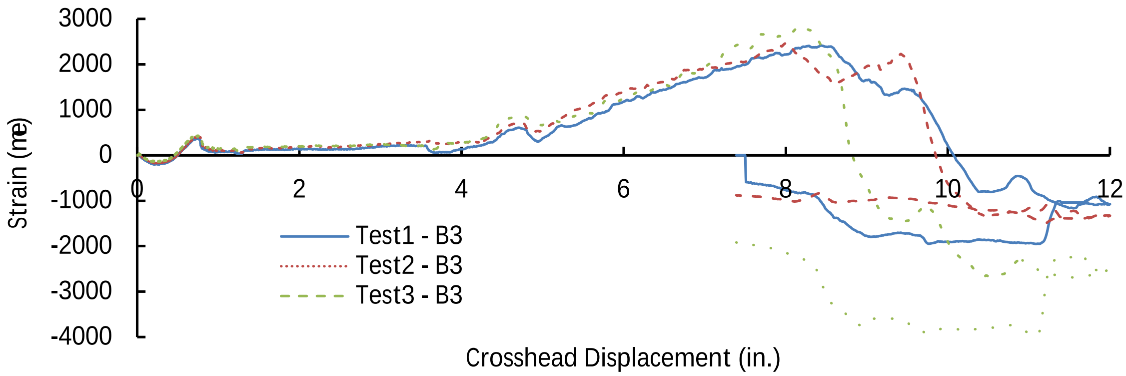

Figure E-114. Strain Gage B3 Response of Three Repeated Tests of the G5x-4/3-0.3 GLARE Panel Under 45-Degree Angle Penetration

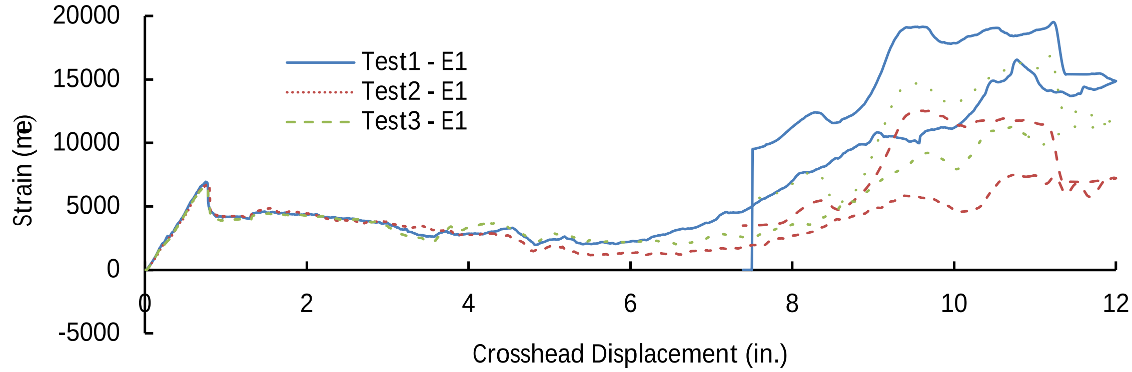

Figure E-115. Strain Gage E1 Response of Three Repeated Tests of the G5x-4/3-0.3 GLARE Panel Under 45-Degree Angle Penetration

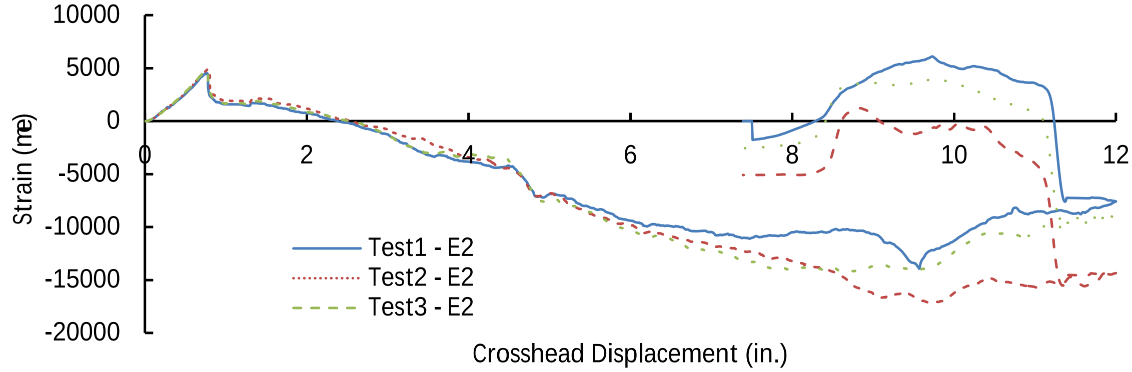

Figure E-116. Strain Gage E2 Response of Three Repeated Tests of the G5x-4/3-0.3 GLARE Panel Under 45-Degree Angle Penetration

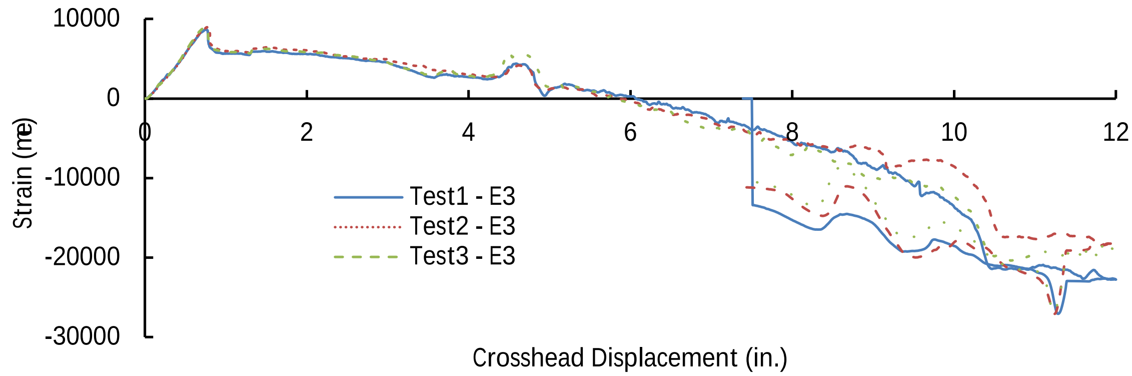

Figure E-117. Strain Gage E3 Response of Three Repeated Tests of the G5x-4/3-0.3 GLARE Panel Under 45-Degree Angle Penetration

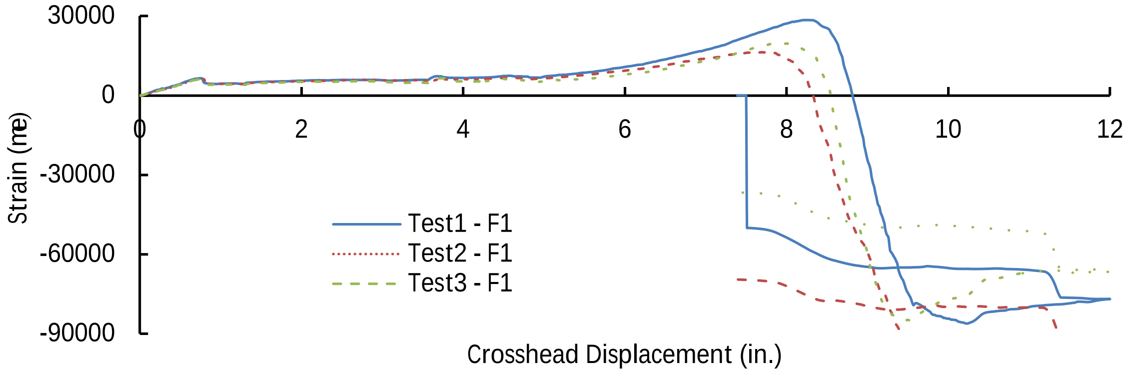

Figure E-118. Strain Gage F1 Response of Three Repeated Tests of the G5x-4/3-0.3 GLARE Panel Under 45-Degree Angle Penetration

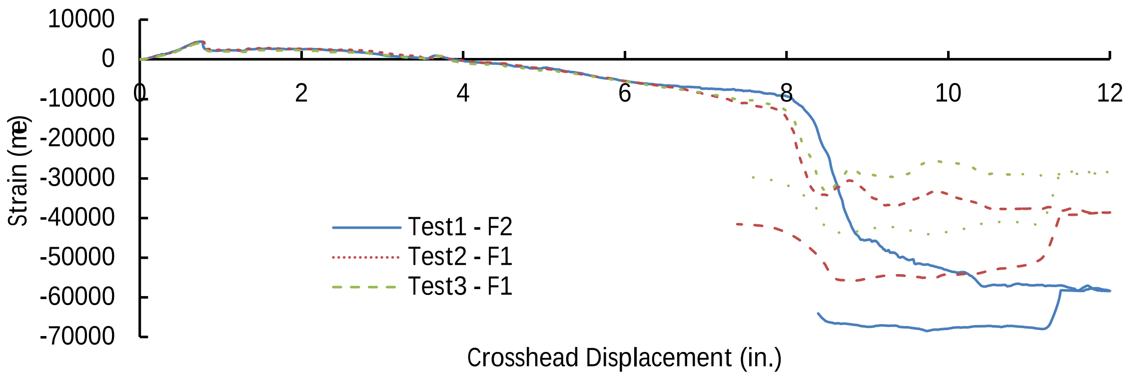

Figure E-119. Strain Gage F2 Response of Three Repeated Tests of the G5x-4/3-0.3 GLARE Panel Under 45-Degree Angle Penetration

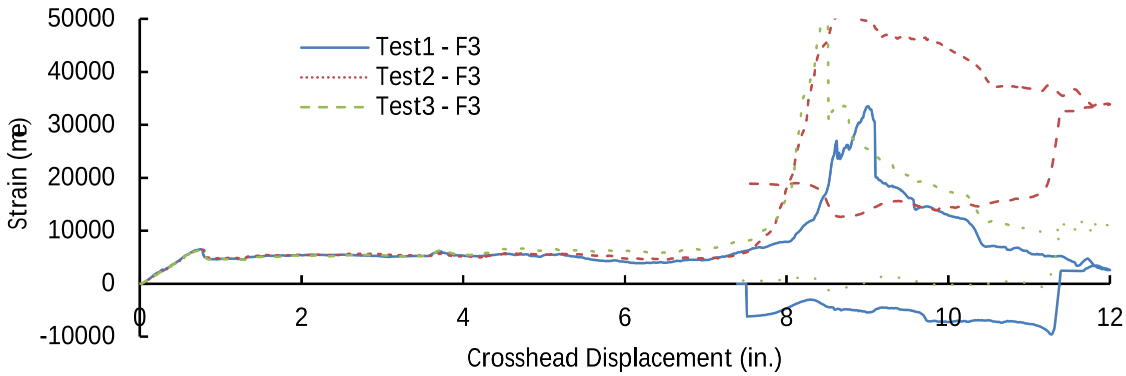

Figure E-120. Strain Gage F3 Response of Three Repeated Tests of the G5x-4/3-0.3 GLARE Panel Under 45-Degree Angle Penetration

E.2.7 The 12-Ply CFRP Panel Under 45-Degree Angle Penetration.

The strain gage locations of the first of three repeated tests (Test1) for the 12-ply CFRP panel under angle penetration are shown in figure E-121. A total of four rosette strain gages were instrumented: two on the top surface, A series (A1, A2, A3) and B series (B1, B2, B3), and two on the bottom surface, E series (E1, E2, E3) and F series (F1, F2, F3). All four rosette strain gages were mounted 2-in. radial distance from center. Strain gages A2, B2, E2, and F2 were mounted to measure radial strain and the rest of the strain gages were mounted to measure ±45-degree angle strain with respect to the radial direction. The same strain gage configuration was used in subsequent tests (Test2 and Test3). The arrow in the figure indicates the fiber direction of the first glass/epoxy layer (second overall layer) from the top or penetrating side of the panel. The strain comparison of the three repeated tests of strain gages A1, A2, A3, B1, B2, B3, E1, E2, E3, F1, F2, and F3 are shown in figures E-122 through E-133. The results confirm the repeatability of the tests.

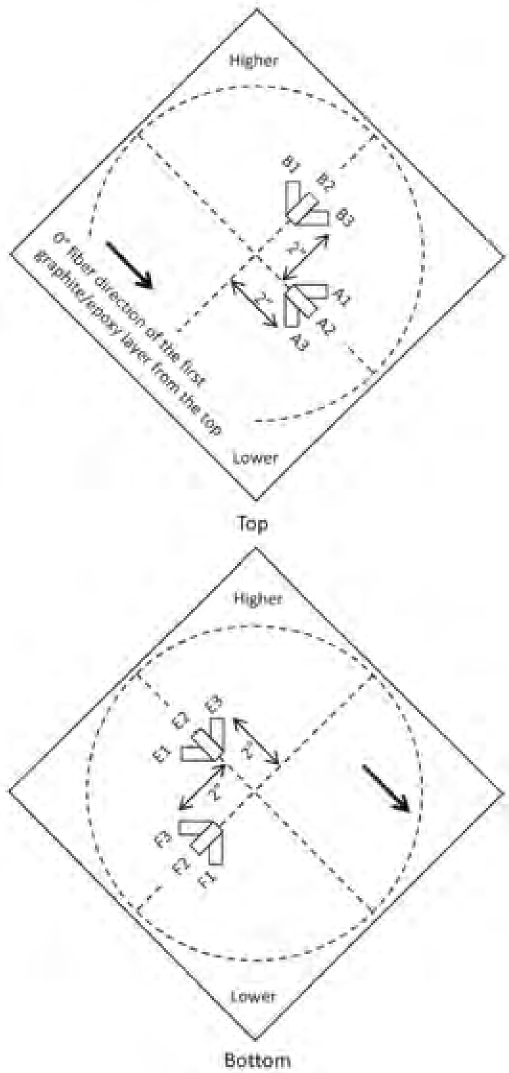

Figure E-121. Strain Gage Locations of the 12-ply CFRP Panel Under 45-Degree Angle Penetration

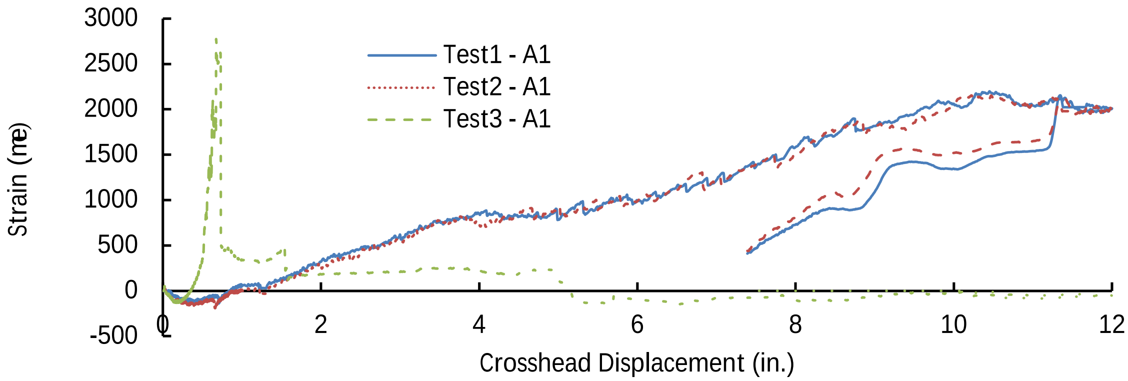

Figure E-122. Strain Gage A1 Response of Three Repeated Tests of the 12-ply CFRP Panel Under 45-Degree Angle Penetration

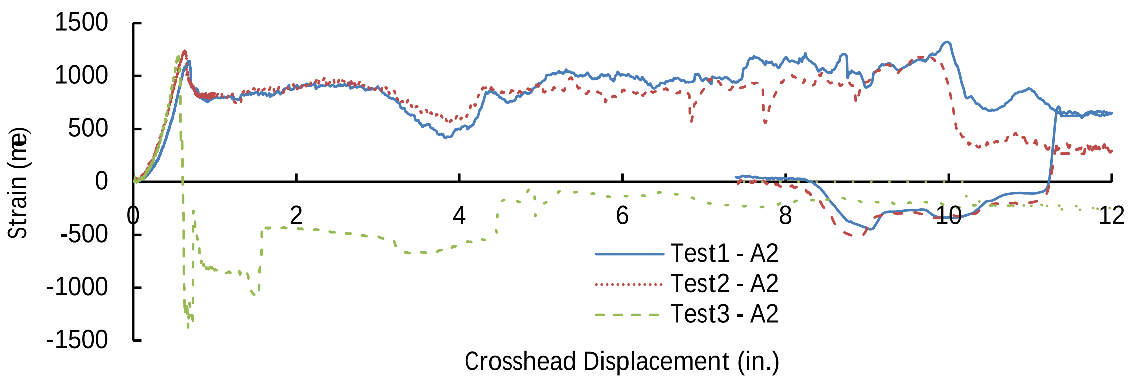

Figure E-123. Strain Gage A2 Response of Three Repeated Tests of the 12-ply CFRP Panel Under 45-Degree Angle Penetration

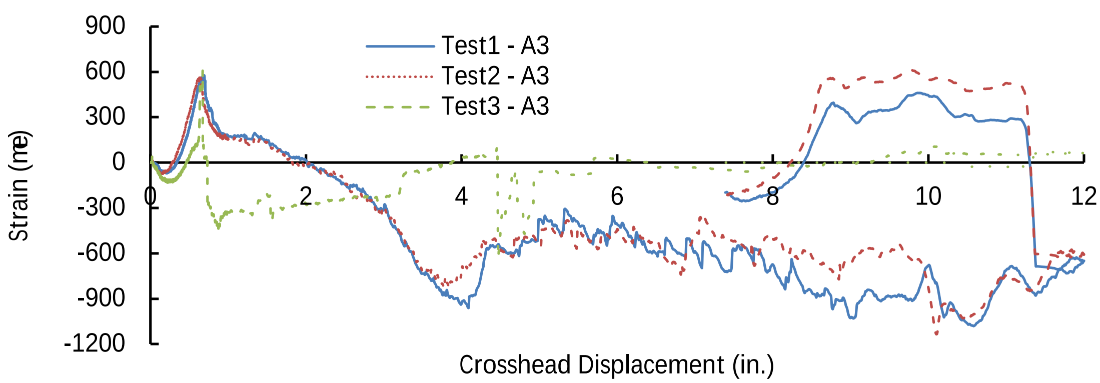

Figure E-124. Strain Gage A3 Response of Three Repeated Tests of the 12-ply CFRP Panel Under 45-Degree Angle Penetration

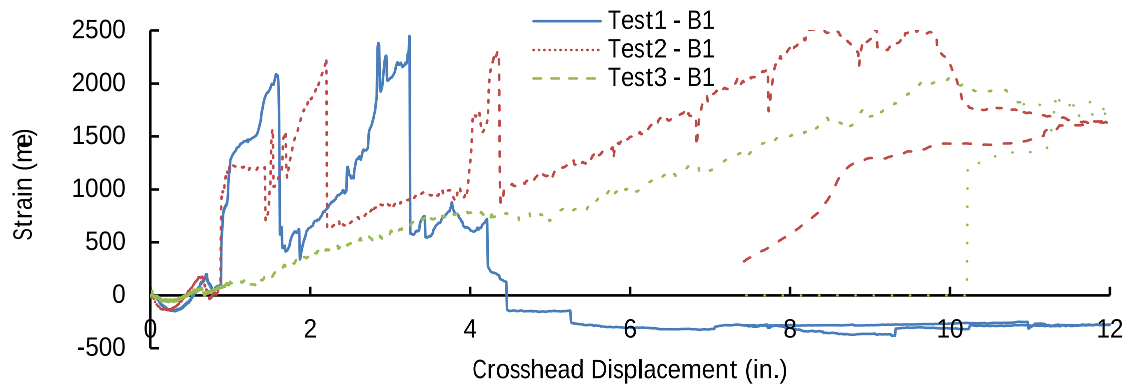

Figure E-125. Strain Gage B1 Response of Three Repeated Tests of the 12-ply CFRP Panel Under 45-Degree Angle Penetration

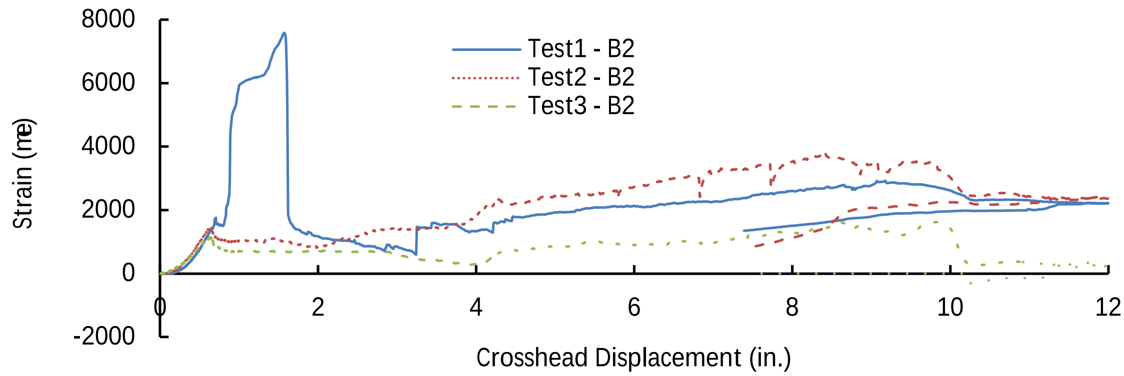

Figure E-126. Strain Gage B2 Response of Three Repeated Tests of the 12-ply CFRP Panel Under 45-Degree Angle Penetration

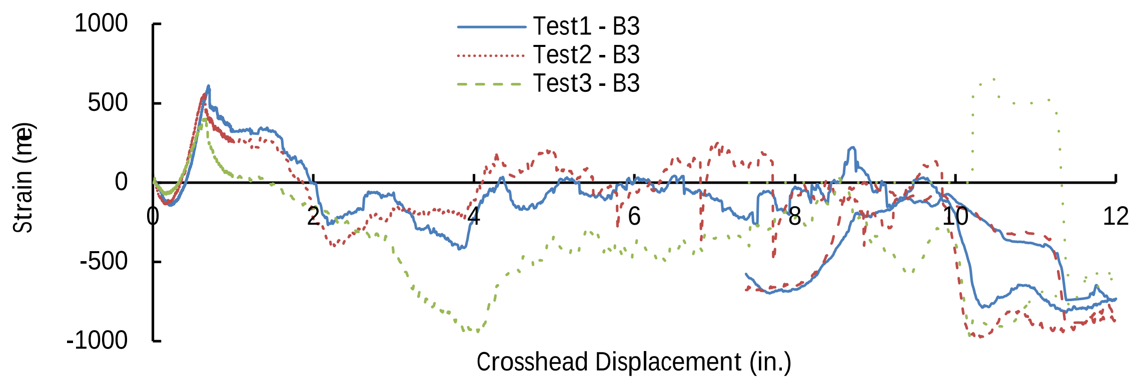

Figure E-127. Strain Gage B3 Response of Three Repeated Tests of the 12-ply CFRP Panel Under 45-Degree Angle Penetration

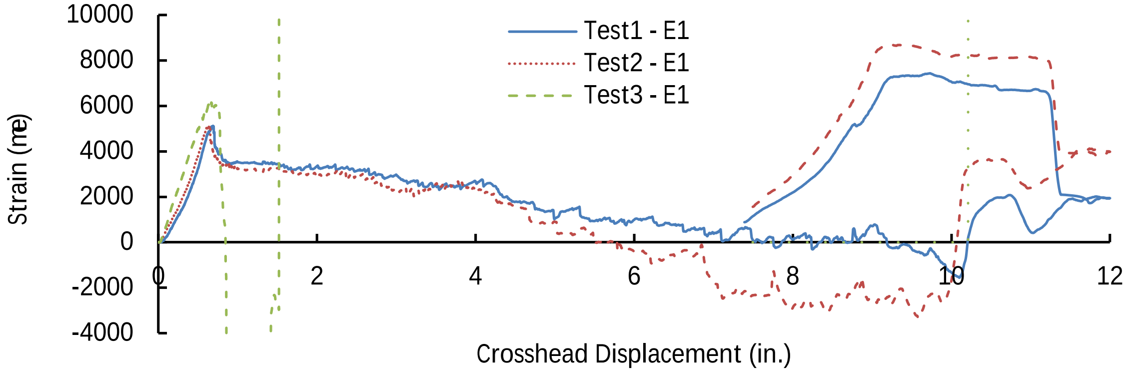

Figure E-128. Strain Gage E1 Response of Three Repeated Tests of the 12-ply CFRP Panel Under 45-Degree Angle Penetration

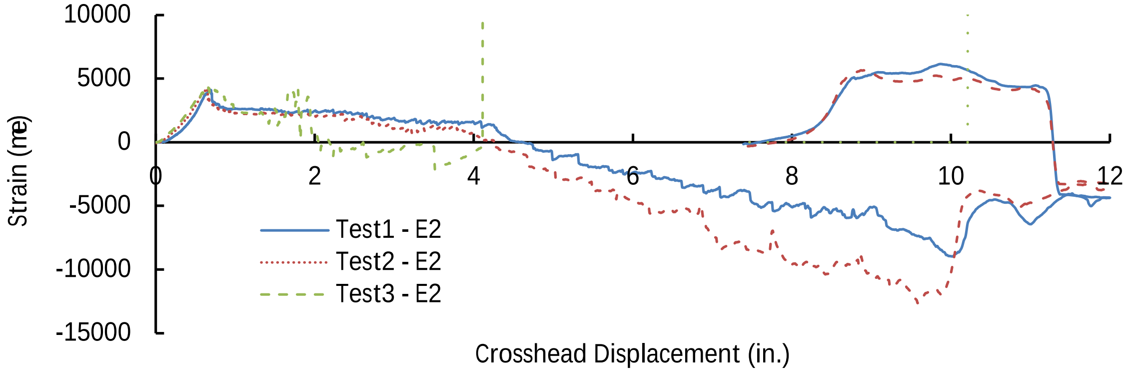

Figure E-129. Strain Gage E2 Response of Three Repeated Tests of the 12-ply CFRP Panel Under 45-Degree Angle Penetration

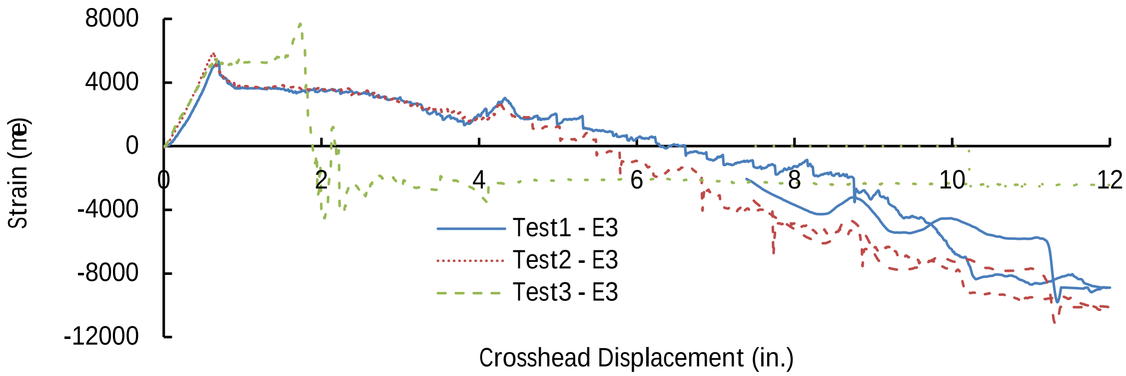

Figure E-130. Strain Gage E3 Response of Three Repeated Tests of the 12-ply CFRP Panel Under 45-Degree Angle Penetration

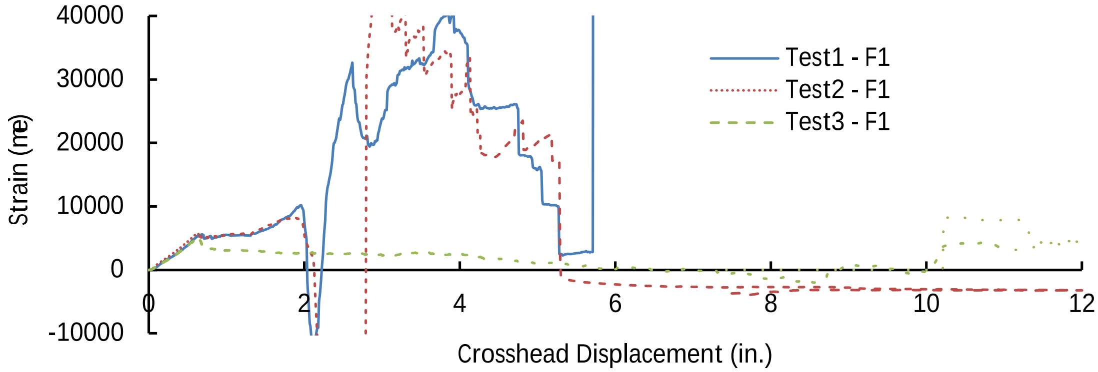

Figure E-131. Strain Gage F1 Response of Three Repeated Tests of the 12-ply CFRP Panel Under 45-Degree Angle Penetration

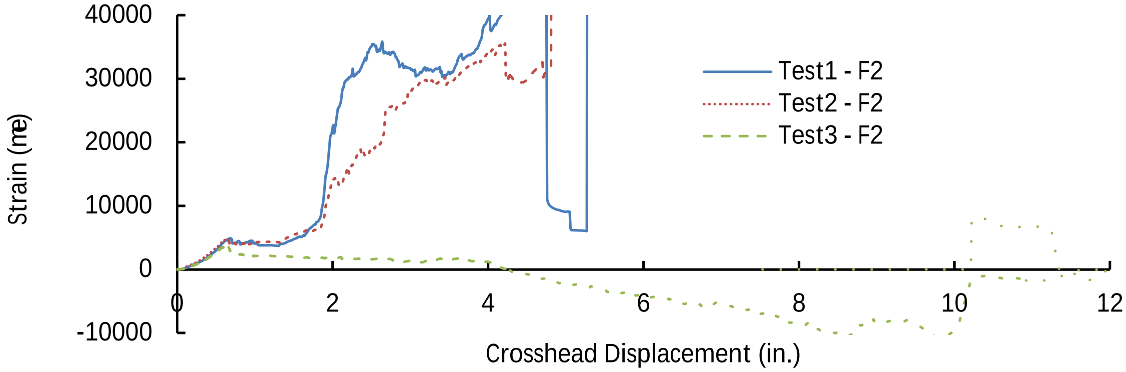

Figure E-132. Strain Gage F2 Response of Three Repeated Tests of the 12-ply CFRP Panel Under 45-Degree Angle Penetration

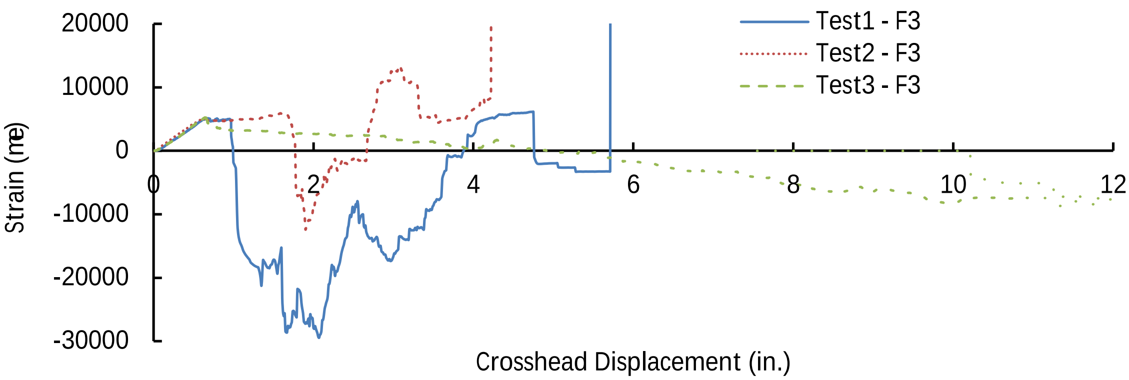

Figure E-133. Strain Gage F3 Response of Three Repeated Tests of the 12-ply CFRP Panel Under 45-Degree Angle Penetration

E.2.8 The 16-Ply CFRP Panel Under 45-Degree Angle Penetration.

The strain gage locations of the first of three repeated tests (Test1) for the 16-ply CFRP panel under angle penetration are shown in figure E-134. A total of four rosette strain gages were instrumented: two on the top surface, A series (A1, A2, A3) and B series (B1, B2, B3), and two on the bottom surface, E series (E1, E2, E3) and F series (F1, F2, F3). All four rosette strain gages were mounted 2-in. radial distance from center. Strain gages A2, B2, E2, and F2 were mounted to measure radial strain and the remaining strain gages were mounted to measure ±45-degree angle strain with respect to the radial direction. The same strain gage configuration was used in subsequent tests (Test2 and Test3). The arrow in the figure indicates the fiber direction of the first glass/epoxy layer (second overall layer) from the top or penetrating side of the panel. The strain comparison of the three repeated test of strain gages A1, A2, A3, B1, B2, B3, E1, E2, E3, F1, F2, and F3 are shown in figures E-135 through E-146. The results confirm the repeatability of the tests.

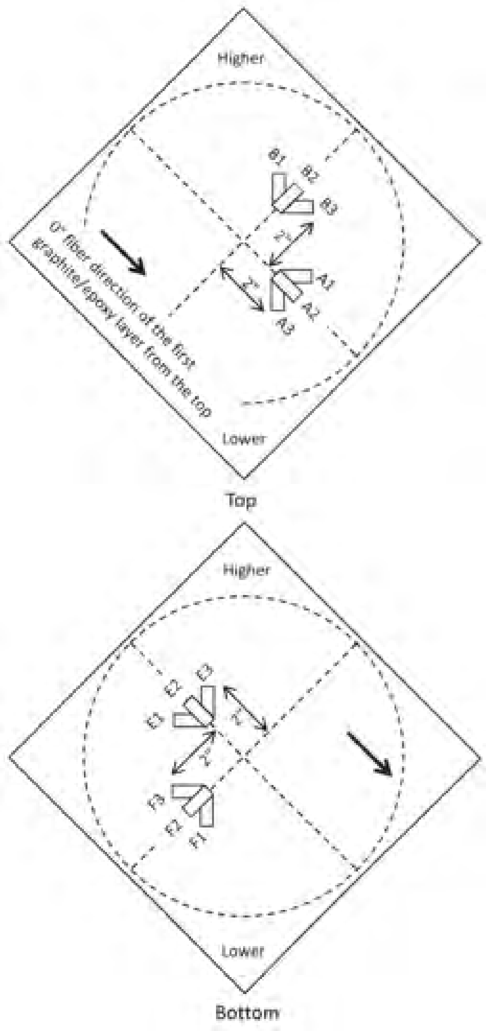

Figure E-134. Strain Gage Locations of the 16-ply CFRP Panel Under 45-Degree Angle Penetration

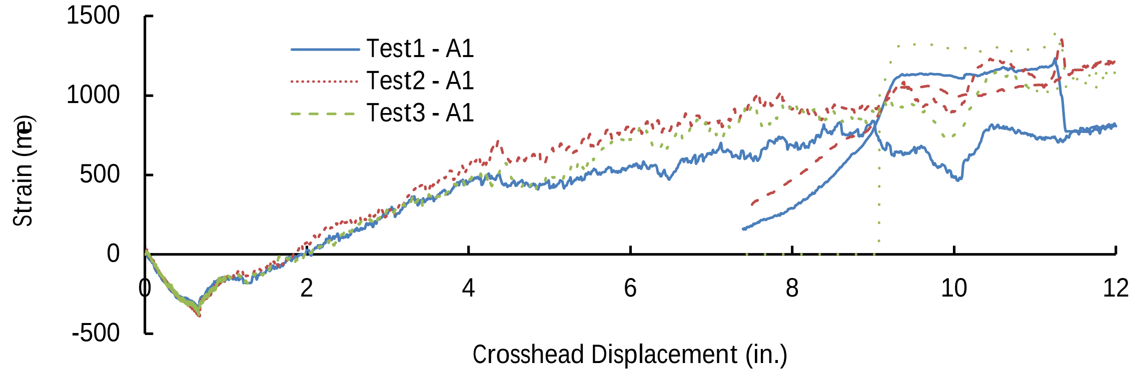

Figure E-135. Strain Gage A1 Response of Three Repeated Tests of the 16-ply CFRP Panel Under 45-Degree Angle Penetration

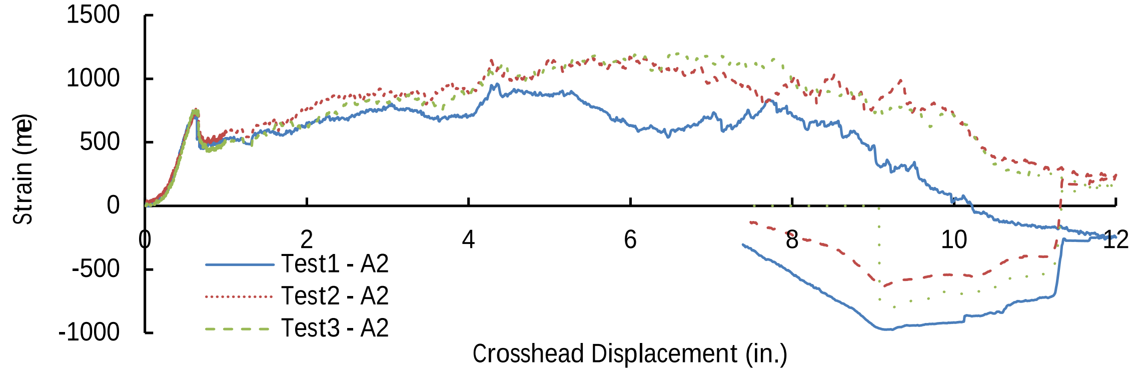

Figure E-136. Strain Gage A2 Response of Three Repeated Tests of the 16-ply CFRP Panel Under 45-Degree Angle Penetration

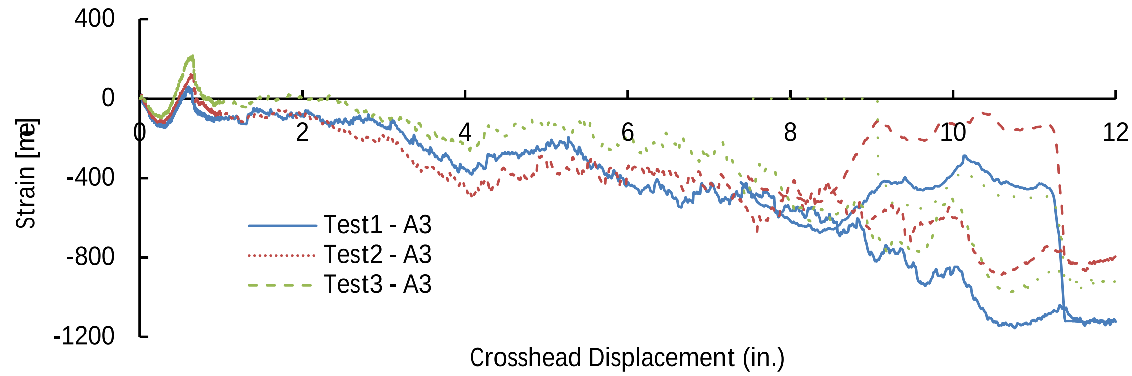

Figure E-137. Strain Gage A3 Response of Three Repeated Tests of the 16-ply CFRP Panel Under 45-Degree Angle Penetration

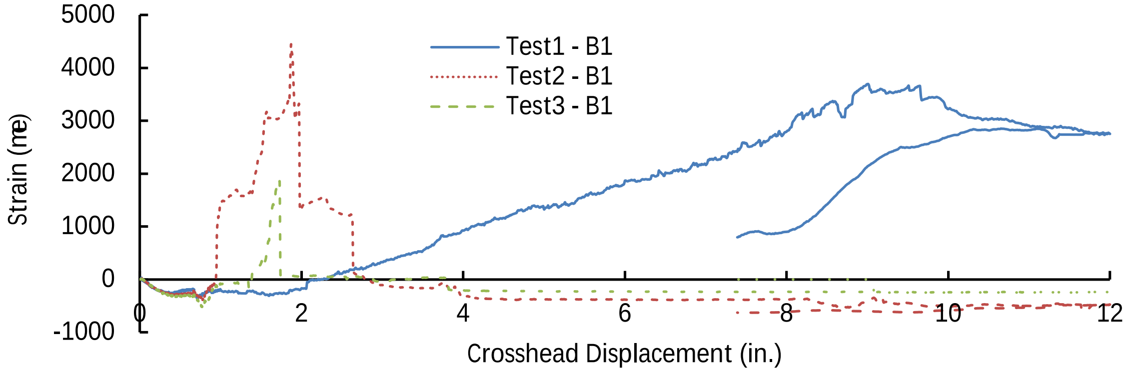

Figure E-138. Strain Gage B1 Response of Three Repeated Tests of the 16-ply CFRP Panel Under 45-Degree Angle Penetration

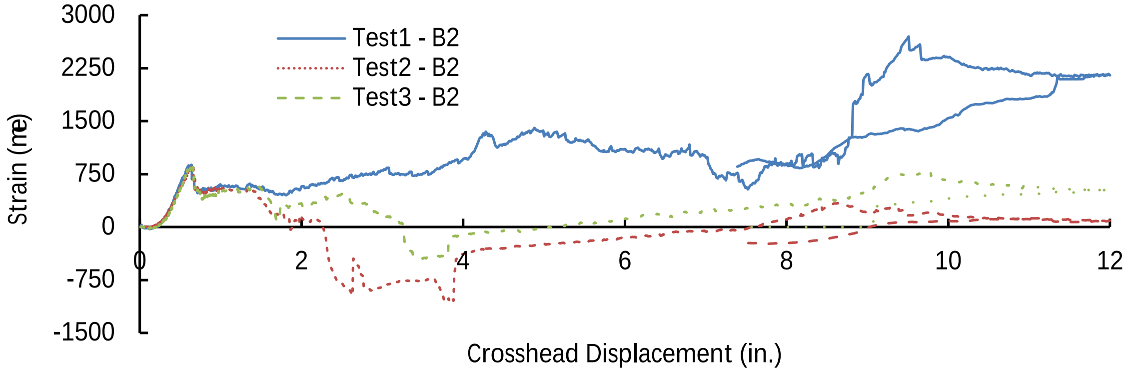

Figure E-139. Strain Gage B2 Response of Three Repeated Tests of the 16-ply CFRP Panel Under 45-Degree Angle Penetration

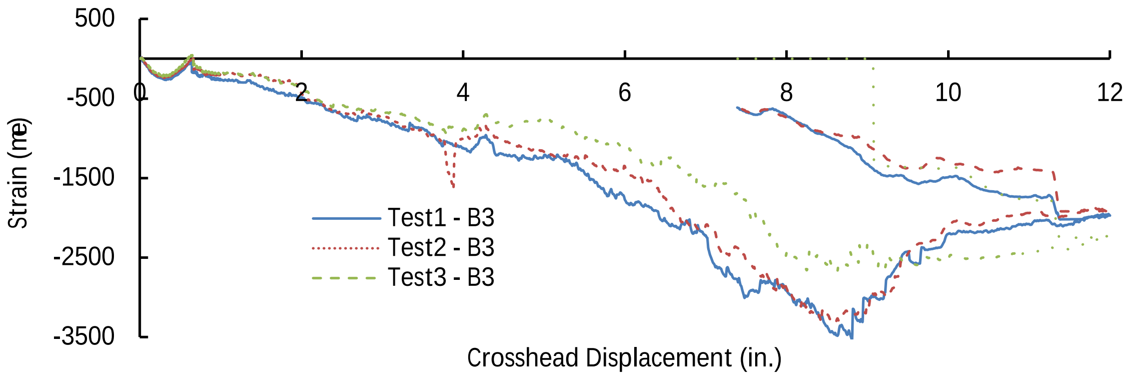

Figure E-140. Strain Gage B3 Response of Three Repeated Tests of the 16-ply CFRP Panel Under 45-Degree Angle Penetration

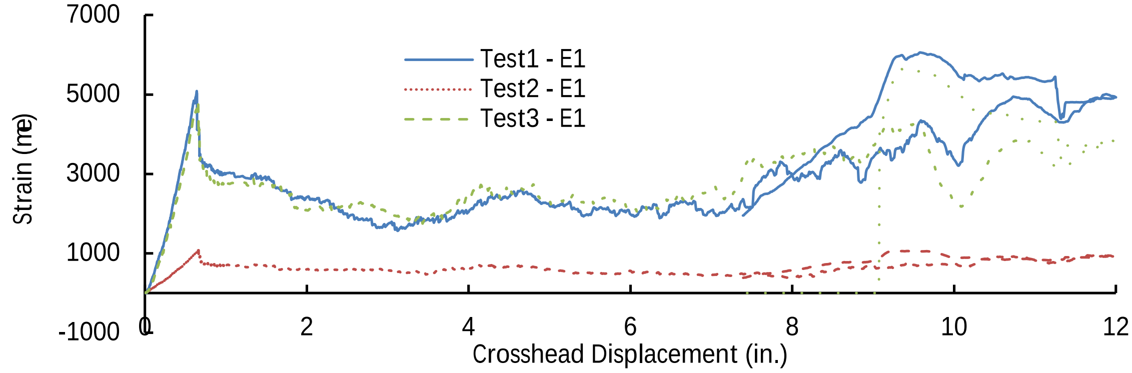

Figure E-141. Strain Gage E1 Response of Three Repeated Tests of the 16-ply CFRP Panel Under 45-Degree Angle Penetration

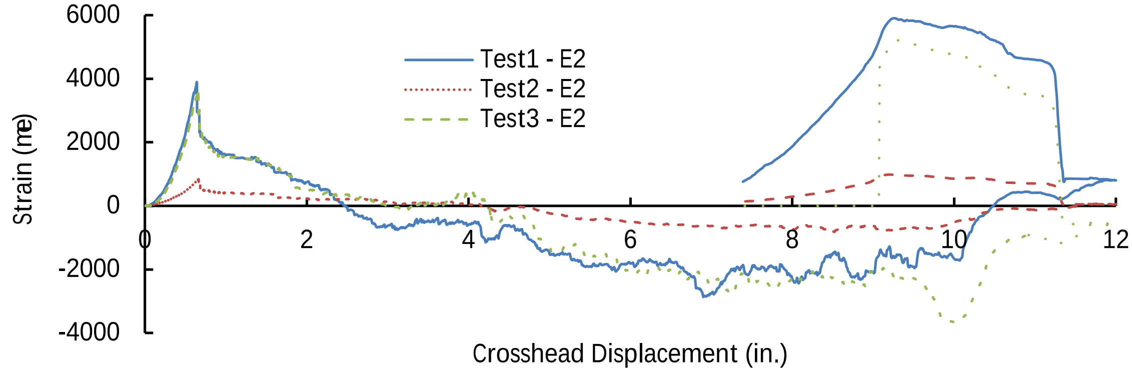

Figure E-142. Strain Gage E2 Response of Three Repeated Tests of the 16-ply CFRP Panel Under 45-Degree Angle Penetration

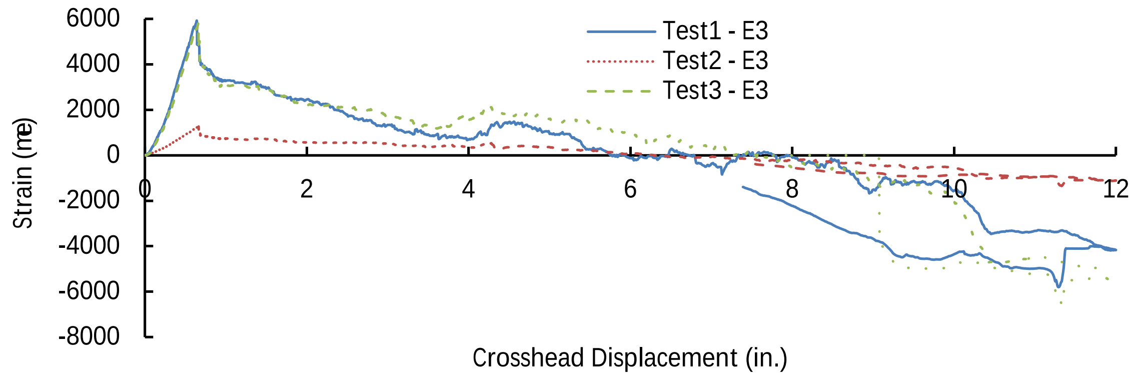

Figure E-143. Strain Gage E3 Response of Three Repeated Tests of the 16-ply CFRP Panel Under 45-Degree Angle Penetration

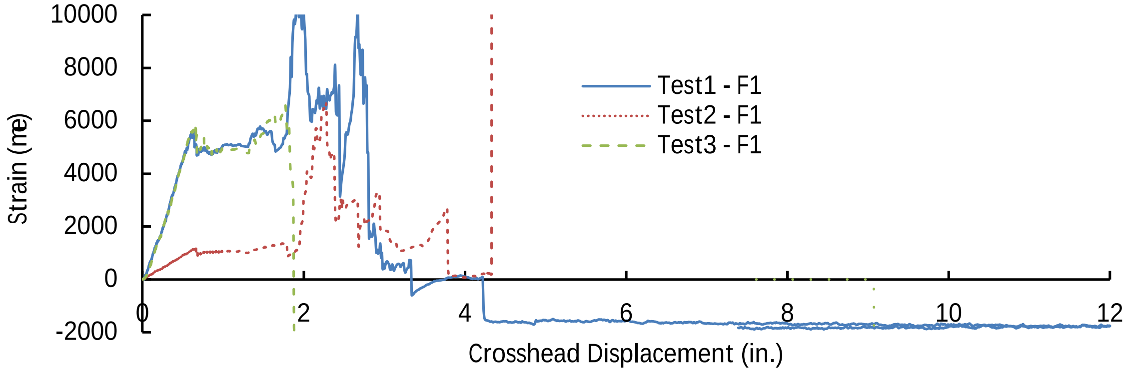

Figure E-144. Strain Gage F1 Response of Three Repeated Tests of the 16-ply CFRP Panel Under 45-Degree Angle Penetration

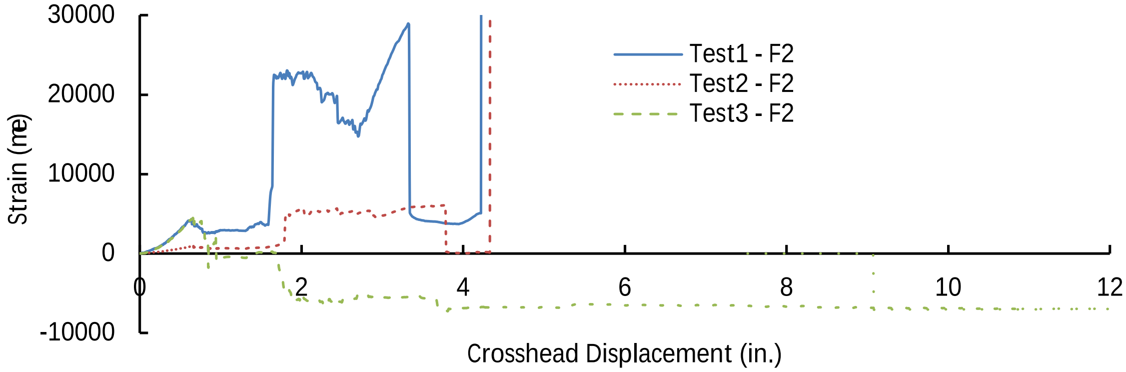

Figure E-145. Strain Gage F2 Response of Three Repeated Tests of the 16-ply CFRP Panel Under 45-Degree Angle Penetration

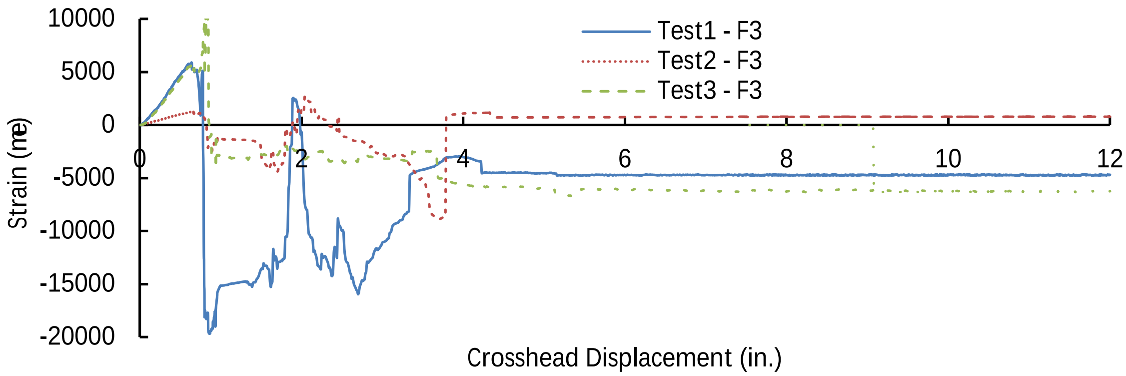

Figure E-146. Strain Gage F3 Response of Three Repeated Tests of the 16-ply CFRP Panel Under 45-Degree Angle Penetration

E.2.9 The 24-Ply CFRP Panel Under 45-Degree Angle Penetration.

The strain gage locations of the first of three repeated tests (Test1) for the 24-ply CFRP panel under angle penetration are shown in figure E-147. A total of four rosette strain gages were instrumented: two on the top surface, A series (A1, A2, A3) and B series (B1, B2, B3), and two on the bottom surface, E series (E1, E2, E3) and F series (F1, F2, F3). All four rosette strain gages were mounted 2-in. radial distance from center. Strain gages A2, B2, E2, and F2 were mounted to measure radial strain and the rest of the strain gages were mounted to measure ±45-degree angle strain with respect to the radial direction. The same strain gage configuration was used in subsequent tests (Test2 and Test3). The arrow in the figure indicates the fiber direction of the first glass/epoxy layer (second overall layer) from the top or penetrating side of the panel. The strain comparison of the three repeated tests of strain gages A1, A2, A3, B1, B2, B3, E1, E2, E3, F1, F2, and F3 are shown in figures E-148 through E-159. The results confirm the repeatability of the tests.

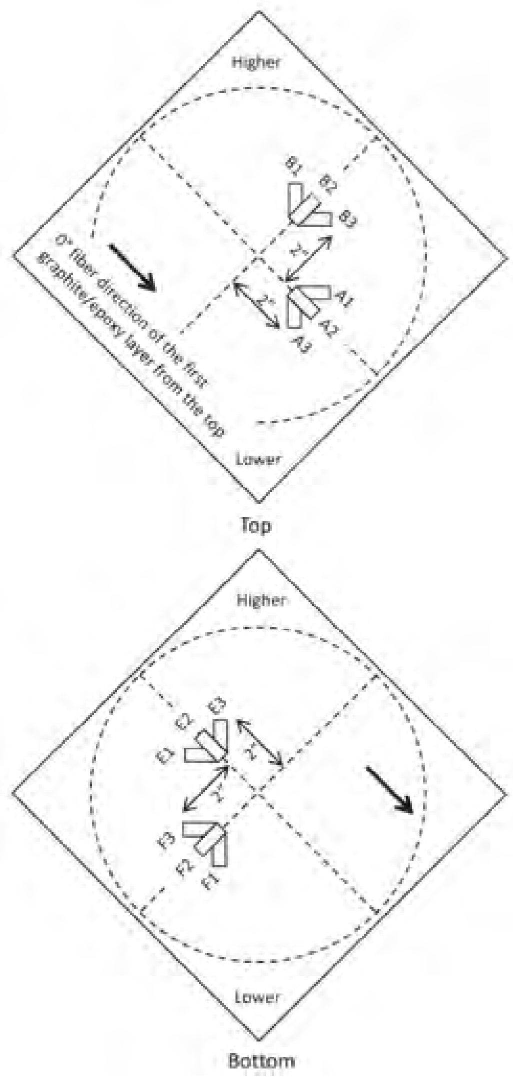

Figure E-147. Strain Gage Locations of the 24-ply CFRP Panel Under 45-Degree Angle Penetration

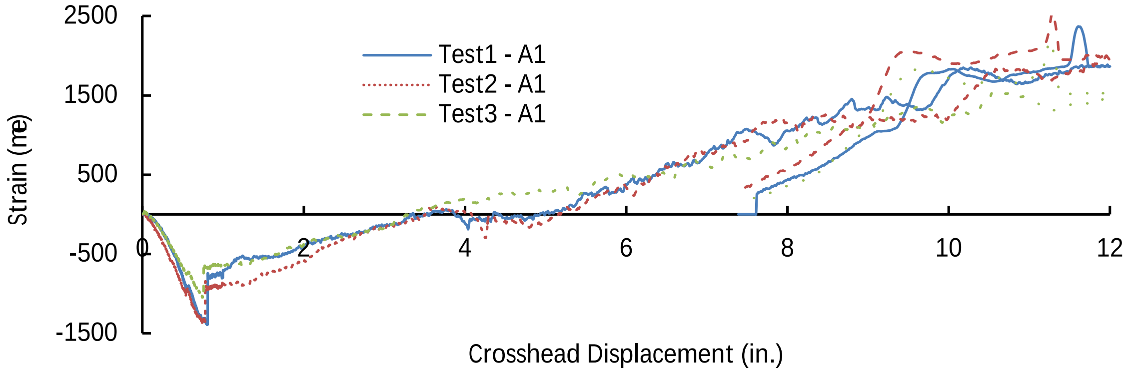

Figure E-148. Strain Gage A1 Response of Three Repeated Tests of the 24-ply CFRP Panel Under 45-Degree Angle Penetration

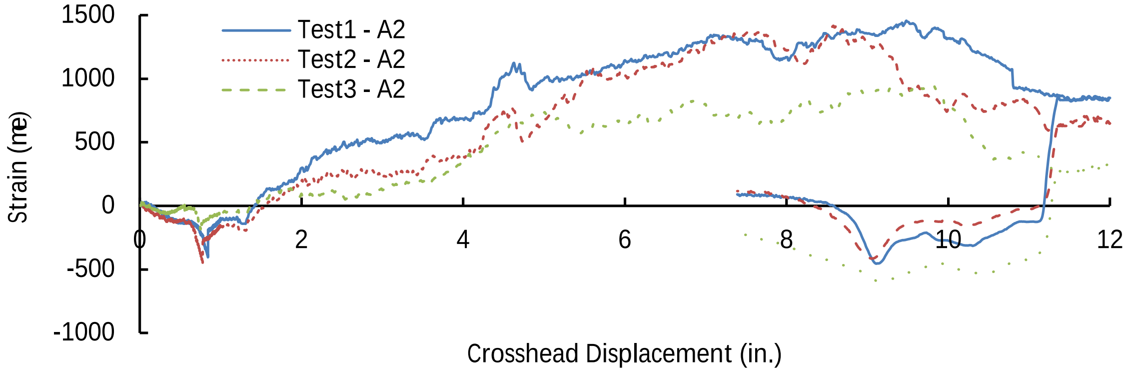

Figure E-149. Strain Gage A2 Response of Three Repeated Tests of the 24-ply CFRP Panel Under 45-Degree Angle Penetration

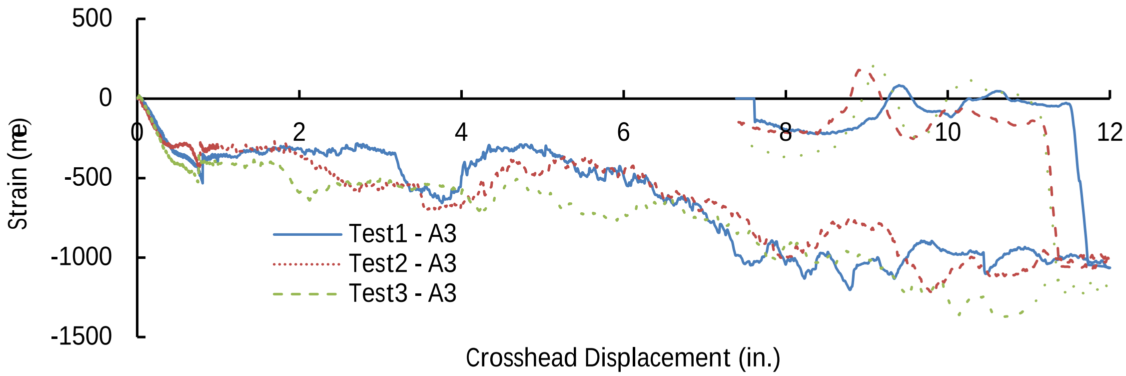

Figure E-150. Strain Gage A3 Response of Three Repeated Tests of the 24-ply CFRP Panel Under 45-Degree Angle Penetration

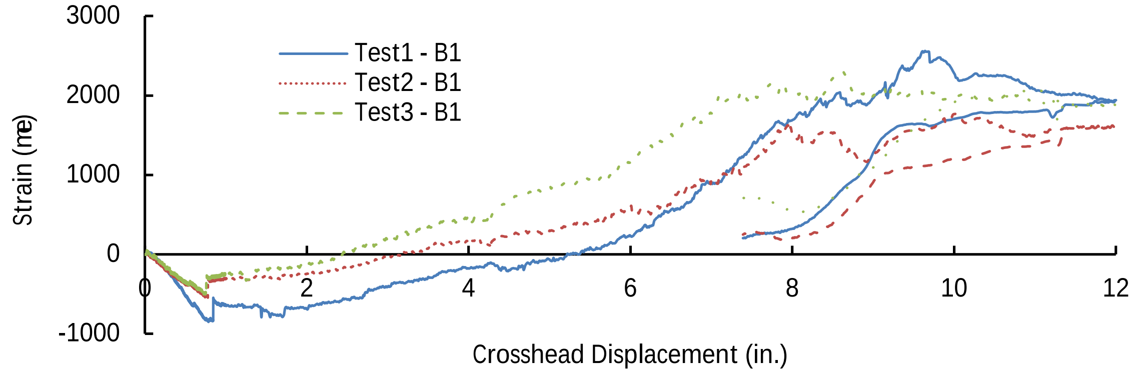

Figure E-151. Strain Gage B1 Response of Three Repeated Tests of the 24-ply CFRP Panel Under 45-Degree Angle Penetration

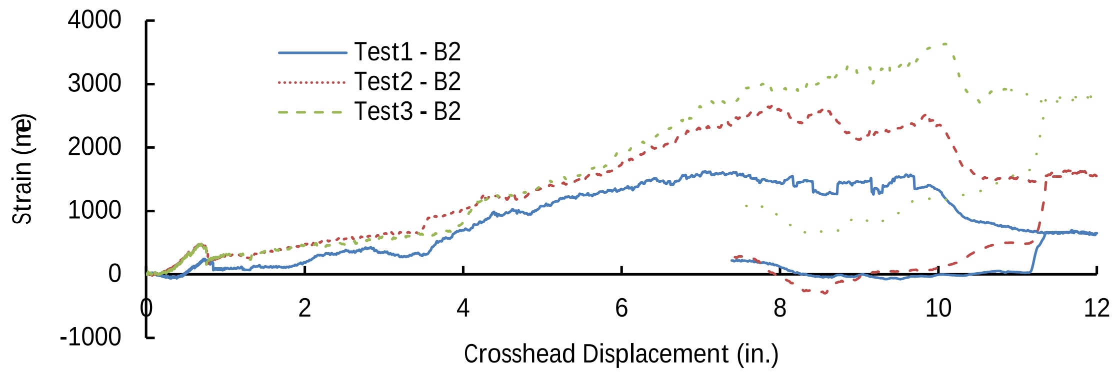

Figure E-152. Strain Gage B2 Response of Three Repeated Tests of the 24-ply CFRP Panel Under 45-Degree Angle Penetration

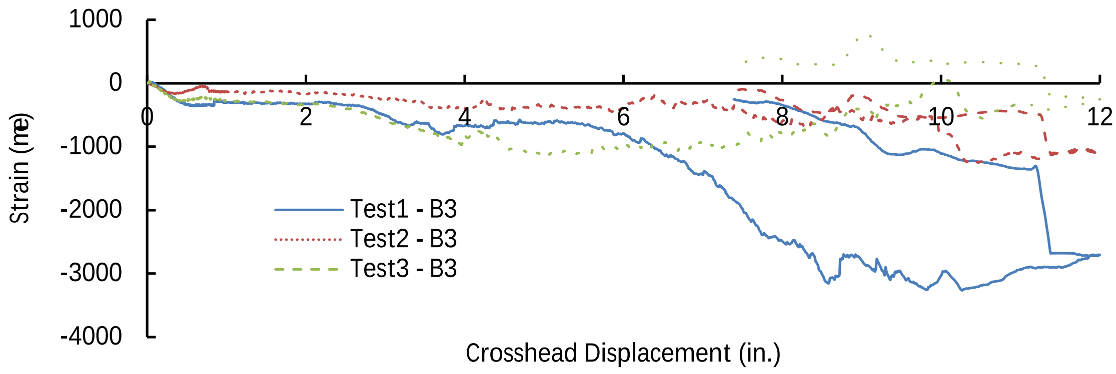

Figure E-153. Strain Gage B3 Response of Three Repeated Tests of the 24-ply CFRP Panel Under 45-Degree Angle Penetration

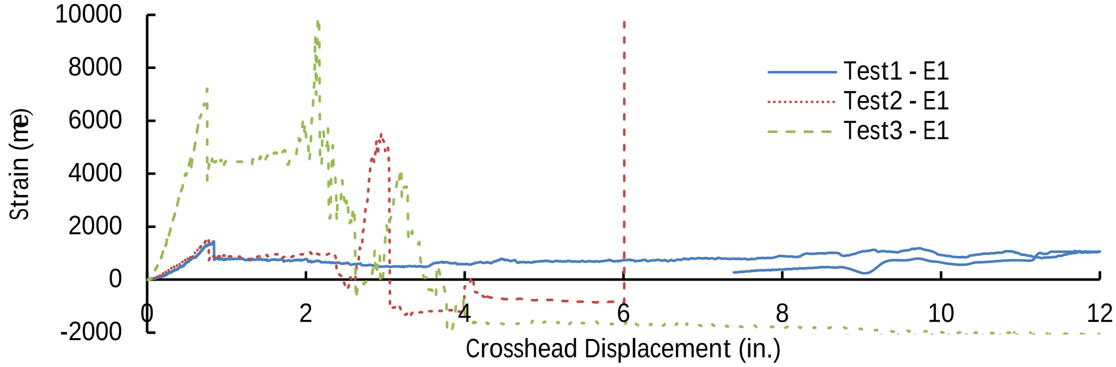

Figure E-154. Strain Gage E1 Response of Three Repeated Tests of the 24-ply CFRP Panel Under 45-Degree Angle Penetration

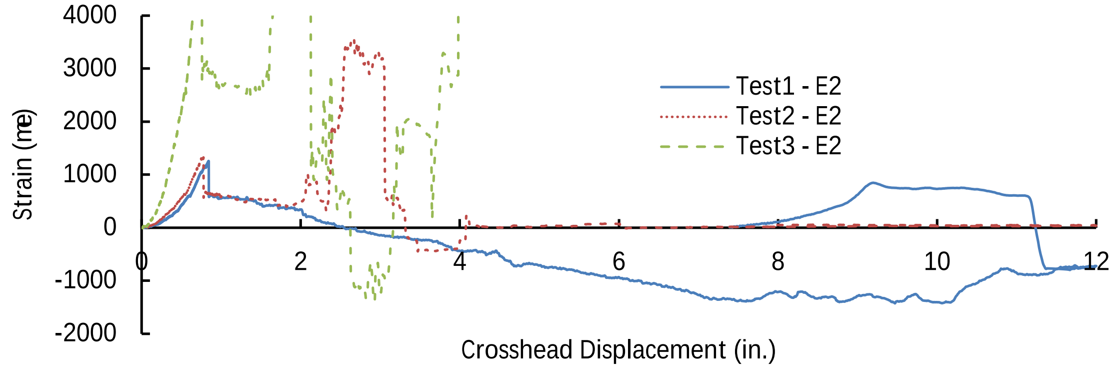

Figure E-155. Strain Gage E2 Response of Three Repeated Tests of the 24-ply CFRP Panel Under 45-Degree Angle Penetration

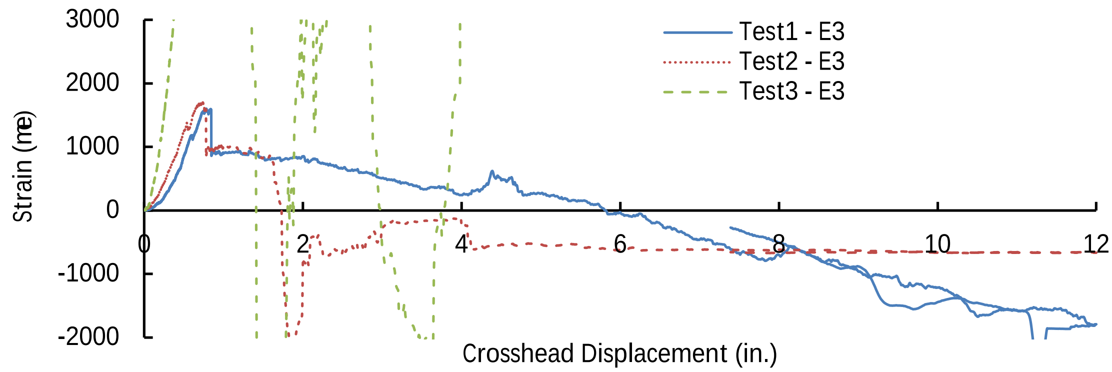

Figure E-156. Strain Gage E3 Response of Three Repeated Tests of the 24-ply CFRP Panel Under 45-Degree Angle Penetration

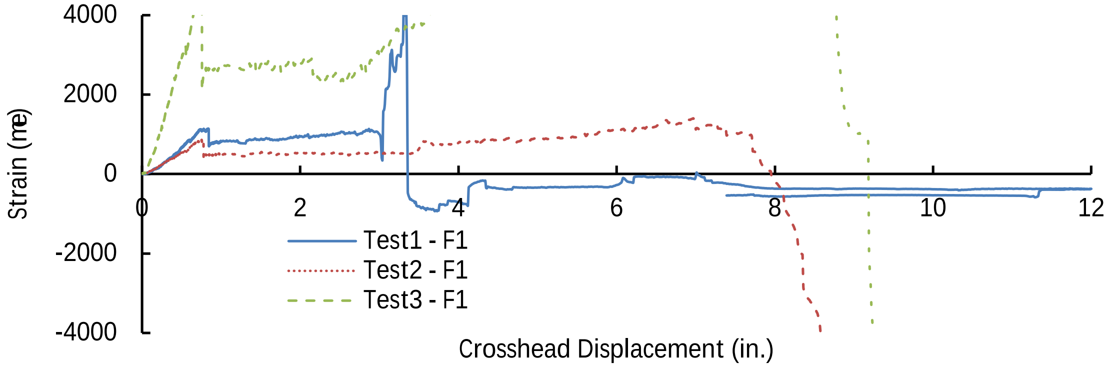

Figure E-157. Strain Gage F1 Response of Three Repeated Tests of the 24-ply CFRP Panel Under 45-Degree Angle Penetration

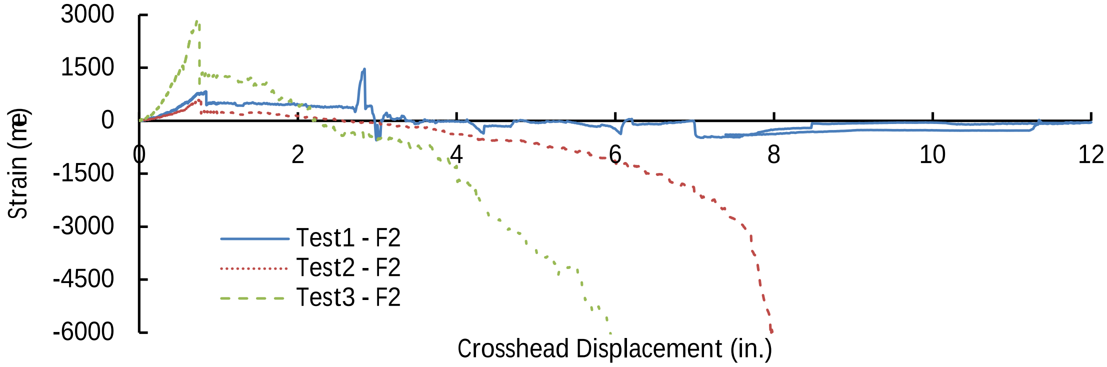

Figure E-158. Strain Gage F2 Response of Three Repeated Tests of the 24-ply CFRP Panel Under 45-Degree Angle Penetration

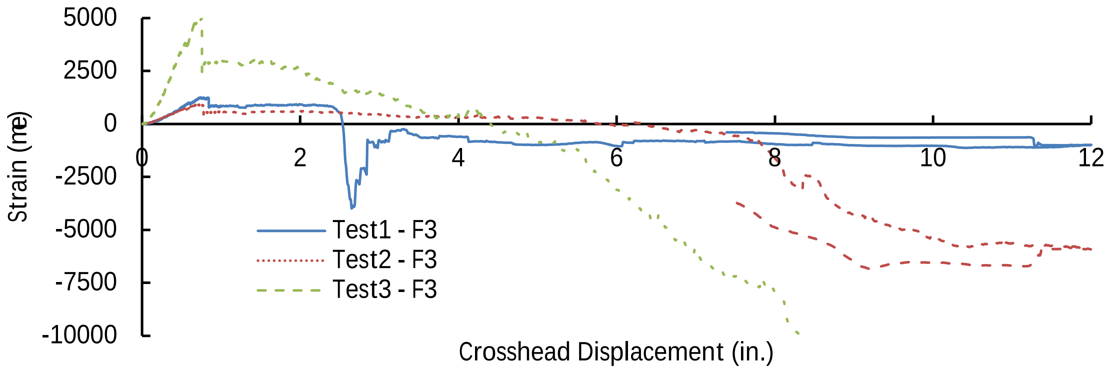

Figure E-159. Strain Gage F3 Response of Three Repeated Tests of the 24-ply CFRP Panel Under 45-Degree Angle Penetration

APPENDIX F—DIGITAL IMAGE CORRELATION RESULTS

F.1 NORMAL PENETRATION.

This appendix shows the deflection plots at increasing load, up to back surface crack initiation for the panels under test, which included three thicknesses each of aluminum panels, glass fiber-reinforced (GLARE) aluminum laminate panels, and carbon fiber-reinforced plastic (CFRP) laminate panels. Figures F-1 through F-9 show the plots for tests under normal (90-degree) penetration condition.

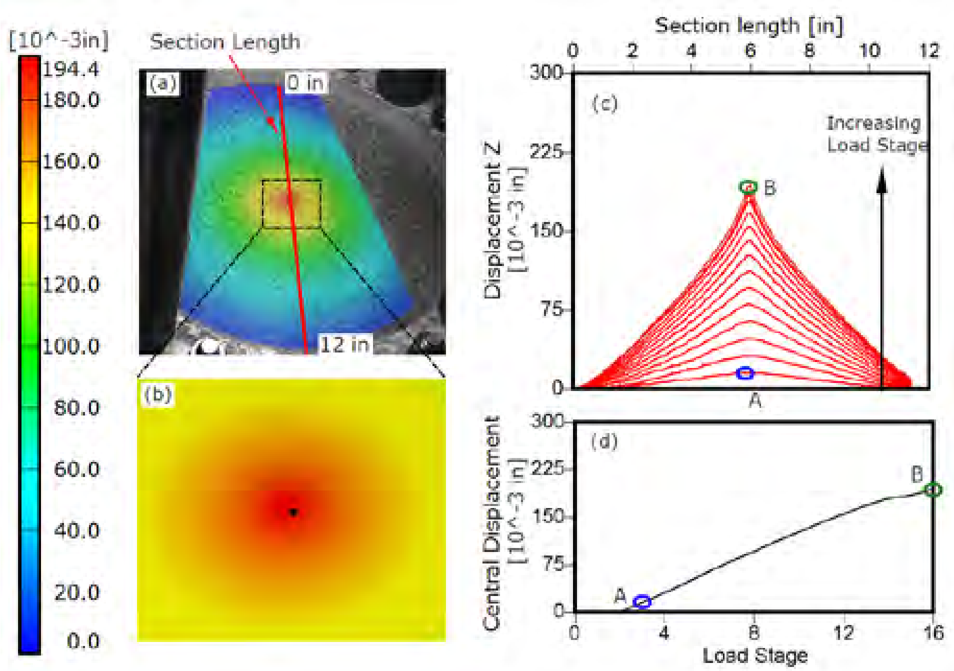

Figure F-1. Deflection Plots of a 0.04-in.-Thick Aluminum Panel Under Normal Penetration Condition Subjected to a Loading Rate of 0.001 in./s

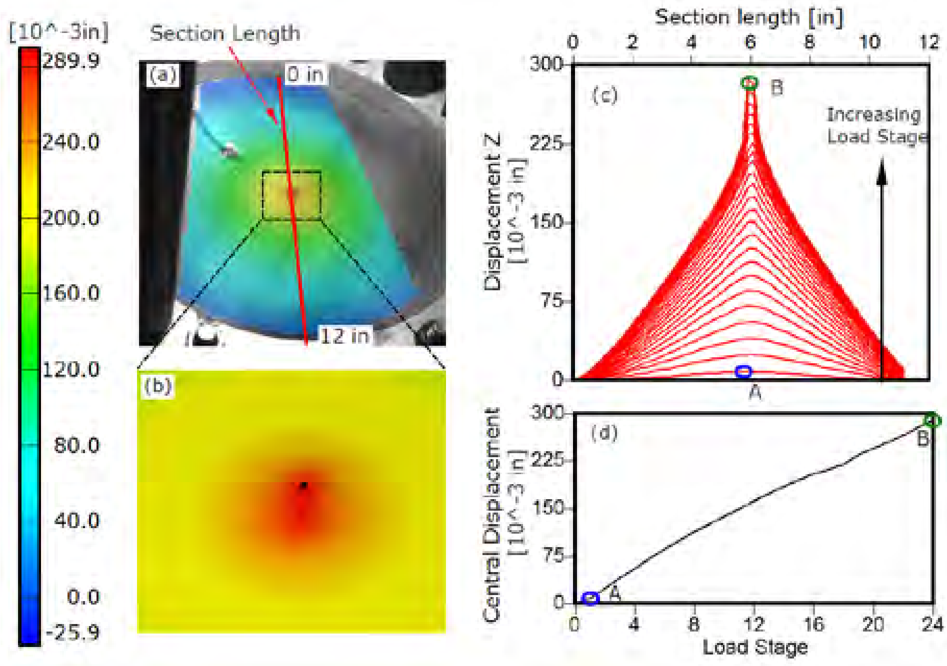

Figure F-2. Deflection Plots of a 0.06-in.-Thick Aluminum Panel Under Normal Penetration Condition Subjected to a Loading Rate of 0.001 in./s

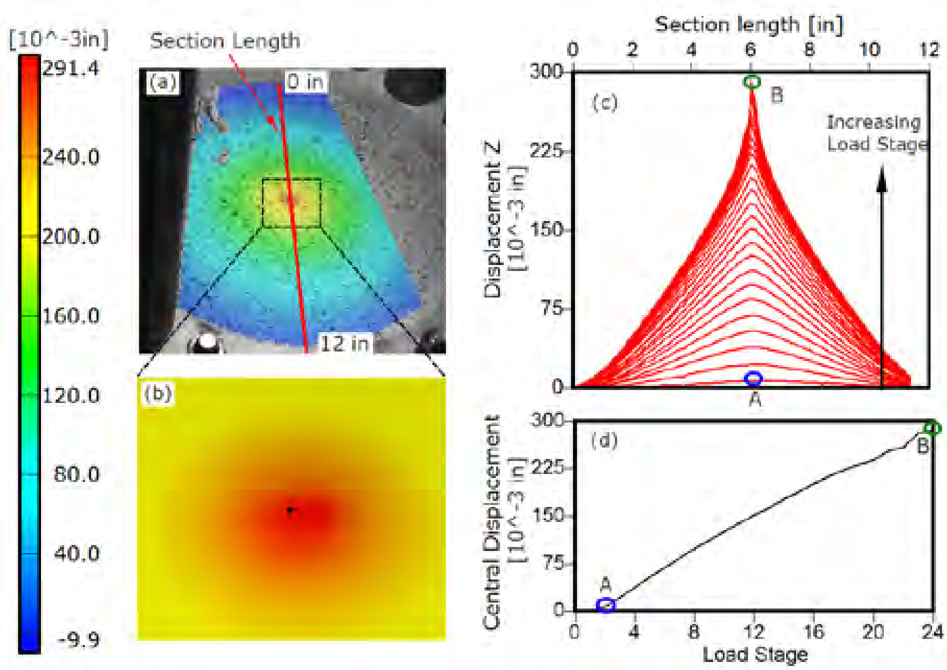

Figure F-3. Deflection Plots of a 0.08-in.-Thick Aluminum Panel Under Normal Penetration Condition Subjected to a Loading Rate of 0.001 in./s

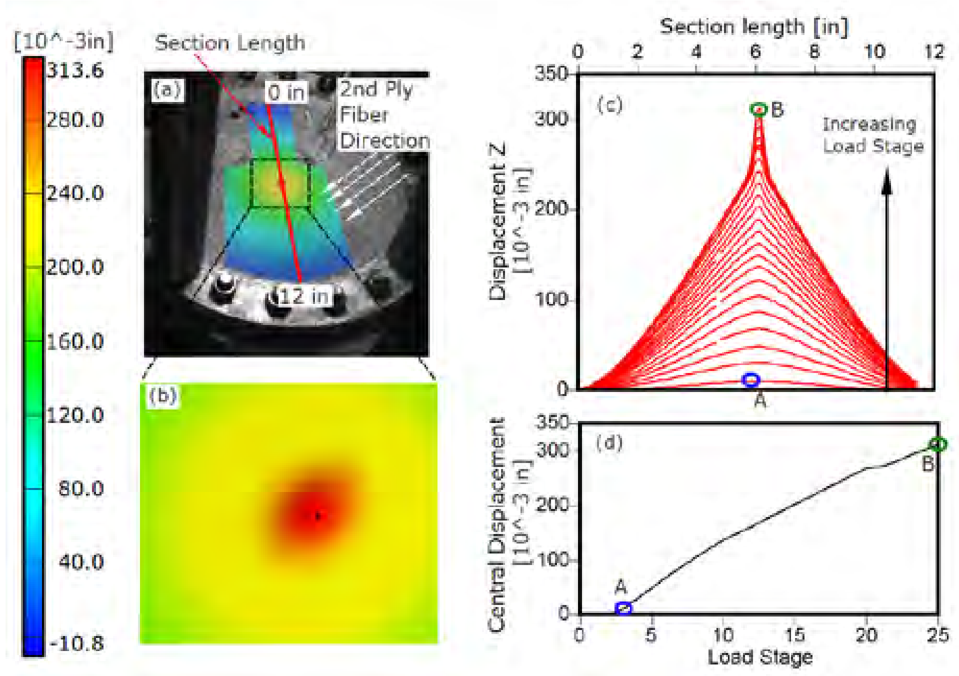

Figure F-4. Deflection Plots of a G3-4/3-0.4 GLARE Panel Under Normal Penetration Condition Subjected to a Loading Rate of 0.001 in./s

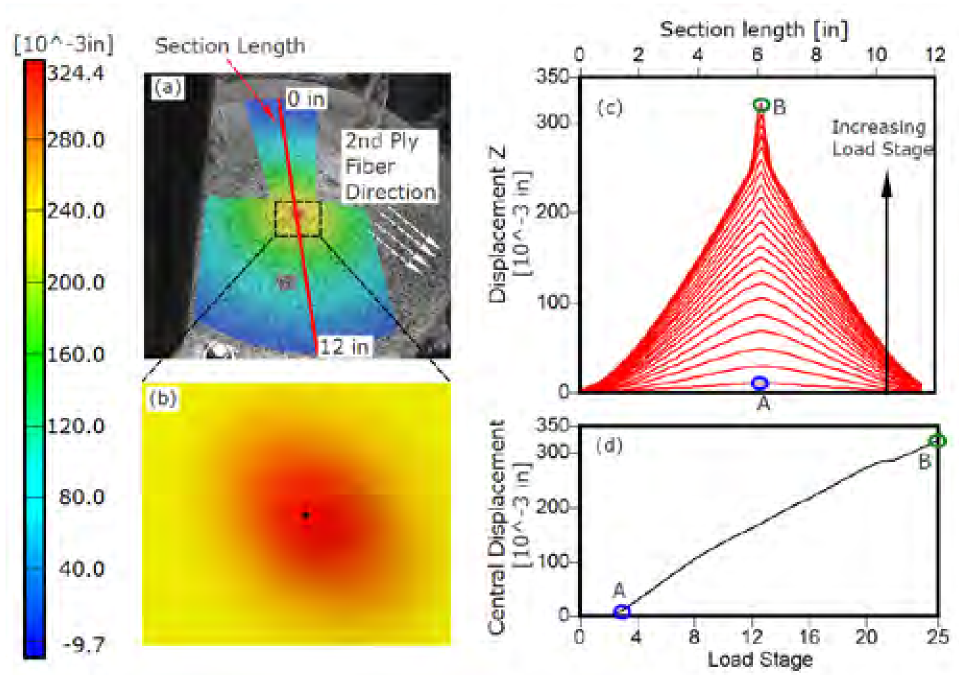

Figure F-5. Deflection Plots of a G3-5/4-0.3 GLARE Panel Under Normal Penetration Condition Subjected to a Loading Rate of 0.001 in./s

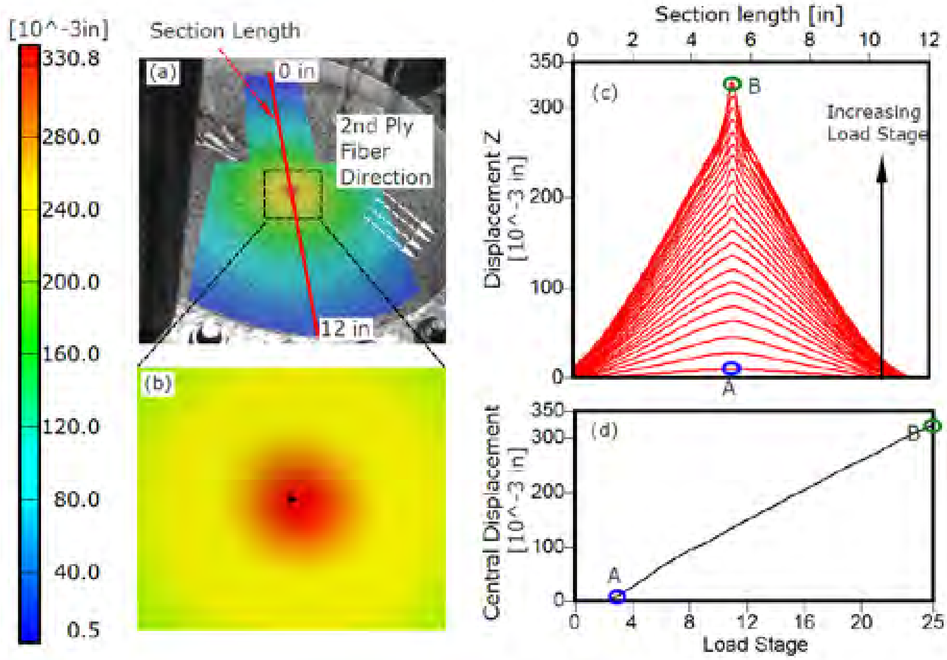

Figure F-6. Deflection Plots of a G5x-4/3-0.3 GLARE Panel Under Normal Penetration Condition Subjected to a Loading Rate of 0.001 in./s

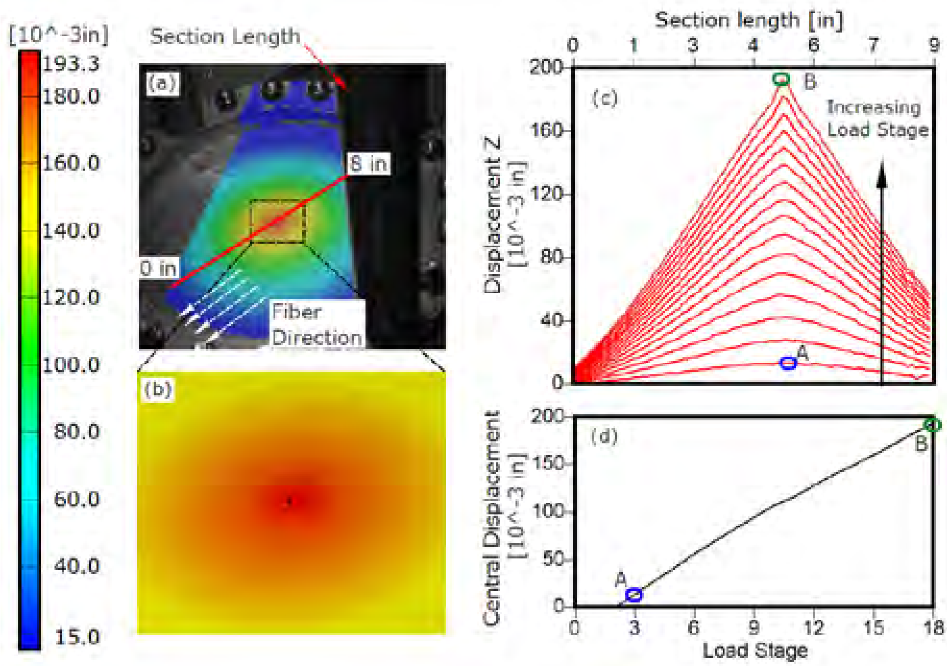

Figure F-7. Deflection Plots of a 12-ply CFRP Panel Under Normal Penetration Condition Subjected to a Loading Rate of 0.001 in./s

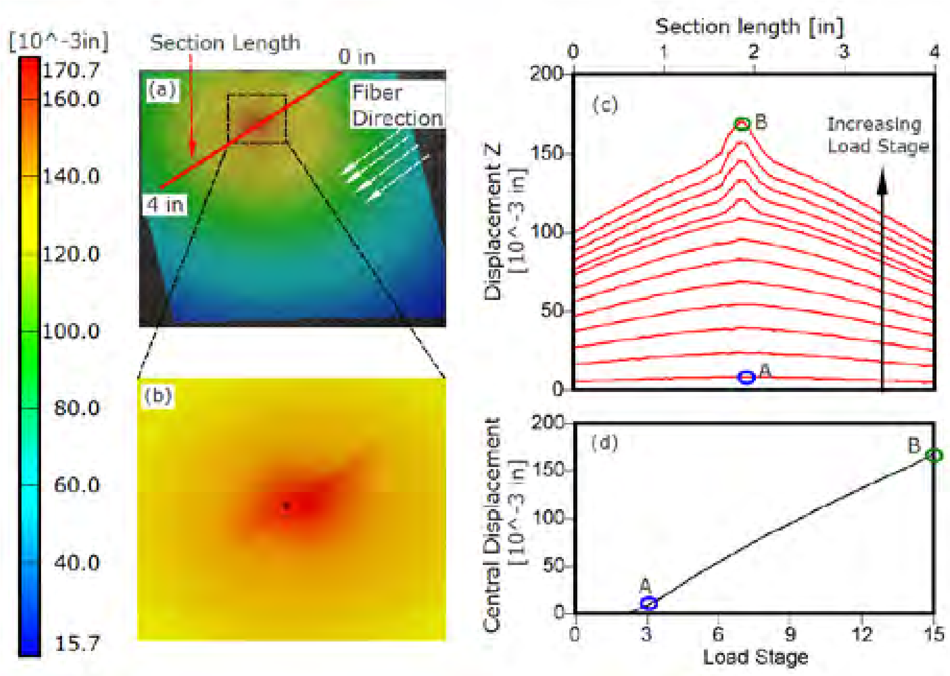

Figure F-8. Deflection Plots of a 16-ply CFRP Panel Under Normal Penetration Condition Subjected to a Loading Rate of 0.001 in./s

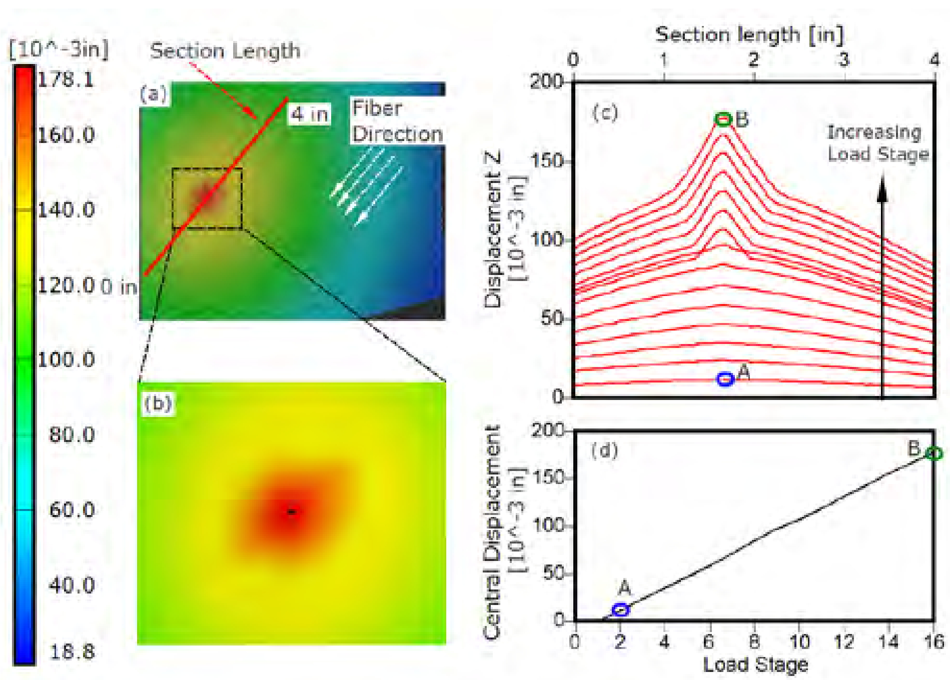

Figure F-9. Deflection plots of a 24-ply CFRP Panel Under Normal Penetration Condition Subjected to a Loading Rate of 0.001 in./s

F.2 THE 45-DEGREE ANGLE PENETRATION.

Figures F-10 through F-18 show the deflection plots at increasing load, up to back surface crack initiation for the panels under a 45-degree angle penetration condition, which included three thicknesses each of aluminum, GLARE laminate, and CFRP laminate panels.

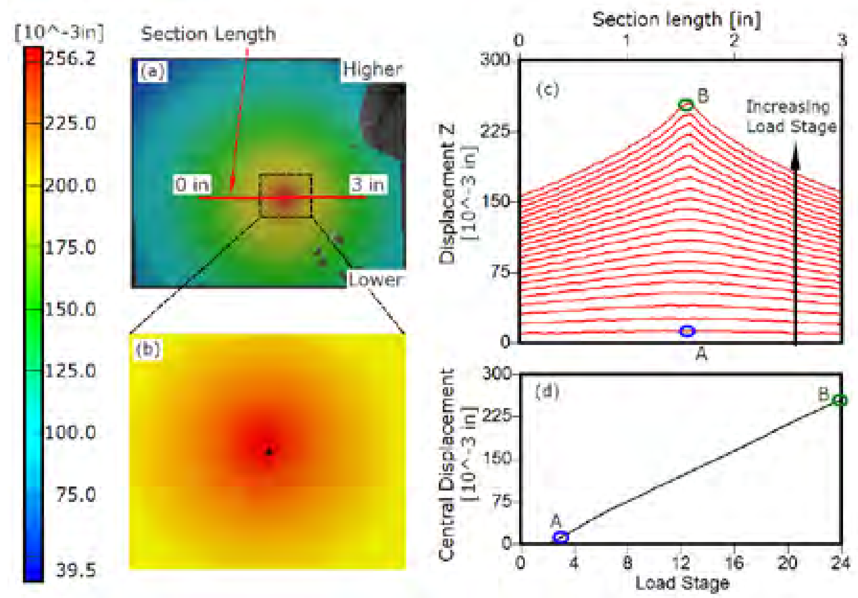

Figure F-10. Deflection Plots of a 0.04-in.-Thick Aluminum Panel Under 45-Degree Angle Penetration Condition Subjected to a Loading Rate of 0.001 in./s

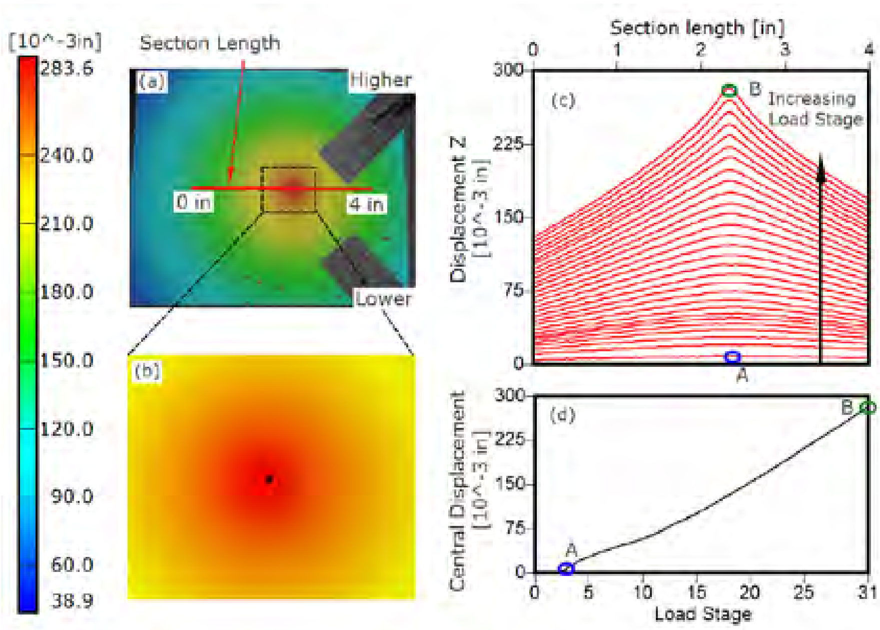

Figure F-11. Deflection Plots of a 0.06-in.-Thick Aluminum Panel Under 45-Degree Angle Penetration Condition Subjected to a Loading Rate of 0.001 in./s

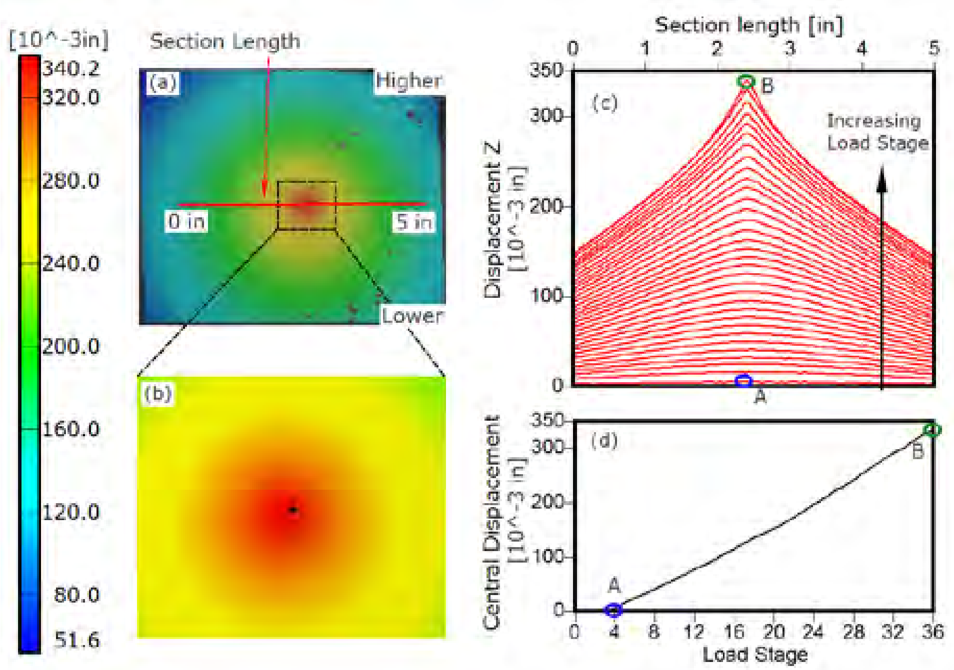

Figure F-12. Deflection Plots of a 0.08-in.-Thick Aluminum Panel Under 45-Degree Angle Penetration Condition Subjected to a Loading Rate of 0.001 in./s

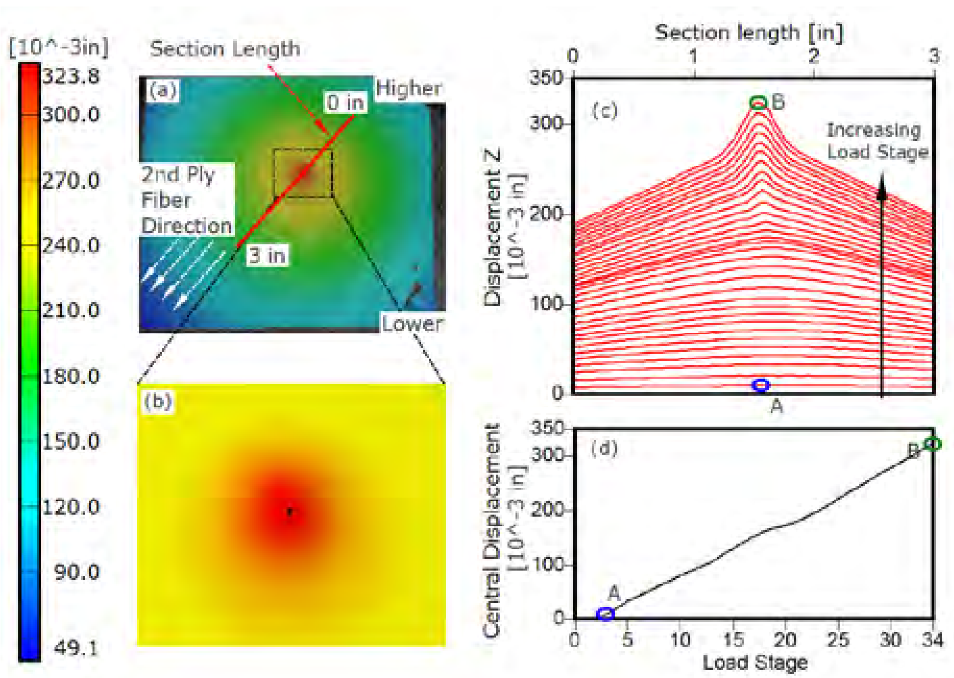

Figure F-13. Deflection Plots of a G3-4/3-0.4 GLARE Panel Under 45-Degree Angle Penetration Condition Subjected to a Loading Rate of 0.001 in./s

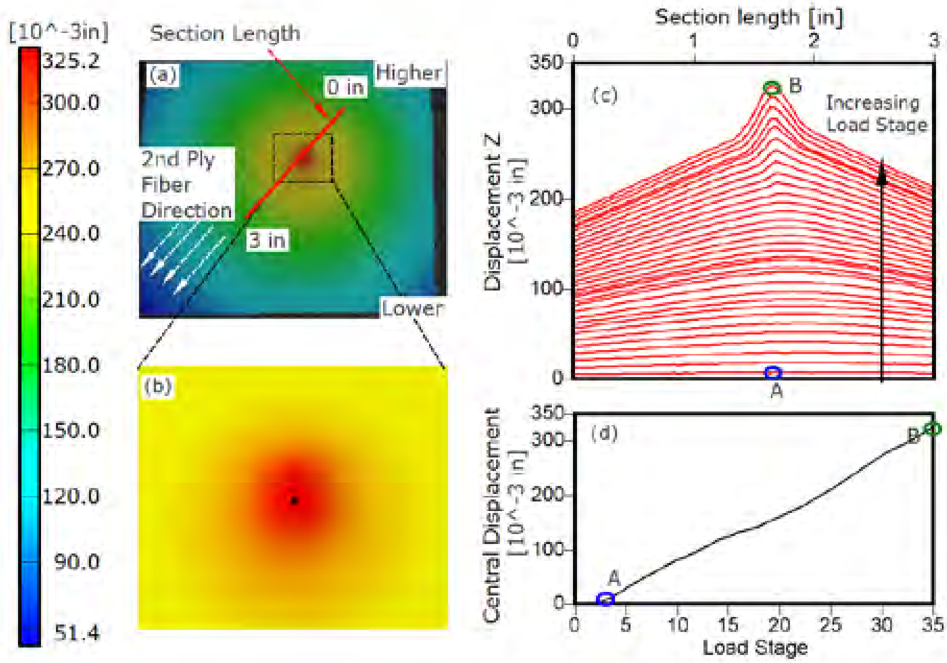

Figure F-14. Deflection Plots of a G3-5/4-0.3 GLARE Panel Under 45-Degree Angle Penetration Condition Subjected to a Loading Rate of 0.001 in./s

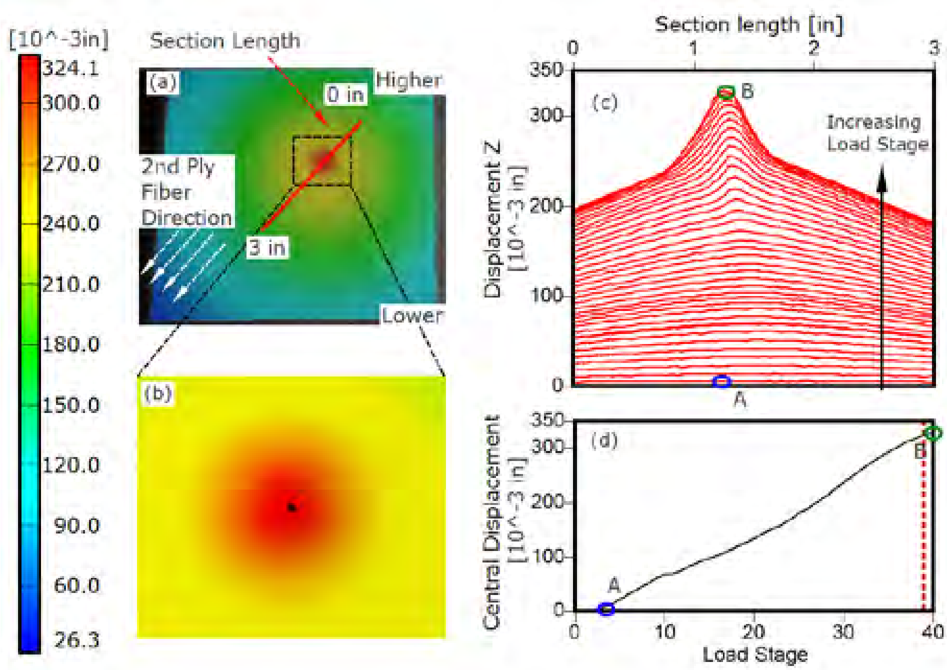

Figure F-15. Deflection Plots of a G5x-4/3-0.3 GLARE Panel Under 45-Degree Angle Penetration Condition Subjected to a Loading Rate of 0.001 in./s

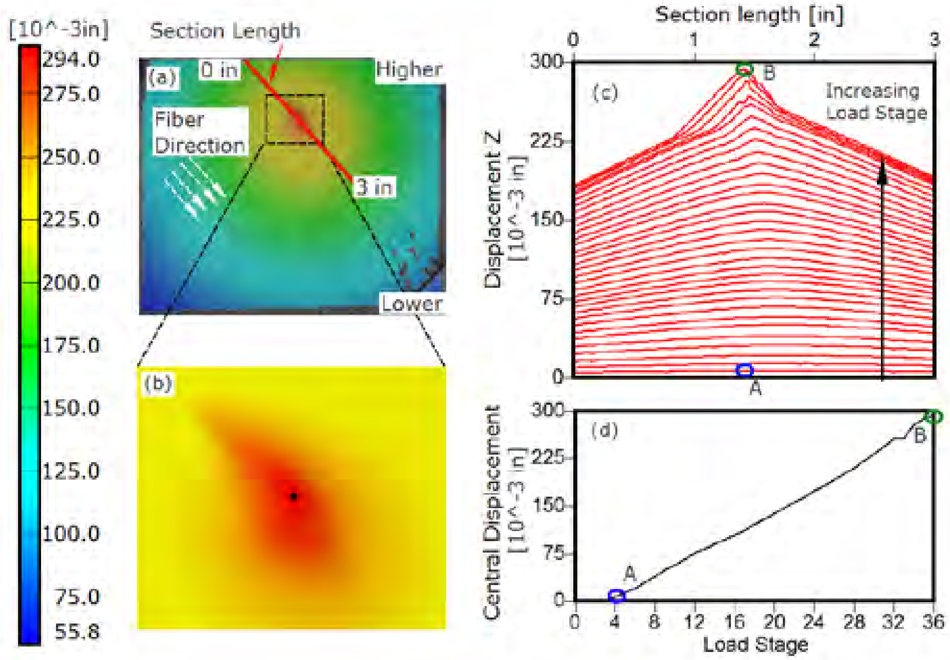

Figure F-16. Deflection Plots of a 12-ply CFRP Panel Under 45-Degree Angle Penetration Condition Subjected to a Loading Rate of 0.001 in./s

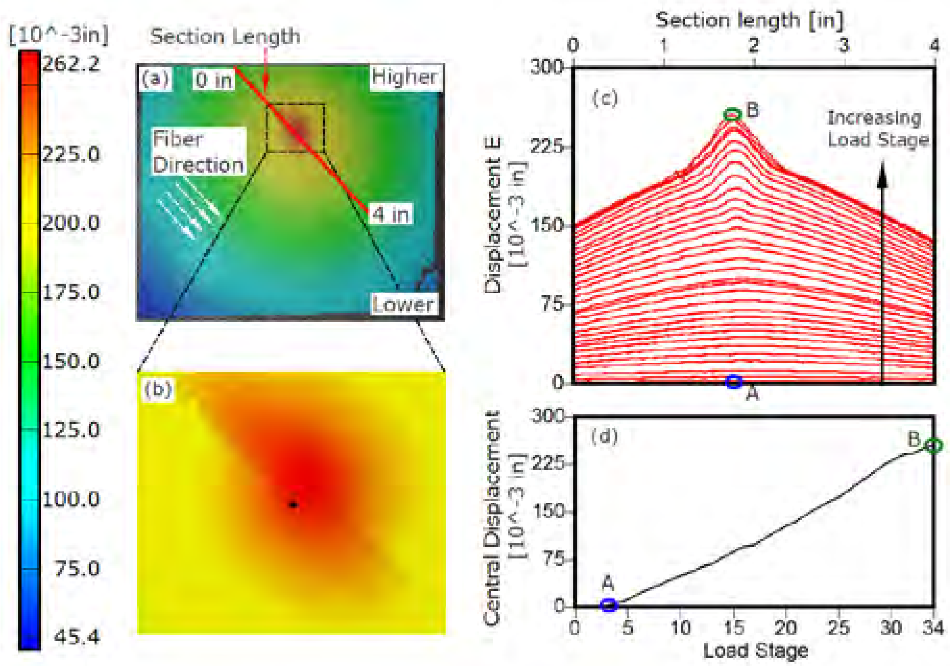

Figure F-17. Deflection Plots of a 16-ply CFRP Panel Under 45-Degree Angle Penetration Condition Subjected to a Loading Rate of 0.001 in./s

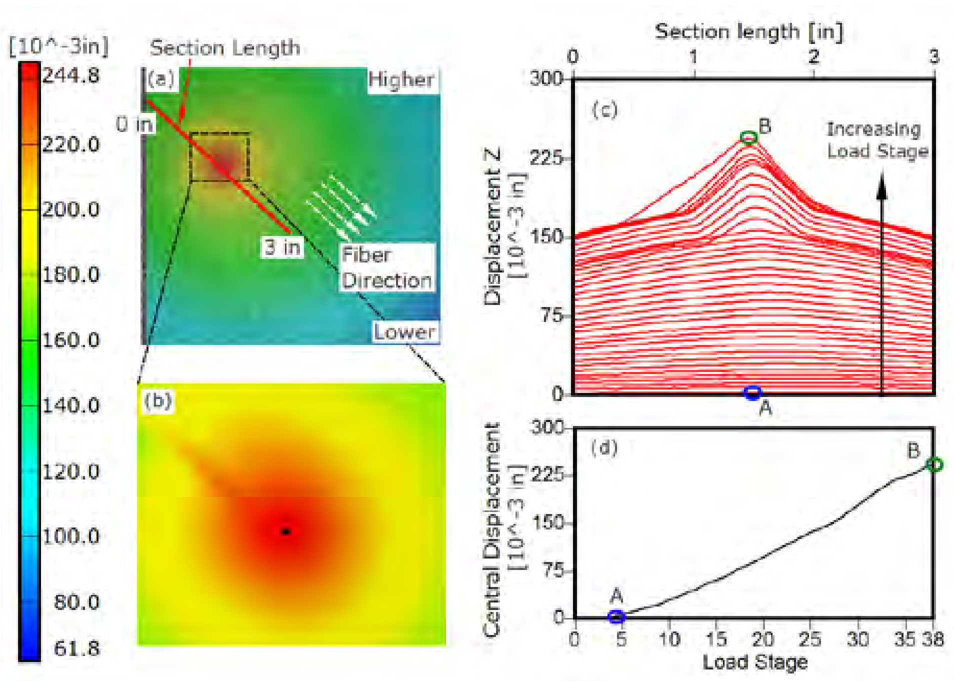

Figure F-18. Deflection Plots of a 24-ply CFRP Panel Under 45-Degree Angle Penetration Condition Subjected to a Loading Rate of 0.001 in./s

APPENDIX G—POLISHED MICROGRAPH RESULTS

Figures G-1 and G-2 show the cross-sectional images of the damage evolution of glass fiber-reinforced (GLARE) aluminum laminate panels at different loading stages.

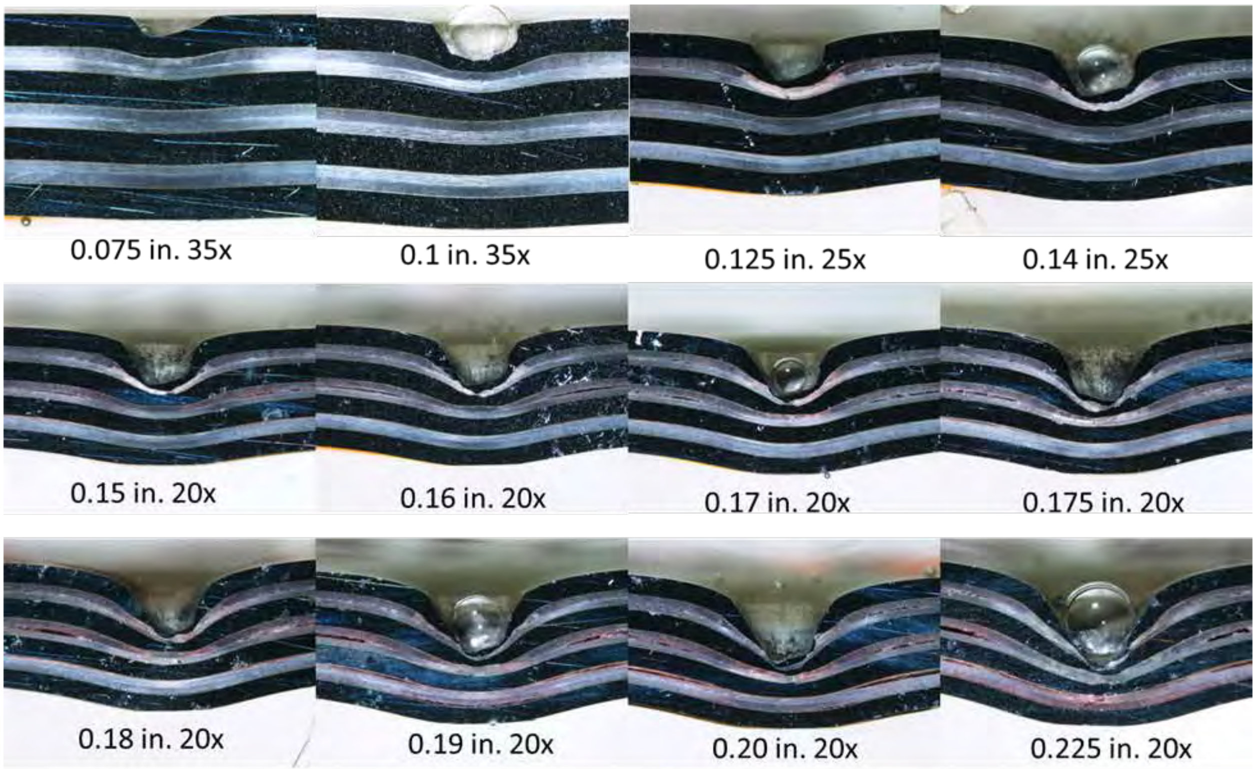

Figure G-1. Cross-Sectional Images of the GLARE 3-4/3-0.4 Panels

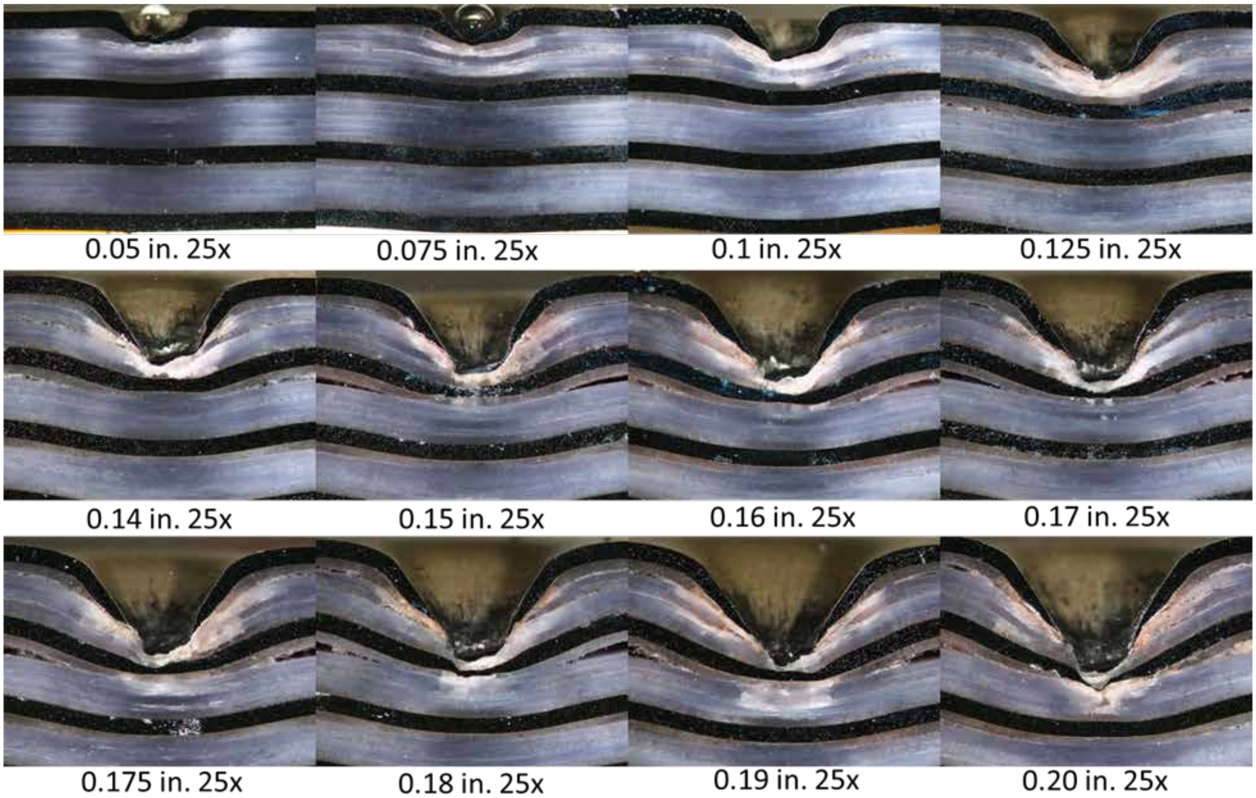

Figure G-2. Cross-Sectional Images of the GLARE 5x-4/3-0.3 Panels